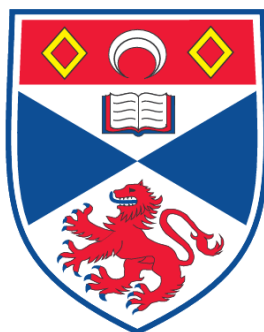


**A STUDY OF SUPERCONDUCTIVITY IN SINGLE CRYSTALS AND  
THIN FILMS USING MUON-SPIN ROTATION AND NEUTRON  
SCATTERING**

**David Owen Goudie Heron**

**A Thesis Submitted for the Degree of PhD  
at the  
University of St. Andrews**



**2009**

**Full metadata for this item is available in the St Andrews  
Digital Research Repository  
at:**

**<https://research-repository.st-andrews.ac.uk/>**

**Please use this identifier to cite or link to this item:**

**<http://hdl.handle.net/10023/742>**

**This item is protected by original copyright**

# A Study of Superconductivity in Single Crystals and Thin Films using Muon-Spin Rotation and Neutron Scattering

David Owen Goudie Heron



Thesis submitted to the School of Physics and Astronomy  
at the University of St Andrews for the degree of Doctor of Philosophy  
July 2008

**Supervisor: Professor Stephen Lee**



# Declaration

I, David Heron, hereby certify that this thesis, which is approximately 40000 words in length, has been written by me and is the record of work carried out by me and has not been submitted in any previous application for a higher degree.

David Heron

July 21, 2008

I was admitted as a research student in June 2004 and as a candidate for the degree of Doctor of Philosophy in June 2004; the higher study for which this is a record was carried out in the University of St Andrews between 2004 and 2008.

David Heron

July 21, 2008

I hereby certify that the candidate has fulfilled the conditions for the Resolution and Regulations appropriate for the degree of Doctor of Philosophy in the University of St Andrews and that the candidate is qualified to submit this thesis in application for this degree.

Stephen L. Lee

July 21, 2008

# Copyright Declaration

In submitting this thesis to the University of St Andrews we understand that we are giving permission for it to be made available for use in accordance with the regulations of the University Library for the time being in force, subject to any copyright vested in the work not being affected thereby. We also understand that the title and abstract will be published, and that a copy of the work may be made and supplied to any bona fide library or research worker, that the thesis will be electronically accessible for personal or research use unless exempt by award of an embargo as requested below, and that the library has the right to migrate the thesis into new electronic forms as required to ensure continued access to the thesis. We have obtained any third-party copyright permissions that may be required in order to allow such access and migration, or have requested the appropriate embargo below.

The following is an agreed request by candidate and supervisor regarding the electronic publication of this thesis:

Access to Printed copy and electronic publication of thesis through the University of St Andrews.

Date..... signature of candidate ..... signature of supervisor .....

## Abstract

The archetypal high temperature superconductor  $\text{Bi}_2\text{Sr}_2\text{CaCu}_2\text{O}_{8+\delta}$  has been extensively investigated. However, until now, little has been known about the behaviour of the magnetic vortices inside the Vortex Glass and liquid state.  $\mu\text{SR}$  measurements have shown a negative skewness for the field probability distributions in these regimes. Such a negative skewness has only recently been explained as being a direct consequence of three-body correlations between vortices in a similar layered superconductor. With a new understanding and knowledge of the physics of these systems, it is instructive to re-visit the superconductor  $\text{Bi}_2\text{Sr}_2\text{CaCu}_2\text{O}_{8+\delta}$  to explain the evolution of these three-body correlations occurring here.

Comparing this with the ion-irradiated superconductors (of the same  $\text{Bi}_2\text{Sr}_2\text{CaCu}_2\text{O}_{8+\delta}$  material), allows one to observe how three-body correlations between vortices evolve differently to that in the pristine material. Moreover, in the region of the macroscopic irreversibility line, entropically driven disorder exists below the matching field  $B_\phi$ , whilst there is the appearance of relatively straight vortex lines at fields above  $B_\phi$ . Such phenomena suggest a significant difference in the evolution of three-body correlations compared with the unirradiated material.

There has been much work conducted on the interplay between superconductivity and magnetism in materials of reduced dimensions. Work presented here on the ferromagnet/superconductor trilayer system (Permalloy/Nb/Permalloy) has shown a novel magnetic profile at the interface between the ferromagnetic and superconducting boundary, where, contrary to what is expected, the magnetism appears to be significantly suppressed at the interface before increasing towards the centre of the Nb layer.

# Acknowledgements

It would not have been possible for me to complete the work in this thesis without the continued support of my supervisor Prof. Stephen Lee whose help and perseverance with me has been much appreciated over the past four years. Dr. Alan Drew and Dr. Stephen Lister have been instrumental in developing my knowledge of this field. The latter for the initial stages and the former for taking the skills I had acquired and guiding me through applying them. Thank you also to Dr. Matthew Wismayer with whom I have shared many insightful conversations. I am also extremely appreciative of the many others who have, at some time or another, given their professional and personal time up for me. These include the many muon and neutron users I have had the pleasure of working with as well as those colleagues (both academic and administrative) at St. Andrews. The time and patience you have shown me is greatly appreciated.

Personally, the work in this thesis would not have been possible without the ongoing support of my family both close and extended. All family members (Finn and Heron) have always shown interest in my work, which has meant a great deal to me. Thank you all for being supportive.

Finally, I would like to mention my parents. Thank you for having faith in me throughout this time and supporting me through the difficult times. I hope I had managed to make you proud (Remember, "How the mighty have fallen?"). Thank you for inspiring me to achieve this stage. This is for you.

ME: Mum, I've just submitted my thesis!

MUM: Well, thank God for that!

*This thesis is dedicated to my parents, Tom and Clare.*

# Contents

<b>1</b>	<b>Introduction</b>	<b>1</b>
<b>2</b>	<b>Introduction to Theory</b>	<b>3</b>
2.1	Introduction to Superconductivity . . . . .	3
2.1.1	Layered Superconductors . . . . .	7
2.1.2	Pinning . . . . .	9
2.1.3	Melting of the Flux Line Lattice (FLL) and the Macroscopic Irreversibility line . . . . .	10
2.2	Introduction to Magnetism . . . . .	14
<b>3</b>	<b>Experimental Techniques</b>	<b>20</b>
3.1	Muon Spin Rotation . . . . .	20
3.1.1	Muon production . . . . .	20
3.1.2	The Transverse Field $\mu$ SR Technique . . . . .	22
3.1.3	The Maximum Entropy Method (MEM) . . . . .	27
3.1.4	The $\mu$ SR lineshape of a FLL . . . . .	29
3.1.5	The Low Energy Muon Technique . . . . .	33
3.2	Neutron Scattering Techniques . . . . .	37
3.2.1	Neutron Production . . . . .	37
3.2.2	Introduction to scattering . . . . .	38
3.2.3	Scattering from a crystal lattice . . . . .	41
3.2.4	Scattering from the FLL . . . . .	46
3.2.5	Small Angle Neutron Scattering (SANS) . . . . .	47
3.2.6	Polarised Neutron Reflectivity . . . . .	48
3.3	Bulk Magnetisation Measurements . . . . .	52
3.3.1	Macroscopic Features of Superconductors . . . . .	54
<b>4</b>	<b>Measurements on the FLL of <math>\text{Bi}_{2.15}\text{Sr}_{1.85}\text{CaCu}_2\text{O}_{8+\delta}</math></b>	<b>58</b>
4.0.2	Background and Motivation . . . . .	58
4.0.3	Experimental Preparation . . . . .	62
4.0.4	Discussion of results . . . . .	63
4.0.5	Conclusions and Further Work . . . . .	79
<b>5</b>	<b>Measurements on the irradiated FLL of <math>\text{Bi}_{2.15}\text{Sr}_{1.85}\text{CaCu}_2\text{O}_{8+\delta}</math></b>	<b>82</b>

---

5.1	Background and Motivation . . . . .	82
5.2	Discussion of Experimental Results . . . . .	85
<b>6</b>	<b>Measurements on the layered material: Nb(20Å) / Py(200Å) / Nb(500Å)</b>	
	<b>/ Py(500Å) / Si</b>	<b>113</b>
6.1	Overview of Previous LEM $\mu$ SR Work . . . . .	113
6.2	Sample Preparation . . . . .	116
6.3	Discussion of PNR results . . . . .	116
6.4	Discussion of Low Energy $\mu$ SR results . . . . .	123

# Chapter 1

## Introduction

This thesis comprises work conducted over the period June 2004 / June 2008. The initial premise of the work was to investigate the possible co-existence of magnetism and superconductivity in thin films. However, due to the recent upgrade of the low energy muon instrument at the Paul Scherrer Institut in Switzerland, which meant that no experiments took place on this apparatus, the programme for this thesis had to be revised. As such, there are two experimental chapters detailing experimental work conducted on both pristine and irradiated  $\text{Bi}_2\text{Sr}_2\text{CaCu}_2\text{O}_{8+\delta}$  (BSCCO) superconducting crystals and one investigating the interplay between magnetism and superconductivity in a ferromagnetic (FM) / superconducting (SC) multilayer film.

Chapter 1 explains the underlying theory and history associated with the superconductivity and magnetism investigated within this thesis. For the superconductivity theory, the main focus is on the formation and behaviour of the flux line lattice (FLL) within the high temperature superconductors (HTSCs). An explanation of basic phenomena as well as relevant highlights of previous work is presented.

The magnetism theory associated with the FM/SC material described in Chapter 5 is then discussed, starting with the direct exchange interaction and Pauli paramagnetism before discussing the phenomena of the RKKY interaction associated with the rare earth metals and the FFLO theory used to help explain behaviour in certain superconductors.

The experimental methods used throughout this work are explained in Chapter 3, detailing the muon spin rotation ( $\mu\text{SR}$ ) techniques (both bulk and low energy), and the neutron scattering theory associated with Small Angle Neutron Scattering (SANS) and Polarised Neutron Reflectivity (PNR). Aside from this, macroscopic characterisation measurements were performed on all the samples detailed within this thesis using the MPMS SQUID device, whose operation is also described.

Chapter 4 discusses new experimental work performed on the archetypal HTSC BSCCO. This work follows that conducted by Menon et al (2006) in which three body correlations were shown and explained for the first time in a bulk 3D system ( $\text{La}_{2-x}\text{Sr}_x\text{CuO}_4$ ). It has therefore been intuitive, with new data and a new understanding of the physics associated with these materials, to revisit some of the work conducted on BSCCO in order to resolve some of the outstanding issues.

Subsequently, it is of interest to see how such three-body correlations evolve inside a highly irradiated sample of BSCCO. By irradiating the HTSC crystals with heavy ions (for

example, Sr), it is possible to create defect tracks through the material - each of which acts as an attractive pinning site for a magnetic vortex. Chapter 5 investigates the behaviour of the FLL (using the bulk  $\mu$ SR and SANS techniques) in two BSCCO materials for which the matching field  $B_\phi$  (the point at which the number of vortices is equal to the number of columnar defect tracks) is 0.2T and 0.1T.

Finally, Chapter 6 details work conducted on a thin film sample comprising predominantly the layers, Permalloy/Nb/Permalloy, where the Permalloy (Py) consists of 20% Fe and 80% Ni and the layer thicknesses are: 200Å/500Å/500Å respectively. The aim of this particular work was to investigate the interplay of magnetism and superconductivity within materials of reduced dimensions and follows on from similar work recently conducted on Fe/Pb bilayers (Drew 2006).

# Chapter 2

## Introduction to Theory

### 2.1 Introduction to Superconductivity

Since the discovery of superconductivity in 1911 (Onnes 1911), there has been much interest in materials that exhibit this phenomenon - more so, since the advent of the high temperature superconductors (HTSCs) in 1987 (Bednorz & Muller 1987). These type of materials are those that, when cooled below a certain critical temperature  $T_c$ , exhibit two very interesting properties: zero resistance and magnetic flux expulsion - both dependent upon the number of superconducting electrons available. In the normal metallic state, repulsion occurs between two or more electrons due to the Coulombic interaction. However, a theory was presented by Cooper (1956) (and shown experimentally by Bardeen & Schrieffer (1957)) in which it was hypothesised that two electrons can attract one another - when cooled below  $T_c$  into the superconducting state - through the mediation of lattice phonons (Figure 2.1). The resulting size of this pair (which has zero net momentum and its individual spins aligned anti-parallel to one another), is characterised by the coherence length  $\xi$  as is shown in Figure 2.2. Moreover, these electron pairs condense into the same quantum state, described by a single superconducting wavefunction that is proportional to the square root of the superelectron number density  $n_s$ :

$$|\Psi| = \sqrt{n_s} \quad (2.1)$$

As one cools the superconducting material below  $T_c$ , the number of superconducting electrons increases as described by a two-fluid model (Tinkham 1975):

$$n_s(T) = n_s(0) \left[ 1 - \left( \frac{T}{T_c} \right)^4 \right] \quad (2.2)$$

where  $n_s(0)$  and  $n_s(T)$  are the superelectron densities at  $T=0\text{K}$  and at a defined temperature  $T$  respectively. Such a model describes those electrons with energies below the superconducting energy gap  $\Delta$ .

It was the London brothers who, in 1935, combined Maxwell's equations with the notion of a quantum coherent state to relate the supercurrent density  $J_s$  to the magnetic flux (London & London 1935):

$$\Lambda \mathbf{J}_s = -\mu_0 \mathbf{A} \quad (2.3)$$

where  $\Lambda = m_e / n_e e^2$ ,  $m_e$  is the effective mass and  $n_e$  is the number density of the electrons. Using this and combining it with Maxwell's equations gives:

$$\nabla^2 \mathbf{B} = \frac{\mathbf{B}}{\lambda_L^2} \quad (2.4)$$

where  $\lambda_L$  denotes the London penetration depth - a characteristic length-scale representing the distance over which the applied magnetic field  $\mathbf{B}$  is screened by the circulating supercurrents. Such a description is valid for steady-state currents and fields (i.e. not varying as a function of time). The solution of this demonstrates the exponential decay of the flux as a function of distance  $r$  as it enters the bulk of the superconductor:

$$B(r) = B(0) \exp\left(\frac{-r}{\lambda_L}\right) \quad (2.5)$$

However, it was Ginzburg & Landau (1950) who first proposed a lengthscale over which the number of superconducting electrons changed appreciably. This was different to the previously assumed infinitely thin boundary between these and the normal conduction

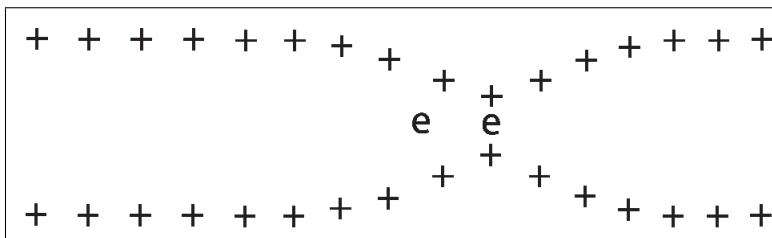


Figure 2.1: *In this schematic cartoon, an electron “e” moves through a material and consequently the positive ions “+” are attracted to its negative charge. This lattice distortion consequently results in the attraction of another electron.*

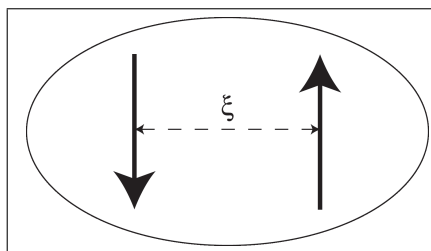


Figure 2.2: *The length of a Cooper pair is characterised by the coherence length  $\xi$ . It comprises 2 electrons, each with spins anti-parallel to one another, and with a total net momentum of zero.*

electrons. This new quantity was known as the coherence length  $\xi$  and its magnitude determined a characteristic length over which the supercurrent rose from zero to its maximum value.

Indeed, understanding the boundary between the superconducting and normal magnetic regions is important in determining whether such a material is either type I or type II superconducting. As was shown by Abrikosov (1957), the ratio

$$\kappa = \frac{\lambda}{\xi} \quad (2.6)$$

can be used to determine the type of superconductor under investigation and it was shown that a crossover value for  $\kappa$  of  $1/\sqrt{2}$  exists, where type I superconductors are characterised by  $\kappa < 1/\sqrt{2}$  and type II by  $\kappa \geq 1/\sqrt{2}$ .

More specifically, the relationship between  $\lambda$  and  $\xi$  can be used to explain the surface energy at the boundary of the normal and superconducting regions. For type I superconductors  $\xi$  is greater than the penetration depth  $\lambda$ . If  $\kappa \ll 1$ , then the difference between the two quantities ( $\xi - \lambda$ ) describes a positive surface energy between the normal and superconducting states (see Figure 2.3).

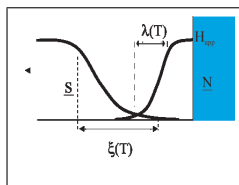


Figure 2.3: *At the boundary between a normal  $N$  region and superconducting  $S$  region for type I superconductors. Moving from right to left; as one leaves the normal metallic region (denoted by the blue area) and enters the superconducting region, the number density of superelectrons increases and the extent of the penetration depth  $\lambda$  becomes less than the coherence length  $\xi$ .*

However, if a material has  $\kappa \gg 1$ , the surface energy at the interface becomes negative (Figure 2.4). In this scenario, a reduction in the mean free path of the electrons reduces the coherence length and thus increases the penetration depth. As such, there is a negative surface energy. The material assumes the position of lowest free energy and a normal magnetic region serves to reduce this energy. Thus, the inclusion of small amounts of flux inside the sample create more normal/superconducting boundaries and hence produce a minimum free energy. More specifically, quantised amounts of magnetic flux are admitted into the bulk superconductor and such a material is known as a type II superconductor.

The quantised flux (characterised by an amount  $\Phi_0 = h/2e$ ) allowed into a type II superconductor takes the form of magnetic vortices, as shown in Figure 2.5. Each vortex is made up of a central core of radius  $\xi^1$  that comprises normal electrons with the magnetic flux itself being generated from a supercurrent that circulates around with a radius of

<sup>1</sup>Note that this is not the same as the definition of  $\xi$  for the length of the Cooper Pair

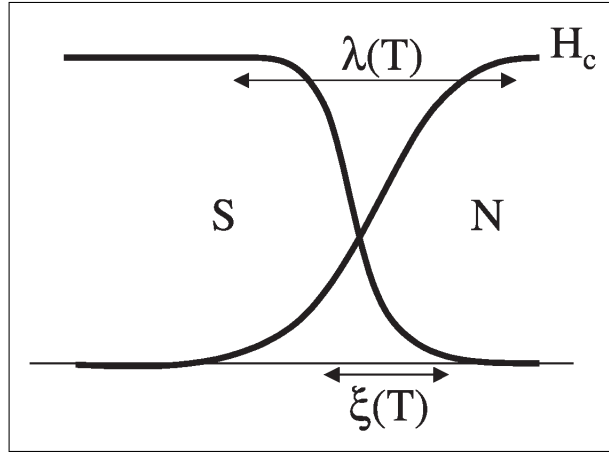


Figure 2.4: At the boundary between a normal  $N$  region (denoted by the blue area) and superconducting region  $S$  in a type II superconductor. Moving from right to left; as one leaves the normal metallic region (denoted by the blue area) and enters the superconducting region, the number density of superelectrons increases but the extent of the penetration depth  $\lambda$  is less than the coherence length  $\xi$ . This leads to a negative surface energy and, consequently, the formation of magnetic vortices inside the material.

the penetration length  $\lambda$ . The flux quantisation originates from the nature of the electron wavefunction at a particular position. The electron wavefunction should possess an integer number of wavelengths as it circulates the vortex core and thus be single-valued at any point along the wave. In order for this to occur the total phase difference  $\Delta\phi$  between two points X and Y on a closed loop of length  $l$  must be:

$$\Delta\phi = \frac{4\pi m}{\hbar n_s e} \int_X^Y \mathbf{J}_s \cdot d\mathbf{l} + \frac{4\pi e}{\hbar} \int_X^Y \mathbf{A} \cdot d\mathbf{l} = 2\pi n \quad (2.7)$$

where  $\mathbf{A}$  is the magnetic vector potential,  $\mathbf{J}_s$  is the supercurrent density, and  $m$  is the effective mass of the superconducting electron. This, when re-arranged, gives:

$$\frac{m}{n_s e^2} \oint \mathbf{J}_s \cdot d\mathbf{l} + \int_S \int \mathbf{B} \cdot d\mathbf{S} = n \frac{h}{2e} \quad (2.8)$$

over an area  $S$  and produces the flux quantisation value defined above.

This flux decays in the form of a zeroth order Hankel function that can be approximated over two different ranges (Tinkham 1975)

For  $\xi \ll r \ll \lambda$ :

$$B(r) \rightarrow \frac{\Phi_0}{2\pi\lambda^2} \ln \frac{\lambda}{r} \quad (2.9)$$

For  $r \gg \lambda$ :

$$B(r) \rightarrow \frac{\Phi_0}{2\pi\lambda^2} \sqrt{\frac{\lambda}{r}} \exp\left(\frac{-r}{\lambda}\right) \quad (2.10)$$

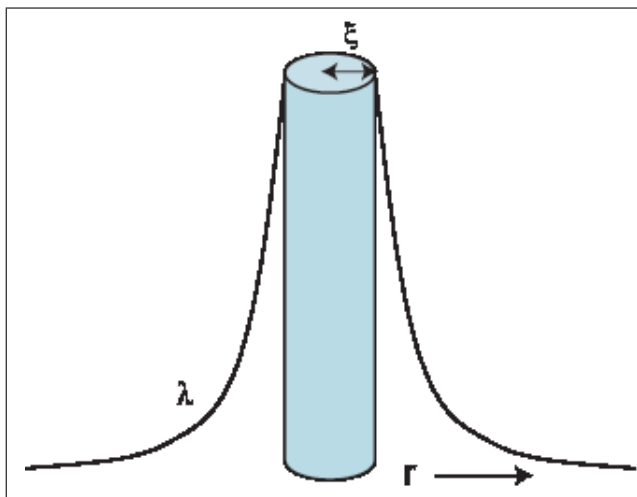


Figure 2.5: *The magnetic vortex (shown by the cartoon in blue) has a field profile, characterised by a radius  $\xi$ , that can be described by the zeroth order Hankel function; the form of which depends upon the distance  $r$  away from the vortex core.*

Below a critical applied field  $H_{c1}$ , complete flux expulsion occurs for a type II superconductor (denoted as “A” in Figure 2.7). As the applied field is increased beyond this value, an increasing number of vortices enter the material. This phase is known as the “mixed state”.

A system consisting of many vortices is known as a flux line lattice (FLL) and it has been shown that for most type II superconducting systems the ideal arrangement of these vortices is in a hexagonal regular lattice as this is the lowest free energy configuration (Tinkham 1975).

### 2.1.1 Layered Superconductors

In 1986, superconductivity at a higher temperature was discovered in  $\text{La}_{2-x}\text{Ba}_x\text{CuO}_4$  (Bednorz & Muller 1987) and, as such, led to a dramatic resurgence of interest in the field. Indeed, other similar systems - known collectively as high temperature superconductors (HTSCs) - soon followed (Cava 1987)(Wu 1987), all displaying higher transition temperatures than those found prior to this new discovery. One difference was clear, however. These new systems were crystals comprising layers of rock salt structure and CuO sandwiched together and the physics of such layered materials was different compared to the “lower  $T_c$ ” superconductors. Indeed, it is possible to utilise a model devised by Lawrence & Doniach (1971) to help describe some aspects of superconductivity in layered systems. Prior to the HTSC discovery, this model was used to explain certain types of behavior in layered materials

(Klemm 1974) (Prober 1977). However, when applied to the HTSCs it uses the fact that the superelectrons are preferably located in the CuO planes in order to construct a model to explain the magnetic response of such systems. One could then visualise the HTSC material as a sequence of 2D superconductors stacked on top of one another, each of which coupled through Josephson currents and electromagnetic interactions to the next superconductor in an adjacent layer. Moreover, such systems could exhibit varying degrees of electronic anisotropy. The strength of the coupling between adjacent layers can be described by a term known as the anisotropy parameter:

$$\gamma = \frac{\lambda_c}{\lambda_{a,b}} \quad (2.11)$$

where  $\lambda_{a,b,c}$  represents the ability of the currents in the a,b, and c axis to screen out the applied field  $H_a$ . Typical values range from  $\sim 5$  (YBa<sub>2</sub>Cu<sub>3</sub>O<sub>7- $\delta$</sub> ) through  $\sim 30$  (La<sub>2-x</sub>Sr<sub>x</sub>CuO<sub>4</sub>) (Drew 2005a) to  $\sim 150$  (Bi<sub>2</sub>Sr<sub>2</sub>CaCu<sub>2</sub>O<sub>x</sub>) (Martinez 1992).

One can then take this one step further and consider the anisotropy associated with a FLL. A high value of  $\gamma$  can consequently lead to a possible reduction in coherence along the vortex axis when the FLL is perpendicular or at an angle to the CuO planes. Indeed, it was later shown that these layered HTSCs (Figure 2.6) allowed the vortices to exist in different regimes depending upon their environment (i.e. applied temperature and field) (Feinberg 1994) (Giamarchi & Bhattacharya 2001) (Fisher 1991).

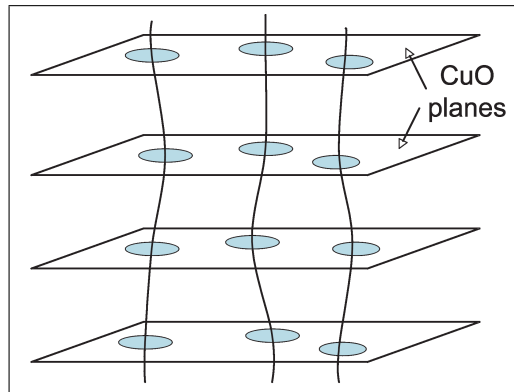


Figure 2.6: A cartoon showing that the circulating supercurrents produce vortices (blue) confined to the CuO planes (known as pancake vortices - see text) but coupled to adjacent layers via electromagnetic and Josephson interactions (solid lines).

In exotic superconductors the mixed state can be further divided into sub-regions due to the extreme anisotropy of the materials. The low field, low temperature regime (represented by B in Figure 2.7) is known as the Bragg Glass regime (Klein 2001) (Giamarchi & Le Doussal 1995). Such a state obtains its name from the fact that the vortices have quasi-long-range order that produce Bragg peaks like a solid. However, they exist within a glass of various metastable states (Giamarchi & Le Doussal 1995) due to intrinsic defect pinning

within the crystal (see Section 2.1.2). Indeed, neutron scattering (discussed in the next chapter) has shown the appearance of large Bragg spots from vortices in this state.

If one now increases the applied field, a state known as the Vortex Glass is entered (C on Figure 2.7). Strong competition between attractive defect pinning and repulsive dipolar interactions between increasing numbers of vortices result in the lattice becoming disordered in-plane and along their longitudinal axis, leading to a glassy state.

Further, increasing the temperature gives these vortices additional thermal energy moving them into the liquid state (marked D in Figure 2.7). Here, as the name suggests, the vortices are moving around freely, having enough kinetic energy to free them from the influence of defect pinning and inter-vortex interactions. Indeed, in systems where the electronic anisotropy is extreme, these vortices can break up further into “pancake” vortices as coupling between the crystals layers is lost. These pancake vortices (as shown in Figure 2.6) are quasi-2D and reside in the CuO planes. Finally, if one then increases the applied field above the upper critical point  $H_{c2}$  or the temperature above  $T_c$ , the cores of the vortices significantly overlap and the system enters the normal metallic state E.

### 2.1.2 Pinning

Fabricating a perfect crystal is extremely difficult as it is nearly impossible to remove defects from the atomic lattice. Such defects play an important role in the underlying arrangement of the magnetic vortices in the FLL as they represent areas where the superconducting electron density is suppressed. Moreover, it becomes energetically favourable for a vortex to accommodate itself on one of these defects. This type of behaviour is known as pinning.

When considering layered HTSCs, there are predominantly two types of material defect pinning. The first of these is known as “point defect” pinning and is a result of anomalies within the crystal structure - for example, the misplacement of an oxygen atom in the oxide planes. Such a region has its order parameter suppressed and is therefore energetically favourable. It has been shown by Pastoriza (1992) that depinning from such point defects in  $\text{Bi}_2\text{Sr}_2\text{CaCu}_2\text{O}_{8-\delta}$  occurs at approximately 15K and appears to be field independent for much of the B-T plane diagram. This depinning has a characteristic temperature such that the potential energy  $U$  for the defect can be described by:  $U \sim kT$ .

In addition to these intrinsic defects, it is also possible to artificially produce pinning sites using high energy ions. Indeed, it was Civale (1991) who first used Sn ions (of the order of MeV) to create a random distribution of defect tracks, known as columnar defects, through the bulk of material. Such tracks possess an enhanced pinning potential compared with the point defects described above. A characteristic induction value is the matching field  $B_\phi$  which denotes the point at which the number of vortices equals the number of columnar defects in the sample.

Nelson and Vinokur (Nelson & Vinokur 1992)(Nelson & Vinokur 1993) have demonstrated that such a system can be mapped onto an arrangement of 2-D localised bosons. Further to this, they have shown that different regions are evident within the H-T plane diagram and that there exists a Mott Insulator state around the matching field - demonstrating both 3-body and trivial 2-body correlations, dictated by the random arrangement of the columnar defects. However, in other areas of this diagram, non-trivial behaviour, or

glassy correlations, such as partial depinning along a vortex axis (known as the entangled liquid phase) can be observed.

### 2.1.3 Melting of the Flux Line Lattice (FLL) and the Macroscopic Irreversibility line

The magnetic vortices in the cuprate superconductors are not perfectly rigid “tubes” of flux quanta. Indeed, as one changes the external, environmental conditions, they can become susceptible to various forms of deformation, described by different elastic moduli. Within the confines of this thesis, the only parameters concerned here are the shear and tilt moduli.

The shear modulus  $c_{66}$  characterises the ability of a vortex to withstand in-plane shearing (see cartoon of Figure 2.8) and is of the form:

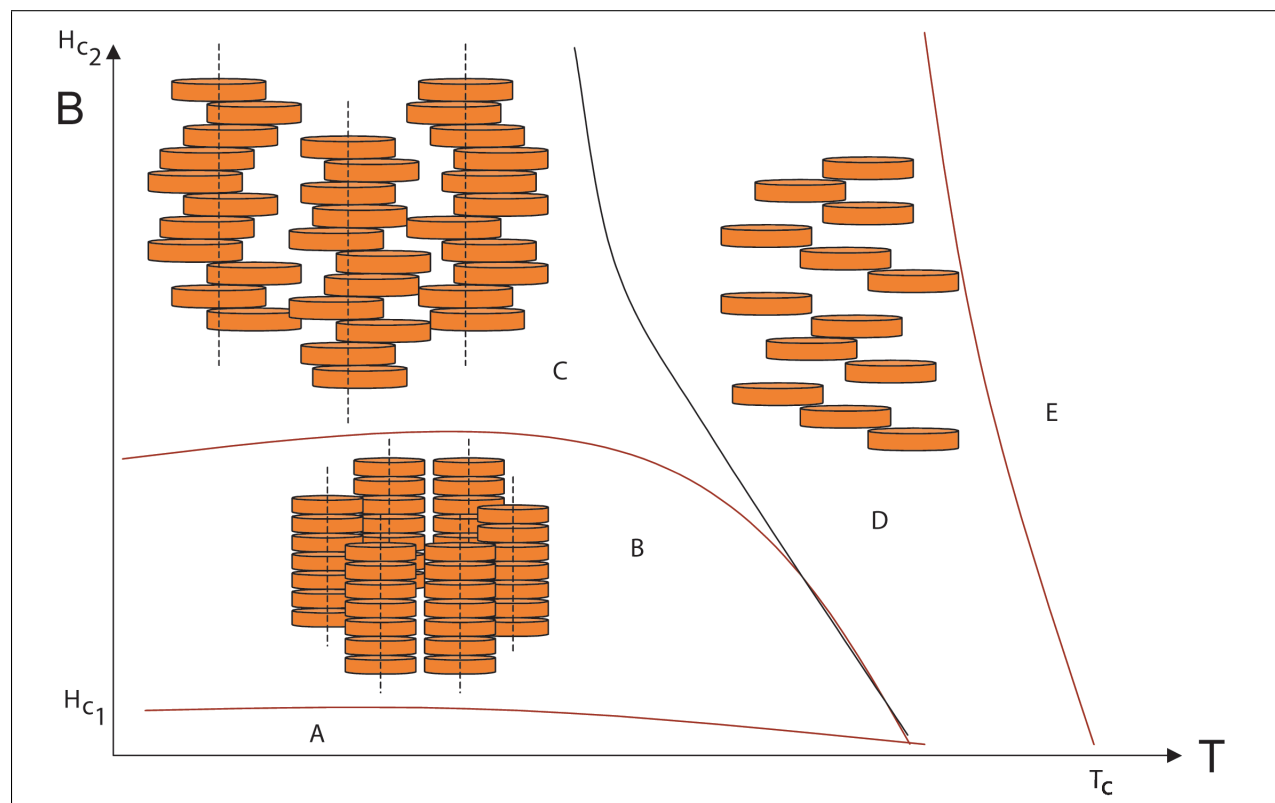


Figure 2.7: A plot showing the different vortex states as a function of field  $B$  and temperature  $T$ . When one increases the field and temperature above the Meissner phase (A), one enters the mixed state. In exotic systems this can be further sub-divided into the Bragg Glass (B), Vortex Glass (C) and liquid state (D). One enters the normal metallic state (E) upon increasing above  $T_c$  and the upper critical field  $H_{c2}$ .

$$c_{66} = \frac{\phi_0 B}{16\pi\mu_0\lambda_{ab}^2} \quad (2.12)$$

with small corrections depending upon the regime (Blatter 1994). It has been suggested

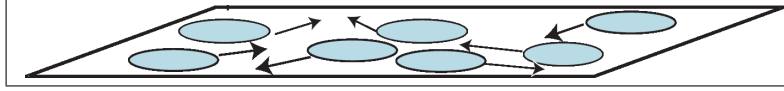


Figure 2.8: *The shearing of magnetic vortices (blue) in the same layer is characterised by the shear modulus  $c_{66}$ . The arrows denote the direction of movement of these vortices in the same plane.*

that such a property becomes important when one considers the increasing effect of thermal fluctuations and vortex-vortex interactions (Forgan 1995). Indeed, a phenomenon concerning the layered, type II superconductors that generally sets it apart from its predecessors, is the melting behaviour observed at high temperatures, approaching  $T_c$ .<sup>2</sup> As mentioned previously, thermal excitation can remove a vortex from a pinning site, but as one increases the temperature further the vortices begin to move about, analogous to particles moving in a liquid. The Josephson coupling between layers in BSCCO is extremely weak and so the electromagnetic interactions dominate (Lee 1993c). However, due to the high anisotropy of some particular perovskite-structure superconductors, the total intra-vortex coupling between adjacent layers is significantly decreased and the coherence along the vortex axis reduces. The tilt modulus  $c_{44}(\mathbf{k})$  gives a measure of how much a vortex has shifted along its length and in the isotropic continuum case can be described by (Blatter 1994):

$$c_{44}(\mathbf{k}) = \frac{\mathbf{B}^2}{4\pi} \frac{1}{1 + \lambda^2 \mathbf{k}^2} \quad (2.13)$$

However, for the samples detailed within this thesis it is necessary to take into account the influence of anisotropy in the crystal lattice. Consequently, the tilt modulus can be modified to comprise both a bulk term  $c_{44}^0(\mathbf{k})$  and single vortex contribution  $c_{44}^c(\mathbf{k})$ . According to Blatter (1994), it is possible to describe these terms thus:

$$c_{44}^0(\mathbf{k}) = \frac{\mathbf{B}^2}{4\pi} \frac{1}{1 + \lambda_c^2 \mathbf{K}^2 + \lambda^2 \mathbf{k}_c^2} \quad (2.14)$$

$$c_{44}^c(\mathbf{k}) = \frac{\alpha}{\lambda_c^2} \ln \left( \frac{\beta}{1 + (\lambda_{ab}\gamma^2)\mathbf{K}_{BZ}^2 + \lambda^2 \mathbf{k}_c^2} \right) + \frac{\alpha}{\lambda_c^3 \mathbf{k}_c^2} \ln \left( 1 + \frac{\lambda^2 \mathbf{k}_c^2}{1 + \lambda^2 \mathbf{K}_{BZ}^2} \right) \quad (2.15)$$

where  $\mathbf{k}_z$  is the wavevector along the vortex axis in the z-direction,  $\mathbf{K}$  is a vortex reciprocal lattice vector and  $\mathbf{K}_{BZ}$  is the Brillouin-zone wavevector.  $\alpha$ ,  $\beta$  and  $\gamma$  are constants defined elsewhere (Blatter 1994).

<sup>2</sup>However, it should also be noted that melting in Nb has been observed close to  $H_{c2}$ .

When the thermal fluctuations of the vortices exceed a fraction  $c_L \sim 0.1 - 0.4$  of the lattice spacing  $a_0$ , the FLL is said to have “melted” and this is governed by the Lindemann criterion:

$$\langle u^2(T_m) \rangle_{th} \sim c_L^2 a_0^2 \quad (2.16)$$

where  $\langle u^2(T_m) \rangle$  is the mean squared thermal displacement,  $c_L$  is the Lindemann number, and  $T_m$  is the temperature at which the “melting” takes place. It is possible, and indeed has been shown by Lee (1993b) and Lee (1995) that one can observe the melting transition in  $\mu$ SR measurements. This is discussed further in Section 3.1.4. However, it is important to understand that the nature of the moduli depends upon the field regime that one is operating in. It is clear from Equation 2.16 that  $\langle u^2(T_m) \rangle$  is dependent upon  $B$  since the lattice spacing  $a_0$  is inversely proportional to  $B^2$ .

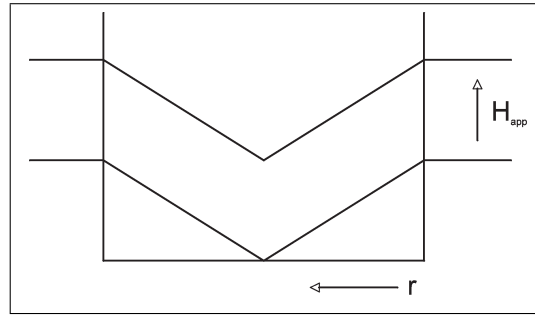


Figure 2.9: A cartoon showing the field profile into the bulk of a superconductor. The distance  $r$  from the surface of the superconductor into the bulk is shown by the arrow. As one increases the applied field  $H_{app}$  a flux gradient occurs towards the centre of the superconductor.

Subsequently, one can plot the melting transition in the  $B$ - $T$  plane, where two regions lie with different dependencies. The first of these regions is the high field / low temperature state which begins at a crossover field. Here, the associated melting line can be described by (Lee 1993c):

$$B(T) = \frac{\phi_0^3 \pi c_L}{8\pi \mu_0 k_B \gamma \sqrt{\beta} \lambda_{ab}^3 T} \quad (2.17)$$

The low field melting regime (dominated by electromagnetic coupling (Blatter 1996)(Lee 1993c)) is independent of the anisotropy parameter  $\gamma$ :

$$B(T) = \frac{\phi_0^3 c_L^2 s}{8\pi \mu_0 k_B \beta \lambda_{ab}^4 T} \quad (2.18)$$

It is clear from equations 2.17 and 2.18 that the main difference between the two is the additional power of the  $\lambda$  term in the denominator of the latter. Coupled with the  $c_L^2$  term, the expression for the low field melting line reflects the fact that in such a dilute region the

influence of the magnetic penetration depth consequently further reduces the field at which melting takes place.

Curiously, as shown in Chapter 4, the two regions of the microscopic melting line tend to agree well with the macroscopic irreversibility point as measured by bulk magnetisation measurements. As mentioned within Section 3.3.1 the irreversibility line is the temperature above which the system becomes fully reversible.

Below this point however, hysteretic effects can take place due to collective interactions and these can be described using the critical state model (Bean 1962). Such a model states that the effect of pinning serves to determine the maximum flux density gradient (i.e. the magnitude of the gradient from the applied field at the surface to zero inside the bulk of the superconductor). Indeed, as shown in Figure 2.9, when increasing the applied field at a constant temperature, the field density profiles can be described by straight lines of slope:

$$\frac{d\Phi}{dr} = \frac{4\pi J_c}{c} \quad (2.19)$$

However, when one subsequently decreases the applied field, pinning prevents the removal of vortices from the superconductor. Hence, trapped flux occurs, resulting in hysteresis (Figure 2.10). This type of phenomenon occurs within the irreversibility region. However, as one increases the temperature further, the thermal excitation of the vortices overcomes the pinning potential and the system enters the reversible regime. It should, though, be noted that in  $\text{Bi}_2\text{Sr}_2\text{CaCu}_2\text{O}_{8+\delta}$ , it is not clear whether the surface pinning barrier actually disappears due to the FLL melting or whether it is in fact the bulk point pinning that is overcome.

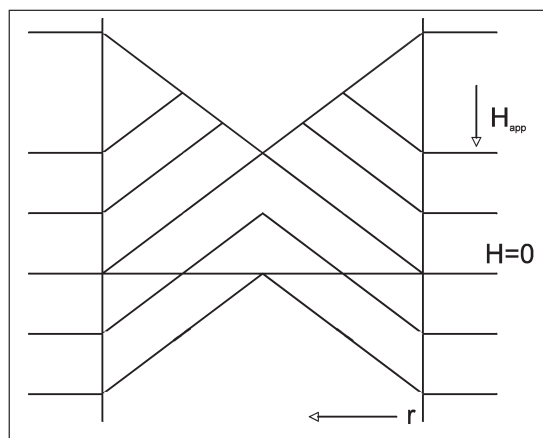


Figure 2.10: A cartoon showing the field profile into the bulk of a superconductor when hysteresis occurs. The distance  $r$  from the surface of the superconductor into the bulk is shown by the arrow. As one decreases the applied field  $H_{app}$  flux trapping can occur within the bulk of the superconductor. The zero applied field state  $H=0$  is also shown to have some flux existing in the bulk of the superconductor.

The situation however is altered slightly when one considers the columnar defect samples described above. Here, both  $c_{66}(\mathbf{k})$  and  $c_{44}(\mathbf{k})$  are enhanced, stabilising the coherence along the vortex axis. In particular, melting (and the irreversibility point) is prevented until much higher temperatures and the effect on the FLL due to inter-vortex interactions is reduced due to the favourable pinning potential offered by the tracks (see discussion in Chapter 5).

## 2.2 Introduction to Magnetism

Magnetic materials possess a vector property known as the magnetic moment  $\boldsymbol{\mu}$  that originates from the angular momentum associated with charges. This can either be in the form of a spin  $s$  or orbital momentum  $l$  component and the magnitude of each can be calculated via:

$$|\boldsymbol{\mu}_L| = \mu_B \sqrt{l(l+1)} \quad (2.20)$$

and

$$|\boldsymbol{\mu}_S| = g\mu_B \sqrt{s(s+1)} \quad (2.21)$$

where  $\mu_B$  is the Bohr magneton constant and  $g$  is the Landé g-factor. For a multi-electron atom, the individual spins and orbital quantum numbers can be summed individually, both combining to form a total angular momentum  $\mathbf{J}$  thus:

$$\mathbf{J} = \mathbf{S} + \mathbf{L} \quad (2.22)$$

where  $\mathbf{S}$  and  $\mathbf{L}$  constitute the total spin and orbital momentum components.

Such a vector addition can help in determining the final total magnetic moment contribution, as shown in Figure 2.11.  $\boldsymbol{\mu}_S$  is anti-parallel to  $\mathbf{S}$ ,  $\boldsymbol{\mu}_L$  is anti-parallel to  $\mathbf{L}$  but because of the arrangement of the vectors  $\boldsymbol{\mu}_J$  does not lie along  $\mathbf{J}$ . In order to calculate the magnetic moment along the axis of  $\mathbf{J}$ , one has to take the component of  $\boldsymbol{\mu}_J$  *along*  $\mathbf{J}$  (Haken & Wolf 2000), i.e.

$$(\boldsymbol{\mu}_J)_J = |\boldsymbol{\mu}_J| \cos(\theta) \quad (2.23)$$

When an applied magnetic field  $B_{app}$  is present, the orientation of the  $\mathbf{J}$  vector can alter. Moreover, the vectors  $\mathbf{S}$  and  $\mathbf{L}$  change direction. This is the consequence of a torque acting on  $\mathbf{J}$  and thus gives rise to the precession of  $\mathbf{J}$  about  $B_{app}$  due to the discrete quantised values that  $\mathbf{J}$  can take. As shown in Section 3.1.2, if a particle with an angular momentum is subjected to an applied magnetic field the torque acting on it is:

$$\boldsymbol{\Gamma} = \boldsymbol{\mu}_J \times \mathbf{B} \quad (2.24)$$

and its energy can be described by:

$$U = -\boldsymbol{\mu} \cdot \mathbf{B} = -\mu B \cos \theta \quad (2.25)$$

where  $\theta$  describes the angle subtended between the magnetic moment vector  $\boldsymbol{\mu}$  and the direction of  $B_{app}$ . Indeed, one can see that the energy is lowest when the angle between both vector quantities is zero. Energy configurations, however, are important when considering

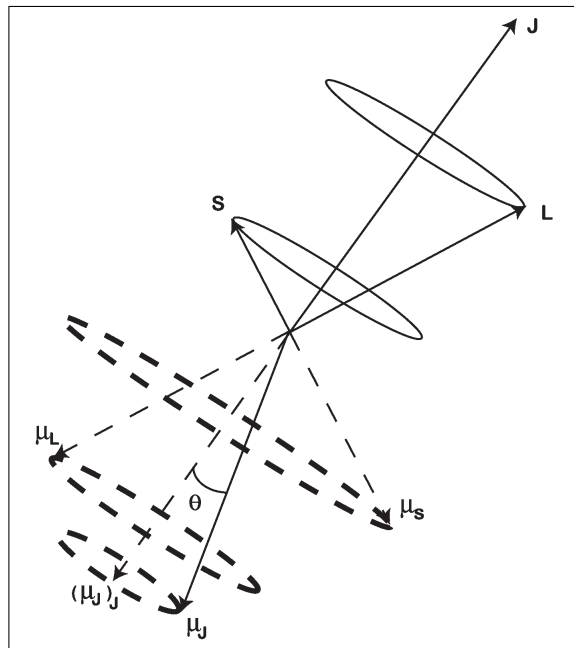


Figure 2.11: A diagram showing the relative directions of the angular momentum vectors. The spin  $\mathbf{S}$  and orbital angular momentum  $\mathbf{L}$  components vectorially add up to form the total angular momentum vector  $\mathbf{J}$ . The corresponding magnetic moment components are aligned along the axis of their spin counterparts but in the opposite direction (except for  $\mu_J$  - see text).

different types of magnetism, of which there is a large range. For the purposes and relevance of this thesis, a few types are explained briefly now.

When the individual unpaired magnetic moments undergo no interaction between neighbours and in the absence of an applied field, there is no specific overall direction of alignment so their arrangement is deemed to be *paramagnetic*. In zero applied field, free paramagnetic ions point in random directions and, consequently, have a temperature-dependent susceptibility<sup>3</sup>:

$$\chi = \frac{n\mu_0\mu^2}{3k_B T} \quad (2.26)$$

This is otherwise known as the Curie Law (Curie 1895) and demonstrates that as the thermal excitation of the ions is increased, the overall magnetic susceptibility will reduce. Such materials can be described by a Hamiltonian that comprises three main parts:

$$H = H_0 - \boldsymbol{\mu}_1\mu_0\mathbf{H} - \frac{\mu_0}{2}\mathbf{H}\mu_2 \quad (2.27)$$

Looking at the right hand side of this equation, the first term  $H_0$  describes the normal Hamiltonian for an ensemble of non-interacting electrons. The second term is the electromagnetic energy expression for a dipole in a field, whilst the third term describes the

<sup>3</sup>In the limit of small fields.

*diamagnetic* energy.  $\mu_1$  and  $\mu_2$  correspond to the magnetic moment contributions from the respective parts described. The latter contribution describes a small effect in which the electron spins attempt to arrange themselves, resulting in a negative susceptibility coefficient:

$$\chi = -\frac{e^2}{6mc^2} \sum_i \langle r_i^2 \rangle \quad (2.28)$$

where  $\sum_i \langle r_i^2 \rangle$  represents the summing over all the position vectors  $i$  of the electron spins. This determination of the susceptibility for diamagnetic moments was shown by Langevin ((Langevin 1905a) (Langevin 1905b)) and later by Pauli (1920).

Indeed, it was Pauli who explained a further progression of paramagnetism, now known as Pauli Paramagnetism. Here, he explained that when a magnetic field is applied to a gas of conduction electrons, extra energy is required to align those spin components that are initially anti-parallel to the direction of the field. The work done is that which extracts the electrons from within the Fermi surface to unoccupied levels outside it and results in an adjustment to the respective density-of-states (DOS)  $g(\epsilon)$  for the sets of both the parallel (para) and anti-parallel (anti-para) spin configurations. Before the field is applied, the DOS at a given energy  $\epsilon$  for each orientation is equal:

$$g(\epsilon)_{para} = g(\epsilon)_{anti-para} = \frac{1}{2}g(\epsilon)_{total} \quad (2.29)$$

and one can describe the filled energy bands as shown in (a) of Figure 2.12. When a magnetic field is applied however, a shift occurs along the energy axis and those electrons with moments that are aligned with the field lower their energy by an amount  $\mu_B H$ . Further to this, it may be energetically favourable for some electrons with moments initially arranged anti-parallel to subsequently re-configure themselves parallel with the field. This is possible if the amount by which they can lower their potential energy is sufficient enough to enable them to access energy levels beyond the Fermi surface  $\epsilon_F$ , as dictated by the exclusion principle. Consequently, the overall difference in energy between the two states will be  $2\mu_B H$  as shown in parts (b) and (c).

In some paramagnets, as the material is cooled, a phase transition occurs - the electron spins all spontaneously align in the same direction and acquire a large, positive susceptibility. (Alternate spin up and spin down on neighbouring sites is known as an antiferromagnetic arrangement.) This arrangement is known as being *ferromagnetic*. If the wavefunctions of neighbouring electrons overlap via a large enough Coulomb force a *direct exchange* is said to occur and this can be understood further by considering the associated spin-dependent Hamiltonian of the form (Krupicka & Sternberk 1968):

$$H_{ex} = -2 \sum_{ij} J_{ij} \mathbf{S}_i \cdot \mathbf{S}_j \quad (2.30)$$

Here, the exchange constant  $J$  is the same sign as the Weiss Constant  $\theta$  so that in order for the exchange energy to be lowered (corresponding to a ferromagnetic transition),  $J > 0$ .

In addition to this, interactions between electron spins can also take place over a longer range. In this scenario, wavefunctions from next-nearest-neighbours and further afield

overlap only very slightly but can interact through a process known as *indirect exchange*, of which there are two distinct forms: The RKKY interaction and the Kramers-Andersen scheme. The latter of these describes the indirect exchange mechanism for non-metallic materials and is outside the scope of this thesis. The RKKY (Ruderman-Kittel-Kasuya-Yosida) interaction however, occurs within the rare earth metallic compound systems. These materials comprise magnetic ions located within the 4f shells and existing in systems where the atomic spacing is approximately  $3.5\text{\AA}$  (Haken & Wolf 2000) - an order of magnitude greater than the radius of the 4f shell (Krupicka & Sternberk 1968). This makes direct magnetic coupling difficult. However, it is possible for the 4f ions to couple via the conduction electron gas: a local magnetic ion spin-polarises the conduction electrons which, in turn, polarise a neighbouring ion a distance  $r$  from the first (see cartoon in Figure 2.13). The Hamiltonian for such an interaction can be described by Equation 2.30 (neglecting orbital components) but now the exchange constant  $J$  is described by:

$$J(r) = -Af(2k_F r) \quad (2.31)$$

where  $A$  is a constant of proportionality and explained further in Krupicka & Sternberk (1968). The important aspect of this equation though, is the function  $f$  which has the form:

$$f(x) = \frac{x \cos x - \sin x}{x^4} \quad (2.32)$$

and describes the oscillatory spin polarisation of the conduction electrons, otherwise known as a spin density wave (SDW) (depicted in Figure 2.14).

The subsequent real-space magnetic susceptibility can be shown (for example, Blundell (2001)) as being:

$$\chi(r) = \frac{2k_F^3 \chi_P}{\pi} f(2k_F r) \quad (2.33)$$

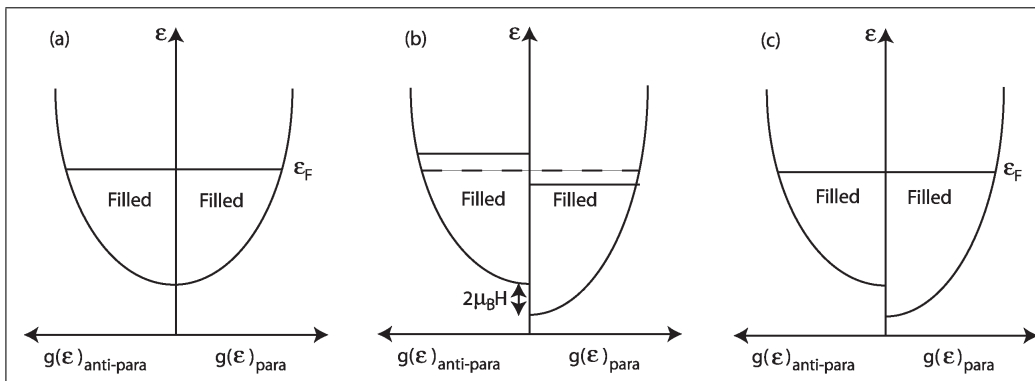


Figure 2.12: (a) In the absence of an applied field,  $g(\epsilon)$  for both the parallel and antiparallel spin components is equal. ( $\epsilon_F$  denotes the Fermi energy level.) (b) However, when a field is applied, those with spins parallel lower their energy by an amount  $\mu_B H$  while those with spins aligned anti-parallel increase their energy by that amount. (c) The thermodynamic equilibrium condition obliges some of the electrons in the anti-parallel band to lower their energy by moving into the parallel band.

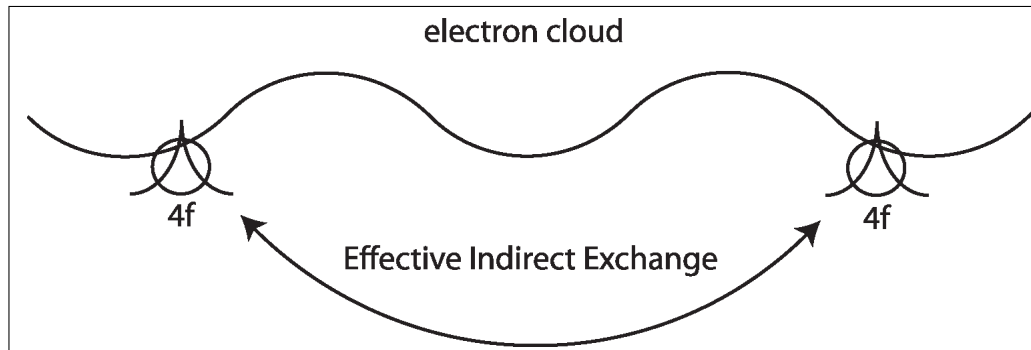


Figure 2.13: A simple, but effective, cartoon diagram shows how the wavefunctions of the  $4f$  ions are too tight to overlap with each other but can couple through interacting with the conduction electron gas, polarising it, and, in turn, undergoing an indirect exchange (known as the RKKY interaction).

where the susceptibility pertaining to the Pauli paramagnetic component is defined as:

$$\chi_P = \frac{3n\mu_0\mu_B^2}{2\varepsilon_F} \quad (2.34)$$

Such explanations sufficiently describe the different interactions within single magnetic materials.

However, it was De Gennes (1966) who first proposed that it was possible to couple two ferromagnets through a superconducting layer. Indeed, the coexistence of magnetism and superconductivity, despite being anticipated as far back as 1959 (Anderson & Suhl 1959), has recently experienced great interest (detailed further in Chapter 6). One of the defining interpretations for this behaviour is that of the FFLO mechanism (Fulde & Ferrell 1964), (Larkin & Ovchinnikov 1964). Here, an adaptation to the BCS ground state is taken. One considers a superconducting layer interfaced with a ferromagnet and assumes that the exchange field from the latter is spatially uniform. When this exchange field is within a particular normalised limit (more specifically covered by Fulde & Ferrell (1964)), it is possible for a small fraction of the Cooper pairs to undergo pair-breaking. The superconducting energy gap decreases and a resulting non-zero momentum occurs with the production of normal conduction electrons. The spins of these electrons then become polarised by the exchange field. However, if the exchange field is increased further still, the amount of pair-breaking will increase, producing un-paired electrons. Subsequently, the superconducting energy gap will eventually vanish and the superconductor will enter the normal metallic state.

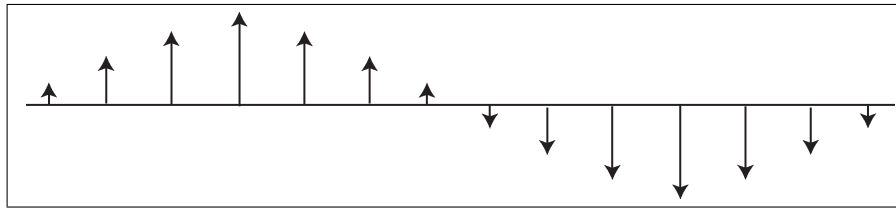


Figure 2.14: A cartoon diagram demonstrating the form of the spin density wave induced in the conduction electrons.

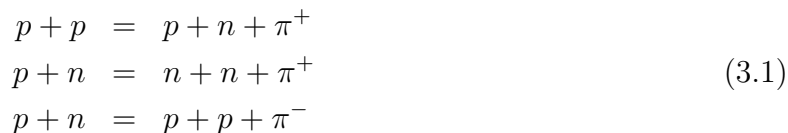
# Chapter 3

## Experimental Techniques

### 3.1 Muon Spin Rotation

#### 3.1.1 Muon production

The spallation source at the Paul Scherrer Institut (PSI) in Switzerland produces a continuous beam of protons of energy 590MeV. The protons are produced by stripping the unbound electrons from accelerating  $H^-$  ions which originate from an ion source. These protons then collide with a 5mm thick, graphite target and can undergo any of the following interactions:



where p, n and  $\pi$  denote the proton, neutron and pion respectively.

The choice of target must be such that it has a high melting point and low atomic number to avoid producing an excessive amount of neutrons that in turn will scatter the beam.

The pions that result from these 3-body decays are short lived, with a lifetime of approximately 26ns. However, both types possess momentum, have zero spin and decay accordingly:

$$\begin{aligned}
 \pi^- &= \mu^- + \bar{\nu}_\mu \\
 \pi^+ &= \mu^+ + \nu_\mu
 \end{aligned}
 \tag{3.2}$$

The muons are then guided by a series of bending and quadrupole magnets toward the experimental instruments as shown in Figure 3.1. Such magnets change the direction and maintain the focus of the muon beam respectively. Both positive and negative muons are used in  $\mu$ SR experiments. However, the resulting  $\mu^-$  is extremely susceptible to nuclear capture from a positively charged nucleus and for the studies discussed within this thesis, it is not useful and will not be mentioned further.

The resulting positive pion (first observed by Powell in 1947 (Lattes 1947)) decays either close to the surface of the target (surface beam) or further down the beam channel (decay beam), the latter being a result of the pion kinetic energies being greater.

The decay beam pions produce muons that are either ‘forward’ (with momentum in the same direction as that of the parent pion’s and possessing an energy of  $\sim 160\text{MeV}$ ) or

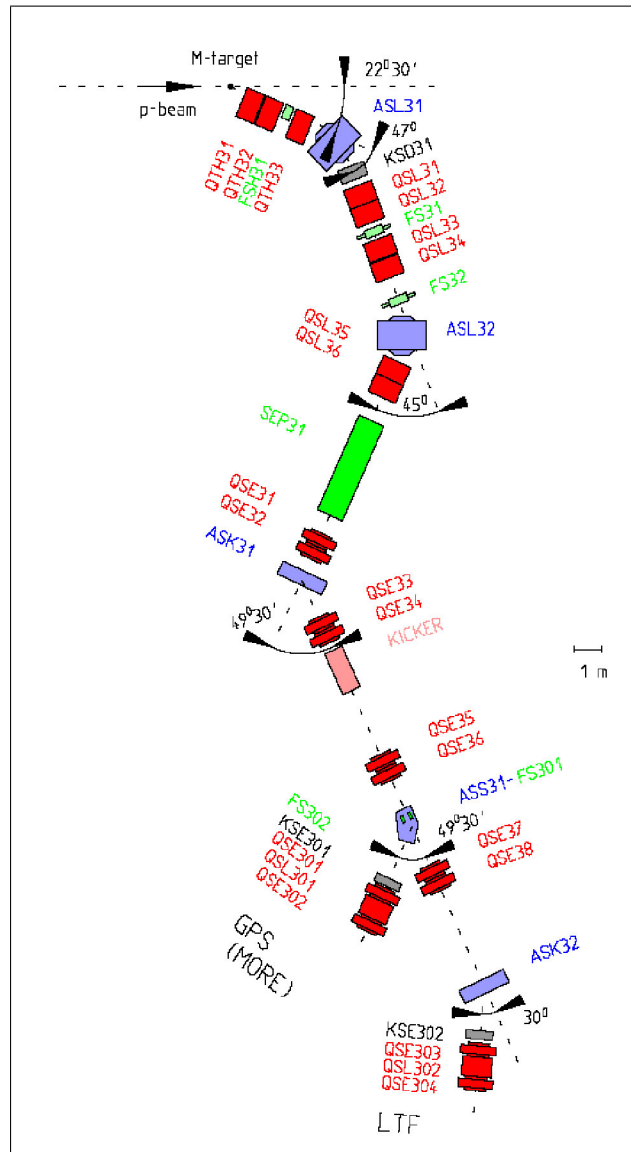


Figure 3.1: The muons are guided to the respective experimental instruments by a series of bending and quadrupole magnets (blue and red blocks respectively) as shown in this schematic of the  $\pi M3$  beamline at PSI. The Spin Rotator that sets the spin of the muons to approximately  $50^\circ$  is shown in green and marked “SEP31”. (Source: [www.psi.ch](http://www.psi.ch))

‘backward’ (moving in the opposite direction to the pion’s momentum and having an energy  $\sim 70\text{MeV}$ ). The subsequent muons produced have large penetration depths  $\sim 4\text{g/cm}^2$  (Greer & Kossler 1995) due to their large kinetic energies and therefore a sufficient sample size is required or such muons will pass through and not interact with it.

A surface beam describes those pions that are barely able to escape the vicinity of the target surface before decaying. The muons that result from this type of decay possess a kinetic energy of  $\sim 4.1\text{MeV}$  and have been used in all the bulk  $\mu\text{SR}$  experiments reported here. They provide implantation depths of  $\sim 150\text{mg/cm}^2$  in air (Greer & Kossler 1995) - compatible with the dimensions of the samples investigated within this thesis. (The energy of the muons can be depleted further by the introduction of a moderator. This method is fundamental to the low energy muon technique and will be discussed in Section 3.1.5.)

However, surface beam muons possess two other important properties that also make them ideal for  $\mu\text{SR}$  studies on high temperature superconductors. Firstly, the parent pion has little kinetic energy and so, for simplicity, one can make the assumption that it is virtually at rest. When the resulting decay occurs, the subsequent neutrino is known to have spin  $1/2$  and negative helicity. Therefore, in order to conserve lepton number, and momentum, the muon must be a fermion, have its spin in the opposite direction to the neutrino’s, and have its momentum anti-parallel to its own spin. Thus, the muon spin has almost perfect longitudinal polarisation with respect to its momentum. Note that this leads to a violation of parity.

Secondly, the muon is of mass  $105.67\text{MeV}/c^2$  and has a half-life of  $2.2\mu\text{s}$  (*Particle Data Group* 1947). When it decays, it undergoes the following interaction:

$$\mu^+ = \bar{\nu}_\mu + \nu_e + e^+$$

Such a decay is anisotropic and leads to a preferential emission of the resulting positron that is predominantly in the direction of the muon’s spin. The probability  $dW$  that the positron is emitted with a reduced energy  $\varepsilon$  into a solid angle  $\theta$  is given by: (Okun 1965)

$$dW(\varepsilon, \theta) = \frac{e^{(t/\tau_\mu)}}{\tau_\mu} [1 + a(\varepsilon)\cos(\theta)]n(\varepsilon) \cdot d(\varepsilon)d\cos(\theta) \quad (3.3)$$

where  $a(\varepsilon) = (2\varepsilon - 1)/(3 - 2\varepsilon)$ ,  $n(\varepsilon) = 2\varepsilon^2(3 - 2\varepsilon)$ , and  $e^{t/\tau_\mu}$  is the probability that a muon still exists after a time  $t$ . ( $\varepsilon$  is the reduced muon energy  $E_\mu/E_{max}$  and  $\tau_\mu$  is the muon lifetime.)

The fundamental part of Equation 3.3 is the  $[1 + a(\varepsilon)\cos \theta]$  term which can be understood further by making reference to Figure 3.2. The highest probability occurs when the positron is emitted in exactly the direction of the muon’s spin. When this occurs it can have a maximum energy of  $52.32\text{MeV}$ . Conversely, the probability of the positron being emitted in the direction  $\theta=180^\circ$  is close to zero. Thus, Figure 3.2 shows how the resulting positron is preferentially emitted in the direction of the muon’s spin.

### 3.1.2 The Transverse Field $\mu\text{SR}$ Technique

It is now appropriate to discuss the  $\mu\text{SR}$  technique in the context of the HTSCs where positive muons are used to analyse the magnetic vortex lattice.

The general setup involves the sample being perpendicular to the incoming muon beam. For the bulk  $\mu$ SR measurements detailed here, the crystal is setup such that its c-axis is parallel to an external magnetic field  $H$  applied by a set of Helmholtz coils. The sample chamber is surrounded by an array of detectors (discussed below) and the temperature of the system is controlled using a Conductus Inc. Temperature Controller. Principally, this manages a heater and a  $^4\text{He}$  Continuous Flow Cryostat - able to operate within a temperature range of 2 - 300K.

Before the muon enters the sample, it passes through a Spin Rotator (indicated in Figure 3.1) that comprises an electric field  $E$  orthogonal to a magnetic field  $B$  where the former is used to maintain the direction of the muon's momentum and the latter sets the muon's spin  $S$  at approximately  $50^\circ$  to  $H$ . All muons will thus arrive in the sample with the same polarisation state and begin to Larmor precess about the local flux density  $B$  with a frequency:

$$\omega_L = \gamma_\mu \mathbf{B} \quad (3.4)$$

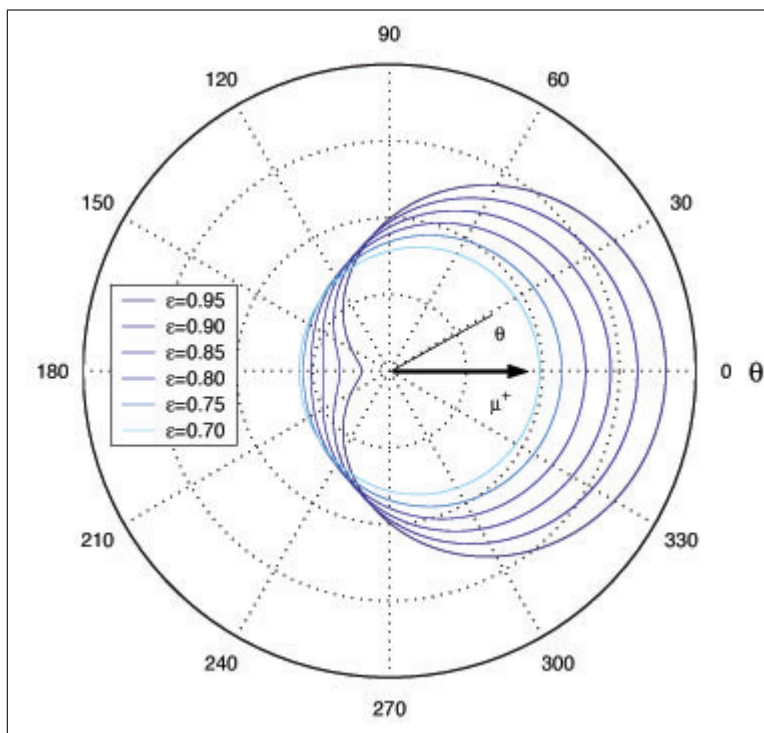


Figure 3.2: *The emission of the positron resulting from the muon's decay is highly anisotropic and is dependent upon the muon's energy (shown by the reduced energy  $\epsilon$  and the direction of its spin. Emission is predominantly in the direction of the muon's spin. (Source: (Drew 2005))*

where  $\gamma_\mu/2\pi = 135.53\text{kHz/G}$  is the gyromagnetic ratio of the muon.

According to quantum mechanics, the maximum value that the muon's spin  $S_Z$  parallel to  $B$  will take is:

$$S_Z = m_s \hbar$$

where:

$$m_s = \pm \frac{1}{2}$$

thus showing that the muon's spin cannot align exactly with the local magnetic induction.

The ability of the muon to precess originates from the combination of both classical and quantum mechanical ideas of a magnetic flux  $B$  exerting a torque  $\Gamma$  on a particle with a spin component  $S_\perp$  that is perpendicular to  $B$ .

$$\Gamma = \frac{d\mathbf{S}}{dt}$$

$$\Gamma = -\mu_0 \boldsymbol{\mu} \times \mathbf{B} = -\frac{\mu_0 e}{2m} \mathbf{S} \times \mathbf{B} \quad (3.5)$$

(Note that in Equation 3.5,  $\boldsymbol{\mu}$  corresponds to the magnetic dipole moment vector of the muon.) The fact that the muon has a half-integer spin and thus a perpendicular spin component, allows the torque to act and, consequently, precession will occur. This type of  $\mu\text{SR}$  technique is commonly referred to as the Transverse Field (TF) method and has been applied

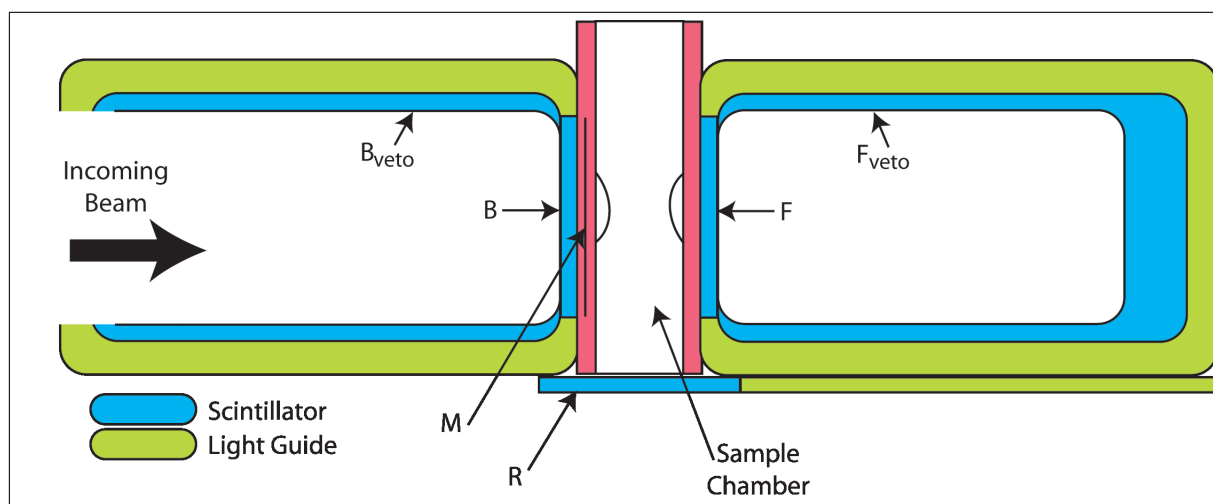


Figure 3.3: A schematic of the GPS detector arrangement at PSI.  $B$  is the backward detector,  $F$  is the forward detector,  $R$  is the right detector,  $M$  is the trigger detector to start the timer,  $F_{\text{veto}}$  and  $B_{\text{veto}}$  are the forward and backward veto detectors respectively.

to all  $\mu$ SR experiments detailed within this thesis. Other variations of this technique include the “Longitudinal Field” (in which the field is aligned parallel to the muon spin) and “Zero Field” methods but these are not covered here.

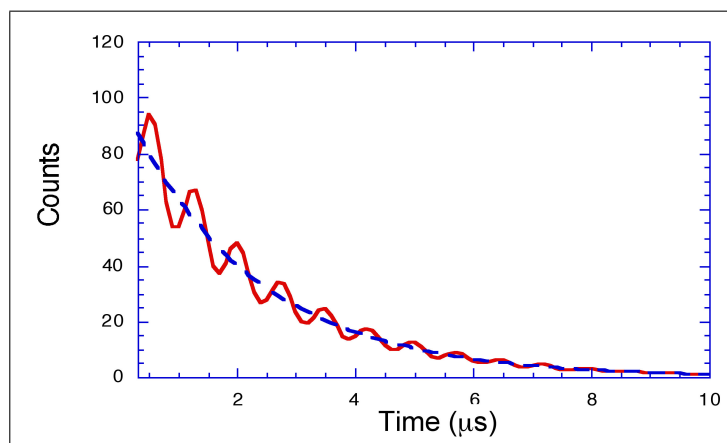


Figure 3.4: A generic example of a histogram generated for a positron detector in the GPS. (The data is denoted in red.) The time window has a maximum of  $10\mu\text{s}$  beyond which noise becomes significant. (NB. The blue dashed line is to highlight the exponential component.)

The TF technique on the General Purpose Spectrometer (GPS) at PSI makes use of a time differential method. When the muon enters the sample chamber a timer is started by a trigger detector (denoted by M in Figure 3.3). It then enters the superconductor and undergoes thermalisation through ionising atoms and scattering from electrons (Schenck 1985). When its kinetic energy has been reduced to at least  $35\text{keV}$ , it forms muonium (an atom comprising an electron orbiting a muon). Further energy is lost as the muonium atom collides with other atoms within the crystal (continually breaking-up and reforming muonium) until its energy is approximately  $15\text{eV}$ . At this point, the muonium atom breaks up as the muon becomes free from its electron due to the Coulombic screening influence of the other free electrons in the superconductor.<sup>1</sup> It has been shown that such thermalisation has little effect on the polarisation of the muon spin (Ford & Mullin 1957) and therefore, one can assume that it has the same polarisation when it starts to precess as it did approximately  $1\text{ns}$  before, when it first entered the crystal.

The GPS instrument has five positron detectors (Up, Down, Right, Forward and Back), each of which is a scintillation counter connected to a photomultiplier. There are also two veto detectors - registering positrons that are emitted backwards or pass beyond the sample. These veto detectors can register double-coincidence events too (for example, when a muon enters the time window before the previous one has decayed) and thus both are connected to two photomultipliers in order to detect and eliminate such scenarios. For

<sup>1</sup>In semi-conductor and insulating materials the muonium atom does not break up but this is discussed elsewhere (Cox 1984).

the bulk HTSCs investigations detailed here, only the up, down and right detectors are used.

A positron detector registers a “count” upon detection and the timer is stopped. This count is subsequently added to a histogram displaying the number of counts against time for that particular detector (see Figure 3.4) described by (Schenck 1985):

$$N(t) = N_0 \exp(-t/\tau_\mu) [1 + A_0 G(t) \cos(\langle \omega \rangle t + \phi)] + b \quad (3.6)$$

Here,  $N_0$  is the count rate at  $t = 0$ ,  $b$  is the background noise,  $A_0$  is the initial asymmetry between two orthogonal detectors, and  $G(t)$  is an envelope function (detailed below).

Such a histogram comprises an exponentially decaying function (arising from the effect of the muon’s lifetime) and a dampened oscillatory signal. This latter response is a direct consequence of the muon not just experiencing one field value but an entire field distribution arising from a magnetic vortex lattice.

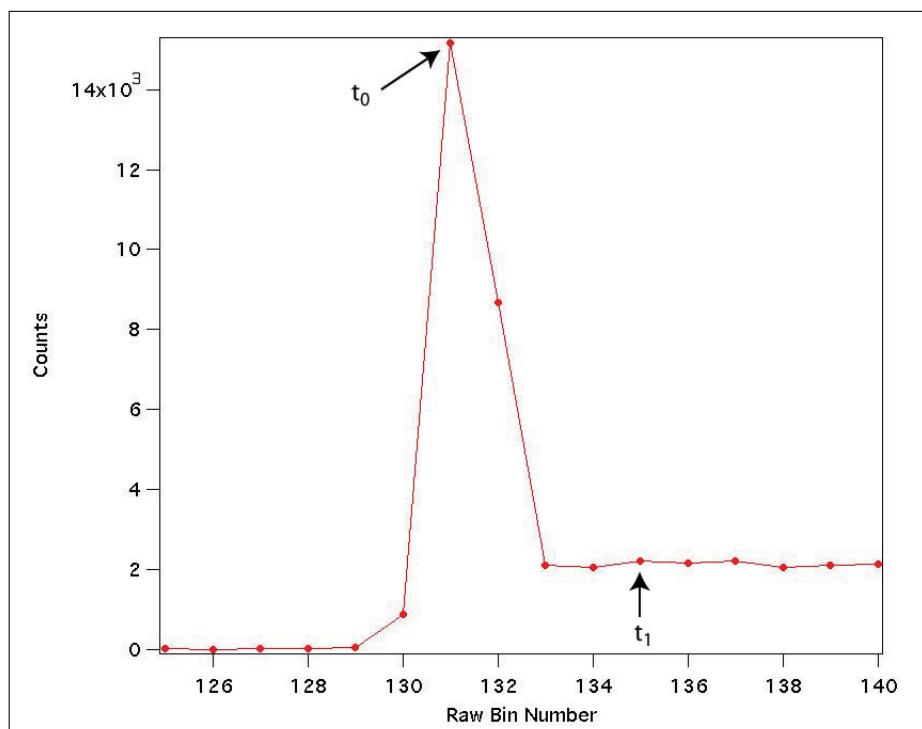


Figure 3.5: A plot showing the number of positron counts against time. For each detector in the GPS, the positron peak,  $t_0$  must be removed prior to analysis. Good data taking starts at  $t_1$  and ends at  $t_2$  (the latter not shown).

However, before one is able to process the  $\mu$ SR data, it is necessary to remove the effect of positrons resulting from decay beam muons. In order to do so, the analysis program, Windows Muon Data Analysis (WiMDA), is used (Pratt 2000). WiMDA operates within the time domain and for the purposes of work detailed within this thesis, is very useful in helping

identify the initial positron peak and the location of three, essential times. By selecting the data sets from each of the detector histograms and focusing on the region of the positron peak, one can obtain a plot similar to that shown in Figure 3.5.

It is then possible to ascertain three different times:  $t_0$ ,  $t_1$  and  $t_2$ .  $t_0$  corresponds to a point approximately where the positron peak occurs; determining the point at which the muons enter the sample chamber,  $t_1$  indicates the point at which good muon data begins, and  $t_2$  determines the point at which the data ends. If one continues to try and obtain data beyond this latter time interval, the inclusion of ‘no data’ for a period of time will adversely influence the subsequent analysis. It is also important to realise that the positron peak is not necessarily the ‘real’  $t_0$  which represents the approximate time at which the muons enter the sample. Indeed, in order to obtain this value, one must take measurements over a range of fields and observe the point at which the  $t_0$ s converge. If the true value of  $t_0$  is not correct, then the initial phases of the muon’s spin for the different fields will be different. By using WiMDA, it is possible to extract the data which corresponds specifically to those muons which interact with the sample.

One can then calculate the asymmetry from one detector or between two orthogonal detectors, reflecting the difference between the amplitudes of the two oscillating time domain signals and eliminating the effect of the non-essential muon lifetime. The resulting asymmetry plot has a dampened envelope function that can be described by  $G(t)$  in Equation 3.6 and is shown in Figure 3.6. The asymmetry between, for example, the forward F and backward detectors B can then be plotted using Equation 3.7:

$$A_{FB}(t) = \frac{[N_F(t) - b_F] - [N_B(t) - b_B]}{[N_F(t) - b_F] + [N_B(t) - b_B]} \quad (3.7)$$

where  $b$  and  $N$  represent for the background noise and number of counts associated with each detector. (F and B denote forward and backward respectively.) However, for the data recorded within this thesis the signal from each detector is analysed separately. Thus, the asymmetry can be obtained simply by removing the effect of the decaying muon lifetime.

Upon obtaining such a graph it is possible to Fast Fourier Transform the data to obtain a corresponding frequency spectrum. The data can then be used (via the relationship in Equation 3.4) to obtain a graph of count against internal field. However, another analysis technique known as the Maximum Entropy Method has been utilised for work detailed within this thesis and is now described.

### 3.1.3 The Maximum Entropy Method (MEM)

The concept of maximum entropy in information systems was first properly proposed by Claude Shannon (Shannon 1948a)(Shannon 1948b). In his work he stated that the entropy  $S$  of a system could be calculated by summing all the products of the individual probabilities  $p_i$  with their associated logarithms. This was shown using the Boltzmann equation:

$$S = -k \sum p_i \ln p_i \quad (3.8)$$

To incorporate a continuous distribution, this can be extended to:

$$S = -k \int P(x) \ln \frac{P(x)}{M(x)} dx \quad (3.9)$$

where  $P(x)$  is the entire probability distribution and  $M(x)$  is a function determined by the exact nature of the problem. If one specifies the mean and variance, and fixes  $M(x)$  constant, such a distribution is normal or Gaussian.

E.T. Jaynes (Jaynes 1957) advanced this idea further by noticing the analogy with thermal physics in which the entropy of a thermodynamic system could be expressed by the Boltzmann equation:

$$S = -k \ln W \quad (3.10)$$

where  $W$  is the multiplicity of a macrostate of interacting particles. It is possible to use this technique devised by Shannon as a tool when trying to explain the behaviour of magnetic vortices in high temperature superconductors.

Entropy is a measure of disorder or uncertainty and, when maximised, it can be used to determine realistic probability models which make no assumptions about the system and only include that information which is known. Such a process is in agreement with good probabilistic reasoning (Buck & MacCaulay 1994).

The analysis program used for work detailed within this thesis is known as MaxEnt (Cubitt 1994)(Rainford & Daniell 1994)(Riseman & Forgan 2000). It is used to provide a model that reflects the probability distribution  $P(B)$  of the fields inside the superconductor. Such a distribution (as explained later) reflects the shape and behaviour of the magnetic

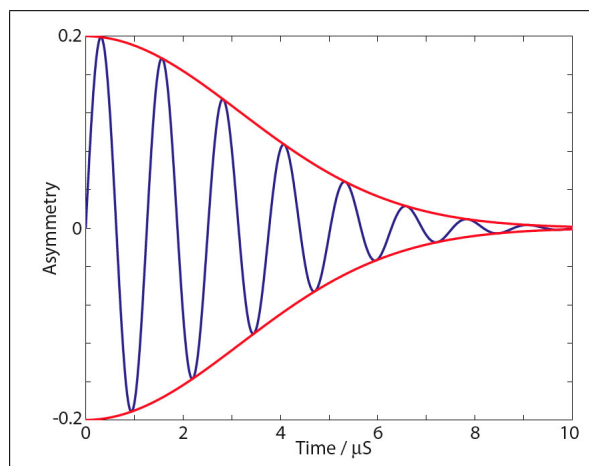


Figure 3.6: *An asymmetry plot for two orthogonal detectors can be plotted to remove the effect of the muon lifetime and focus on the dampened oscillatory signal from the field distribution of the vortex lattice.*

vortex lattice.

Initially, a theoretical fit parameter  $P(B_i)$ , that is not based on any model or assumptions of how the field distribution should be, is assigned to a range of field values  $B_i$ . Such a starting  $P(B)$  will be flat as all initial probabilities will be uniform. The distribution is then inverse Fourier Transformed and the resulting calculated asymmetry signal is compared to the actual data. One can obtain the value  $\chi^2$  from the relationship (Drew 2005a):

$$\chi^2 = \sum_{m=1}^M \sum_{h=t_1/\Delta t}^{t_2/\Delta t} \frac{[D_m(t_h) - d_m(t_h)]^2}{\sigma_m^2(t_h)} \quad (3.11)$$

where  $m$  is a positive, real integer,  $M$  is the total number of points,  $D_m$  is the theoretical fit function,  $d_m$  is the actual data and  $\sigma_m^2$  is the variance.

The entropy  $S$  associated with the fit is also simultaneously calculated via an adapted version of equation 3.9:

$$S = - \sum_i \frac{P(B_i)}{P_d} \ln \frac{P(B_i)}{P_d} \quad (3.12)$$

where  $P_d$  reflects the default noise level of the distribution, above which  $P(B)$  is significant.

The gradients of both  $\chi^2$  and  $S$  are then calculated to provide the next set of  $P(B_i)$  values for the trial distribution and the process is iterated until  $\chi^2$  reaches a minimum and  $S$  is maximised (Drew 2005a). With regards to this, it is important to denote a minimum value for which  $\chi^2$  can be. Without such a limit, MaxEnt will continue to search for a minimum indefinitely. Therefore the  $\chi^2$  minimum requirement is determined by:

$$\chi^2 = MN \quad (3.13)$$

where  $M$  is the number of points in each of the  $N$  positron-count histograms.

Using these parameters, one can obtain a new, constrained maximised entropy  $S_c$ :

$$S_c = \lambda S - \frac{\chi^2}{2l^2} \quad (3.14)$$

where  $\lambda$  is a Lagrange multiplier. The ‘‘looseness’’  $l$  can be adjusted such that the emphasis between  $S$  and  $\chi^2$  can be changed to account for other factors intrinsic to the experimental setup (e.g. noise in the circuitry of the detectors). Typical values are between 1.02 and 1.04. This enables the fit to be shifted towards the entropy term. The final MEM spectra must be the one that describes the data without any assumptions but is as uniform as possible.

### 3.1.4 The $\mu$ SR lineshape of a FLL

The MEM is a useful tool to extract the magnetic field probability distribution  $P(B)$  of a flux line lattice (FLL) in type II superconductors. Unlike a Fast Fourier Transform which gives equal weighting to all the data in the spectra, MEM reduces the weighting given to those points at long time scales that are subject to increased noise. Nevertheless, it should

also be noted that with such a control over the looseness of the fit, one has to be aware not to overlook peaks or troughs in the data that may, in fact, reflect the intrinsic behaviour of the sample.

Figure 3.7 shows the resulting  $P(B)$  plot for an ideal, perfect lattice (i.e. a FLL that comprises a hexagonal orientation with long range order). Such a distribution can be described as follows.  $B_{min}$  refers to the minimum field that the muon experiences when it enters the sample (point ‘a’ on the schematic). Here, the value is non-zero due to the overlapping of the fields attributed to adjacent vortices.  $B_{core}$  refers to the value of the field at the centre of the vortex (denoted by ‘b’).  $B_{av}$  is the average field value and  $B_{pk}$  is the field that the muon will most likely experience inside the FLL (point ‘c’)(Lee, Kilcoyne & Cywinski 1999a).

A numerical simulation can be used to derive the  $P(B)$  for an ideal FLL. Such a description of the field from a single vortex can be expressed by a Fourier series in reciprocal space:

$$B(r) = \langle B \rangle \sum_{\mathbf{q}} B_{\mathbf{q}} \exp(i\mathbf{q} \cdot \mathbf{r}) \quad (3.15)$$

where  $\mathbf{q}$  is the reciprocal lattice vector and  $B_{\mathbf{q}}$  represents the Fourier components at each field  $B_i$ , which, in the presence of the London limit, are given by a generalised form factor  $F_m(\mathbf{q})$ :

$$B_{\mathbf{q}} = F_m(q) = \frac{1}{1 + \lambda^2 |\mathbf{q}|^2} \quad (3.16)$$

Having obtained a  $P(B)$  for the FLL, it is then possible to extract the various moments of the distribution, each of which helps describe the behaviour and arrangement of the vortices inside the sample and can be understood in terms of the generic equation:

$$\langle \Delta B^N \rangle = \left( \frac{\sum_{i=1} p(B_i) (B_i - \langle B \rangle)^N}{\sum_i p(B_i)} \right) \quad (3.17)$$

where  $B_i$  is the field value at a particular point in the distribution,  $\langle B \rangle$  is the mean field (the first moment), and  $N$  is the total number of data points.

The second moment, or the variance of the distribution, reflects the range of accessible fields. Within the mixed state and in the limit where  $\lambda \mathbf{q} \gg 1$ , this can, for a triangular FLL, be described in the London limit by (Barford & Gunn 1988):

$$\langle \Delta B^2 \rangle^{1/2} = \left( \frac{0.00371 \Phi_0^2}{\lambda^4} \right)^{1/2} \quad (3.18)$$

The third moment of the distribution  $\langle \Delta B^3 \rangle$  describes the skewness of the distribution. However, it has been shown by Lee et al. (Lee 1993b) that a more useful parameter is:

$$\alpha = \frac{\langle \Delta B^3 \rangle^{1/3}}{\langle \Delta B^2 \rangle^{1/2}} \quad (3.19)$$

Such a dimensionless quantity can be useful in trying to describe the underlying FLL orientation and structure. Indeed, it has been shown by Menon (1999) that  $\alpha=1.2$  represents an ideal vortex lattice.

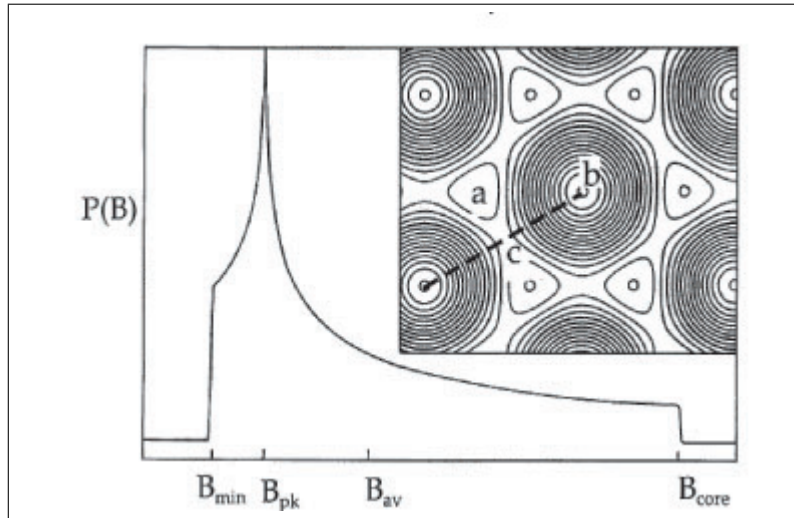


Figure 3.7: A probability spectra for the magnetic field distribution arising from a perfect FLL. Such a positive skewness reflects a hexagonally orientated lattice with long range order. On the schematic: ‘a’ is the minimum field  $B_{min}$  that the muon will experience, ‘b’ is the field at the vortex core ( $B_{core}$ ), and ‘c’ is the saddle point between vortices ( $B_{pk}$ ).  $B_{av}$  represents the mean field. (Source: (Drew, 2005))

When considering a FLL, it is known that as the applied field increases, so too do the number of vortices that enter the bulk of the superconductor. This leads to an increase in the overlapping of the superconducting vortices and, consequently, *within the dilute limit*, a rise in the minimum field of the lattice. As a result this can effect the  $P(B)$  lineshape. In particular, as one increases the field towards the vortex glass phase, an increase in the width  $\langle \Delta B^2 \rangle^{1/2}$  occurs as the range of accessible fields increases. However, as one moves into the liquid regime upon increasing the temperature, the lineshape narrows. This is because there is a reduction in the phase coherence along the vortex axis and consequently a reduction in the overall field in the  $z$  ( $c$ -axis) direction.

Such behaviour though, only occurs within a small region of the Field-Temperature (B-T) diagram. Outside of this small limit, as one increases the applied field, there is no change in  $\langle \Delta B^2 \rangle^{1/2}$  since this quantity is dependent upon the in-plane ordering of the FLL. As one moves out of the Bragg Glass region into the Vortex Glass state, the orientation of

the vortices in a pristine material does not change and therefore the lineshape of the  $P(B)$  distribution remains constant.

It is also important to note that the  $P(B)$  value for  $B_{core}$  in highly anisotropic superconductors can often be obscured due to the small coherence length  $\xi$  of the vortices. This occurs more specifically in the region  $H \ll H_{c2}$  and means that even when relatively high statistics are taken, the high field tail becomes comparable with the default noise value  $P_d$ . Subsequently, this means that the width of the distribution can be systematically underestimated leading to an overestimate of  $\lambda$ . For a triangular FLL, one can also measure the skewness by (Song 1993) (Song 1995) (Lee 1993b):

$$\langle B \rangle - B_{pk} = \frac{2}{3} \ln 2 \frac{\Phi_0}{4\pi\lambda^2} \quad (3.20)$$

the modulus of which has been shown to be inversely proportional to  $\lambda^2$  (Sidorenko 1990). This relationship can be continued further to exclude the variation in the width of the distribution. Thus:

$$\beta = \frac{\langle B \rangle - B_{pk}}{\langle \Delta B^2 \rangle^{1/2}} \quad (3.21)$$

However, it is clear that the proper extraction of  $\lambda$  is still a problem and that one relies on high statistics in order to correctly identify  $B_{core}$ .

At fields closer to  $H_{c2}$ , one has to take into the account the overlap of the coherence lengths  $\xi$  originating from different vortices within the FLL. Thus, more sophisticated models are required to obtain accurate values of both  $\lambda$  and  $\xi$ . This has been made possible by calculating analytically the field probability distribution  $P(B)$  from Abrikosov's solution to the Ginzburg-Landau equations (see (Sidorenko 1990) (Brandt 1997)). Another method, involving the use of a scaling function to extend the London approximation for the full range of fields has been developed by Yaouanc (1997) and successfully used experimentally (Sonier 1994), (Sonier 1997a), (Sonier 1997c) (Sonier 1997b), (Aegeter 1998). Simplified, it includes an extra term in the London form factor  $F_m(q)$  of Equation 3.49 to account for the presence of the normal state cores within this particular applied field regime, thus transforming it to:

$$F_m(q) = \frac{\exp(-\xi^2 \mathbf{q}^2/4)}{1 + \lambda^2 |\mathbf{q}|^2} \quad (3.22)$$

Indeed, one can also account for thermal fluctuations within the FLL that reduce the range of available field values, thus narrowing the linewidth, by including a term known as the Debye Waller factor ( $\exp(-\langle u^2 \rangle \mathbf{q}^2)$ ). This changes equation 3.18 to (Harshman 1991):

$$\langle \Delta B^2 \rangle^{1/2} = B^2 \left[ \frac{\exp(-\mathbf{q}^2 \langle u^2 \rangle)}{(1 + \lambda^2 |\mathbf{q}|^2)^2} \right] \quad (3.23)$$

### 3.1.5 The Low Energy Muon Technique

Over the past decade there has been an increasing interest in the physics of thin films and materials of low dimensions. Until recently, investigations into such systems using muons had been limited by experimental restrictions. However, a continued development of the conventional  $\mu$ SR method has successfully managed to reduce such limitations. The recently upgraded Low Energy Muon (LEM) instrument, on the purpose-built beamline  $\pi$ E4 at PSI, is able to tune the energy of the muons between 0eV and 30keV, via a tertiary beam of mean energy  $\sim 15$ eV that is produced from an initial muon beam momentum of 28MeV/c. Being able to vary the energy of the incoming muons allows for the control of the implantation depth into the sample which can be of the order of a few hundred nanometers (Morenzoni 1994) (Harshman 1987). The recent upgrade has now resulted in an increase in the incident low-energy muon flux of up to  $\sim 8000$ /s (Prokscha 2005) (Prokscha 2006).

Initially, the 4MeV surface muon beam passes through a moderator (Figure 3.8) - an insulating frozen Nitrogen layer (of band-gap energy  $\sim 20$ eV (Klein & Venables 1976)) deposited onto a substrate of Ag ( $\sim 125\mu\text{m}$ ). Before the experiment can commence, the moderator area is isolated from the rest of the LEM apparatus. Then, after flushing, the liquid nitrogen is deposited onto a substrate until it reaches a thickness of a few hundred nm. This layer is then maintained by a continuous flow of Nitrogen.

The substrate (of good thermal conductivity at low temperatures) acts to degrade the beam to a few tens of keV through ionisation processes and is cooled down to  $\sim 10$ K *in vacuo*. Such UHV conditions prevent any uncontrolled deposition onto the target which would result in a decrease in its efficiency as a moderator. Aside from this, it also contributes by reducing the number of low momentum muons scattered by impurities.

The muons then pass into the solid Nitrogen layer where they are then thermalised to only a few keVs. At this point, the main inelastic interaction is a charge-exchange process but, as the energy of the muons drops below  $\sim 50$ eV, the scattering cross section for such collisions reduces. Further to this, the particles in this Van der Waals material are only weakly interacting (to a first approximation), and so there are no other possibilities for further efficient energy loss. Even elastic interactions only result in a change in the direction of the muons as their size is much smaller than the nuclei they interact with. This imposed lower energy limit results in an escape depth of up to 100nm in which the angular distribution of the emitted muons is essentially isotropic. Such a small active layer thickness significantly reduces the total number of incoming muons that can be moderated to become epithermal. Consequently the majority of the initial muons leave with an energy  $\sim 500$ keV. The moderators currently used have a moderation probability between  $10^{-4}$  and  $10^{-5}$  per incoming muon and have been shown to have no significant effect on the polarisation of the muon's spin (Schenck 1985).

A small number of the incoming muons exit the moderator target with energies  $\sim 10$ eV. These very slow muons are then accelerated via an applied electric field up to 20keV. At this point they are classified as 'low energy muons' and are separated from those muons of energy  $\sim 500$ keV by an electrostatic transport system comprising a number of lenses that select and focus the low energy muons towards the sample as shown on the schematic in Figure 3.9.

Firstly, after passing through the moderator, the low energy muons are focused down

an electrostatic mirror by an Einzel lens (Figure 3.9) which is Nitrogen cooled to ensure voltage stability. The muons of lower energy are then deflected through  $90^\circ$ . However, because of their high energy, the fast muons pass through this mirror and are registered by a Multi-Channel-Plate counter (denoted as MCP1 on Figure 3.9). The second Einzel lens then focuses the low energy beam onto the trigger detector (which starts the time window) and a final lens sets the beam onto the sample itself. This latter focusing is aided by a conical lens which reduces the beam spot size further ( $\sim 10\text{mm}$  FWHM).

The low-energy muons can be identified using a time of flight method (TOF), between the trigger detector and the initial beam counter. The trigger detector is used to set the start time of each muon (Figure 3.10). It comprises a thin carbon foil ( $2.2\mu\text{g}/\text{cm}^2$ ) that causes the muons to emit electrons that, in turn, are deflected  $90^\circ$  to another MCP (MCA on Figure 3.10). The detector is subsequently calibrated with a delay such that the start of each event corresponds to the time the muon arrives in the sample. As a result of this extra distance to the sample and the loss of energy through the carbon foil, the muon implantation energy decreases slightly (by approximately  $0.42\text{keV}$ ) (Prokscha 1999).

The sample itself is insulated from the sample holder. As such an electric field of up to  $\pm 12\text{kV}$  can be applied to the sample holder to enable the acceleration or deceleration of the muons. In this way the energy of the muons can be controlled and thus, so can their implantation depth. The temperature is controlled by a cold finger cryostat which has a range 4 -  $700\text{K}$ . A pair of Helmholtz coils is able to provide a parallel magnetic field (relative to the spin of the muon) of up to  $3000\text{G}$  but the maximum field limit in the perpendicular orientation is, however,  $450\text{G}$ . This is due to the space needed for magnets being occupied

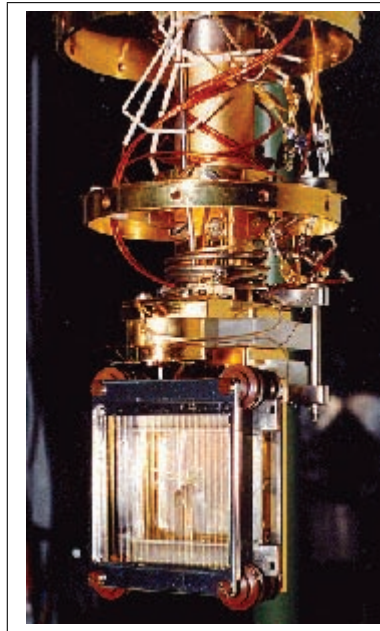


Figure 3.8: A photograph of the moderator for the LEM instrument comprising a frozen Nitrogen layer and Ag substrate. (Source: [www.psi.ch](http://www.psi.ch))

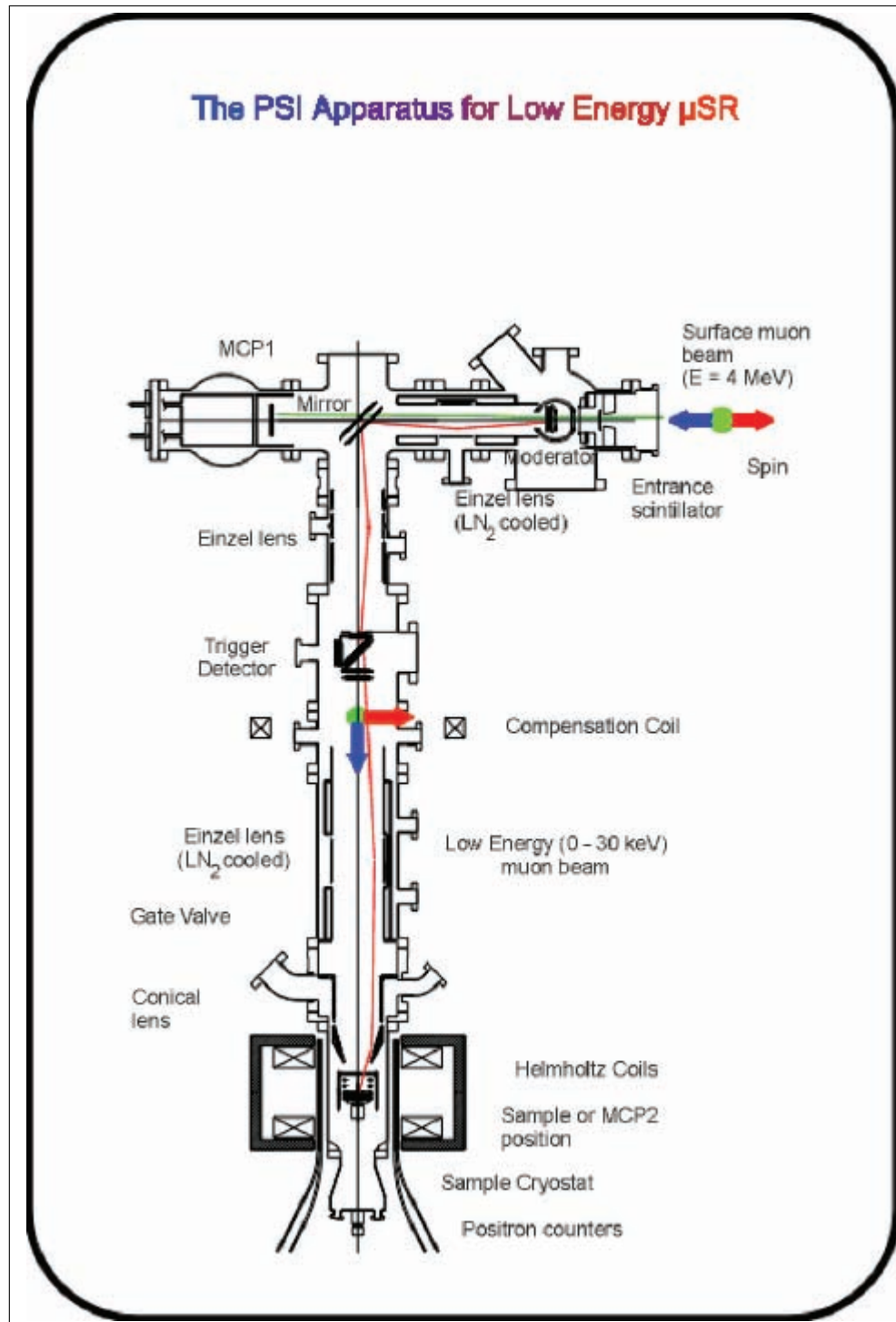


Figure 3.9: A schematic diagram showing the complete LEM beamline apparatus. The Einzel and conical lenses aid in beam focusing; the MCP1 detects high energy muons and the trigger detector starts the time window for the experiment. (Source: [www.psi.ch](http://www.psi.ch))

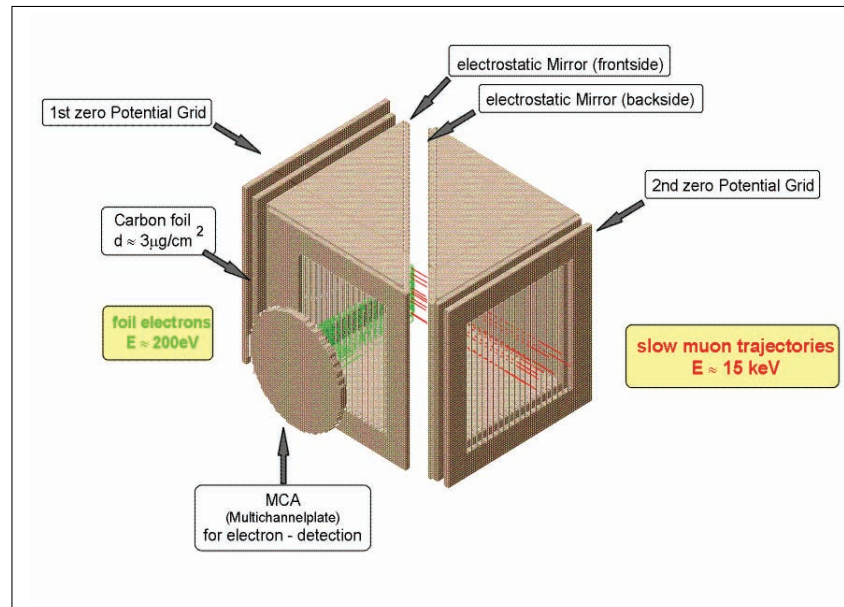


Figure 3.10: *The slow muon trigger detector is used to start the timer of the time window for each muon entering the sample chamber. The incoming muons enter from the bottom right of the diagram. (Source: [www.psi.ch](http://www.psi.ch))*

by the cryostat and to limit the effect on the momentum of the low energy muons.

It is also important to realise how the direction of the applied field can affect the steering of the muon beam. In order to resolve any misalignment problems, a pair of ring anodes apply an electric field to the beam so that the magnetic force is compensated for. The positrons resulting from the muon decay are normally detected by a pair of scintillation detectors surrounding the sample. Each comprises two scintillators coupled to two photomultiplier tubes via a series of waveguides. Such detectors are sub-grouped into pairs to help distinguish between the background positrons and those resulting from decayed muons in the sample. If a “good” positron hits one of the detectors in the pair, it will make contact with the second one too. The background positron rate has been estimated at approximately 5/sec (Prokscha 2006). In the parallel field configuration, however, only the left and right detectors are used. This is because when the magnet is inserted for such an orientation, there is only space for these detectors. Indeed, it does not affect the overall collection of data as the detectors in the up and down positions will each display a constant count rate over time. It is the histograms in the left and right detectors that will produce a precession signal.

## 3.2 Neutron Scattering Techniques

### 3.2.1 Neutron Production

The neutron (first discovered by Chadwick (1932)) has proven to be a useful tool for studying condensed matter systems. In particular, it will be shown in this thesis that it can determine the magnetic profile of thin films, image the arrangement of vortices in bulk, type II superconductors and, overall, give information that complements results obtained from other probing methods.

There are two main sources for the production of neutrons: nuclear reactors and spallation processes. The former creates neutrons for use as microscopic probes by utilising the fission chain reaction process. Such a method is used at the ILL facility in Grenoble and at the HMI in Berlin.

The spallation sources however, used at both PSI and ISIS, provide neutrons through the use of an accelerator and have been used to obtain the data recorded within this thesis. They can either be continuous or pulsed sources. The latter method is utilised by the ISIS facility in Oxford, U.K., and is described now.

As an  $H^-$  ion beam is being accelerated, it is split into two groups by a radio frequency quadrupole (RFQ) accelerator. The RFQs use radio frequency electric fields to accelerate, focus and form small, discrete groups before the ions are passed to the linear accelerator where they are accelerated up to 70MeV. These two pulses are separated by 320ns and have a FWHM of 70ns. By having this double peak structure, it is possible to have an intense beam pulse whilst, at the same time, minimising the effect of heating in the neutron target (approximately 160kW).<sup>2</sup>

At this energy they enter the synchrotron, where upon they are stripped of their electrons by an aluminium foil. The resulting beam then makes approximately 10,000 revolutions and acquires an energy of 800MeV.

A similar scenario occurs at PSI, where the proton beam is “pre-accelerated” in a Cockcroft-Walton column to an energy of 870keV and then increased further by a 4-sector injector cyclotron, before reaching 590MeV in an 8-sector cyclotron. However, unlike at ISIS, the initial proton beam is not pulsed.

The target at ISIS comprises several thick, tantalum clad, tungsten plates, set inside a pressure chamber with water cooling channels allowing for the removal of heat (approximately 90kW). When the protons bombard it, after leaving the synchrotron, neutrons with very high energies are released. These neutrons are not suitable for condensed matter studies and therefore have to be moderated before being used. At PSI, the target is an array of lead rods bathed in heavy-water which helps cool the target and moderate the resulting neutrons to acceptable energies.

Typical energy moderators are those with large scattering cross sections such as hydrogen which maximise the reduction in neutron energy through repeated collisions. Such inelastic collisions are also used experimentally too where Equation 3.25 (discussed in the next section) is adapted to become a function of the change of energy  $dE$  (Squires 1996).

At ISIS, four moderators are used (shown in Figure 3.11): two comprising water at

<sup>2</sup>Such a technique is particularly useful during time dependent measurements (for example,  $\mu$ SR).

room temperature, one using liquid methane at 100K, and another containing liquid hydrogen at 20K. Each reduces the energy of the neutron beam by a certain amount depending on the specific requirements of the individual experiments. The neutrons are then finally directed out of the target down 18 beam channels towards the scattering instruments via neutron guides.

### 3.2.2 Introduction to scattering

Scattering techniques involving neutrons have several advantages over other methods for investigating the samples detailed within this thesis. Firstly, by interacting with atomic nuclei rather than the surrounding electron clouds, the neutron is able to sense light atoms in the presence of heavier ones and distinguish between different isotopes as well as neighbouring elements in the periodic table. This is a property that X-ray and electron scattering methods do not possess.

Knowing that the resulting total neutron wavefunction is equal to the sum of a plane wave and spherically scattered wave, it is possible to calculate the scattering cross-sections  $\sigma_s$  for the number of neutrons passing through a sphere per unit time and undergoing a nuclear interaction. The scattering cross section  $\sigma_s$  can be used to define the scattering length  $b$  which acts as a measure for the strength of the nuclear scattering from each scattering site (Equation 3.24):

$$\sigma_s = 4\pi |b|^2 \quad (3.24)$$

It is then sensible to calculate the neutron flux scattered into a solid angle  $d\Omega$  (see

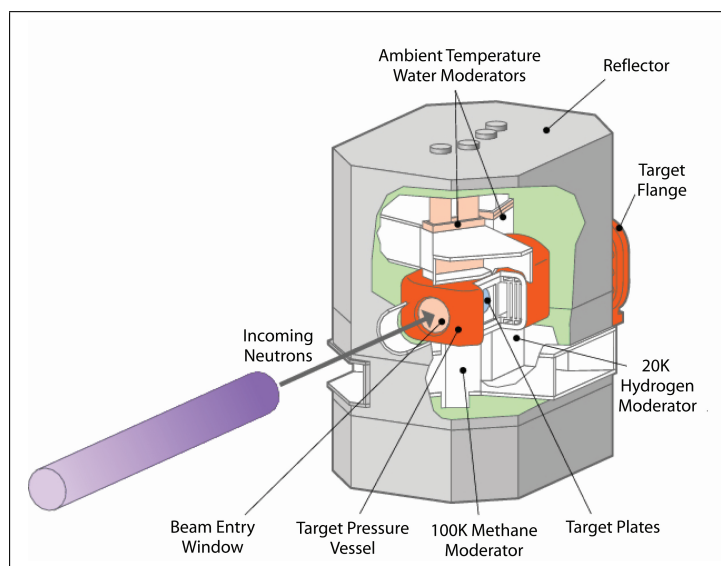


Figure 3.11: *At ISIS there are four types of moderator: two comprising water at room temperature, one containing liquid methane at 100K and one with liquid hydrogen at 20K, all reducing the neutron energy by a different amount. (Source: [www.isis.rl.ac.uk](http://www.isis.rl.ac.uk))*

Figure 3.12) since the areas of the surrounding detectors in a neutron scattering experiment are finite. The differential cross-scattering can be defined over all directions as:

$$\sigma_s = \int \left( \frac{d\sigma_s}{d\Omega} \right) d\Omega \quad (3.25)$$

and in the case of scattering occurring within one plane (i.e. only scattering through  $\theta$  for example - see Figure 3.12):

$$\sigma_s = \int_0^\pi \left( \frac{d\sigma_s}{d\Omega} \right) 2\pi \sin \theta d\theta \quad (3.26)$$

Within the Born approximation the scattering length  $b$  can be described by:

$$b = -\frac{m}{2\pi\hbar^2} \int e^{i(\mathbf{k}'-\mathbf{k})\cdot\mathbf{r}} U(\mathbf{r}) d\mathbf{r} \quad (3.27)$$

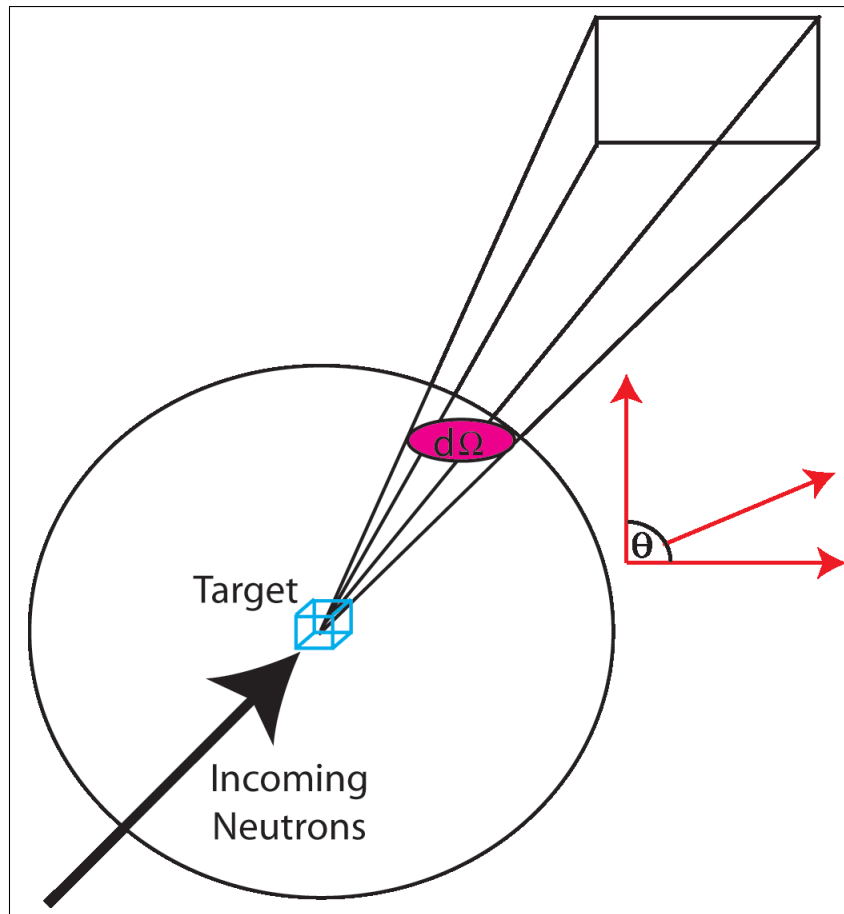


Figure 3.12: Knowing the differential scattering cross section and the amount of flux passing through a sphere per unit time, one can then calculate the neutron flux scattered into a solid angle  $d\Omega$ .  $\theta$  is defined as the angle subtending the  $x$ - $y$  plane as shown.

where

$$U(\mathbf{r}) = \frac{2\pi\hbar^2}{m} b\delta(\mathbf{r} - \mathbf{r}_n) \quad (3.28)$$

is the Fermi Pseudopotential used to describe the interaction potential between the neutron and the nucleus (denoted by the position vectors  $\mathbf{r}$  and  $\mathbf{r}_n$  respectively and shown in Figure 3.13) with a coherent neutron scattering length  $b$ .  $\mathbf{k}$  and  $\mathbf{k}'$  represent the incoming and outgoing wavevectors respectively and  $m$  is the mass of the neutron.

Secondly, the neutron-nuclide interaction is weak, unlike X-ray scattering. As detailed later, this permits it to be a highly penetrative probe, able to investigate not only the surface but inside the bulk of a sample too. Such a weak interaction also results in the neutron being a non-destructive probe, ideal for thin films and other samples of reduced dimensions or increased fragility.

Finally, neutrons possess a magnetic moment (Sherwood 1954) and are therefore able to couple directly to the magnetisation of materials on an atomic level. This means that as well as subject to scattering by atomic nuclei, the neutron can be scattered by the magnetic properties of the sample too and thus is able to map the material's magnetic profile. Because the neutron possesses such a magnetic moment  $\mu$ , when it is subjected to an applied magnetic field  $\mathbf{B}$  it will change its energy by an amount:

$$U = -\boldsymbol{\mu} \cdot \mathbf{B} \quad (3.29)$$

This change in energy is dependent upon the orientation of the neutron moment relative to that of the interacting material's.

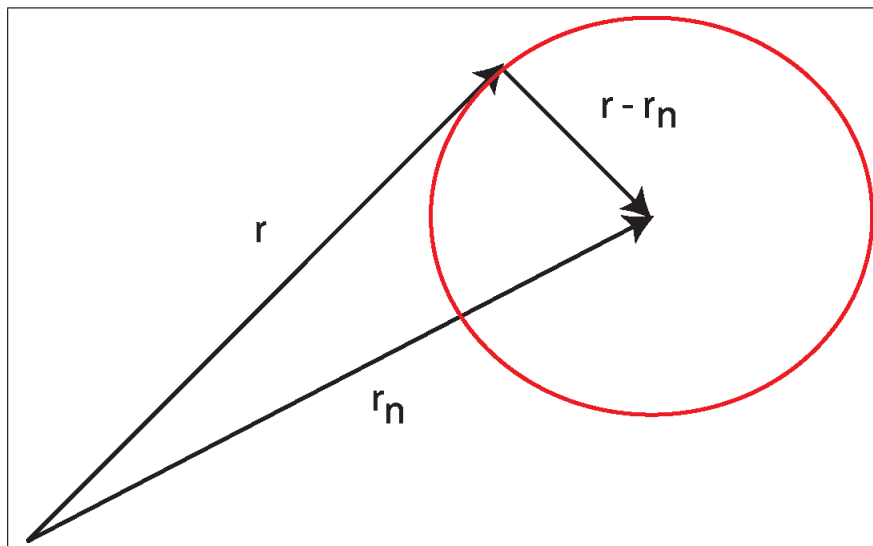


Figure 3.13: *The interaction energy  $U(r)$  between the neutron and the scattering centre (circled red) is dependent upon the position vectors  $\mathbf{r}$  and  $\mathbf{r}_n$  respectively.*

### 3.2.3 Scattering from a crystal lattice

When scattering from nuclear components within a material, one has to consider the arrangement of the atoms inside the lattice. The position of a unit cell within a Bravais lattice can be described by the positional vector  $\mathbf{r}$ , which comprises the basis vectors  $\mathbf{a}$ ,  $\mathbf{b}$  and  $\mathbf{c}$  organised thus:

$$\mathbf{r} = n_1\mathbf{a} + n_2\mathbf{b} + n_3\mathbf{c} \quad (3.30)$$

where  $n_i$  are integer values. One can then expand this to encompass an entire lattice of scattering sites through the vector addition of lattice vectors describing the position of a site within a single unit cell  $\mathbf{R}_{uc}$  and the position of the unit cell within the entire lattice  $\mathbf{R}_{latt}$ . This is shown pictorially in Figure 3.14 and combined, these form the total positional vector  $\mathbf{r}_{tot}$  thus:

$$\mathbf{r}_{tot} = \mathbf{R}_{latt} + \mathbf{R}_{uc} \quad (3.31)$$

Subsequently, it is possible to express these co-ordinate values in terms of the reciprocal lattice vectors,  $\mathbf{a}^*$ ,  $\mathbf{b}^*$  and  $\mathbf{c}^*$  via the relationships:

$$\mathbf{a}^* = \frac{2\pi}{V_0}\mathbf{b} \times \mathbf{c} \quad (3.32)$$

$$\mathbf{b}^* = \frac{2\pi}{V_0}\mathbf{c} \times \mathbf{a} \quad (3.33)$$

$$\mathbf{c}^* = \frac{2\pi}{V_0}\mathbf{a} \times \mathbf{b} \quad (3.34)$$

Here,  $V_0$  represents the volume of the unit cell.

In order to observe constructive interference from neutron scattering, all of the different phases of the scattered waves must add up coherently. This means that the following conditions must be satisfied:

$$\mathbf{q} \cdot \mathbf{a} = 2\pi h \quad (3.35)$$

$$\mathbf{q} \cdot \mathbf{b} = 2\pi k \quad (3.36)$$

$$\mathbf{q} \cdot \mathbf{c} = 2\pi l \quad (3.37)$$

where  $h, k$  and  $l$  are integers representing the well-known Miller indices and  $\mathbf{q}$  is the resultant scattered wavevector in reciprocal space. Hence, the total scattered wavevector can be described by the relationship

$$\mathbf{q} = h\mathbf{a}^* + k\mathbf{b}^* + l\mathbf{c}^* \quad (3.38)$$

According to the Laue equations (von Laue 1913), this means that constructive interference can only occur when  $\mathbf{q}$  equals the vector between the incoming and outgoing wavevectors - otherwise known as the momentum transfer (see Figure 3.15):

$$\mathbf{q} = \mathbf{k}' - \mathbf{k} \quad (3.39)$$

It then becomes clear how one can obtain the familiar Bragg equation for elastic scattering in terms of reciprocal space:

$$|q| = 2k \sin \theta \quad (3.40)$$

The phenomenon of neutron diffraction will produce a series of high and low intensity regions at a detector (analogous to light and dark fringes in photon diffraction).

If the nuclear sites are fixed and one assumes scattering from a point source, the familiar Bragg pattern is obtained in reciprocal space, comprising a series of delta peaks as shown in Figure 3.16. These peaks are separated by a distance  $q=2\pi/r_0$ . Here  $r_0$  is the average interatomic/scattering centre distance in real space. However, in practice such clearly defined Bragg peaks are not often possible. In most cases, the intensity of the diffracted neutron pattern depends predominantly upon the arrangement of the nuclear sites in the lattice and the individual movement of each nucleus. Consequently, this can lead to a slightly altered intensity plot where the resulting peaks are subsequently broadened.

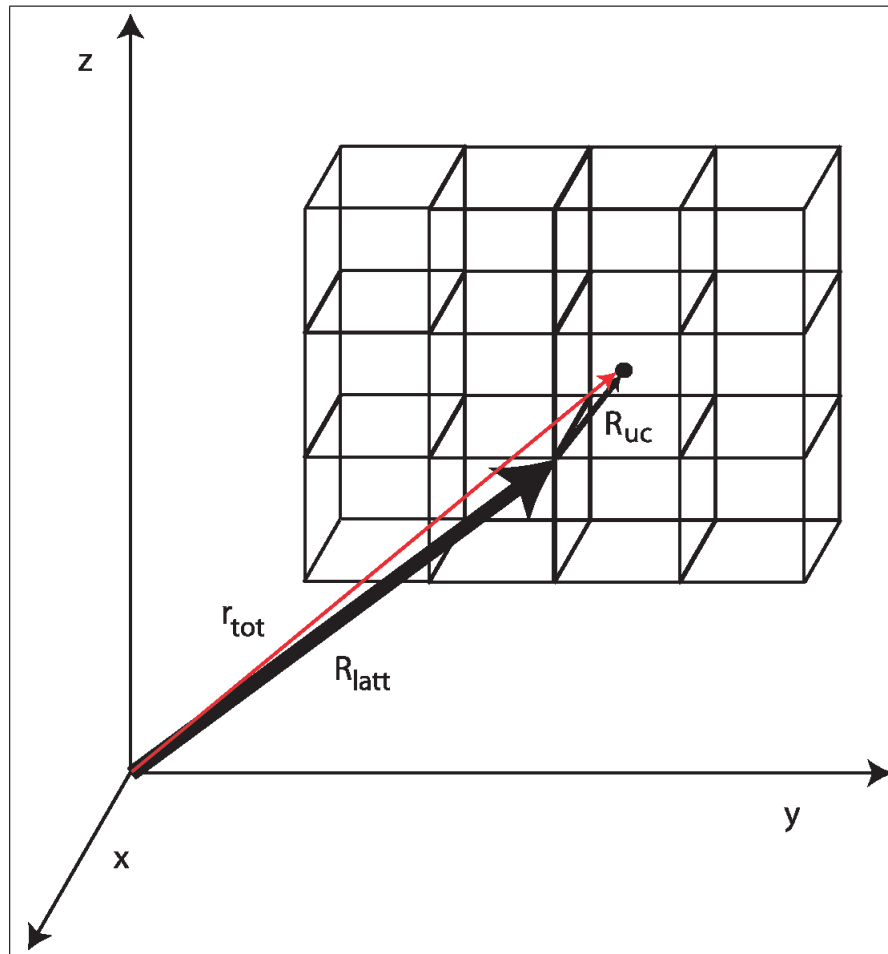


Figure 3.14: *The positional vector of a particular scattering site is determined both by the position of the scatterer within its own unit cell ( $\mathbf{R}_{uc}$ ) and the position of this unit cell within the lattice ( $\mathbf{R}_{latt}$ ). Both sum to the total position vector ( $\mathbf{r}_{tot}$ ) denoted by the red vector.*

Further to this, it is possible to plot a quantity known as the radial distribution function  $g(r)$  that calculates the radial average density of scattering centres from a certain position in real space. Considering first the left hand plot of Figure 3.17, it is clear that peaks occur every integer multiple of 'r' (the interatomic distance). However, if the arrangement of the nuclei is less ordered (as per the right hand plot of Figure 3.17) then the amplitude of  $g(r)$  decreases as a function of r. By taking the Fourier Transform of the radial distribution function:

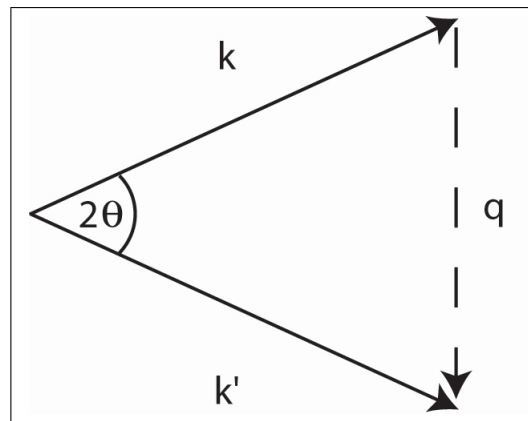


Figure 3.15: The difference between the incident and the scattered wavevector ( $\mathbf{k}$  and  $\mathbf{k}'$  respectively), results in the reciprocal lattice vector  $\mathbf{q}$ .

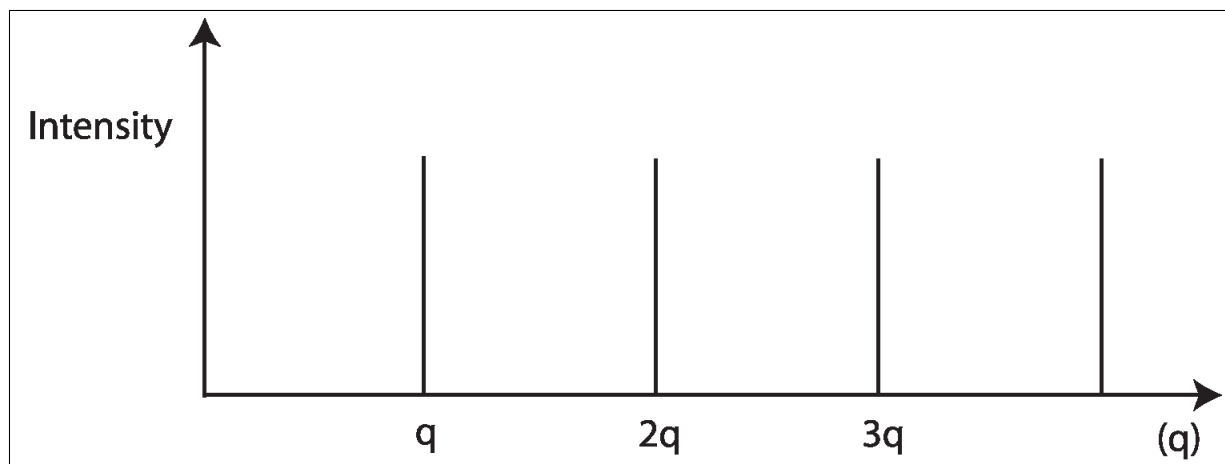


Figure 3.16: Scattering from a series of point nuclei separated by an interatomic real-space distance  $r_0$  (in an ideal case) results in Bragg peaks occurring at multiple-integer values of  $q$  in reciprocal space. This picture shows the basic scattering obtained when considering a 1D plane only.

$$S(q) = A \int g(r) e^{i\mathbf{q}\cdot\mathbf{r}} dr \quad (3.41)$$

where  $A$  is a constant described further by Squires (1996)<sup>3</sup>, one is able to obtain the Structure Factor  $S(q)$  where the peak separation is  $2\pi/r_0$  (shown in Figure 3.18).

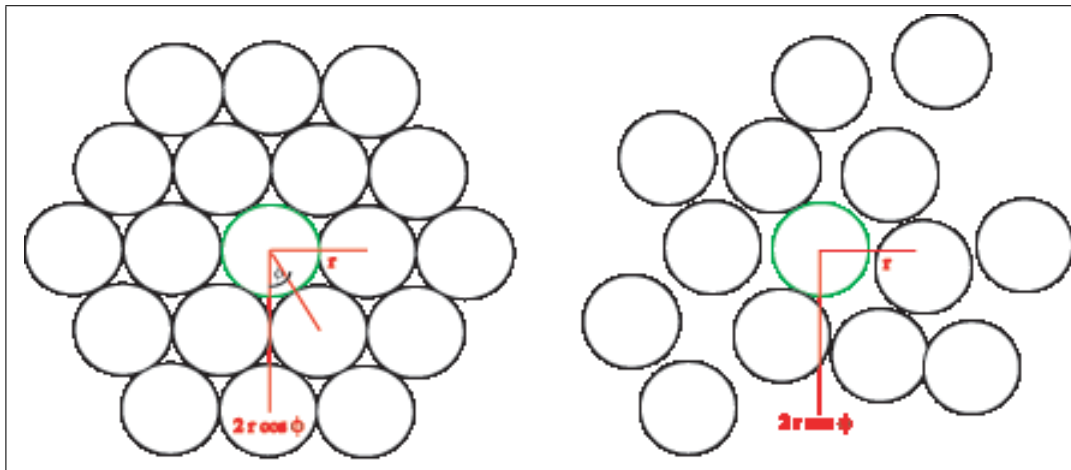


Figure 3.17: *Left hand plot: An ordered array of nuclei with interatomic distance  $r$ . Right hand plot: As the arrangement of the nuclei becomes more disordered the  $g(r)$  peaks reduces significantly with increasing  $r$ .*

The structure factor can also be obtained when one takes into account the contributions to the differential cross scattering term. For a regular lattice this can be described by:

$$\frac{d\sigma_s}{d\Omega} = \left| \sum_{n_1, n_2, n_3} e^{2\pi i(n_1 h + n_2 k + n_3 l)} \sum_m b_m e^{i\mathbf{q}\cdot\mathbf{r}_m} \right| \quad (3.42)$$

Here, the left hand term corresponds to the scattering from within a single unit cell and the term on the right represents scattering over all the unit cells ‘ $m$ ’ in the lattice. This reflects the earlier statement that one needs to consider the total scattering vector  $\mathbf{r}_{tot}$ . Indeed, taking the square of the last term in Equation 3.42 results in a quantity proportional to the nuclear scattering intensity  $I(q)$ :

$$I(q) \propto |S(q)|^2 = \left| \sum_m b_m e^{i\mathbf{q}\cdot\mathbf{r}_m} \right|^2 \quad (3.43)$$

The structure factor alone, however, cannot account for the resulting scattering intensity pattern. To properly match the  $I(q)$ , one must also introduce a form factor  $F(q)$  to account for the reduction in amplitude observed with increasing  $q$ . In terms of nuclear scattering only, the Porod factor takes into account the distribution of nuclear sizes within the lattice and has a  $1/q^4$  dependence. However, such an effect is due to large scale inhomogeneities in the lattice.

<sup>3</sup>See Squires (1996), page 88.

It should also be noted that up to now, the scattering being considered has been elastic with the atomic lattice being stationary. However, in practice, this is not entirely true. Each atom will be subject to thermal vibrations and thus, the overall scattering amplitude will be less. To account for the reduction in scattering intensity from these thermal vibrations one can incorporate a Debye-Waller factor  $e^{-\langle u^2 \rangle \mathbf{q}^2}$  thus:

$$S(q) = \sum_m b_m e^{-\langle u^2 \rangle \mathbf{q}^2} e^{i\mathbf{q} \cdot \mathbf{r}_m} \quad (3.44)$$

where  $\langle u^2 \rangle$  is the mean square displacement of the nucleus from its “rest” position over all nuclear sites  $m$ .

In addition to nuclear contributions though, scattering can also be caused by systems comprising magnetic moments (either nuclear or electronic). The diffracted intensity is therefore affected by the magnetisation of a material and thus can be described by a magnetic form factor  $F_m(q)$  (Squires 1996):

$$F_m(q) = \frac{1}{\mu_N} \int \frac{\boldsymbol{\mu}_{mat}}{V} e^{-i\mathbf{q} \cdot \mathbf{r}} dV \quad (3.45)$$

This equation describes the Fourier transform of the magnetisation  $\boldsymbol{\mu}_{mat}$  of the material over the entire atomic volume  $V$  (where  $\mu_N$  is the magnetic moment of the neutron). Looking at equation 3.45, it becomes clear that the scattering of neutrons is affected by the density of magnetic moments within the lattice. Indeed, one can see that as the magnetisation (the spatial distribution of the magnetic moments) in the sample is increased, the form factor (the Fourier transform of the distribution) falls off more rapidly and vice versa.

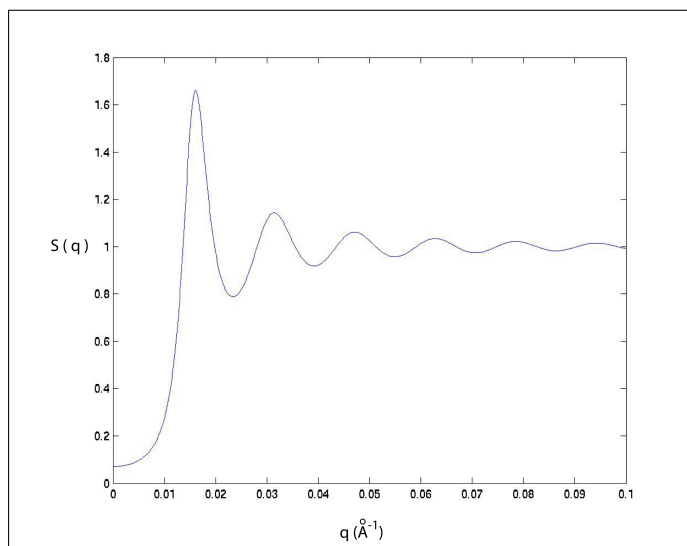


Figure 3.18: From the radial distribution function  $g(r)$ , one can obtain the nuclear structure factor  $S(q)$  in which the peak interval spacing is  $2\pi/r_0$ .

### 3.2.4 Scattering from the FLL

The effect of a variation in the magnetisation is also evident when neutron scattering is performed on a FLL. In this scenario, the distribution of the magnetic flux density within the sample can vary greatly - over the order of several hundred Angstroms.

For an ideal vortex lattice, the magnetic form factor can be defined over two-dimensions  $d_2r$  as

$$F_m(q) = \frac{1}{\phi_0} \int B(\mathbf{r}) e^{i\mathbf{q}\cdot\mathbf{r}} d_2r \quad (3.46)$$

The local magnetic flux distribution can be represented by a Fourier transform over all the scattering vectors  $\mathbf{q}$ ,

$$B(r) = \langle B \rangle \sum_{\mathbf{q}} F_m(\mathbf{q}) e^{i\mathbf{q}\cdot\mathbf{r}} \quad (3.47)$$

where, for a triangular vortex lattice (Lee, Kilcoyne & Cywinski 1999b):

$$\langle B \rangle = \frac{\sqrt{3}\phi_0}{2a^2} \quad (3.48)$$

However, calculations of the magnetic form factor originating from a FLL require an in-depth knowledge of the exact field distribution. A smoothing of the diffracted Bragg peaks emanating from neutrons scattered from the vortex lattice, is a consequence of instrumental resolution (described in the next section) and thermal stimulation of the magnetic vortices. Despite this, a good approximation for the magnetic form factor can be obtained by taking the Fourier expansion of Equation 3.47 to obtain (Tinkham 1975):

$$F_m(q) = \frac{B}{1 + \lambda_L^2 q^2} \quad (3.49)$$

Such a quantity is known as the London form factor and has a core cut-off to account for the field singularity at the centre of the magnetic vortex. Such an approximation though is unphysical. For fields greater than the lower critical field  $H_{c1}$ , the second term in the denominator of Equation 3.49 is dominant. Consequently, the intensity at higher  $q$  is weaker than at lower values as the range over which the flux lines act approaches the order of  $\lambda$ .

Once the structure and form factors are known it is possible to extract the overall scattering intensity for a FLL, namely (Christen 1977):

$$I(q) = S(q) F^2(q) \quad (3.50)$$

More specifically, it can be calculated over a unit volume  $V$  as (Forgan 1998) (Christen 1977):

$$I(\mathbf{q}) = 2\pi\phi \left(\frac{\gamma}{4}\right)^2 \frac{V\lambda^2}{\Phi_0 \mathbf{q}} |F_m(\mathbf{q})|^2 \quad (3.51)$$

where  $\phi$  is the incident neutron flux,  $\gamma$  is the neutron magnetic moment and  $\Phi_0$  is the flux quantum.

### 3.2.5 Small Angle Neutron Scattering (SANS)

The scattering of neutrons from a FLL can be accomplished using the Small Angle Neutron Scattering instrument (SANS-I) at the SINQ facility at PSI since the wavelength of the neutrons is comparable to the spacing between the vortices. This can then image in a 2D plane the FLL. The desired wavelength of the neutrons is obtained through a velocity selector situated just inside the target radiation shielding. This apparatus comprises an array of slits that allow neutrons of the correct wavelength through. Each slit is a passage with a helical trajectory around the rotator's body as it operates at a frequency of approximately 500Hz. This means that neutrons of the correct wavelength will be able to pass through the velocity selector unhindered. For the purposes of investigating the FLL in HTSCs, the desired wavelength is of the order of 5-20Å. When the neutron, with any initial wavevector  $\mathbf{k}$ ,

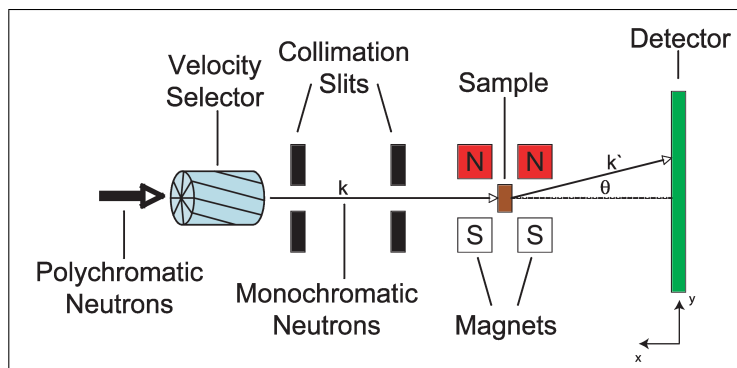


Figure 3.19: *The SANS setup comprises a velocity selector, collimation slits, applied magnetic field and a large-area detector. The muons, in this simple diagram, enter from the left.*

enters the sample, it undergoes scattering from both nuclear and magnetic vortex sources. Any scattered neutron is deflected by an angle  $\theta$  and is registered by a 2D  $^3\text{He}$  detector comprising 128 x 128 elements, each of area 7.5mm<sup>2</sup>. This detector can be manoeuvred either along the axis of the instrument or laterally (X and Y respectively in Figure 3.19) to obtain different q-ranges. As well as this, the distances between the source to the sample and the sample to the detector can each be adjusted between 5-20m. In order to extend the q-range, one has to measure at a particular incident angle and shift the position of the detector along the x or y direction (as in Figure 3.19) to detect the higher q values. By using this particular method of scattering, one is not susceptible to the many finite steps that are needed in monochromatic beam measurements and which contribute to the reduction of the overall experimental resolution. Indeed, resolution in a small angle neutron scattering experiment has been investigated by Pedersen (1990) and the FWHM is shown to be of the form:

$$\Delta\beta = \frac{2r_1}{L} \quad (3.52)$$

for when the aperture angle  $a_1 \geq a_2$  (as shown in the diagram of Figure 3.20) and

$$\Delta\beta = 2r_2(1/l + 1/L) \quad (3.53)$$

for when the aperture angle  $a_1 < a_2$ .  $r_1$  and  $r_2$  represent half the width of the detection area and half the width of the window at the sample position respectively (see Figure 3.20). By increasing the length of the distance  $L$  between the first collimation slits to the sample, and the sample to the detector  $l$ , the intensity resolution can be significantly increased.

### 3.2.6 Polarised Neutron Reflectivity

Because of the neutron's intrinsic properties it is subject to both nuclear and magnetic scattering; the latter making use of the spin of the neutron to give depth dependent magnetisation profiles of single and multilayer magnetic films. Polarized Neutron Reflectivity (PNR) has shown to be an excellent technique for examining such samples by investigating the intensity of the reflected neutrons from an interface as a function of the scattering vector. Knowing  $k = 2\pi/\lambda$  and refining Equation 3.40:

$$q = \frac{4 \pi \sin \theta}{\lambda} \quad (3.54)$$

where  $\theta$  is the angle between the wavevector  $\mathbf{k}$  and the surface of the sample as shown in Figure 3.21.

Because of the neutron's wave-particle duality, its optical properties are similar to

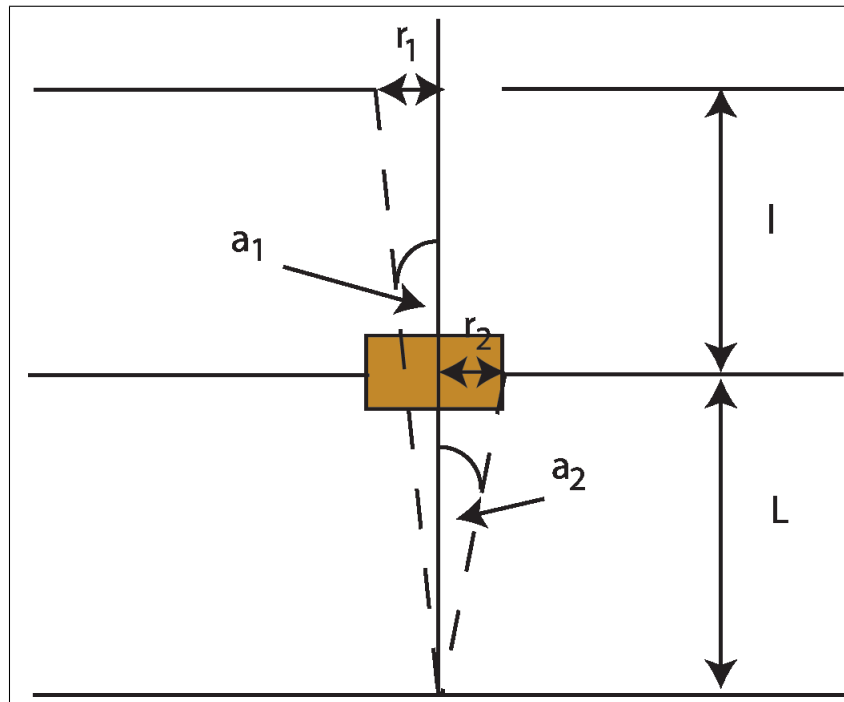


Figure 3.20: *The instrumental resolution for a small angle neutron scattering experiment is dependent upon the the source-sample ( $L$ ) and sample-detector ( $l$ ) lengths. The sample position is shaded brown and the beam enters from the bottom moving upwards. (See text for details.)*

those of a photon crossing the boundary between two different mediums with different refractive indices. When the neutron crosses from one medium to another it undergoes refraction if the refractive indices of each of the layers are different and if its path is not normal to the interface. This results in a change in the neutron's trajectory as stated by Snell's equation:

$$n_1 \sin \phi_1 = n_2 \sin \phi_2 \quad (3.55)$$

where  $n_1$  and  $n_2$  are the refractive indices of the different mediums, and  $\phi_1 = 90 - \theta_1$  and  $\phi_2 = 90 - \theta_2$  are the angles of incidence and refraction of the neutron respectively (see Figure 3.22). This reflects the fact that a more dense medium with a greater scattering length density will increase the perpendicular component of the velocity of the incoming neutron. Combining this with Bragg's law, one obtains the following relationship:

$$\frac{\sin \phi_1}{\sin \phi_2} = \frac{k_2}{k_1} \quad (3.56)$$

For neutrons with a fixed wavelength, total reflectivity can occur whilst the angle of incidence has not surpassed a critical value  $\theta_c$ , defined as:

$$\cos \theta_c = \frac{n_2}{n_1} \quad (3.57)$$

where  $n_2$  is typically less than 1. Any neutrons impinging on the boundary with an angle of incidence greater than  $\theta_c$  are transmitted at the interface and undergo refraction. The resulting reflectivity  $R(q)$  is thus the ratio of the reflected to the incident intensity:

$$R(q) = \frac{I_{out}(q)}{I_{in}(q)} \quad (3.58)$$

This intensity depends upon the interference of the reflected neutron wavelengths. Those reflected from the first interface are not the only contributing factor to the output intensity. Indeed, neutrons that are reflected from subsequent boundaries within a multilayer structure can form constructive or destructive interference depending on whether the neutron wavelengths originating from different layers arrive in or out of phase with one another respectively. In optics, these are observed through the formation of light and dark fringes.

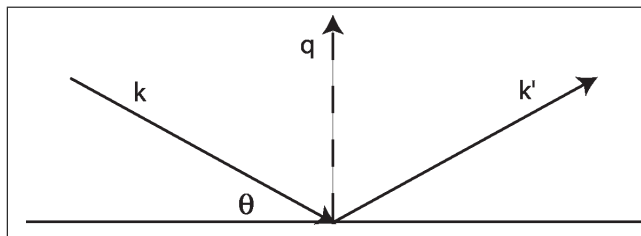


Figure 3.21: Demonstrating the arrangement for the incoming  $k$  and outgoing  $k'$  wavevectors for polarised neutron reflectometry where  $\mathbf{q} = \mathbf{k}' - \mathbf{k}$ .

The same fringes can be detected in neutron reflectivity experiments, where the maxima and minima are detected as a rise and fall in the intensity  $I_{out}$  of the reflected neutron beam.

The resolution  $\Delta q/q$  of these Bragg peaks as seen by the detector has been calculated as (Drew 2005a):

$$\frac{\Delta(q)}{q} = \frac{\tan^{-1}((s_1 + s_2)/2L)}{\theta} \quad (3.59)$$

where  $s_{1,2}$  correspond to the collimation slit widths (as shown in Figure 3.23),  $L$  is the distance between these slits, and  $\theta$  is the incident angle for the neutron impacting on the sample. It is also clear from the above relationships that with the angle of incidence fixed, the reflected intensity becomes dependent upon the variation of the neutron wavevector, and hence its energy  $E$ .

The CRISP instrument at ISIS (shown in the diagram of Figure 3.23) is capable of varying the wavelength of the incoming neutrons within the range 0.5 - 6.5Å while the

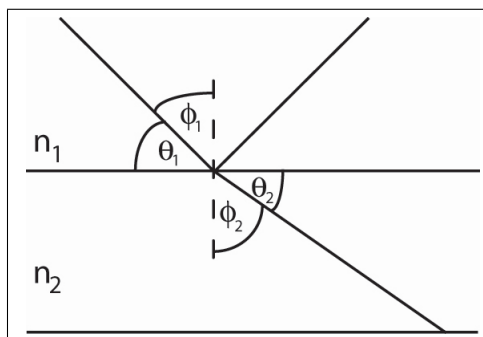


Figure 3.22: A diagram demonstrating refraction and reflection when a neutron impinges on a boundary between two mediums of different refractive indices  $n_1$  and  $n_2$ . Here,  $n_2 < n_1$ .

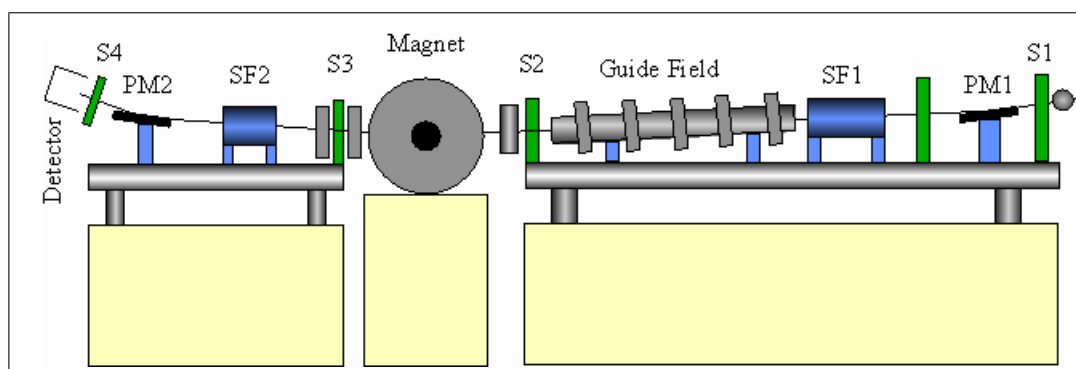


Figure 3.23: The setup for a polarised neutron reflectivity experiment on the CRISP instrument at ISIS, Oxford. The neutrons enter from the right hand side. (Source: [www.isis.rl.ac.uk](http://www.isis.rl.ac.uk))

velocity chopper is operating at 50Hz. (At 25Hz, the range can be extended to 12Å but this reduces the incident flux by half as only 1 in 2 pulses is now used.)

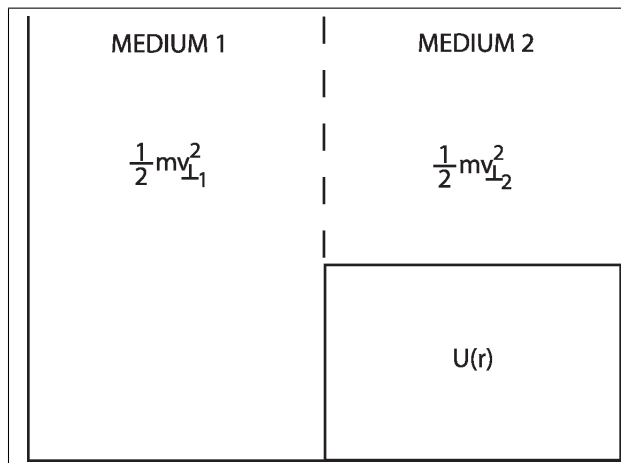


Figure 3.24: Depending upon the orientation of the neutron's magnetic moment relative to the magnetisation of Medium 2 (determined by an interaction energy  $U(r)$ ), the incoming wavevector will be reflected or refracted (see text). NB.  $v_1$  and  $v_2$  represent the incident and refracted neutron velocities respectively and  $m$  corresponds to the neutron mass. The neutron travels from left to right in this picture.

As previously mentioned when a neutron crosses the boundary between two different mediums the perpendicular component of its velocity, like a photon's, changes. In the simplest case, this is demonstrated when the change in the kinetic energy of the particle is considered (see Figure 3.24):

$$\frac{1}{2}mv_{\perp 1}^2 = \frac{1}{2}mv_{\perp 2}^2 + U(r) \quad (3.60)$$

where  $U(r)$  is the Fermi Pseudopotential described in Equation 3.28. If one considers inelastic interactions only, it is clear that the perpendicular component of the velocity of the refracted neutron decreases if the refractive index  $n_2$  is less than  $n_1$ .

Subsequently, with substitution and some rearranging, the refractive index of a medium containing  $N$  scattering nuclei can be written in terms of the neutron incident wavevector  $k_1$  and the average coherent scattering length  $\bar{b}$  (Dobrzynski & Blinowski 1994):

$$\frac{n_2}{n_1} = \sqrt{1 - \frac{4\pi N\bar{b}}{k_1^2}} \quad (3.61)$$

As can be seen by this equation, if one recognises that a typical scattering length  $\bar{b}$  is of the order of  $10^{-15}$  m then the quotient on the right hand side of Equation 3.61 can be calculated to approximately  $10^{-6}$ . This gives a refractive index just slightly less than that of air.

The potential energy  $U(r)$  described in Equation 3.28 encompasses both the nuclear and magnetic interactions. However, the magnetic contribution will change the overall  $U(r)$

according to the spin orientations of both the neutron and the magnetic moment in the sample. Considering *only* the magnetic contribution to  $U(\mathbf{r})$ , this potential can be simplified to<sup>4</sup>:

$$\frac{1}{2}mv_{\perp 1}^2 = \frac{1}{2}mv_{\perp 2}^2 - \boldsymbol{\mu} \cdot \mathbf{B} \quad (3.62)$$

Indeed, if one now considers Equation 3.62 and the orientation of the incoming neutron's magnetic moment relative to that of nuclei in medium 2 (see Figure 3.24), one can determine whether the impinging wavevector is reflected or refracted. If the incident neutron of wavevector  $\mathbf{k}_1$  has an initial energy of  $1/2mv_{\perp 1}^2$  the size of the barrier at the interface between the two mediums is decided by the sign of the second term on the right hand side of Equation 3.62. If the spins of both the neutron and the magnetic moment of medium 2 are aligned parallel to one another, the second term on the right hand side of Equation 3.62 is *subtracted* from the first term because the potential barrier between the two is lowered. Consequently, the boundary for transmission into medium 2 is reduced and thus, refraction occurs. Conversely, if the spins are anti-parallel to one another, the magnetic energy term is *added* to that of the kinetic energy and the neutron is reflected at the interface.

### 3.3 Bulk Magnetisation Measurements

In order to fully explain the phenomena observed using the microscopic methods previously described, one can use bulk measurements to determine whether such events are also reflected at the macroscopic level too.

All bulk magnetisation measurements recorded in this thesis were performed using the MPMS Superconducting Quantum Interference Device (SQUID) with a base temperature of 1.8K, at St. Andrews University. The apparatus comprises four main parts (McElfresh 1994): a superconducting DC magnet, a pickup coil, a SQUID with a DC sensitivity  $\leq 5 \times 10^{-6}$  emu, and a protective superconducting magnetic shield (as shown in Figure 3.25). The basic premise for operation is that the sample, subjected to an external DC field, is passed through a superconducting detection coil. The change in magnetic flux is then detected as a change in the persistent current flowing in the coil via Lenz's law:

$$\frac{d\Phi}{dt} = -L \frac{dI}{dt} \quad (3.63)$$

This signal is then passed via superconducting wires to the SQUID which acts as a very linear current to voltage converter. There are four turns in the detection coil; two turns in the centre and a counter-wound turn at either end of the wire (as shown in Figure 3.26) acting overall as a second-derivative flux gradiometer. This means that any noise created by fluctuations in the magnet that are picked up by the two turns in the centre, will be cancelled out by the turns at the top and bottom of the coil. However, the two counter-wound turns are sensitive enough to detect a change in the magnetic field as the sample is passed through them. The gradiometer coils also reduce background drifts in the SQUID caused by any relaxation in the field of the superconducting magnet. If the field is relaxing uniformly then

<sup>4</sup>Note that the gravitational influence on the neutron has been neglected here for simplicity but is taken into account by Dobrzynski & Blinowski (1994).

any change in the flux detected by the two centre coils will be cancelled out by that detected in the two outer coils. However, when a sample (of the correct dimensions) is moved through the centre coils, the signal is picked up because the centre coils measure the local change in magnetic flux density.

Varying the step size of the field scans can induce additional relaxation effects. If the interval spacing is abruptly increased significantly (say, from 5G to 150G per unit time steps) then the sample is given more time to relax due to the time needed to increase the size of the field step. Such variations can affect the absolute value of the measured magnetic moment of the sample (Nideröst 1996). Thus, waiting times have to be included in the experimental procedure to account for such relaxation effects.

The entire unit is encased in a superconducting shield that helps to protect the SQUID from the large fields generated from the DC magnet, and acts to trap and hold any stray fields within the laboratory at the point when the magnet becomes superconducting (i.e. when the helium dewar in which the magnet resides is filled).

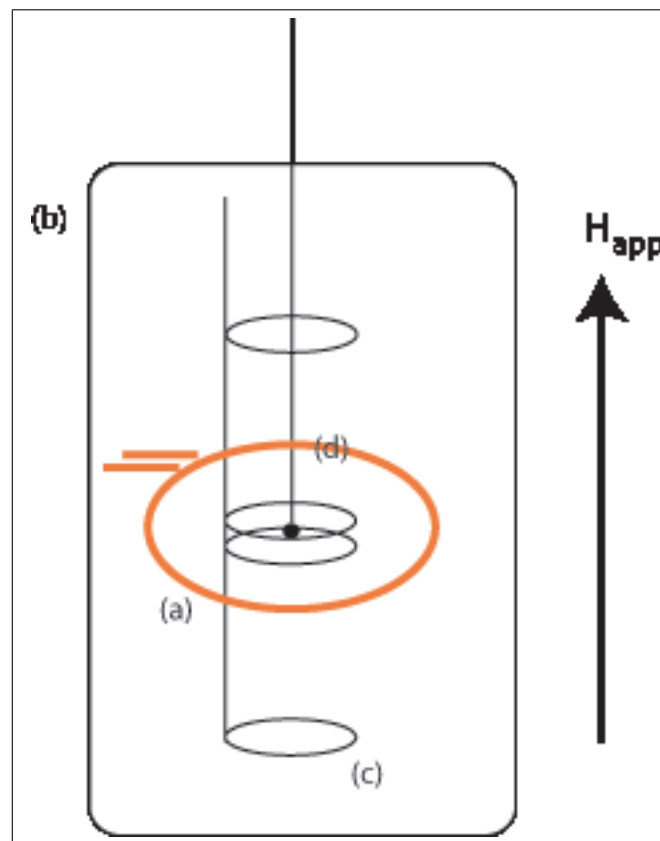


Figure 3.25: *The superconducting magnet (a) applies a DC field  $H_{app}$ . The whole setup is shielded (b) to protect the SQUID and pick-up coils (c) that detect the change in flux from a moving sample (d).*

### 3.3.1 Macroscopic Features of Superconductors

As detailed at the start of the previous section, bulk magnetisation measurements can be taken to corroborate data from  $\mu$ SR and neutron scattering experiments.

The first important macroscopic feature on the B-T phase diagram, common to HTSCs, is the Irreversibility Line (IL). This is the point beyond which (at higher fields and temperatures), the material's magnetisation becomes fully reversible (Schilling 1993) and is similar to another phenomenon, known as the vortex melting line (Zeldov 1995) (discussed in Section 2.1.3 and Chapters 4 and 5), occurs for most HTSCs in the same place as the IL. However, it has been shown that the two events do not necessarily coincide (Majer 1995) and that both depend on different factors.

The points on the IL can be obtained from both the magnetisation temperature scans and hysteresis loops (shown in Figures 3.27 and 3.28 respectively). The former involves both field cool (FC) and zero field cool (ZFC) measurements. ZFC temperature scans (measurements in which the material is cooled down below  $T_c$  in the absence of an applied field) produce magnetic moments that result from the influence of the supercurrents flowing close to the surface of the sample. This serves to expel flux from the centre of the material at low temperatures ( $\sim 5$ K). On the other hand, FC measurements (those in which the sample is cooled in an applied field below  $T_c$ ) already contain trapped flux as they are cooled below the transition temperature and therefore will produce less of a diamagnetic moment than that of the ZFC scan. The irreversibility point is obtained from the temperature value at which the ZFC and FC curves coincide (shown by the red and blue points in Figure 3.27).

Hysteresis loops are performed by firstly cooling the superconductor down through  $T_c$  in zero field to the base temperature of the instrument, before warming up to the desired

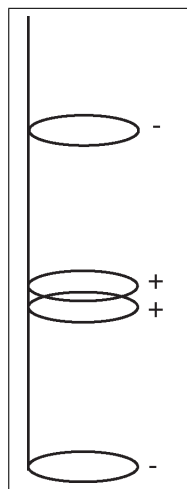


Figure 3.26: *The pick-up coils act as a flux gradiometer, with two turns in the centre of the coil (wound in the same direction “+”) and two counter-wound coils (marked “-”) separated by a distance of 4cm.*

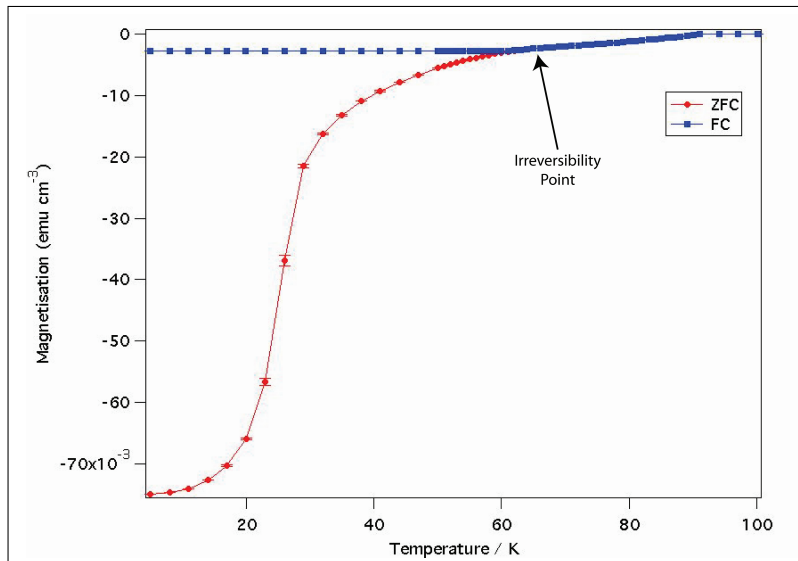


Figure 3.27: A diagram plotting magnetisation against temperature for both Zero Field Cool (ZFC) and Field Cool (FC) measurements. The Irreversibility point can be obtained from taking the temperature at which both the ZFC and FC curves converge.

temperature at which measurements will take place. The field is then increased in small

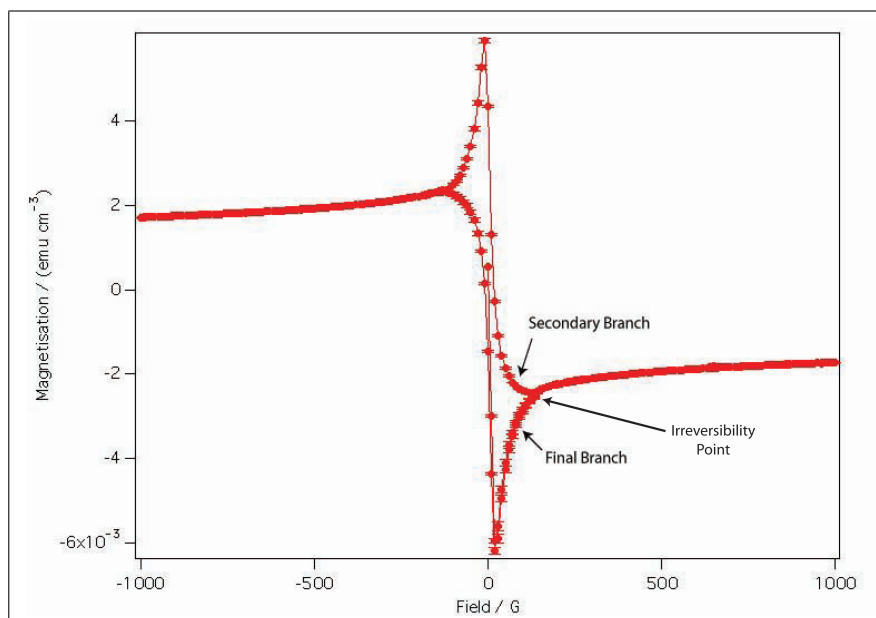


Figure 3.28: The Irreversibility point can also be obtained from hysteresis loops. Here, it is the field at which the secondary and final branches of the loop converge (as indicated). Beyond this convergence, it is clear that the magnetisation begins to saturate with increasing field.

intervals until saturation is reached (as shown in Figure 3.28). This section is known as the virgin branch. At saturation, the secondary branch of the loop commences where the field is reversed, passing through zero and reaching saturation in the negative direction. For the final branch, the field is again reversed and increased until it reaches saturation for the second time in the positive direction. The Irreversibility field is then taken to be the point where the secondary and final branches coincide (as denoted in Figure 3.28). Hysteresis curves for HTSCs can be best explained using the critical state model (Bean 1962) which is detailed in Section 2.1.3.

Another important macroscopic property is the point at which the derivative of the ZFC magnetisation temperature scans,  $dM/dT$ , reaches a peak (Pastoriza 1992). This quantity reflects the dynamic response of the magnetic vortices to changes in the external field or temperature, and thus, the change in the overall magnetisation of the sample. Such data (as shown in Chapters 4 and 5) tends to reach a peak that reflects the greatest rate of change of magnetisation (or greatest dynamic response of the vortices) as a function of temperature (see Figure 3.29). It can be understood that at such a point when the  $dM/dT$  is a maximum, the vortices have gained sufficient energy to remove themselves from a pinning site (either point or columnar defect) (Blatter 1994). In the *unirradiated*  $\text{Bi}_2\text{Sr}_2\text{CaCu}_2\text{O}_{8+\delta}$  samples, this has been used as evidence for a two-step transition to the reversible region in the superconducting phase diagram (Clem 1991)(Glazman & Koshelev 1991) and is explained further in Chapter 4.

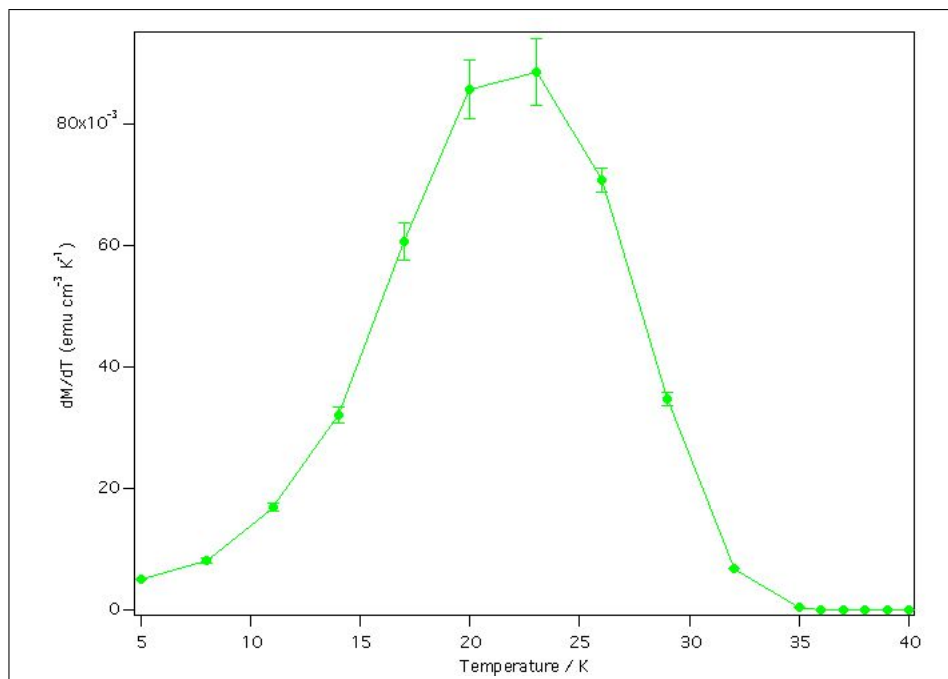


Figure 3.29: *By taking the derivative of the magnetisation curves for each ZFC temperature scan, a peak can be obtained that reflects the greatest number of vortices depinning from intrinsic point defects in the crystal.*

It should also be noted that in *irradiated* HTSCs a double peak in the  $dM/dT$  graphs can occur. This may be a direct result of vortices depinning from both the aforementioned point defects within the crystal structure as well as the columnar defects; the latter requiring the vortices to have a higher energy to break free of the attractive potential provided by the tracks. (More specific data will be presented in Chapter 5.)

The bulk magnetisation measurements detailed within this thesis complement well the microscopic data obtained via  $\mu$ SR and SANS. By overlaying the macroscopic data onto the superconducting phase diagrams for example, one can notice the good correlation between the two types of measurement.

# Chapter 4

## Measurements on the FLL of $\text{Bi}_{2.15}\text{Sr}_{1.85}\text{CaCu}_2\text{O}_{8+\delta}$

### 4.0.2 Background and Motivation

Since the discovery of the High- $T_c$  superconductors in 1987, there has been much work conducted on the layered perovskites. Among the most investigated of these materials is  $\text{Bi}_2\text{Sr}_2\text{CaCu}_2\text{O}_{8+\delta}$ . Its high electronic anisotropy combined with a relatively high  $T_c$  ( $\sim 90\text{K}$ ) allow for exotic behaviour to occur within the mixed state.

Three unirradiated<sup>1</sup> samples are investigated within this thesis and correspond to the stoichiometry:  $\text{Bi}_{2.15}\text{Sr}_{1.85}\text{CaCu}_2\text{O}_{8+\delta}$  (BSCCO). Here, the variation in oxygen content is the factor that differentiates each and this is reflected in a slight variation in  $T_c$  between all three of them. Nevertheless, as will be detailed below, they each display extremely similar behaviour.

The basic primitive unit cell comprises a bilayer, orthorhombic structure in which the copper oxide layers are sandwiched by a rock salt arrangement of bismuth and oxygen as depicted in Figure 4.1. The copper and oxygen atoms are arranged in a square-based pyramid structure with the copper atom centred in the base and where the corners (occupied by oxygen atoms) are shared with neighbouring pyramids. Just between the rock salt and oxide layers exists a Sr atom surrounded by 4 oxygen atoms and separating the double copper oxide planes is a Ca atom. This Sr-Cu-Ca-O arrangement is a typical perovskite structure.

The superconductivity in BSCCO is mediated through the movement of hole charges. In order to maintain this, there has to be a mechanism in place that allows for the introduction of holes into the copper-oxide layers. This in itself is an enormous field and outside the scope of this thesis but is covered by Majewski (1994) and Vanderah (1992). However, it is noted that the insertion of oxygen atoms into interstitial sites on the Bi-O layer as well as the introduction of cation deficiencies on the Bi and Sr sites can contribute to the variation in  $T_c$ .

The effect on the properties of these crystals as a function of oxygen stoichiometry was investigated by Aegeter (1996). Here, it was found that the penetration depth in the  $ab$  plane  $\lambda_{ab}$  (obtained through calculating the second moment of the  $\mu\text{SR}$  lineshape) varied with oxygen content. Further to this, it was shown that the crossover field  $B_{cr}$  (first explained

<sup>1</sup>In the following chapter superconductors that are irradiated with high energy ions are discussed.

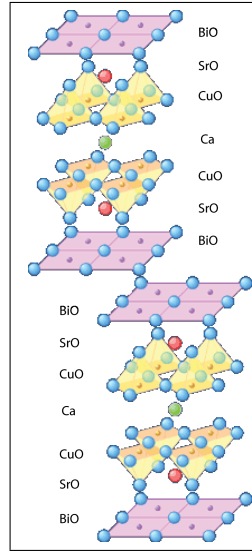


Figure 4.1: *The orthorhombic structure of  $\text{Bi}_2\text{Sr}_2\text{CaCu}_2\text{O}_{8+\delta}$  is easily recognisable by its arrangement of rock salt and copper oxide layers. The perovskite  $\text{CuO}$  layers exist with  $\text{CuO}_3$  chains running perpendicular to them. (Source: J. C. Davis Group, Cornell University.)*

by Glazman & Koshelev (1991) and Feinberg (1994), and demonstrated by Lee (1993b) as denoting the point at which the FLL changes from a 3 dimensional configuration to a more

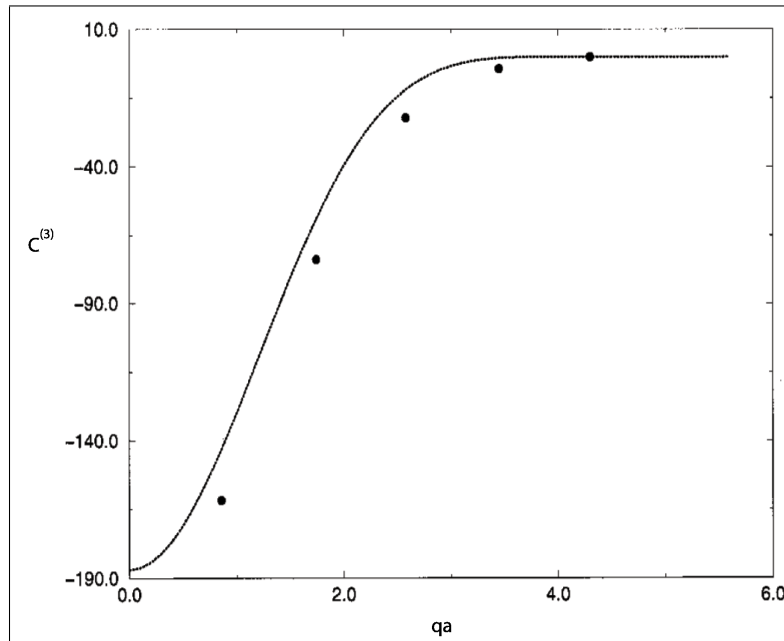


Figure 4.2: *The triplet correlation function  $C^B$  for a hard sphere under certain conditions has been shown to be negative over a small range of  $qa$ . Here  $q$  is a Fourier component and  $a$  is the lattice parameter. (Source: (Zhou & Ruckenstein 2000))*

2 dimensional arrangement) increased as  $\lambda_{ab}^{-2}$ . Interestingly though, the conclusion that  $B_{cr}$  was independent of the electronic anisotropy of the system contradicted work conducted by Bernhard (1995) where it was also added that there was a doping dependence too. Indeed, the effect of doping has also been highlighted by Le Coche (2000) - where a linear temperature dependence on  $\lambda_{ab}$  exists - and Waldmann (1996) - who demonstrated that the value of  $T_c$  increases to a maximum as the charge carrier density (proportional to  $\lambda_{ab}^{-2}$ ) is increased, before reducing to zero thereafter.

The vortex phase diagram<sup>2</sup> of BSCCO has long attracted attention and interest due to the anomalous behaviour it exhibits under certain conditions (Blatter 1994) (Giamarchi & Bhattacharya 2001) (Fisher 1991). Several macroscopic techniques have been used to measure and understand the behaviour within certain vortex regimes. However, microscopic techniques (including muon spin rotation and neutron scattering) have given new insight on a more local level.

A Lindemann criterion for the FLL melting in high- $T_c$  superconductors was successfully demonstrated by Houghton (1989) and was observed in  $\text{Bi}_{2.15}\text{Sr}_{1.85}\text{CaCu}_2\text{O}_{8+\delta}$  by Lee (1993*b*) using  $\mu\text{SR}$ . The latter author also noted the 3D to 2D vortex dimensional crossover detailed above. This was closely followed by the observation that the change in the  $\mu\text{SR}$  lineshape was strongly field dependent (Lee 1993*b*) and that the vortex lines in this anisotropic material begin to recouple again along their axis. This latter observation was made by Blasius (2000) and claimed that after a disorder-induced transition, the vortices began to recouple again with increasing field at low temperatures. This behaviour was explained as being due to a change in the pinning properties of the system, from single-vortex to bundle pinning. Such a change was claimed to occur as the vortex density and thus the inter-vortex interactions increased, although the authors accept that further work is needed before this is conclusive. Indeed, the interaction between pancake vortices in  $\text{Bi}_{2.15}\text{Sr}_{1.85}\text{CaCu}_2\text{O}_{8+\delta}$  is dominated by electromagnetic coupling rather than Josephson, particularly in the low-field phase of the mixed state (Lee 1993*c*) and at lower temperatures, where the irreversibility line begins to plateau, it becomes difficult to distinguish whether this is a consequence of melting or decoupling through increased vortex-vortex interactions in the regime where point pinning is significant. Indeed, in this particular region, it is highly probable that it is combination of the two.

Of all the work conducted on the generic phase diagram of high temperature superconductors most has been on the Bragg Glass state (Giamarchi & Le Doussal 1995) (Klein 2001). Unlike a perfect lattice (where there the vortices exist in a perfect hexagonal configuration), this regime has in-plane disorder caused by the existence of point defect pinning sites that act to distort the angular orientation of the FLL. As well as this, at these low temperatures and in such a dilute vortex limit, there is a reduced thermal stimulation of the FLL and decreased inter-vortex interactions. For a perfect arrangement of vortices one would expect a complete lattice in which the material is free of defects but where the vortex density is such that their repulsive interactions create the ideal hexagonal orientation. The introduction of defects serves to distort the lattice. However, such ideal FLL configurations (Daemen 1992) (Thiemann 1989) are practically impossible. This is because the nature of crystal growing (discussed elsewhere (Li 1994)) makes it extremely difficult to remove im-

<sup>2</sup>NB. In this thesis the “phase” diagram refers to a plot in the B-T plane.

purities and inhomogeneities from within the crystal structure. As mentioned in Chapter 1, these anomalies are known as pinning centres and act as attractive potentials for magnetic vortices. Further to this, increasing the number of vortices in the material beyond a crossover field  $B_{cr}$  deforms the FLL as the energy for in-plane shearing (related to  $c_{66}$ ) becomes greater than the in-plane tilt energy. At this point, the Vortex Glass phase (detailed in Chapter 1) is entered and it was this change in the behaviour of the FLL that was first explained by Giamarchi & Le Doussal (1995) as being a disorder induced transition to a more glassy, vortex array.

As one increases the temperature towards  $T_c$  of the material, the system enters the liquid phase when the FLL passes through the intrinsic melting point, as discussed in depth in Chapter 1. At this point the vortices begin to move freely within the material analogous to particles moving in a liquid. In addition to this, highly anisotropic superconductors can lose some coherence between the CuO layers and, as such, break up into pancake vortices. Consequently, the variance  $\langle \Delta B^2 \rangle^{1/2}$  in the  $\mu\text{SR}$  lineshape undergoes thermal narrowing (Brandt 1991) as the range of fields reduces due to both the motion of the pancakes and the subsequent reduced coupling along the vortex axis. In this region though,  $\alpha$  reduces in value, sometimes becoming *negative* at temperatures approaching  $T_c$ . Such results had never been properly interpreted and explained until recently when Menon (2006) was able to demonstrate in  $\text{La}_{1.9}\text{Sr}_{0.1}\text{CuO}_{4-\delta}$  that  $\alpha$  could only be negative if the three-body correlation function  $C^{(3)}(\mathbf{k})$  became negative and such correlations between vortices exist in the FLL. In order to obtain this, one can approximate the P(B) lineshape skewness as follows (Hansen & MacDonald 1986):

$$\langle \Delta B^3 \rangle = \frac{B}{16\phi_0\pi^2} \int \int d\mathbf{q}_1 d\mathbf{q}_2 S^3(\mathbf{q}_1, \mathbf{q}_2) b_{\mathbf{q}_1} b_{\mathbf{q}_2} b(-\mathbf{q}_1 - \mathbf{q}_2) \quad (4.1)$$

where  $S^{(3)}(\mathbf{q}_1, \mathbf{q}_2)$  is the triplet structure factor defined in terms of two wavevectors and  $b(\mathbf{q})$  is the field of a single vortex in Fourier space. The triplet structure factor can be further defined as:

$$S^3(\mathbf{q}_1, \mathbf{q}_2) = S(q_1)S(q_2)S(|-\mathbf{q}_1 - \mathbf{q}_2|) \times [1 + \rho^2 C^{(3)}(\mathbf{q}_1, \mathbf{q}_2)] \quad (4.2)$$

where  $C^{(3)}(\mathbf{q}_1, \mathbf{q}_2)$  is the triplet correlation function expressed in terms of two wavevectors and  $\rho$  is the vortex density. The triplet correlation function determines the positional relationship of three vortices with respect to one another. The two-body structure factor is always inherently positive and, therefore, the quantity defined in Equation 4.2 can only be negative when the second term in the square brackets is negative too. Figure 4.2, taken from Zhou & Ruckenstein (2000), shows how, for certain states of disorder, the triplet correlation function changes from being negative to positive as a function of  $q$  for a particular lattice spacing  $a$ . This result helps in the understanding that three-body correlations exist within the bulk of the material, are non-trivial, and that they are only functional over length scales which are slightly larger than the inter-vortex spacings (Menon 2006) (Zhou & Ruckenstein 2000). Menon's paper was the first time that three-body correlations had been observed and explained in a bulk, three dimensional system.

In light of this, it is extremely insightful to re-visit the BSCCO work that has previously been done. Combining this with fresh data, an improved Maxent analysis program, and a new understanding of the physics of these superconducting materials provides an excellent motivation for the work now presented.

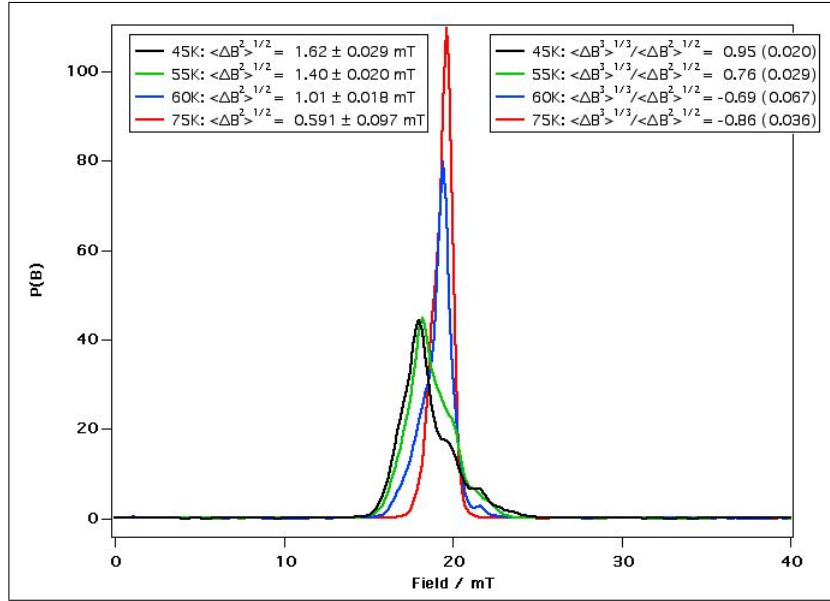


Figure 4.3: As the temperature of BSCCO1 is increased at 200G, one notices a distinct change in both the square root of the second moment  $\langle \Delta B^2 \rangle^{1/2}$  of the  $P(B)$  (measured in Tesla). The asymmetric skewness  $\alpha$  of the  $P(B)$  lineshape changes from being positive to negative. This transition occurs between 55K and 60K and the peak value  $B_{pk}$  also noticeably shifts from left to right as a function of increasing temperature. (Note that the corresponding errors are displayed in brackets.)

### 4.0.3 Experimental Preparation

A slab of haematite ( $\sim 40\text{mm} \times 10.5\text{mm} \times 4\text{mm}$ ) was initially brushed down with acetone to remove contamination. The haematite was then attached to an aluminium sample holder with Bostick, ready for mounting. Due to the slab being smaller than the sample holder, a  $\text{Fe}_2\text{O}_3$  paste was used around its edges to prevent muons from interacting with the aluminium. The haematite is antiferromagnetic and acts to rapidly depolarise any muons not entering the sample.

Three different BSCCO samples were measured (detailed below), each of a mosaic structure comprising eight pieces. These individual crystals were approximately  $7\text{mm} \times 3\text{mm} \times 1\text{mm}$ , though some were thinner than others and consequently were placed on top of one another with a small solution of Bostick and acetone. This dilute solution is made for ease of application of the individual pieces and so that muons do not stop in the glue itself. The c-axis of each material was perpendicular to the surface of the haematite but parallel to the incoming muon beam and the applied magnetic field. Finally, the sample holder was covered in a single layer of mylar to prevent the sample from falling into the chamber as well as helping in reflecting excess radiation.

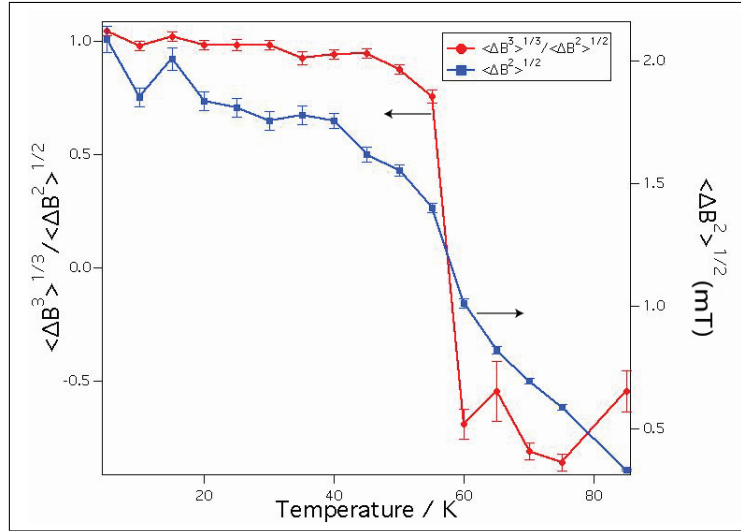


Figure 4.4: A plot of  $\alpha$  and  $\langle \Delta B^2 \rangle^{1/2}$  against temperature at  $0.02T$  in BSCCO1. The melting line is obtained when observing the discontinuous drop in  $\langle \Delta B^2 \rangle^{1/2}$  as a function of temperature. Here, the change in the sign of  $\alpha$  occurs at the same point ( $\sim 58\text{K}$ ) and adds weight to a transition occurring here. However, until now a negative alpha has not been properly explained on its own.

#### 4.0.4 Discussion of results

The three measured samples have different transition temperatures: BSCCO1  $T_c = 92\text{K}$ , BSCCO2  $T_c = 84\text{K}$ , and BSCCO3  $T_c = 84\text{K}$ . These three samples were investigated by Aegeter (1996) and shown to have the following in-plane penetration depths respectively: 270nm, 180nm and 260nm. For the temperature scans, all the samples were cooled in an applied field to 5K. The sample is then warmed and measured at various intervals. Subsequently, after several temperature scans it is possible to construct 2D B-T diagrams in which the third axis can represent the square root of the variance in the P(B) linewidth  $\langle \Delta B^2 \rangle^{1/2}$  (the range of accessible fields) or the asymmetric skewness parameter  $\alpha$  that is sensitive to both the in-plane angular correlations of the FLL and the coherence of the vortices along their length. We will first consider the low field regime in BSCCO1.

Figure 4.3 shows the sudden change in the  $\mu\text{SR}$  P(B) lineshapes as one increases the temperature in an applied field of  $200\text{G}^3$  (i.e. from region B to region D in Figure 2.7). It is clear, even by just observing the P(B)s, that at the transition ( $\sim 58\text{K}$ )  $\langle \Delta B^2 \rangle^{1/2}$  is dramatically reduced (from  $0.00140\text{T}$  to  $0.00101\text{T}$ ) corresponding to a decrease in the range of fields due to a thermal decoupling of the pancake vortices along their axis. Correspondingly, there is also a significant difference in  $\alpha$  which changes dramatically from being largely positive ( $0.76 \pm 0.029$ ) to largely negative ( $-0.69 \pm 0.067$ ). This is shown more clearly in Figure 4.4. Such a low-induction transition is also apparent in the low field region of BSCCO2 as shown in Figure 4.5.

As mentioned, a large amount of work has been conducted on this material in the

<sup>3</sup>Note that for ease of viewing, the four points closest to this transition have been selected.

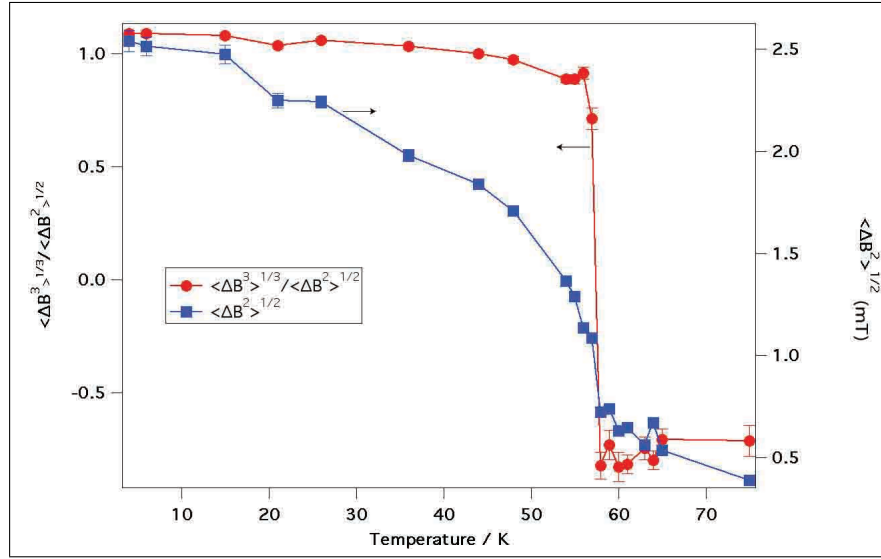


Figure 4.5: A plot of  $\alpha$  and  $\langle \Delta B^2 \rangle^{1/2}$  against temperature at  $0.0452T$  in BSCCO2. Again, the melting line can be observed (Lee 1993) in the low-field, Bragg Glass regime. It also occurs at approximately 55-60K and is made evident by both the change in  $\alpha$  and  $\langle \Delta B^2 \rangle^{1/2}$ .

Bragg Glass state. However, at higher applied fields there is a significant change in behaviour. Figure 4.6 demonstrates a distinct change in  $\alpha$  as one increases the temperature of the system from 5K in a field of 2000G whilst the diminishing of  $\langle \Delta B^2 \rangle^{1/2}$  appears to remain monotonic.

Indeed, if one examines the actual shape of the probability distributions (as in Figure 4.6), it becomes clear how different the transition is to the one that occurs within the Bragg Glass regime in Figure 4.3. As explained by many authors, this region of the phase diagram is termed the Vortex Glass regime (Giamarchi & Le Doussal 1995). The transition from the Bragg Glass to the Vortex liquid state has been explained as a first order transition (Zeldov 1995). However, when one considers a transition from a glassy type behaviour to that of a liquid, it becomes extremely difficult to determine what order of a transition this should be.<sup>4</sup> Indeed, it has been shown that there is no distinct change in magnetisation in this regime as shown by Giamarchi & Bhattacharya (2001) Zeldov (1995). The latter author demonstrated this using the Clayperon-equation:

$$\frac{dH_m}{dT} = -\frac{\Delta S}{\Delta M} \quad (4.3)$$

where  $H_m$  is the value of the applied field when melting occurs,  $\Delta S$  is the change in entropy of the system, and  $\Delta M$  is the change in overall magnetisation of the material.

BSCCO2 also demonstrates within the Vortex Glass state (when  $H_{app} = 1000\text{G}$  for example - see Figure 4.7) that there is a distinct change in the sign of  $\alpha$  as a function of temperature (moving from region C to D in Figure 2.7). However, in agreement with BSCCO1, it is also clear that a small anomalous discontinuity in  $\langle \Delta B^2 \rangle^{1/2}$  remains as with the 452G data set (Figure 4.5).

<sup>4</sup>Although Fisher (1991) has suggested that in the strong pinning scenario, a second order transition is expected.

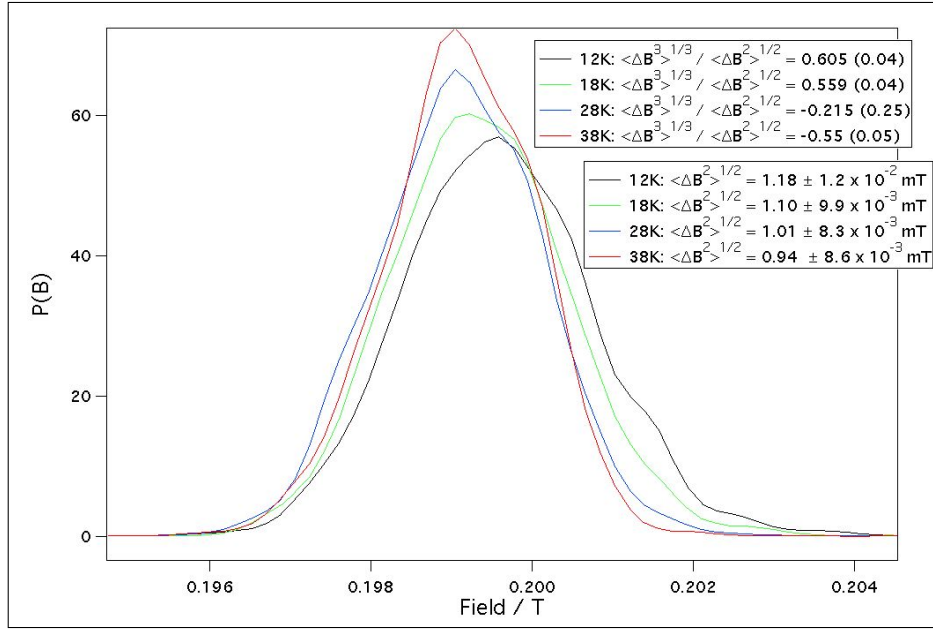


Figure 4.6: A plot showing the probability distributions for a range of temperature from 12K to 38K for BSCCO1 at 0.2T. Within the Vortex Glass regime, even though the decrease in  $\langle \Delta B^2 \rangle^{1/2}$  appears relatively continuous (in comparison to that at 200G), there is a sudden change in  $\alpha$  occurring at approximately 25K.

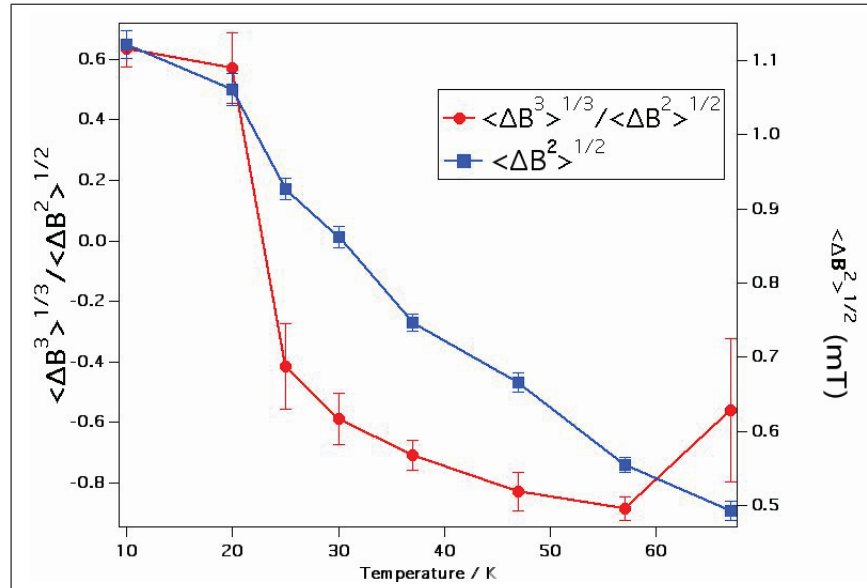


Figure 4.7: BSCCO2 also demonstrates similar behaviour to BSCCO1 in the Vortex Glass regime. Here, as one increases the temperature at 1000G,  $\alpha$  changes sign dramatically between 20 and 25K, whilst the square root of the variance of the  $P(B)$  lineshape (shown in blue) undergoes a small deviation from its constant narrowing throughout this point.

Having taken a series of temperature scans it becomes possible to map out a 2D phase diagram of  $\text{Bi}_{2.15}\text{Sr}_{1.85}\text{CaCu}_2\text{O}_{8+\delta}$  as a function of both  $\alpha$  and  $\langle\Delta B^2\rangle^{1/2}$ . A culmination of the data is displayed through the use of an interpolation routine. For all measured samples a cubic spline interpolation is used. This method is able to interpolate between both dense and sparse data sets.

Considering first the logarithm plot shown in the bottom plot of Figure 4.8, the Bragg Glass regime in BSCCO1 is most obvious with its sharp transition to the liquid state at higher temperatures. As reported by several authors, the melting transition closely follows that of the irreversibility line within both the Bragg Glass and Vortex Glass regions (see the white points of Figures 4.8 and 4.12). However, as one takes a field cut at low temperatures (i.e. observes the change in the behaviour of the FLL for different applied field values at a particular temperature)<sup>5</sup>, the Vortex Glass domain also becomes apparent. This regime is noticeable by the decrease in the  $P(B)$  variance. For example, at 7K (in the top plot of Figure 4.11), when the applied field is 250G,  $\langle\Delta B^2\rangle^{1/2}$  reaches a maximum at  $2.2 \pm (3.2 \times 10^{-2})$  mT before a sudden decrease at 500G to  $1.1 \pm (1.1 \times 10^{-2})$  mT.

Indeed, the changes occurring at higher fields as a function of temperature (as detailed above) are again reflected in the macroscopic data (overlaid on top of the contour plots of Figures 4.8 and 4.12). What has not been reported and understood significantly is the overall behaviour of the FLL within this Vortex Glass region. Firstly, as seen more clearly in the 1D  $\alpha$  plots for both BSCCO1 and BSCCO2 (the top and bottom plots of Figure 4.10 respectively), there is a sudden sharp transition at low temperatures for different values of increasing applied field.<sup>6</sup>

However, as the field is increased beyond approximately 1000G in both cases,  $\alpha$  undergoes a re-entrant behaviour at temperatures less than  $\sim 30\text{K}$  and becomes positive again. Here, as more vortices enter the superconductor, they begin to lose coherence along their axis due to increased inter-vortex interactions and the effects of point-pinning. The large electronic anisotropy of the BSCCO crystals make it more energetically favourable for an individual pancake to position itself on one of these defect sites. These two effects combined will lead to a decrease in the 3D structure of the vortices, reflected by a change in  $\alpha$  - the resulting skewness of the lineshape reflects this disorder.

In this regime, there is increased competition between the tilt and shear moduli ( $c_{44}(\mathbf{k})$  and  $c_{66}(\mathbf{k})$  respectively) as the total elastic energy varies with  $\tau^2$ . Here,  $\tau$  is the associated strain on the FLL and depends upon the lattice parameter  $a$ . As the applied field increases at low temperatures,  $\alpha$  decreases and the corresponding tilt and shear energies are subsequently affected.  $c_{44}(\mathbf{k})$  greatly reduces in value compared to  $c_{66}(\mathbf{k})$  as the in-plane interactions outweigh the inter-layer coupling. The vortices will then become distorted along their length, between the CuO layers.

This, however, does not explain why the transition between the Bragg and Vortex glass states (at temperatures below 50K) is so well defined and why the value of  $\alpha$  becomes negative (at approximately 500G and 750G for BSCCO1 and BSCCO2 respectively) before changing back to being positive again at fields above 1000G. It has been proposed that at

<sup>5</sup>What is meant here is the observation of the change in the FLL behaviour at the same applied field value for different temperature scans, i.e. a field ‘‘cut’’ and not a hysteresis loop.

<sup>6</sup>Again, note that this is not a hysteresis loop.

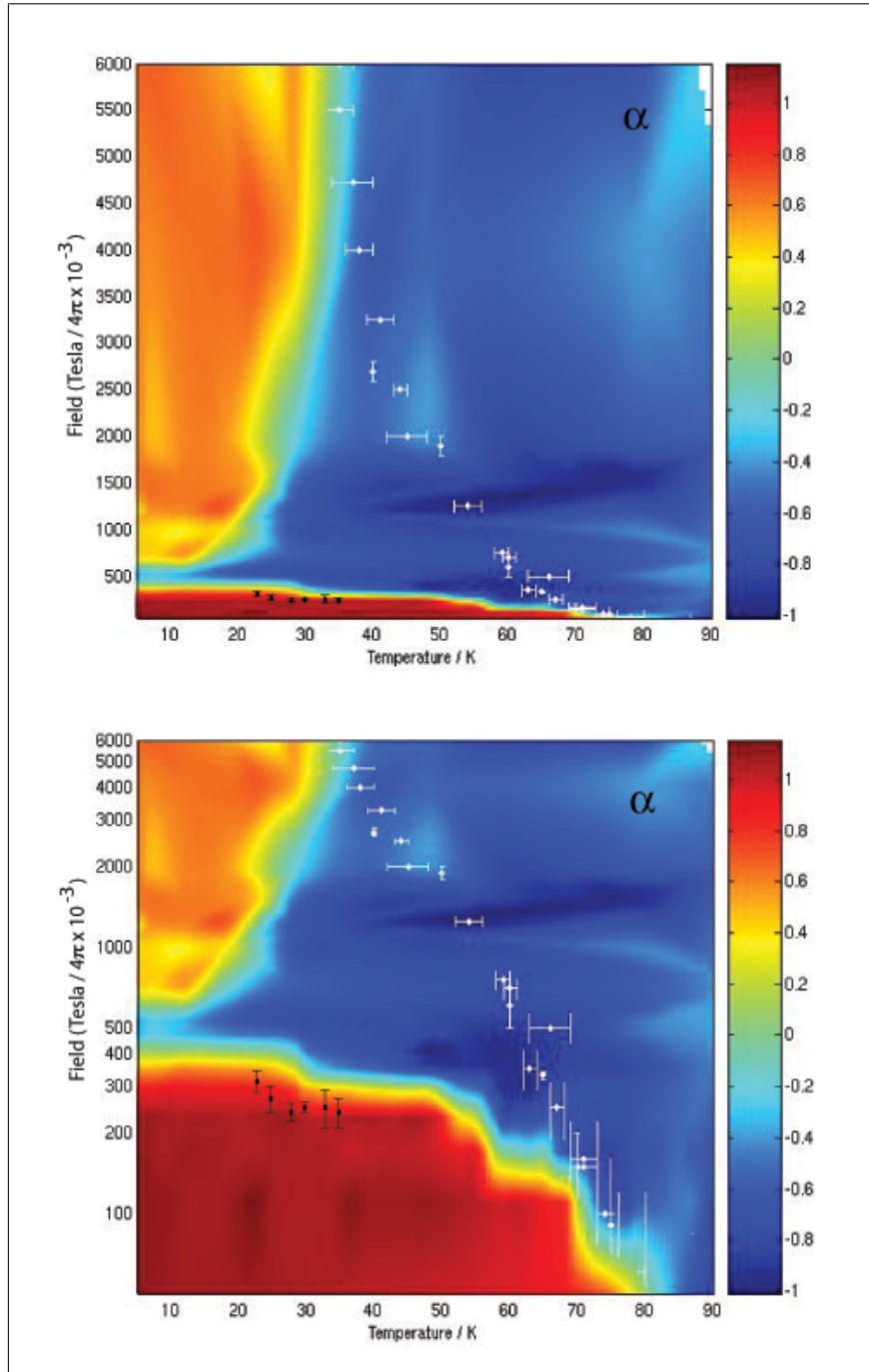


Figure 4.8: One can map out the  $\alpha$  phase diagram of  $\text{BSCCO1}$  by interpolating the individual data sets. Both a linear (top) and logarithm plot (bottom) are displayed, each, in particular, showing the transition of  $\alpha$  from positive to negative and back to positive again at low temperatures as a function of field. Further, within the liquid regime,  $\alpha$  is noticeably negative. The white data indicates the irreversibility points obtained from macroscopic SQUID measurements, whilst the black data represents  $B_{\text{onset}}$  acquired from magnetisation hysteresis loops.

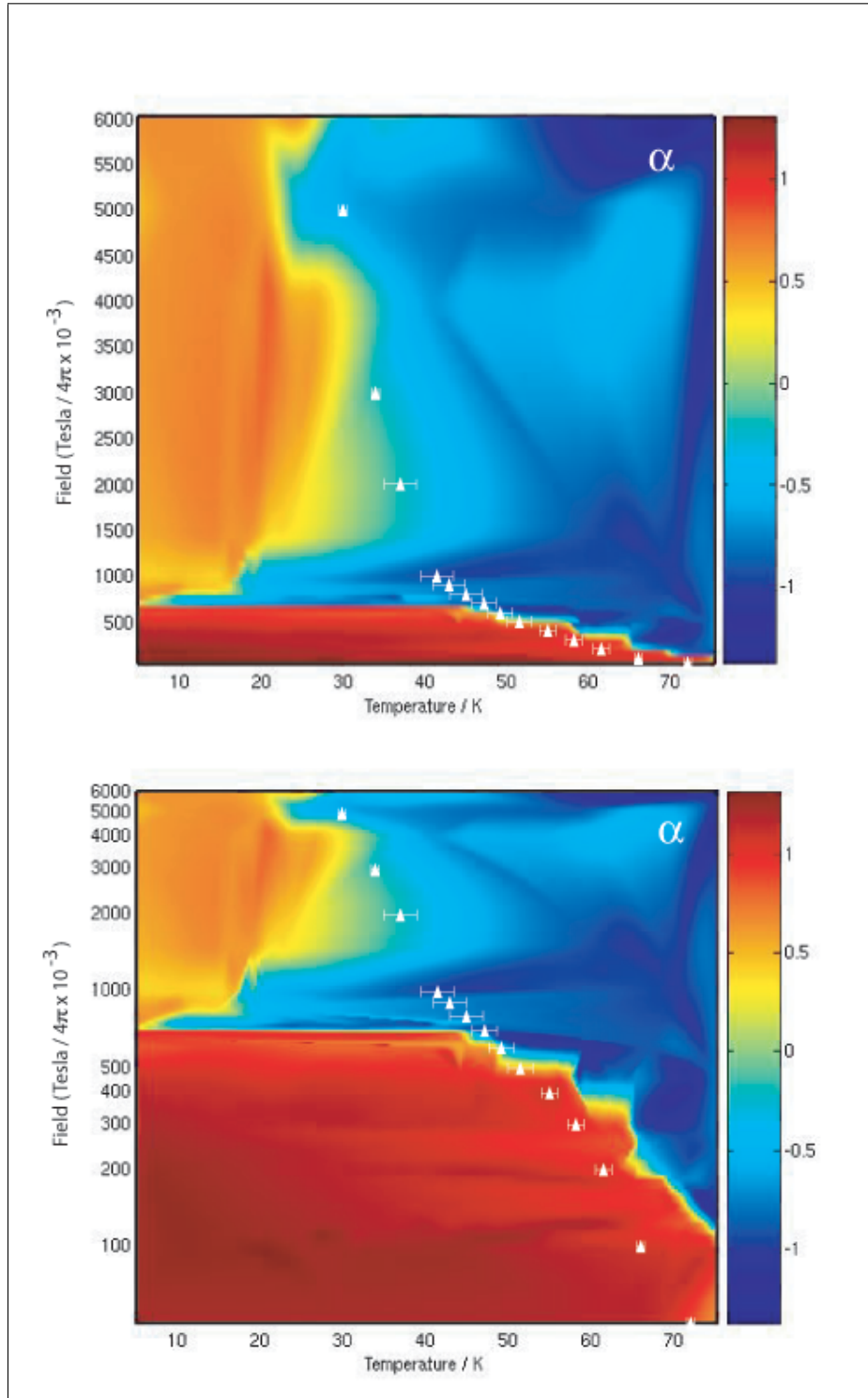


Figure 4.9: The sharp transitions from the Bragg to Vortex Glass and Bragg to liquid state are also evident in the  $\alpha$  2D B-T diagram of BSCCO2. Here, the top plot is on a linear scale, the bottom plot is the corresponding logarithmic plot and the white points on each denote the irreversibility line.

$B_{cr}$  where tilt deformations dominate (Glazman & Koshelev 1991), it is more energetically favourable for the vortices to be distorted along their length due to a sufficient combination of the repulsive inter-vortex interactions and attractive defect pinning potentials rather than aligning exactly with pancakes in successive layers. Yet, as explained by Menon (2006), a negative value of  $\alpha$  can only arise from 3-body correlations that exist over the order of a few lattice spacings. Hence, as one goes beyond  $B_{cr}$ , it appears as though the system does not immediately become a disordered quasi-2D FLL but instead, remains 3D (i.e. is still well correlated along the vortex axis) but where three-vortex correlations become more prominent. Gradually, as one increases the applied field beyond this, these three-body correlations are masked by the increasing c-axis disorder.

If one considers field scans at higher temperatures (for example when  $T > 30\text{K}$  in the top and bottom plots of Figure 4.10), it is clear that the values are significantly more negative than those observed at low temperatures. In BSCCO1 at an applied field of 500G,  $\alpha \sim -0.31 \pm 0.17$  and  $-0.41 \pm 0.09$  for 7K and 12K respectively. Similarly, in BSCCO2 at 750G,  $\alpha \sim -0.51 \pm 0.04$  and  $-0.54 \pm 0.06$  for 15K and 20K each. However, these values are small in comparison to higher temperatures where in BSCCO1  $\alpha \sim -0.70 \pm 0.05$  at 30K and  $\sim -0.77 \pm 0.03$  at 40K. For BSCCO2  $\alpha \sim -0.70 \pm 0.08$  at 30K and  $-1.03 \pm 0.09$  at 60K. In addition to this, one can observe that despite the increase in  $\alpha$  beyond  $\sim 1000\text{G}$ ,  $\langle \Delta B^2 \rangle^{1/2}$  on the other hand remains almost constant.

Such a contrast in behaviour is highlighted when one considers that the second moment of the P(B) lineshape is unaffected by triplet correlations (Brandt 1988):

$$\langle \Delta B^2 \rangle = \frac{B}{4\phi_0\pi^2} \int_{q \neq 0} S(\mathbf{q})b(\mathbf{q})d\mathbf{q} \quad (4.4)$$

but that these three-body correlations result in a negative skewness for  $\alpha$ . This can be understood when one considers that at temperatures below  $T_{dp}$  (the vortex depinning temperature), the FLL lacks long-range order due to the point defect sites. However, above this critical temperature, the vortices have a greater degree of freedom. Thus, unrestrained by the crystal defects, the ability to form three-body correlations is enhanced and the values of  $\alpha$  become more negative.

One might be able to understand why  $\alpha$  noticeably becomes more negative in this way by combining both the effects of disorder - longitudinal and in-plane - and 3-body correlations. It is possible that the enhancement comes about when one considers 3-body correlations between *pancakes in the same layer* or pancakes that are coupled over a few CuO layers (i.e. 3D vortices with a small c-axis coherence length). Such an increase in three body correlations might contribute to the enhanced negative values of  $\alpha$  before falling off just before  $T_c$ . However, since the muon is measuring the magnetic field screened over a distance  $\sim \lambda$ , it is currently difficult to conclusively state whether the difference in three-body correlations between pancakes in a single layer and vortices whose coherence spanning several layers can be measured.

Strangely, the sharp change in  $\alpha$  from positive to negative and back to positive again as one traverses the Bragg to Vortex Glass transition does not even appear to happen for BSCCO3 (see the top plot of Figure 4.14), although it should be noted that the data set is sparse for this particular sample and thus the resolution in terms of field steps is not as fine as it is for BSCCO1 and BSCCO2.

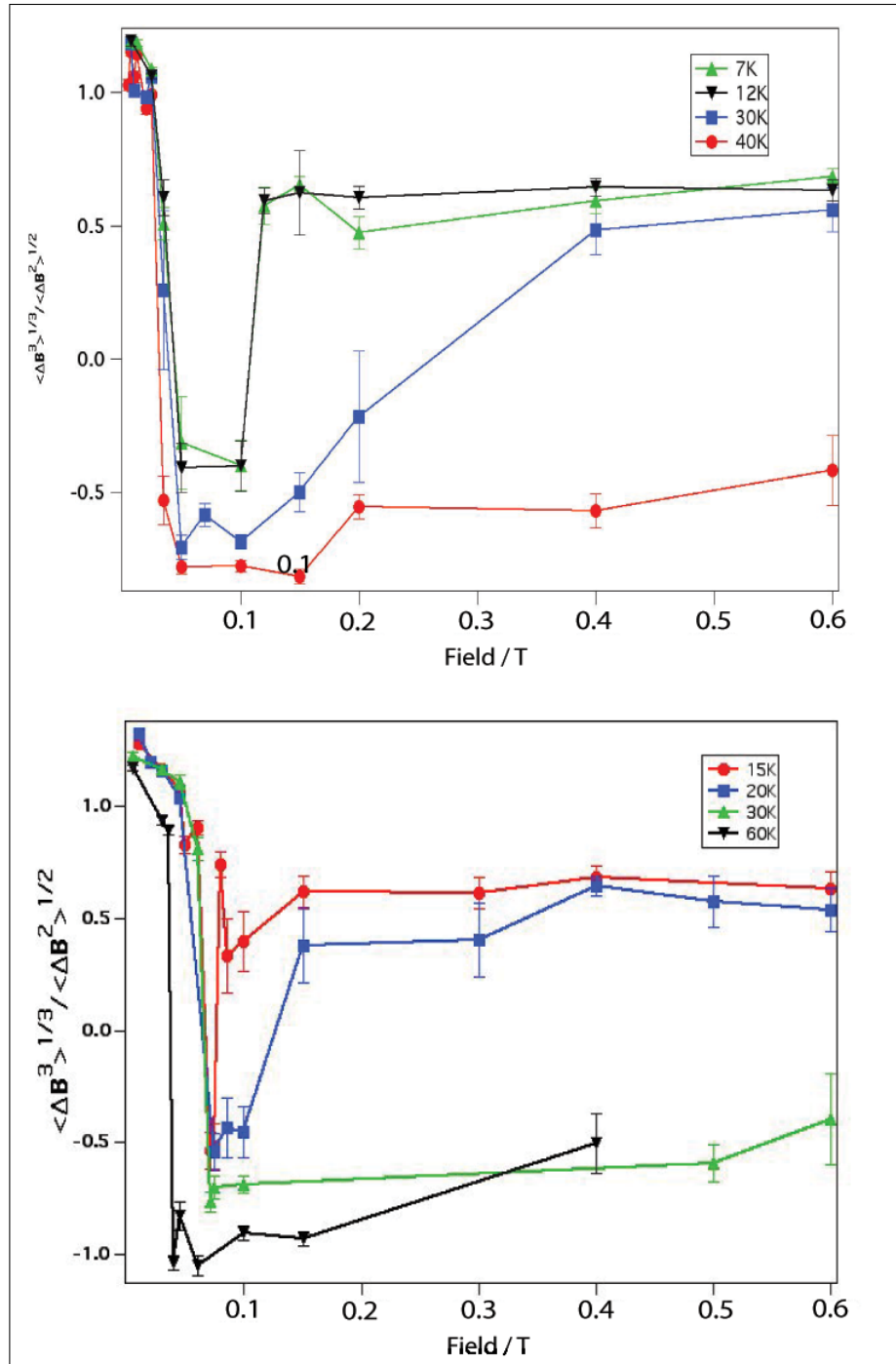


Figure 4.10: *Top plot: As the applied field is increased at low temperatures in BSCCO1, the sharp drop in  $\alpha$  at  $\sim 500\text{G}$  is temperature independent before reaching the melting line. Bottom plot: Similar behaviour to BSCCO1 occurs as one increases the field in BSCCO2. This time, the change of sign of  $\alpha$  occurs at  $750\text{G}$ . The  $P(B)$  linewidths for both BSCCO1 and BSCCO2 also show similar trends (see Figure 4.11).*

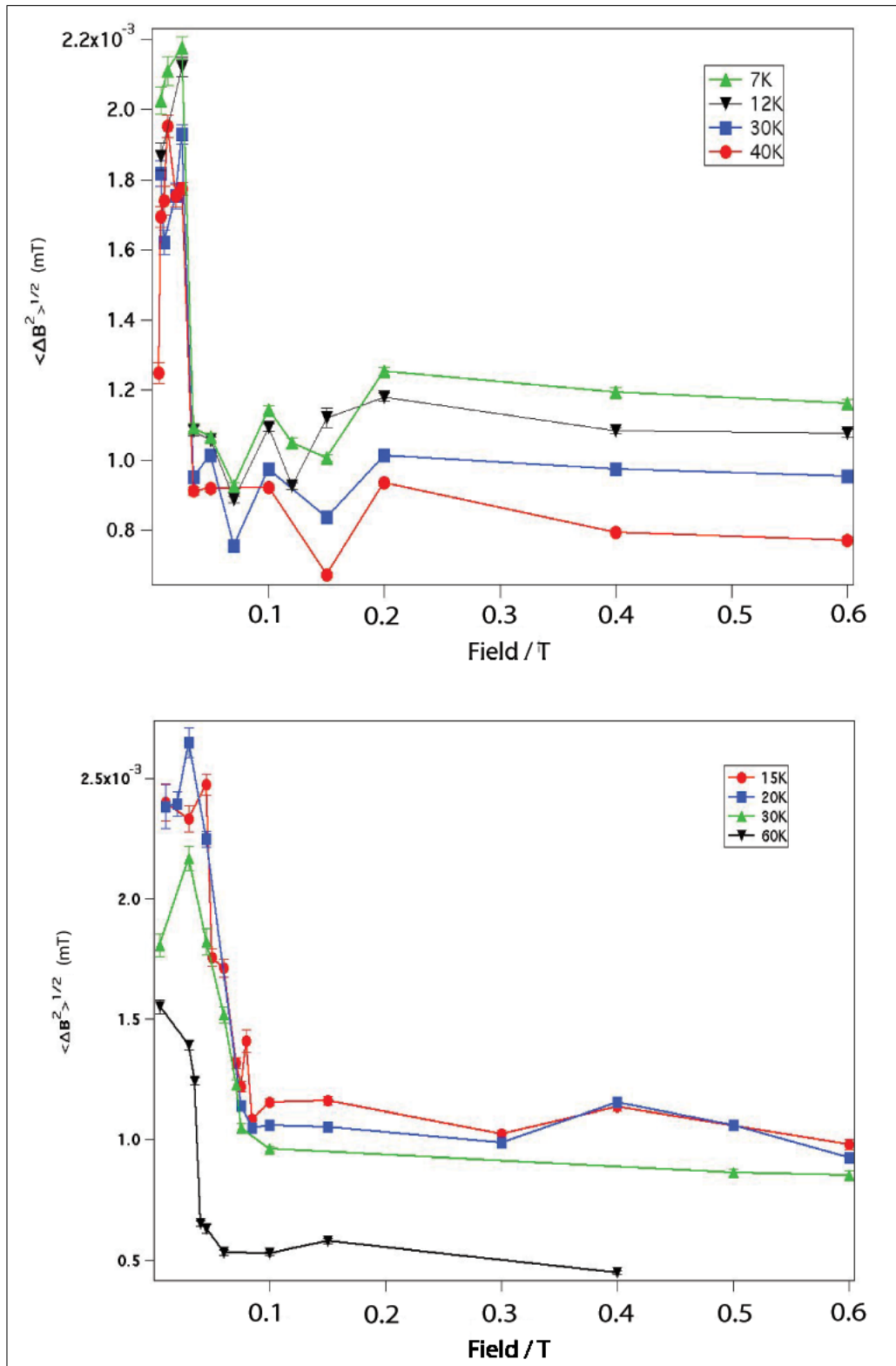


Figure 4.11: Top plot: The variation in  $\langle \Delta B^2 \rangle^{1/2}$  as a function of field for BSCCO1. Bottom plot: The variation in  $\langle \Delta B^2 \rangle^{1/2}$  as a function of field for BSCCO2. The sudden narrowing in the linewidth occurs at the same point as the corresponding  $\alpha$  decreases.

Again, there is a strong possibility that the variation in the electronic anisotropy over the three samples may explain that, in this case, although three-body correlations exist everywhere, at low temperatures they are masked by 2D in-plane disordering of the FLL by inter-vortex interactions and point defect pinning. This is work that would require further investigation.

Further to examining the behaviour of  $\alpha$ , it is instructive to understand how  $\langle \Delta B^2 \rangle^{1/2}$  varies as a function of B and T. Figures 4.12 and 4.13 show the B-T phase diagrams respectively for BSCCO1 and BSCCO2.

If one first considers the data set for BSCCO1, it is clear that there is close agreement between the macroscopic irreversibility line and a microscopic melting transition occurring in the same region. It was stated by Majer (1995) that both microscopic and macroscopic events do not necessarily have the same origin. One can somewhat agree with this statement when considering the lack of agreement between the low-field regime of  $\alpha$  as shown in the log plot of Figure 4.9. However, it is hard to comprehend that they both have completely different origins when looking at the close agreement between them in Figure 4.12.

Further to this, it is also possible to observe a two-step change in the macroscopic data (described in Chapters 1 and 3). This change has also been noted by Blasius (1999) in terms of  $\mu\text{SR}$ . However, unlike Blasius, the data set presented here is more dense (showing a more convincing change in behaviour as a function of temperature) and this is the first time that such microscopic data has been presented in this format and compared to the  $dM/dT$  peak line.

At  $T \sim 20\text{K}$  (as shown in Figure 4.12), most of the vortices are expected to gain sufficient thermal energy  $kT$  to overcome the pinning potential offered by the point defects. This activated process is clearly evident in the linear plot of Figure 4.12 where the contour colour changes from green/yellow to turquoise. Further to this, it is also possible to see a slight kink around 20K in the temperature scans of  $\langle \Delta B^2 \rangle^{1/2}$  in Figures 4.4, 4.5, and 4.7. However, it is the excellent agreement between the macroscopic  $dM/dT$  peak line and the  $\mu\text{SR}$  data that is most significant and it is now clear that this point-defect depinning occurs at the same place on both the local and global scale too.

A remark must also be made on the feature known as  $B_{onset}$  which denotes an upturn or second peak in the hysteresis loops obtained through magnetisation measurements (see Figure 4.15 for example). In the  $\text{La}_{1.9}\text{Sr}_{0.1}\text{CuO}_4$  system, it was shown by Divakar (2004) that the onset of the Vortex Glass, as one increased the applied field from within the Bragg Glass regime, could be associated with an upturn in the magnetisation hysteresis loops. Such data has also been seen by Giller (1997) in a Nd-Ce-Cu-O crystal and indeed occurs within the similar reduced temperature range as that seen in BSCCO1. However, the effect in the Nd-Ce-Cu-O crystal occurs over most of the B-T diagram whereas in BSCCO1 it takes place over a small fraction of the Bragg Glass regime. Moreover, the lowest temperature at which the effect is seen is at 23K. Below this, the hysteresis loop becomes very broad and the  $B_{onset}$  feature begins to get smoothed out (see Figure 4.16). This is because the activation energy is less and thus the vortices show no significant response to pinning in this regime.

The variation of  $B_{onset}$  has been shown in the  $\text{Bi}_2\text{Sr}_2\text{CaCu}_2\text{O}_{8+\delta}$  system by Khaykovich (1997) and Wen (2000) but never before shown in conjunction with the  $\mu\text{SR}$  data. On the left hand side of both plots in Figure 4.8 one can see  $B_{onset}$  plotted (black data points) on top of the 2D  $\alpha$  log plot. Despite the lack of available data, one can see that macroscopic

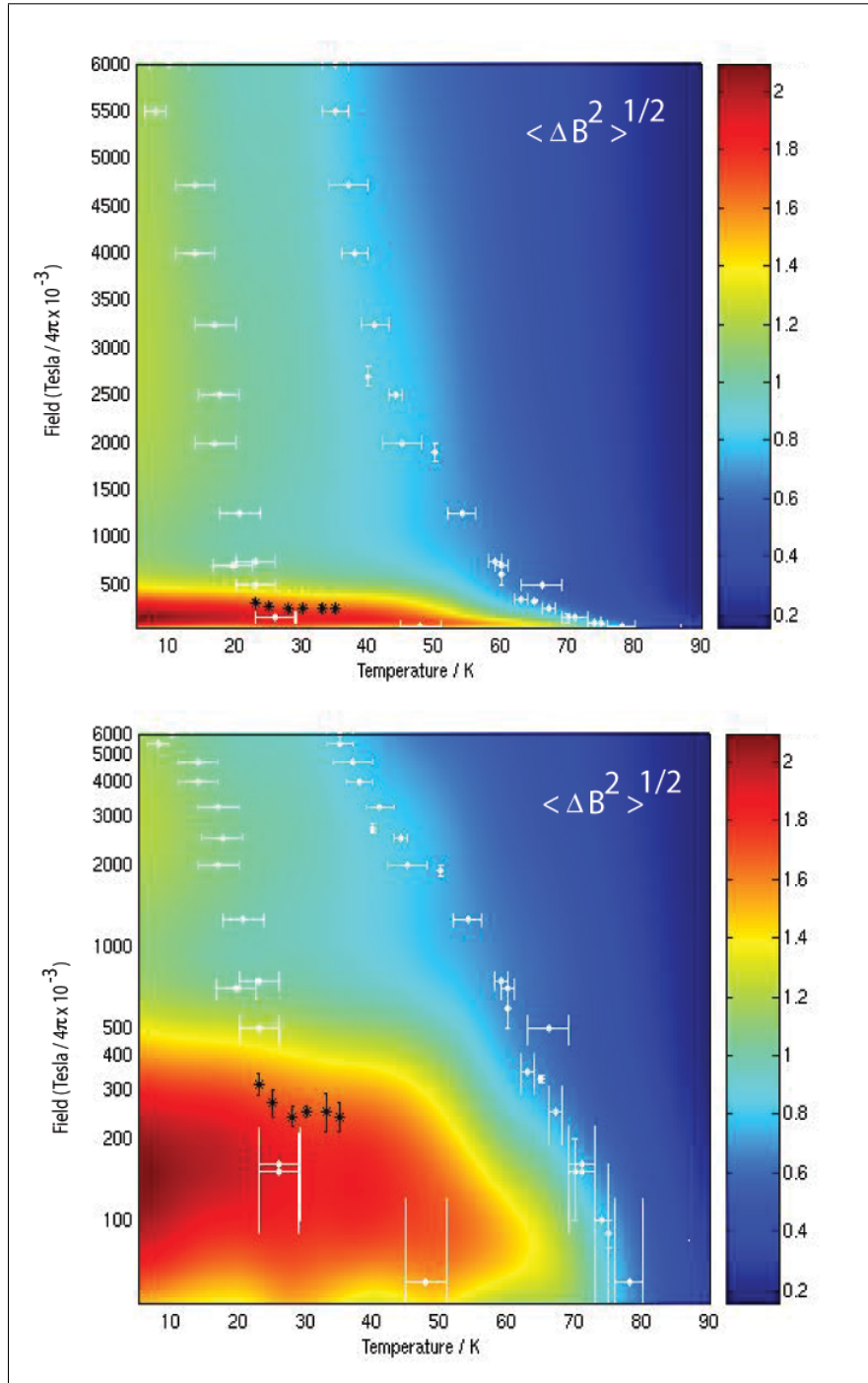


Figure 4.12: *BSCCO1*: A 2D plot showing the variation in  $\langle \Delta B^2 \rangle^{1/2}$  as a function of field and temperature on a linear scale (top) and on a logarithmic scale (bottom). This shows the close relationship between the irreversibility line (white points on right hand side of plot) and the microscopic melting transition (the latter being evident from the contour change). The black data points and the white points on the left hand side of the plot indicate  $B_{onset}$  and the  $dM/dT$  peaks respectively.

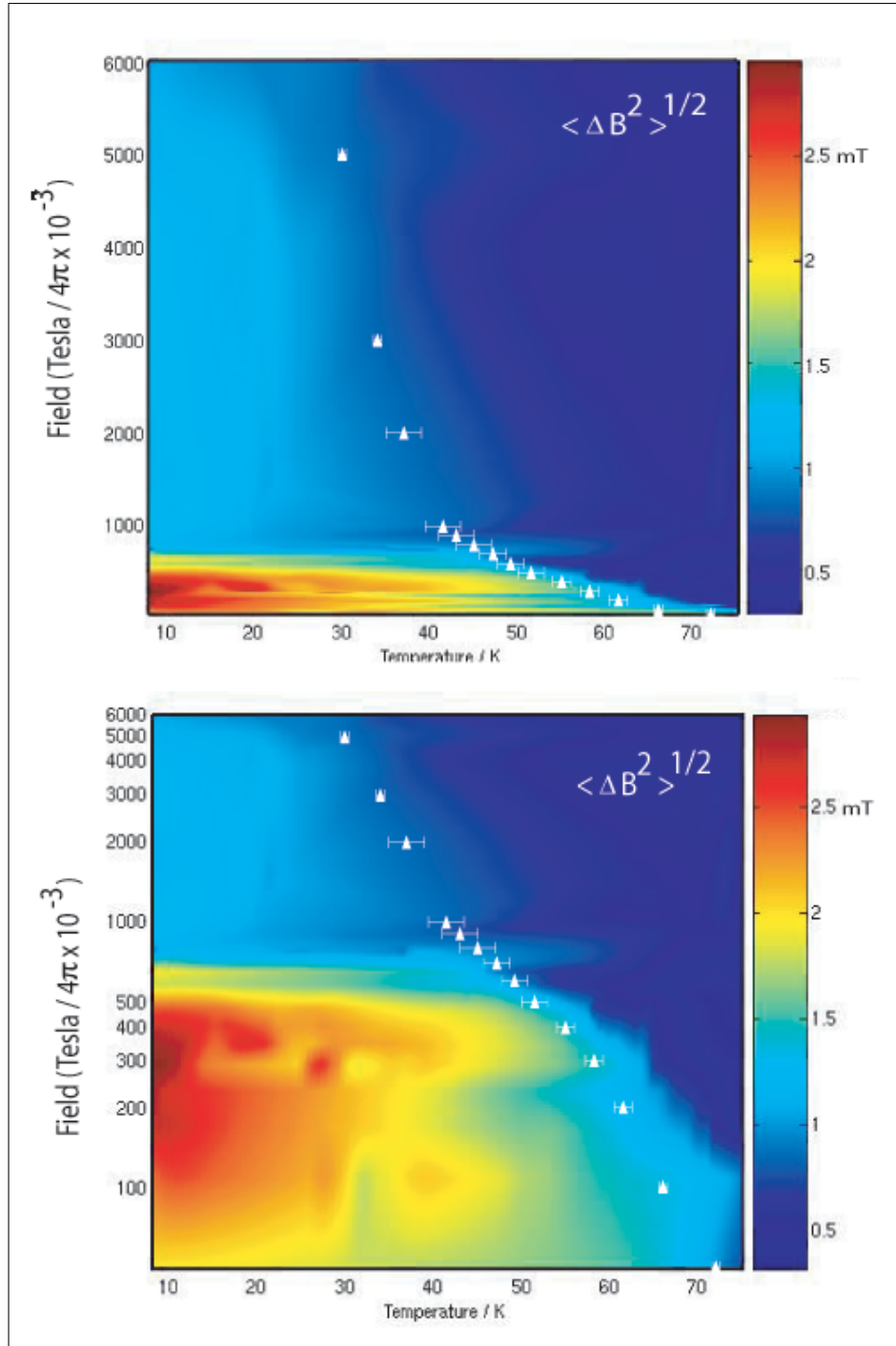


Figure 4.13: A similar behaviour for  $\langle \Delta B^2 \rangle^{1/2}$  as a function of temperature and field in BSCCO1 is observed in BSCCO2 here. The top and bottom plots display the linear and logarithmic scales respectively. It should be noted that the variation between the vortex glass and liquid region in the BSCCO2 sample is reduced due to a lack of data. Nevertheless, the interpolation routine still shows signs of a distinct change as a function of temperature around the irreversibility line.

set is in relative agreement with the  $\mu\text{SR}$  measurements. Indeed, it appears as though  $B_{onset}$  increases slightly as the temperature is lowered - in agreement with that seen by Divakar (2004) and Giller (1997) in the other superconducting systems. Importantly, Khaykovich (1997) notes that the form of  $B_{onset}$  is a function of temperature which is dependent upon the amount and strength of pinning in the crystal. Indeed, the effect on  $B_{onset}$  by increased pinning is discussed further in the following chapter.

Finally, when one considers the variation in the mean field as measured by  $\mu\text{SR}$  it is clear that an up-turn in  $\langle B \rangle$  occurs as a function of decreasing temperature before a local maximum at approximately 5K.<sup>7</sup> Such behaviour is most notable at higher fields, in particular at 4000G and 6000G (see Figure 4.17 and 4.18 respectively). Indeed, at low fields well within the Bragg Glass regime, the effect of a maximum is difficult to observe (see Figure 4.19).

The lowest mean field value at 4000G is  $-0.74 \pm (1.42 \times 10^{-2})$  mT for the  $\mu\text{SR}$  data compared with  $-0.42 \pm (1.23 \times 10^{-2})$  mT for the SQUID data. At 6000G, it is similar at  $-0.74 \pm (3.08 \times 10^{-2})$  mT for the  $\mu\text{SR}$  data compared with  $-0.41 \pm (3.25 \times 10^{-2})$  T for the MPMS. In addition to this, at both 4000G and 6000G, the local maximum in the  $\mu\text{SR}$  data happens at approximately 5K where  $\langle B \rangle = -0.17$  mT and  $-0.12$  mT respectively. The corresponding maxima in the MPMS data occur at  $-0.30$  mT and  $-0.68$  mT for 4000G and 6000G respectively.

The points at which the local maximum in the  $\mu\text{SR}$  data appears to lie is at temperatures slightly lower than where the macroscopic  $dM/dT$  peaks occur. Indeed, as one increases the temperature from 3.8K (the lowest measured value), the mean field in the  $\mu\text{SR}$  data is high due to increased pinning and inter-vortex interactions in this regime. As discussed earlier, although there is c-axis disorder (as shown in the asymmetric skewness parameters of Figures 4.8 and 4.9) which acts to reduce the mean field, the values of  $\langle \Delta B^2 \rangle^{1/2}$  (Figures 4.12 and 4.13) demonstrate in-plane disorder which reflects the dominance of point pinning in this region.

Increasing the applied temperature results in increased vortex dynamics. As stated earlier, depinning occurs and one observes a maximum in the  $dM/dT$  measurements. Such a peak in the MPMS SQUID data is also corroborated by the large change in the  $\mu\text{SR}$  mean field as a function of changing temperature. As noted by the  $\alpha$  plots of Figures 4.8 and 4.9, c-axis disorder still exists in the Vortex Glass state for temperatures less than  $\sim 30$ K. In addition to this, the increased activation energy of the vortices (as shown by the  $dM/dT$  peaks) and the subsequent reduction in  $\langle \Delta B^2 \rangle^{1/2}$  as a function of temperature demonstrates that there is a decrease in in-plane disorder as depinning from point defects occurs. With this combined effect of c-axis disorder and increased vortex dynamics, one expects and observes a reduction in the mean field and magnetisation of the  $\mu\text{SR}$  and MPMS data respectively.

By increasing the temperature further still, the effect of screening by the surface supercurrents becomes less and one observes the rise in  $\langle B \rangle$  as expected.

Figure 4.20 overlays the minimum in the mean field  $\langle B \rangle$  obtained from the MPMS SQUID data onto the variation of  $\langle B \rangle$  from  $\mu\text{SR}$  measurements. It is clear however, that despite the general agreement between the two different measuring methods, the values of  $\langle B \rangle$  as obtained by  $\mu\text{SR}$  and MPMS SQUID measurements do differ for the local maximum

<sup>7</sup>In order to compare the magnetisation from the MPMS SQUID and the mean field obtained from  $\mu\text{SR}$ , the former data set is converted to Tesla /  $\text{cm}^3$ .

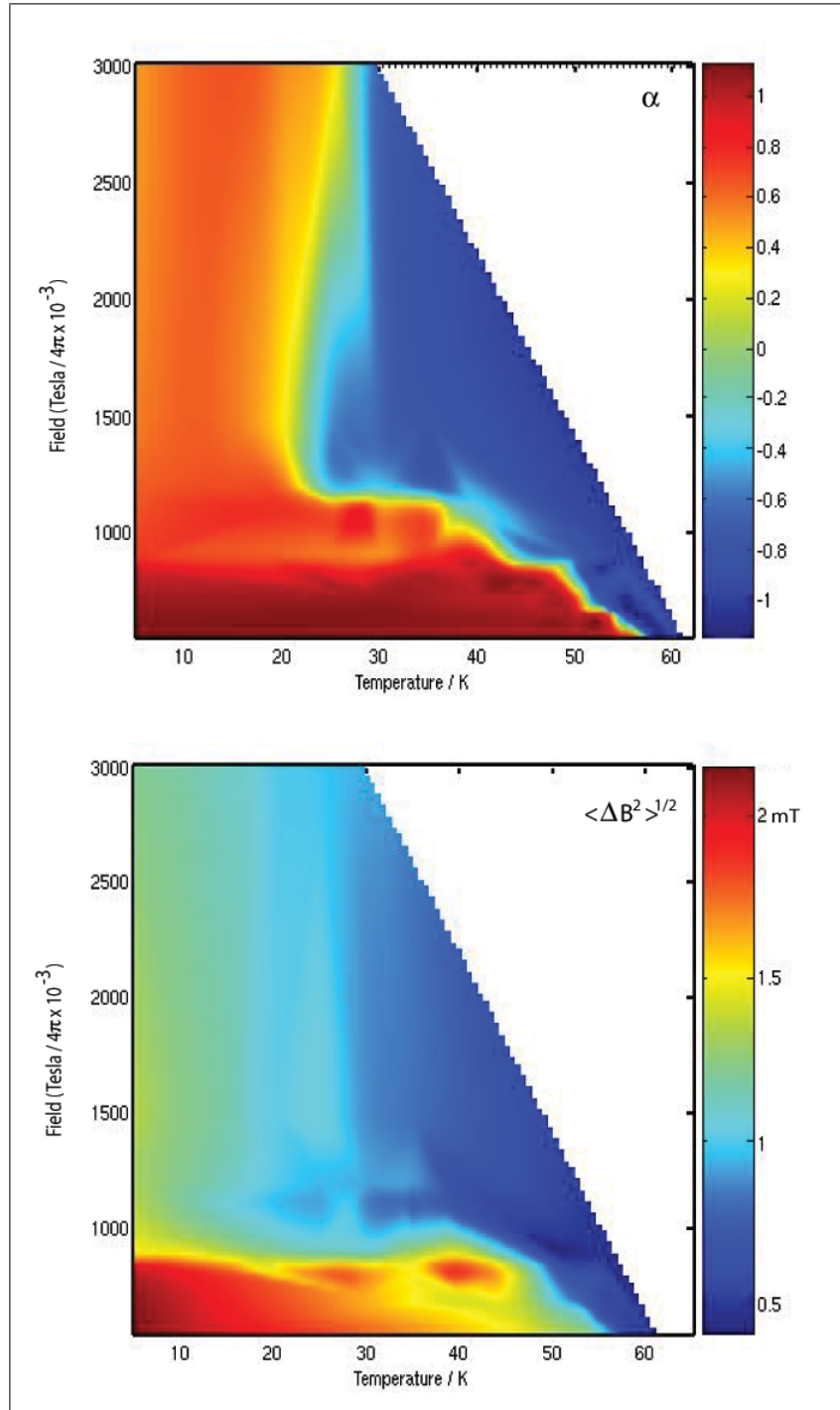


Figure 4.14: *The data taken here on BSCCO3 is sparse. However one can still note similarities with the other two samples. The top plot shows the variation of  $\alpha$  as a function of  $B$  and  $T$ . Interestingly the negative alpha “gap” does not exist here. The bottom plot shows the change in  $\langle \Delta B^2 \rangle^{1/2}$  where the two step change in the Vortex Glass phase is still slightly evident.*

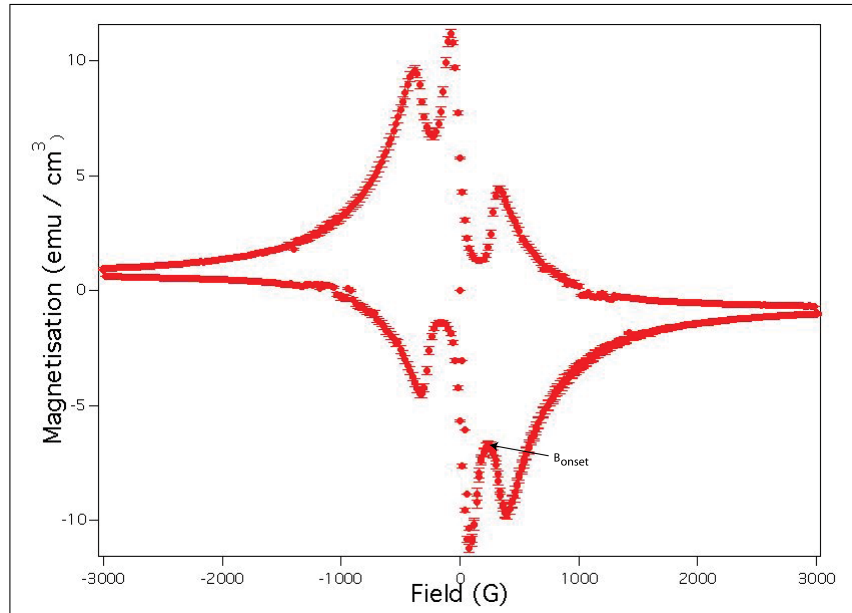


Figure 4.15: A plot showing the hysteresis field scan measurement at 28K in BSCCO1. The effect of  $B_{onset}$  occurs only between the region 20-35K. The small peak in the magnetisation hysteresis loop has been explained in the  $\text{La}_{1.9}\text{Sr}_{0.1}\text{CuO}_4$  system by Divakar (2004) as being the point  $B_{onset}$  which is associated with the Vortex Glass transition.

at approximately 5K. Such dissonance is not fully understood, but the effect may be due to

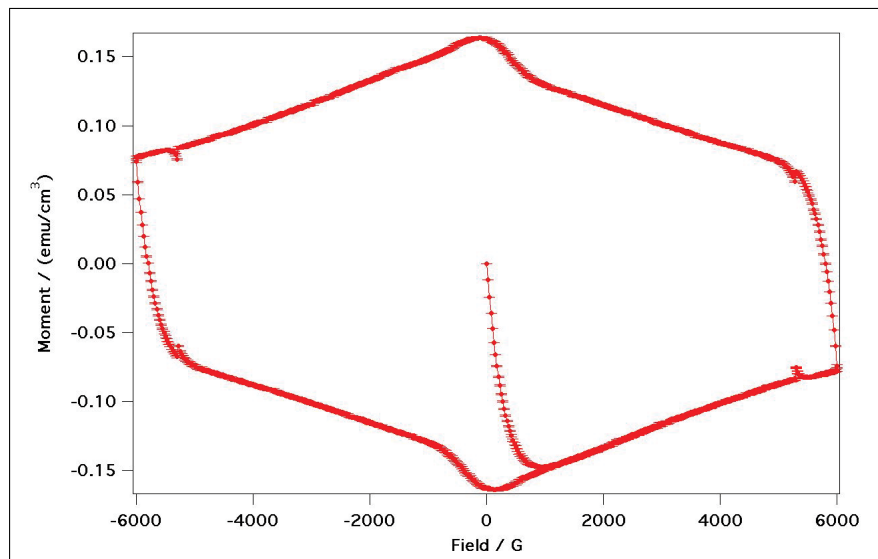


Figure 4.16: This plot shows a hysteresis loop at 20K for BSCCO1. Below approximately 23K, the  $B_{onset}$  feature (shown in Figure 4.15) begins to significantly reduce making it difficult to obtain.

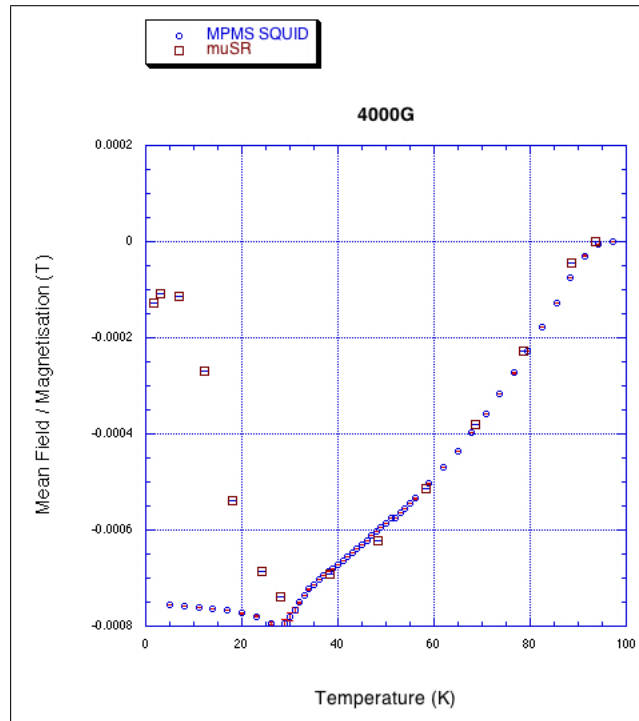


Figure 4.17: A plot showing the mean field and magnetisation as a function of temperature for the  $\mu\text{SR}$  and SQUID data respectively. At  $0.4T$ , one can observe that the dip in  $\mu\text{SR}$  mean field is also apparent in the MPMS magnetisation data; occurring at approximately  $28\text{K}$ . The SQUID data is obtained by cooling the material to the base temperature of the apparatus from above  $T_c$  in the applied field before warming and measuring. The  $\mu\text{SR}$  and MPMS data points are denoted by the red squares and blue circles respectively.

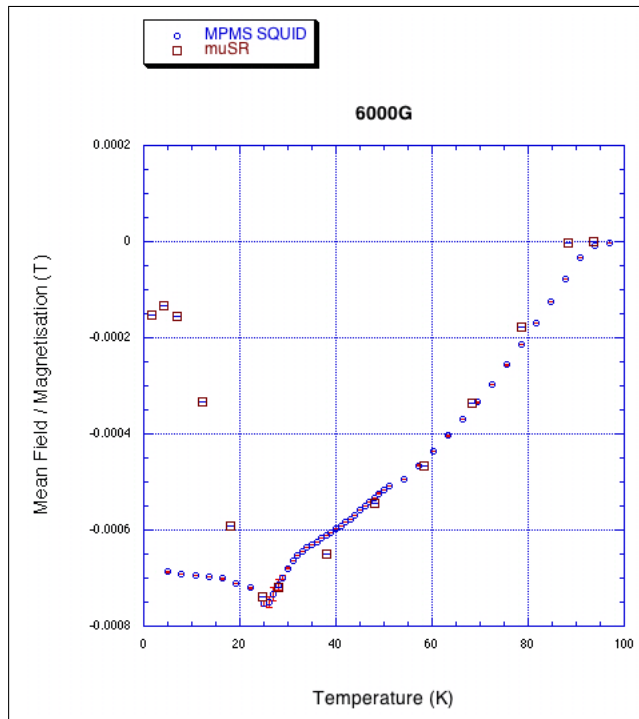


Figure 4.18: A plot showing the mean field and magnetisation as a function of temperature for the  $\mu\text{SR}$  and SQUID data respectively. At  $0.6\text{T}$ , the minimum in the  $\mu\text{SR}$  mean field occurs at approximately  $25\text{K}$ , in agreement with the MPMS magnetisation data. The SQUID data is obtained by cooling the material to the base temperature of the apparatus from above  $T_c$  in the applied field before warming and measuring. The  $\mu\text{SR}$  and MPMS data points are denoted by the red squares and blue circles respectively.

differences intrinsic to the techniques themselves. The MPMS SQUID measurements have substantially longer measuring times than those of the  $\mu\text{SR}$  technique. As such, the MPMS will see a more averaged value of the mean field than that of the latter technique, which has measuring times that are more comparable to the times over which the vortex motion occurs. Such investigation is subject to further work, however it is interesting that this effect is also apparent in other materials including  $(\text{Pb}_{1.0}, \text{Bi}_{1.0})(\text{Sr}_{1.62}, \text{La}_{0.38})\text{CuO}_{6+\delta}$  (Khasanov 2008) and the columnar defect sample detailed within the next chapter.

#### 4.0.5 Conclusions and Further Work

Despite the great deal of interest and work conducted on  $\text{Bi}_2\text{Sr}_2\text{CaCu}_2\text{O}_{8+\delta}$ , the behaviour of the FLL in the Vortex Glass regime, until now, has still not fully been understood. In particular, the sudden negative value of  $\alpha$  just above  $B_{cr}$ , the subsequent re-entrant behaviour of  $\alpha$  as one increases the applied field further still, the transition from the glass to liquid state and the highly negative  $\alpha$  in the latter region.

The work conducted within this chapter has shown that the negative  $\alpha$  that suddenly occurs above the Bragg Glass regime reflects residual three-body correlations. The sub-

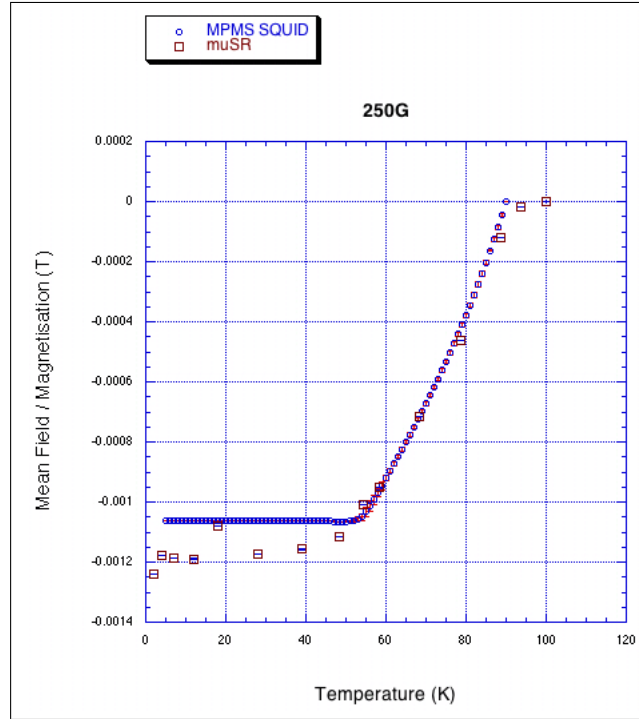


Figure 4.19: A plot showing the mean field and magnetisation as a function of temperature for the  $\mu\text{SR}$  and SQUID data respectively. At applied fields within the Bragg Glass regime (here, at 250G), the mean field obtained from  $\mu\text{SR}$  and the MPMS SQUID magnetisation data does not exhibit an upturn at low temperatures. The SQUID data is obtained by cooling the material to the base temperature of the apparatus from above  $T_c$  in the applied field before warming and measuring.

sequent increase in  $\alpha$  thereafter (for fields above 1000G at low temperature) to give a more symmetric P(B) lineshape signifies that the subtle balance between three-body correlations and disorder to give the negative  $\alpha$  is lost.

The transition from the vortex glass to liquid state has long been of interest but it is interesting to note that as one increases the temperature to the liquid state from a region comprising c-axis and in-plane disorder, a negative alpha occurs. Since the value of  $\langle \Delta B^2 \rangle^{1/2}$  does not change significantly, this suggests that in the liquid regime 3-body correlations are important. However, instead of considering those that pertain to bulk 3D vortices (i.e. vortices with long c-axis coherence lengths), one perhaps interprets them as 3-pancake correlations or three-body correlations between vortices with short c-axis coherence lengths (i.e. a reduction in the volume for angular correlations) as being the cause of such behaviour in the asymmetric skewness parameter.

It would be interesting to further certain aspects of the work presented in this chapter. Firstly, a closer investigation of  $B_{cr}$  as a function of oxygen doping. The lack of such a crossover in the data presented for BSCCO3 demonstrates that three-body correlations that occur as one increases the field above this region may strongly depend upon the variation in the electronic anisotropy of each material (through, for example, the possible introduc-

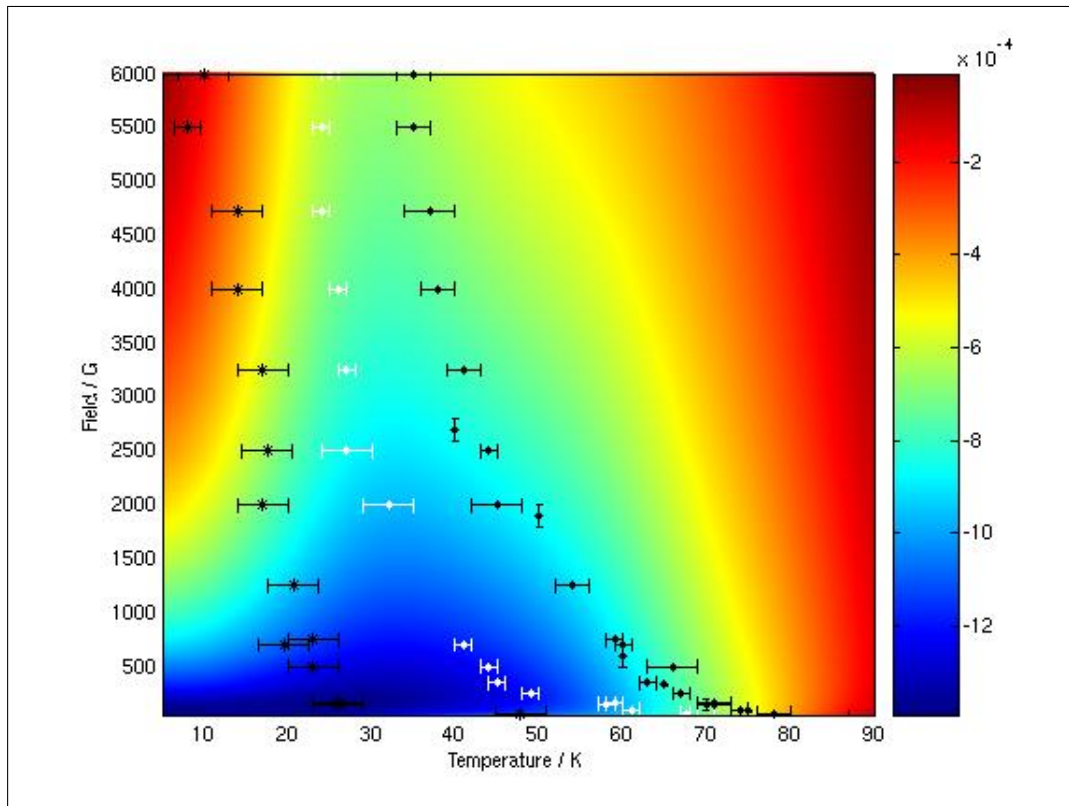


Figure 4.20: A 2D contour plot showing the variation in the mean field as obtained from  $\mu\text{SR}$ . Overlaid on top are the white data points showing the minimum point in the MPMS field cooled temperature scans (*i.e.* cooling the material in the applied field before warming and measuring). Also included is the  $dM/dT$  peak line and the irreversibility line (black data points on left and right hand side of plot respectively).

tion/removal of oxygen). Indeed, no negative  $\alpha$  has been reported within the liquid regime of a similar system  $(\text{Pb}_{1.0}, \text{Bi}_{1.0})(\text{Sr}_{1.62}, \text{La}_{0.38})\text{CuO}_{6+\delta}$  (Khasanov 2008) and therefore such behaviour clearly only occurs for a fragile set of conditions.

Further to this, numerical simulations as well as small angle neutron scattering focused on this region might provide more insight into the structure and arrangement of the flux lines and complement this  $\mu\text{SR}$  data well. Moreover, the former method may also provide further evidence that 3-body correlations (resulting in a highly negative  $\alpha$ ) are enhanced in the liquid regime of this archetypal superconductor.

Overall, the work presented in this chapter has shown that it is the subtle balance of three-body correlations and disorder that results in a negative asymmetric skewness parameter for the  $\mu\text{SR}$   $P(B)$  lineshape. As such, several issues regarding the behaviour and angular correlation of the vortices within the B-T diagram of this archetypal HTSC have been addressed and brought to conclusion.

## Chapter 5

# Measurements on the irradiated FLL of $\text{Bi}_{2.15}\text{Sr}_{1.85}\text{CaCu}_2\text{O}_{8+\delta}$

### 5.1 Background and Motivation

After the advent of the high-temperature superconductors, much work has been done at trying to push the superconducting transition temperature  $T_c$  to higher values. Despite this, certain physical factors limit the ability to do so. However, a few years after the discovery of the Ba-La-Cu-O system by Muller & Bednorz (1986), it was shown by Civale (1991) in a similar system ( $\text{YBa}_2\text{Cu}_3\text{O}_7$ ) that the irreversibility line could be enhanced to higher temperatures through the introduction of irradiation. They reported that if one used high energy ions (of the order of GeV) to irradiate a superconducting crystal, defect tracks would appear in the material. In this particular case the lines had a diameter of  $50\text{\AA}$  and were  $15\mu\text{m}$  long. In addition, the potential commercial applications of such a technique are of continuing interest (Science 2006) and will help add weight to furthering the work in this field.

Aside from the commercial applications, there has been much work conducted on how and why such systems operate. Indeed, Lee (1993*a*) showed that Monte Carlo simulations on a variety of disordered vortex line systems were in agreement with the results of Civale (1991). Of particular note was the fact that a system of line defects (commensurate with the FLL) gave a higher resulting  $T_c$  than that of random line defects but that the latter were most effective around  $B_\phi$  (the point at which the number of defects is equal to the number of vortices in the superconductor). However, it was Nelson & Vinokur (1993) who furthered the understanding of the FLL under the influence of columnar defects by drawing analogies with the behaviour of bosons in a 2D array (as mentioned in Chapter 2).

At low applied fields and temperatures, a Bose Glass phase exists. In this region all the flux lines occupy a columnar defect (Zech 1995). As one increases the temperature, the vortex movement is limited to hopping where either a whole vortex jumps from one pinning track to another or where part of a vortex moves to another site resulting in a kink along the vortex axis as shown in Figure 5.1 (Blatter 1994).

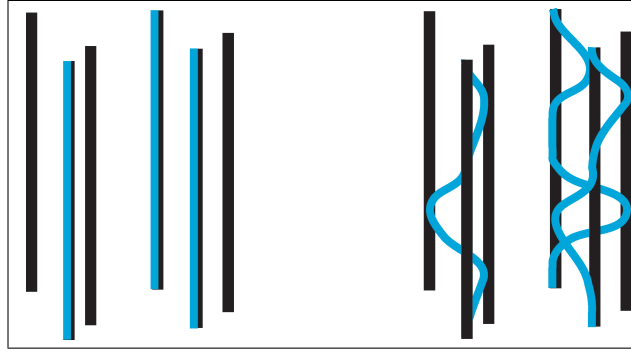


Figure 5.1: Flux “hopping” occurs when a whole vortex (blue) jumps from one defect (in black) to another as can happen in the left hand plot. However, it is also possible for hopping to occur when part of a vortex can jump to another pinning site (due to the extreme anisotropy of certain superconductors) and produce kinks in the longitudinal axis of the vortex (see right hand plot).

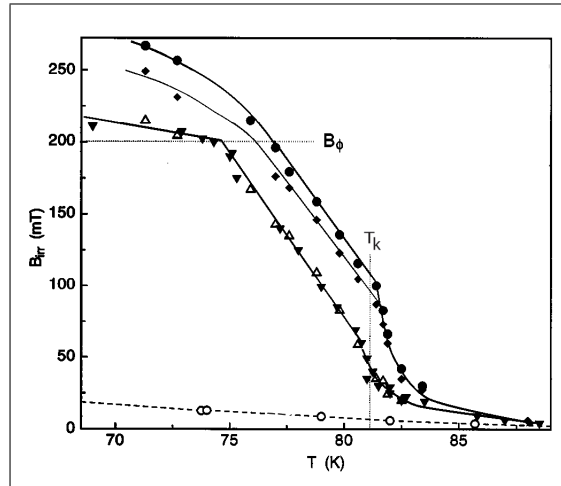


Figure 5.2: The kink in the irreversibility line at the temperature  $T_k$  in irradiated  $\text{Bi}_2\text{Sr}_2\text{CaCu}_2\text{O}_{8+\delta}$  was first explained by Van der Beek (1995) and separates two regions with different dependencies. The plot is taken from Zech (1996) and the points correspond to different measuring techniques as defined by the latter author. The lines are guides to the eye. Here  $B_{irr}$  refers to the irreversibility field obtained from hysteresis measurements and  $B_\phi$  is the matching field of the material.

Raising the temperature further results in FLL distortions that increase until the Bose Glass melts into a liquid. At this point, the energy of a pancake vortex is sufficient to move without hindrance from any of the defect tracks. The irreversibility point for such a transition does not have an exact theory at this time but can be parameterized in terms of a scaling theory that expects the transverse wandering  $l_\perp$  of the flux line to diverge at this

point as:

$$l_{\perp}(T) \sim \frac{1}{(T_{BG} - T)^{\nu}} \quad (5.1)$$

where  $T_{BG}$  is the transition temperature from the Bose Glass state and  $\nu$  is an undetermined exponent.

Further to this, it was shown by Sato (1997) that even when one enters the liquid state from the Bose Glass there are still regions where vortices (both decoupled and coupled along their length) co-exist slightly above the irreversibility line. The suppression of the thermal fluctuations of the vortices by columnar defects had already been generally highlighted by Koshelev (1996) where it was also noted that in  $\text{Bi}_2\text{Sr}_2\text{CaCu}_2\text{O}_{8+\delta}$ , like  $\text{YBa}_2\text{Cu}_3\text{O}_7$ , the coupling region could extend beyond that of the pristine material. Subsequently, the macroscopic irreversibility line of irradiated  $\text{Bi}_{2.15}\text{Sr}_{1.85}\text{CaCu}_2\text{O}_{8+\delta}$  was shown as differing from that of the unirradiated sample and comprised two forms - exponential at low fields and linear above a critical field (Zech 1996). Moreover, the kink in this irreversibility curve (shown in Figure 5.2), separating the two dependencies, was explained by Van der Beek (1995) as being due to the sudden crossover from a Bose-Glass vortex hopping to individual pancake hopping as one increased the applied field. This change occurs at the matching field  $B_{\phi}$ . However, at low inductions, Colson (2004) demonstrated that the irreversibility line does not increase beyond the first order melting transition of the pristine crystals. In addition, it was also found that at the Bose Glass to liquid interface, there is a rapid decrease in c-axis phase correlations. This does not negate the results of Sato (1997) and Koshelev (1996) (mentioned above) but serves to highlight that there is some loss of Josephson coupling between the layers within this regime.

A Mott Insulator phase (examined extensively by Fisher (1989)) exists at  $B = B_{\phi}$  where the tilt and compressional moduli are infinite. In this region, every vortex occupies a columnar defect such that the disorder in the FLL is essentially trivial (i.e. it is governed purely by the randomness of the correlated tracks). Indeed, due to the strong attractive potential energy offered by the pinning sites, flux motion is highly non-linear and relaxation times are very long (Nelson & Vinokur 1993).

For applied fields greater than  $B_{\phi}$ , more vortices begin to enter the superconductor and place themselves interstitially between the columnar defects. Still trying to minimise the magnetic energy, they will locate themselves in clusters of occupied defects that are more widely spaced than others so as to reduce the repulsive dipolar potential of the pinned vortices.

Nelson & Vinokur (1993) have considered a theoretical model for the translational order between the vortices in this regime. They have noted that as the root-mean-square thermal fluctuation of a vortex position exceeds that of the pinning energy scale there is a significant thermal enhancement of the translational correlation length. Further to this, an increase in the boundary at which the Vortex Glass appears was observed by Lee (1998). In this region, the asymmetric skewness parameter of the  $P(B)$   $\mu\text{SR}$  lineshape has values of approximately  $\alpha \sim 1$ . This demonstrates that the flux lines still exhibited longitudinal coherence along their axis at fields more than twice  $B_{\phi}$ .

Although much theoretical work has clearly been conducted on the influence of columnar defects on a range of HTSCs as well as plenty of experimental investigation on systems such as  $\text{YBa}_2\text{Cu}_3\text{O}_7$ , little is understood about the effect in the highly anisotropic supercon-

ductor  $\text{Bi}_2\text{Sr}_2\text{CaCu}_2\text{O}_{8+\delta}$ . More specifically, there is still debate about the precise behaviour of the FLL at fields around and above  $B_\phi$ , particularly at high temperatures, close to the irreversibility line. The work presented here continues the investigation of the effect of columnar defects on the behaviour of magnetic vortices within the superconducting state. The sample ( $\text{Bi}_{2.15}\text{Sr}_{1.85}\text{CaCu}_2\text{O}_{8+\delta}$ ) is extremely similar to that measured in the previous chapter except that, with a  $T_c=86\text{K}$ , the superconductor has been irradiated using  $17.7\text{GeV}$  U ions.<sup>1</sup> The main results focus on a crystal (denoted as  $\text{BSCCO1}_{irr}$ ) that has been irradiated such that  $B_\phi = 0.2\text{T}$ . However, data has also been presented on another sample ( $\text{BSCCO2}_{irr}$ ) with  $B_\phi = 0.1\text{T}$  for comparison.

## 5.2 Discussion of Experimental Results

Macroscopic magnetisation measurements were performed first on the irradiated  $\text{Bi}_{2.15}\text{Sr}_{1.85}\text{CaCu}_2\text{O}_{8+\delta}$  material. The irreversibility line and the  $dM/dT$  peak points (whose method of extraction is described earlier) were obtained and immediately show distinct differences to that of the unirradiated sample, as expected. Figure 5.3 clearly shows how there are three prominent energy scales operating within this irradiated material. Firstly, the irreversibility line (shown in black on the right hand side of Figure 5.3) has, as described earlier, been elevated to higher temperatures. Indeed, it is clear that it reaches  $70\text{K}$  and  $50\text{K}$  at applied fields of  $2000\text{G}$  and  $6000\text{G}$  respectively compared with the unirradiated material (which attains  $35\text{K}$  and  $45\text{K}$  at  $2000\text{G}$  and  $6000\text{G}$  respectively). The kink  $T_k$  separating the two regions of different dependencies above and below  $B_\phi$  is shown to be in agreement with Van der Beek (1995) and Zech (1996).

Further to this, the  $dM/dT$  peak data shows two distinct features (see blue data in Figure 5.3). At temperatures  $\sim 20\text{K}$ , one observes the peak in the  $dM/dT$  data as per the unirradiated material. Such behaviour is again a result of vortices depinning themselves from the point defects intrinsic to the crystal structure. One can see that, in agreement with the unirradiated material, the points are asymptotic to  $\sim 10\text{K}$ .

However, there is dissonance with the pristine sample as the irradiated  $\text{Bi}_{2.15}\text{Sr}_{1.85}\text{CaCu}_2\text{O}_{8+\delta}$  also demonstrates a second  $dM/dT$  peak occurring at a slightly higher temperature (between  $40\text{K}$  and  $50\text{K}$ ). The vortices within the FLL are pinned substantially by the columnar defects and, as investigated by Koshelev (1996), this suppresses the thermal fluctuations until higher temperatures. This peak again represents FLL dynamics and reflects the depinning of the vortices from the columnar defects (Koshelev 1996). Indeed, it is clear that since the strength of the vortex pinning by these artificial defect tracks is greater than those of the intrinsic point pinning, the energy required to overcome the attractive pinning potential is higher. Thus, higher activation energies  $\propto kT$  are required and this results in  $dM/dT$  peaks at higher temperatures.

Moreover, when considering Figure 5.4, it is clear that the magnitude of the peaks varies as a function of applied field. At low fields ( $<1000\text{G}$ ), there is no peak resulting from point defect pinning. Indeed, the only  $dM/dT$  peak is that resulting from the columnar defects at approximately  $50\text{-}60\text{K}$ . In this regime ( $B < B_\phi$ ) the vortices are sufficiently

<sup>1</sup>For the  $\mu\text{SR}$  measurements detailed here, the sample was prepared in exactly the same way as that described in the previous chapter.

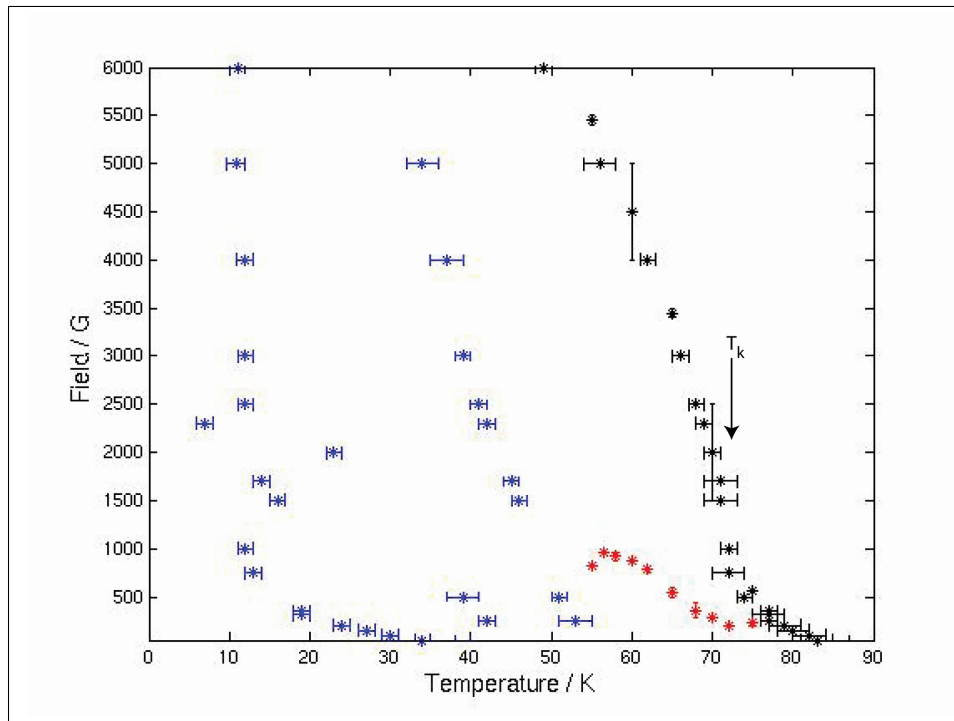


Figure 5.3: A plot showing the position of the significant peaks taken from the magnetisation measurements. The peaks are plotted as a function of applied field and temperature and one can clearly observe that there are three predominant energy scales as a function of temperature. Blue data: Between 10-20K, a peak in the  $dM/dT$  data arises from vortex depinning from point defects. Between 40-50K, the  $dM/dT$  data shows a second peak arising due to depinning from columnar defects - each form of depinning is an activated process dependent upon  $kT$ . Black data: At temperatures approximately 70K, the irreversibility line exists at noticeably elevated temperatures compared to the pristine material. Red data: At low inductions,  $B_{on,set}$  which, similar to the Bragg to Vortex Glass in the pristine material, may be associated with a move from the Bose Glass to liquid state here in this irradiated system.

outnumbered by the density of defect tracks and as such the attractive pinning potential provided by the columnar defects substantially outweighs that of the point defects. This makes it energetically less favourable for a vortex to be pinned by a point defect. Consequently, since pinning is almost predominantly from the columnar defects in this state, there is no evident “depinning” from the intrinsic crystal point defects.

However, at higher applied fields the  $dM/dT$  peak resulting from the columnar defects begins to decrease as the peak originating from the point defect pinning (at approximately 15K) starts to increase in magnitude - reaching a maximum value at the maximum applied field of 6000G. In this region, the number of vortices increasingly outweigh the columnar defect density. Every columnar defect will be occupied whilst an increasing number of vortices will be residing in the spaces between the tracks and will become susceptible to the point defect pinning. The enhanced competition between attractive potentials from the columnar tracks and repulsive vortex-vortex interactions means that the only depinning that

can occur at these high fields is that from point defect pinning (i.e. those not aligned along a defect track).

Knowing the macroscopic behaviour of the irradiated  $\text{Bi}_{2.15}\text{Sr}_{1.85}\text{CaCu}_2\text{O}_{8+\delta}$  material, it is then intuitive to conduct microscopic measurements using  $\mu\text{SR}$  and SANS.

Like the unirradiated  $\text{Bi}_{2.15}\text{Sr}_{1.85}\text{CaCu}_2\text{O}_{8+\delta}$  material investigated in the previous chapter, a series of temperature scans, performed under the same conditions, were conducted on the irradiated sample. Despite some work having been carried out by Lee (1998) within the low field Bose Glass regime, in light of a new understanding of some of the physics of these systems (detailed previously), it is intuitive to investigate a 2D B-T plane (similar to that for the unirradiated material) both as a function of the square root of the second moment of the P(B) linewidth  $\langle \Delta B^2 \rangle^{1/2}$  and the asymmetric skewness parameter  $\alpha$ . In addition to this, it makes for good, overall comparison with the unirradiated material.

Considering first the measurements on  $\text{BSCCO1}_{irr}$ , it is possible, from the  $\langle \Delta B^2 \rangle^{1/2}$  plot of Figure 5.5, that melting of the FLL occurs at  $\sim 75\text{K}$  where the curves for the different fields begin to converge. Although the precise point of melting is field dependent as shown below, at a glance the change in the P(B) linewidth is already elevated to higher temperatures than that of the pristine material (see Figure 5.6).

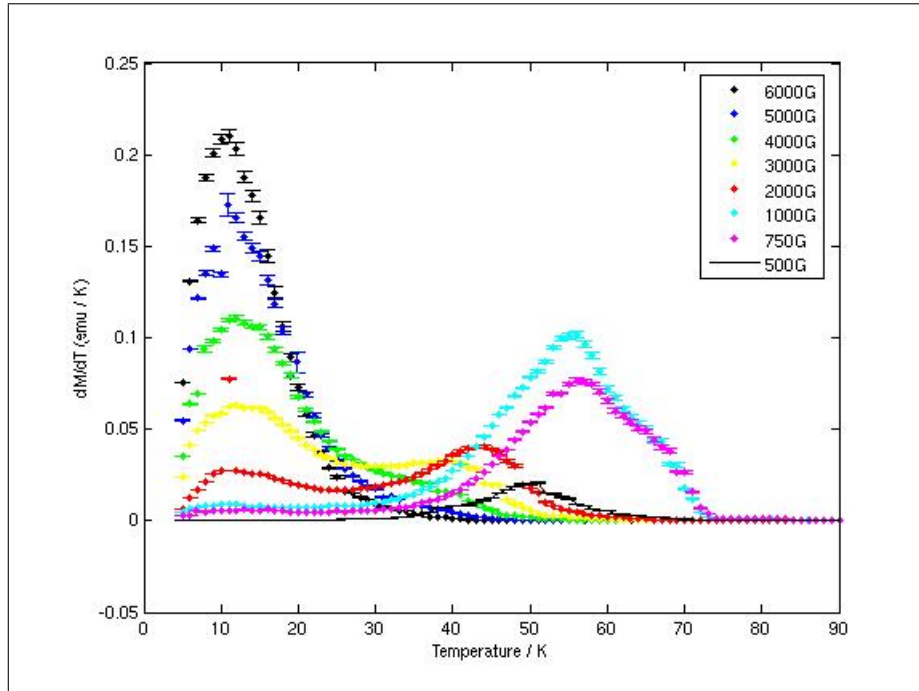


Figure 5.4: *By taking the derivative of the ZFC magnetisation temperature scans, it is possible to obtain two peaks reflecting points of greatest vortex motion. Peaks at low and high temperatures correspond to depinning from point and columnar defects respectively. As one approaches higher magnetic inductions, the peak originating from vortices depinning from the columnar defects reduces substantially whilst the  $dM/dT$  peak for vortices depinning from intrinsic point defects increases.*

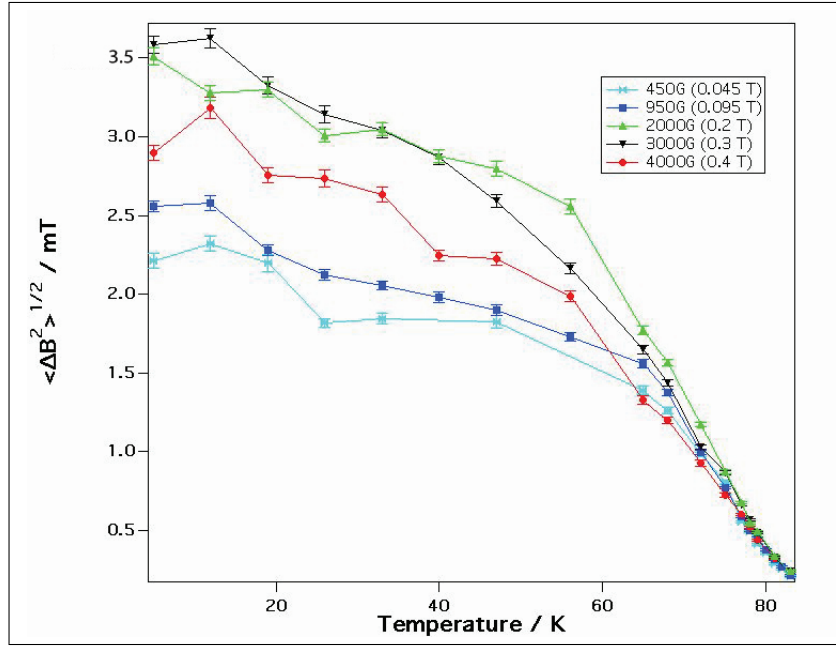


Figure 5.5:  $\text{BSCCO1}_{irr}$ : A plot showing the decrease in  $\langle \Delta B^2 \rangle^{1/2}$  as a function of increasing temperature for a range of inductions. The convergence for the different temperature scans occurs at higher values than that in the pristine material (see Figure 5.6). Here,  $B_\phi = 0.2T$ .

$\text{BSCCO2}_{irr}$  also shows a change in behaviour occurring for fields close to  $B_\phi = 0.1T$  at higher temperatures (compared with the pristine material) where a convergence of  $\langle \Delta B^2 \rangle^{1/2}$  occurs (see Figure 5.7). For this latter sample, the different data sets (taken at 500G and 1500G) converge at approximately 75K.

However, when compared with  $\langle \Delta B^2 \rangle^{1/2}$  for unirradiated  $\text{Bi}_{2.15}\text{Sr}_{1.85}\text{CaCu}_2\text{O}_{8+\delta}$ , it is clear that the overall magnitude of the square root of the second moment is far greater. For the  $\text{BSCCO1}_{irr}$  material, when  $H_{app} = B_\phi$  (i.e. 2000G),  $\langle \Delta B^2 \rangle^{1/2} = 3.26 \pm (4.7 \times 10^{-2})$  mT at 12K, but is only  $1.18 \pm (1.2 \times 10^{-2})$  mT for the unirradiated material ( $\text{BSCCO2}$ ) under the same conditions. Even at higher temperatures  $\langle \Delta B^2 \rangle^{1/2} = 2.64 \pm (4.5 \times 10^{-2})$  mT at 55K compared with  $\langle \Delta B^2 \rangle^{1/2} = 0.74 \pm (6.9 \times 10^{-2})$  mT at 55K for the pristine  $\text{BSCCO1}$  sample. If one then considers the 2D contour plot of Figure 5.8, it is clear that the  $P(B)$  linewidth is substantially broader than the corresponding data for the pristine material over most of the B-T diagram. It is clear that such behaviour results from a FLL lattice that is predominantly disordered in-plane (giving rise to a large variance in  $P(B)$  lineshapes). However, further to this, such broadness can also only come about by having vortices that retain the coupling along their axis (i.e 3D vortices). If decoupling were to happen through thermal activation, then this would be represented by a narrowing of the  $\mu\text{SR}$  lineshape, which does not occur here.

Interestingly though, within the vicinity of  $B_\phi$  for  $\text{BSCCO1}_{irr}$ , at temperatures  $< 20\text{K}$ , the in-plane disorder reaches a maximum, reducing as one increases the field further above  $B_\phi$  (see Figure 5.8). Even as the applied field is increased to four times the matching field (i.e. 0.4T),  $\langle \Delta B^2 \rangle^{1/2}$  still remains distinctly larger than the value obtained from the

pristine sample under the same external conditions. Indeed for  $\text{BSCCO2}_{irr}$ , at 5K the square root of the second moment reaches a maximum of  $3.2 \pm (8.1 \times 10^{-2})$  mT just before increasing to the matching field at 1000G (see Figure 5.9). At 5K for  $H_{app}=0.4\text{T}$ ,  $\text{BSCCO2}_{irr}$  has a square root of the variance of  $1.5 \pm (2.8 \times 10^{-2})$  mT compared with  $1.21 \pm (1.3 \times 10^{-2})$  mT for the pristine material  $\text{BSCCO1}$ . Although acknowledged already, the  $\mu\text{SR}$  data clearly shows that maximum in-plane disorder of 3D vortices occurs at approximately  $B_\phi$ .

However, when one considers the corresponding 2D asymmetric skewness plot (Figures 5.10 (top plot) and 5.11) for the same region, it is noticeable how, for  $\text{BSCCO1}_{irr}$ ,  $\alpha$  actually reaches a minimum of  $0.52 \pm 0.051$  for an applied field of 2000G at 5K.  $\text{BSCCO2}_{irr}$  also demonstrates a minimum of  $0.69 \pm 0.02$  at 250G (see bottom plot of Figure 5.10). Indeed, this is extremely comparable to that of the unirradiated sample,  $\text{BSCCO1}$  which has  $\alpha=0.57 \pm 0.043$ . Such a symmetric lineshape for a large temperature range about  $B_\phi$  indicates that there is a significant effect on the orientational order of the vortices by the columnar defects. Indeed, as discussed in the previous chapters,  $\alpha$  reflects three-body correlations. In the region about  $B_\phi$ , the in-plane order of the FLL is distinctly altered with respect to the same region in the pristine sample. If one considers Figure 5.12, it appears as though the asymmetric skewness remains relatively constant as a function of temperature at inductions close to the matching field. Thus, it is evident that the columnar defects have a significant effect on the three-body correlations within this regime.

Upon closer investigation however, it appears as though a small undulation in the data may occur where  $\alpha$  reaches a minimum before slightly increasing again. If one considers the 950G temperature scan in Figure 5.12 then it can be seen that between 19K and 25K,  $\alpha$

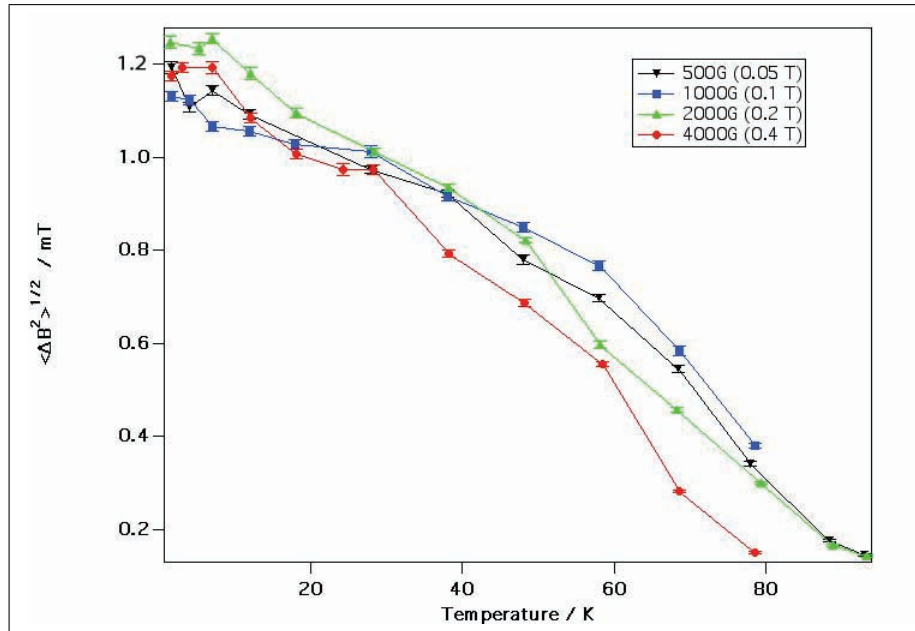


Figure 5.6: A plot showing the decrease in  $\langle \Delta B^2 \rangle^{1/2}$  as a function of increasing temperature for a range of inductions in the pristine material (see for comparison with the irradiated crystal in the previous figure).

drops from  $0.78 \pm 0.023$  to  $0.66 \pm 0.037$  before recovering to  $0.82 \pm 0.031$  at 47K. The effect in  $\text{BSCCO1}_{irr}$  is perhaps more noticeable in the interpolated data set of the 2D contour plot in Figure 5.13. Here, a small up-turn can be observed between 15-20K (denoted by a slightly lighter shade of blue in the plot), before a slight decrease between 25-30K (shown by the change to dark blue). This, coupled with the macroscopic magnetisation measurements of Figure 5.3, demonstrates that there is a small improvement in phase coherence occurring along the vortex axis as the FLL depins from the point defects. However, since the effect is extremely subtle, further investigation is needed before firm conclusions can be made about this feature.

When one considers the variation of  $\langle \Delta B^2 \rangle^{1/2}$  as a function of field for  $\text{BSCCO1}_{irr}$  (i.e. field cuts in the B-T diagram), it is clear that there is a difference between the data at low and high temperatures. Considering first Figure 5.14, one can observe that at 19K,  $\langle \Delta B^2 \rangle^{1/2} = 2.19 \pm (4.7 \times 10^{-2})$  mT at an induction of 100G before rising to  $3.24 \pm (4.6 \times 10^{-2})$  mT at the matching field. In addition, at the higher temperature of 47K for example,  $\langle \Delta B^2 \rangle^{1/2}$  increases from approximately  $1.8 \pm (4.3 \times 10^{-2})$  mT at an applied field of 100G to  $2.8 \pm (4.5 \times 10^{-2})$  mT at  $B_\phi$  before reducing to  $2.24 \pm (4.2 \times 10^{-2})$  mT at  $2B_\phi$ . This data reflects how, as explained before, the vortex lattice is increasingly becoming more disordered in-plane as one approaches the matching field (whilst maintaining a three dimensional structure), before

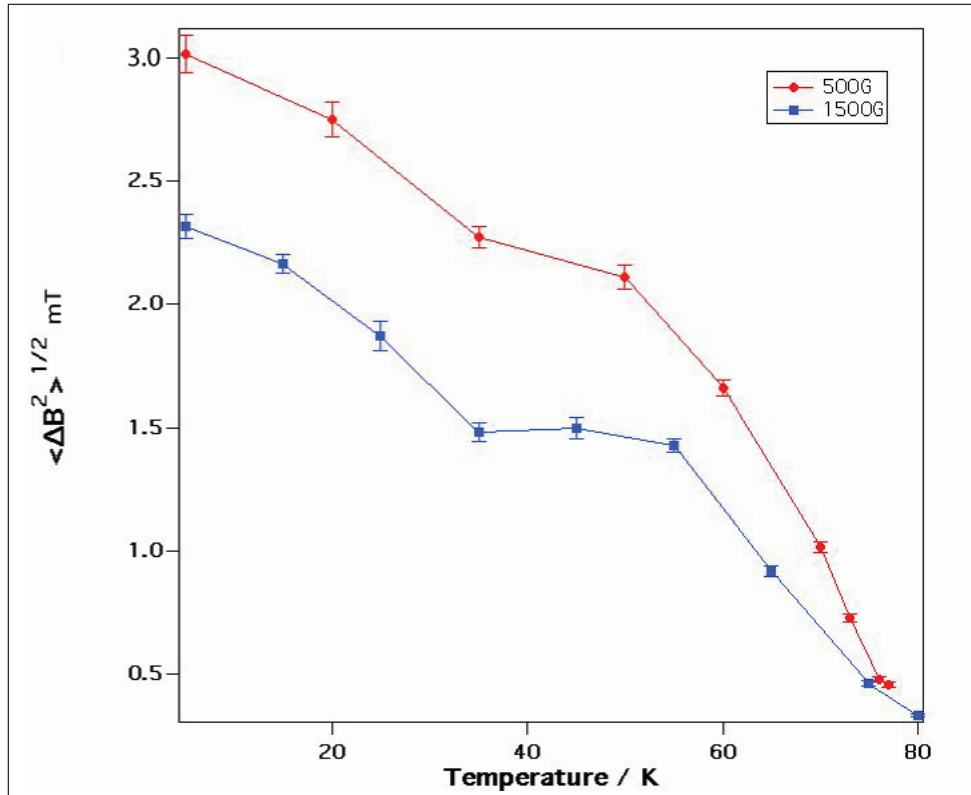


Figure 5.7: In  $\text{BSCCO2}_{irr}$ , the convergence of the  $\langle \Delta B^2 \rangle^{1/2}$  curves (for the two applied fields of 500G and 1500G) as for  $\text{BSCCO1}_{irr}$ , also occurs at higher temperatures around 75K. Here,  $B_\phi = 0.1T$ .

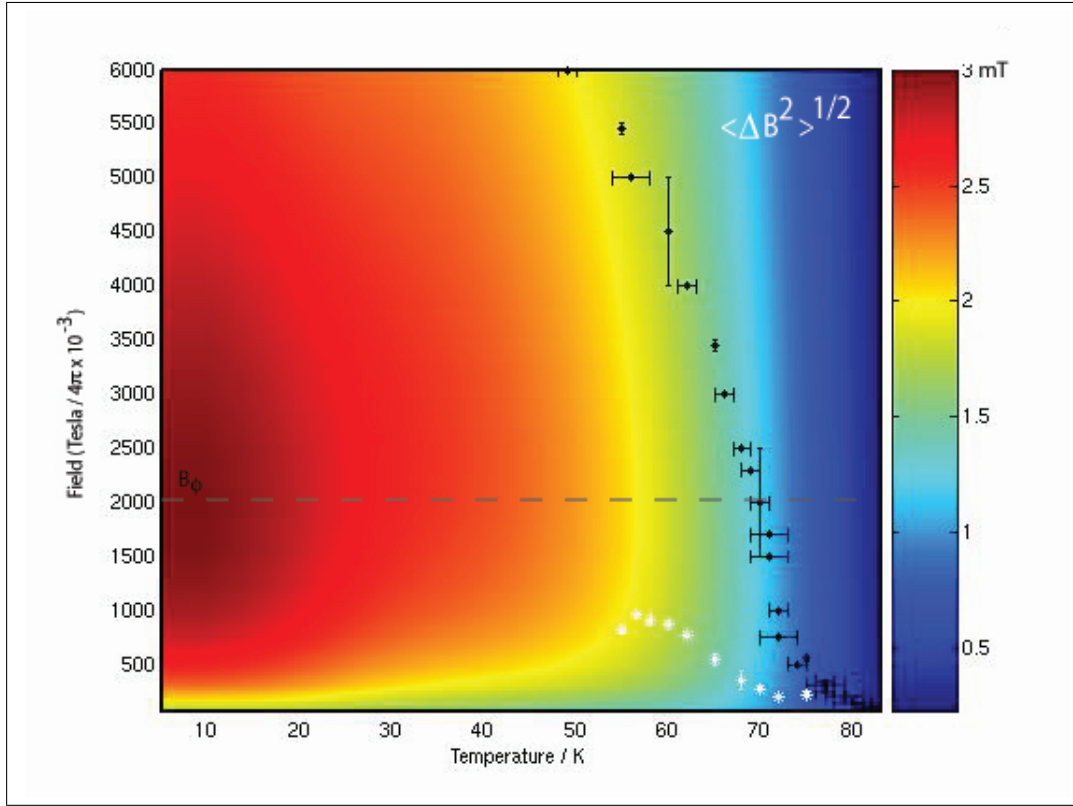


Figure 5.8:  $\text{BSCCO1}_{irr}$ : The 2D  $B$ - $T$  diagram for  $\langle \Delta B^2 \rangle^{1/2}$  differs greatly to the corresponding plot for the pristine material (see Figure 4.12 for comparison). At low temperatures around  $B_\phi = 0.2T$  a broad lineshape occurs reflecting the correlated disorder caused by the columnar defects on 3D vortices. The FLL melts at higher temperatures than in the unirradiated crystal. Here, the black and white data points represent the irreversibility and  $B_{onset}$  lines respectively.

reducing as one increases the applied field further.

However, if one compares these low temperature field “cuts” with those performed at higher temperatures, a distinct difference can be noticed (see Figure 5.15). Again, a peak is reached as one approaches the matching field, although the magnitude of the linewidth is not as great as that at low temperatures. For example, at 250G,  $\langle \Delta B^2 \rangle^{1/2}$  is  $1.43 \pm (2.4 \times 10^{-2})$  mT and  $1.12 \pm (1.6 \times 10^{-2})$  mT at 65K and 72K respectively. At  $H_{app} = B_\phi$ , the square root of the variance is  $1.78 \pm (2.5 \times 10^{-2})$  mT and  $1.17 \pm (1.4 \times 10^{-2})$  mT for 65K and 72K respectively - both significantly less than the values obtained at low temperatures. Nevertheless, this is to be expected, certainly as the effect of the penetration depth is increasingly prominent in this region of the  $B$ - $T$  diagram. However, what is novel is the minimum in the  $P(B)$  linewidth that is reached at an induction of approximately  $B_\phi/3$ . This characteristic field value was highlighted by Sugano (1998) using the Josephson plasma resonance technique (see Figure 5.16). These authors suggested that there is a vortex decoupling transition possibly occurring between the Bose Glass state and the Vortex Glass at  $H_{app} = B_\phi/3$ . In Figure 5.15, one can observe that in particular, there is a clear decrease in the square root of the variance

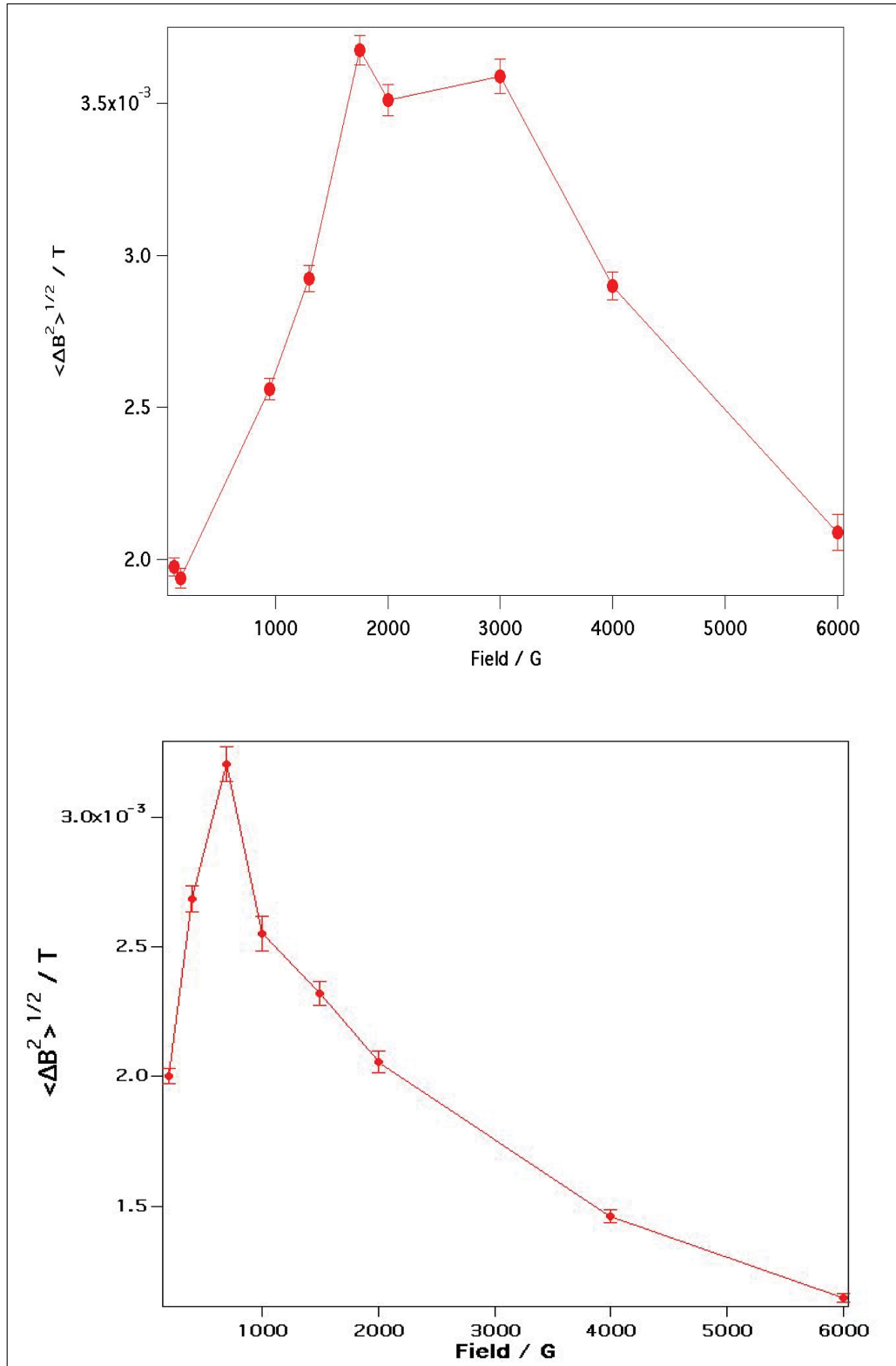


Figure 5.9: *Top: The square root of the variance in the  $P(B)$  linewidth at 5K for the irradiated material  $\text{BSCCO1}_{irr}$  increases to a maximum at  $B_\phi = 0.2\text{T}$  before gradually decreasing towards higher inductions. Bottom: A distinct peak can also be seen in  $\langle \Delta B^2 \rangle^{1/2}$  close to  $B_\phi = 0.1\text{T}$  for 5K when one increases the field deep within the Mott Insulator regime (i.e. at approximately an applied field of 0.2T) for  $\text{BSCCO2}_{irr}$ .*

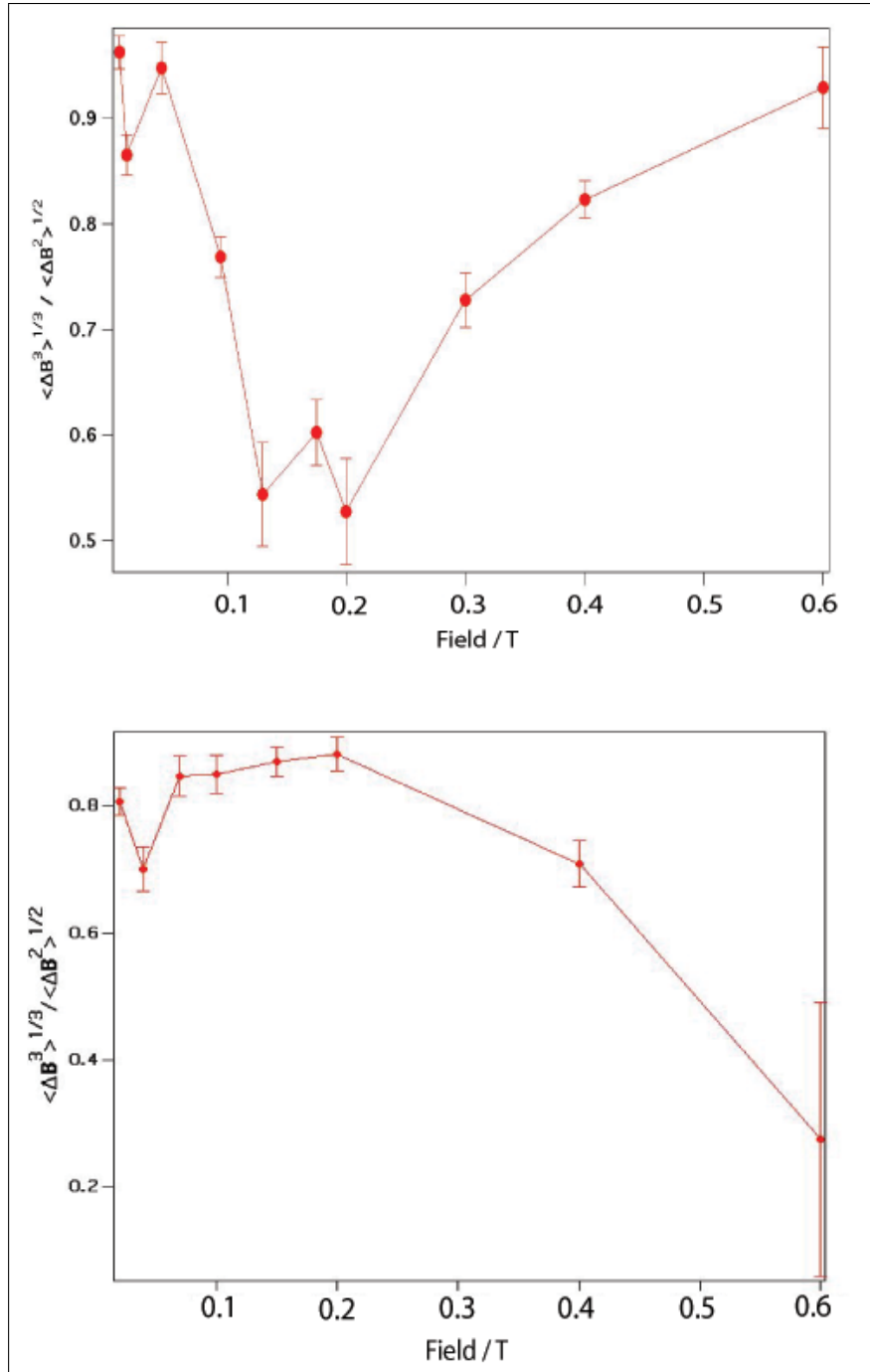


Figure 5.10: *Top: The change in the asymmetric skewness  $\alpha$  at 5K for the irradiated material  $\text{BSCCO1}_{irr}$  decreases to a minimum at  $B_\phi=0.2\text{T}$  before gradually increasing towards higher inductions. Bottom: Similar behaviour can also be seen in  $\alpha$  for  $\text{BSCCO2}_{irr}$  ( $B_\phi=0.1\text{T}$ ) when one increases the field deep within the Mott Insulator regime (i.e. at approximately an applied field of 0.2T), although the dip is not as pronounced as in the  $\text{BSCCO1}_{irr}$  material. There is then a reduction in  $\alpha$  at very high fields.*

at approximately 750G to  $1.32 \pm (1.9 \times 10^{-2})$  mT and  $0.95 \pm (1.2 \times 10^{-2})$  mT for both the 65K and 72K data sets respectively. Indeed, a similar, though smaller effect, can be seen just above the irreversibility line at 75K where  $\langle \Delta B^2 \rangle^{1/2}$  reduces from  $0.76 \pm (1.0 \times 10^{-2})$  mT at 450G to  $0.74 \pm (9.2 \times 10^{-3})$  mT at 750G.

This effect appears to be in agreement with the macroscopic measurements detailed at the beginning of this section. With reference to Figure 5.3, it is clear, as mentioned previously, that vortex depinning from columnar defects occurs between approximately 40K and 50K. Above this temperature the vortices have sufficient kinetic energy to overcome the attractive pinning potential of the tracks and therefore have more mobility than they do at lower temperatures. However, at low inductions there are still a sufficient number of columnar tracks available to the vortices. As such, the FLL undergoes an entropically driven disorder where hopping from one pinning site to another can occur.

Indeed,  $\alpha$  also lends credence to this conclusion. As can be seen in Figures 5.18 and 5.17, at high temperatures there is a distinct decrease in the magnitude of  $\alpha$  at fields approaching  $B_\phi/2$ . Since  $\alpha$  is reduced in this region, it is clear that, combined with the reduction in  $\langle \Delta B^2 \rangle^{1/2}$ , partial hopping of the vortices from one track to another occurs, where part of a vortex is aligned on one defect track but coupled to part of the same vortex

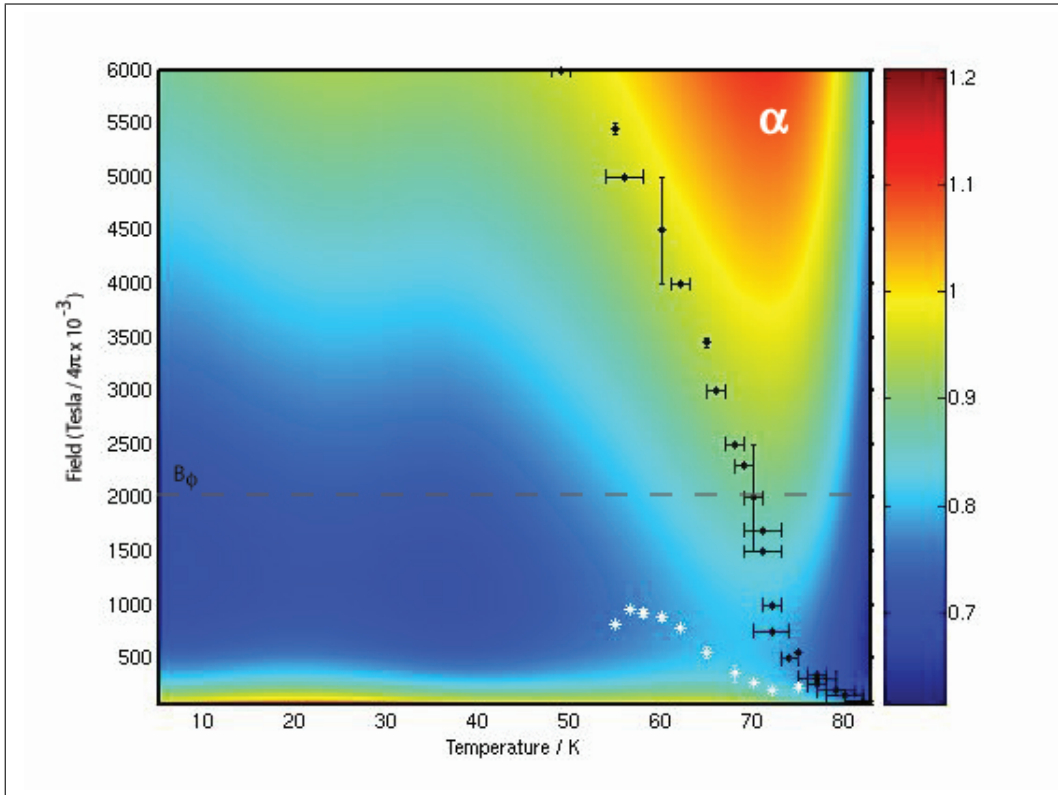


Figure 5.11: The 2D  $B$ - $T$  diagram reflecting the variation of the asymmetric skewness parameter  $\alpha$  across the full temperature scale in  $\text{BSCCO1}_{irr}$  ( $B_\phi = 0.2\text{T}$ ). The black and white points represent the macroscopic irreversibility line and  $B_{onset}$  respectively. One can see a stark difference when compared with that of the pristine material in Figure 4.8.

aligned on another track (as shown in the right hand plot of Figure 5.1). This in turn, would result in a decrease in the range of fields experienced by the muon as well as a reduction in the asymmetric skewness parameter, reflecting a more quasi-2D pancake structure for the FLL.

Further to this, as one approaches the Bose Glass to liquid transition in  $\text{BSCCO}_{1_{irr}}$ , there is notable agreement with  $B_{onset}$  obtained through macroscopic measurements (see the  $\alpha$  plot of Figure 5.11). As discussed in the previous chapter and by others (Divakar 2004) (Chikumoto 1998), in the pristine sample such a feature affiliated with the onset of the Vortex Glass regime. However, in the irradiated crystal we find an even more improved agreement between the micro- and macroscopic measurements where here  $B_{onset}$  signifies the onset of a move to an entropically disordered regime. This region is separated by two main disordered systems. Considering Figure 5.18, it is clear that two disordered areas exist above  $B_{onset}$  both below  $T < 65\text{K}$  and above  $T > 80\text{K}$  (each denoted by blue in the plot). The former disordered region is due to in-plane disorder, whereas the latter is due to decoupling of the FLL along the  $c$ -axis. Between these two areas exists the entropically disordered region where the two mechanisms coincide. Indeed, it is clear from macroscopic data that  $B_{onset}$  tends to approximately  $B_\phi/3$  - the field at which decoupling was observed by Sugano (1998).

Still within this high temperature region, it is clear that at high fields, whilst  $\langle \Delta B^2 \rangle^{1/2}$  decreases for  $\text{BSCCO}_{1_{irr}}$ ,  $\alpha$  increases as a function of temperature towards the irreversibility line and reaches a peak before decreasing just before  $T_c$  (see Figures 5.18 and 5.19). This

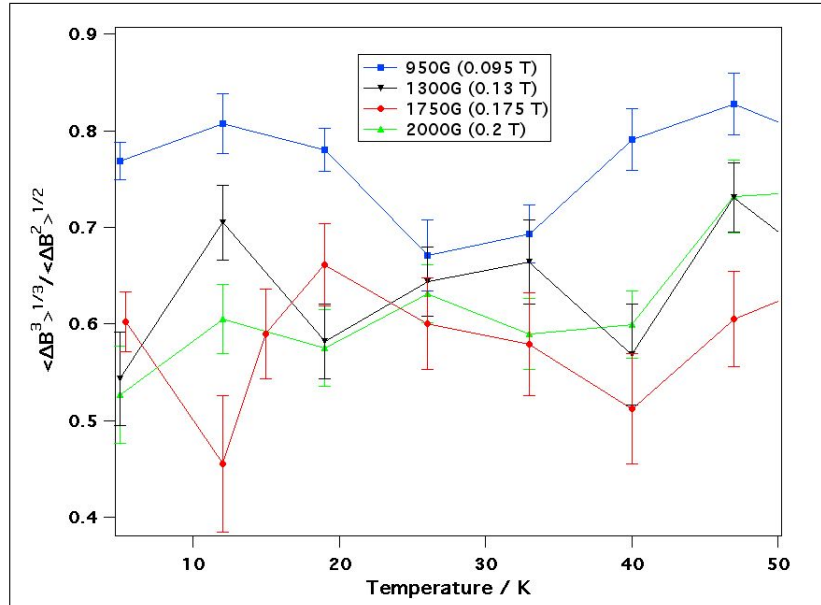


Figure 5.12:  $\text{BSCCO}_{irr}$ : A plot showing the variation of  $\alpha$  as a function of temperature for a range of fields about  $B_\phi=0.2\text{T}$ . Within this Mott Insulator phase (Nelson & Vinokur (1992)), the FLL is predominantly governed by correlated disorder (i.e. a relatively random array of the columnar defects dictates its arrangement). However, one can notice a small rise in  $\alpha$  for the 1300G, 1750G and 2000G scans at approximately 10-20K, highlighted more so in Figure 5.11.

happens for all applied fields and is extremely noticeable in its significant difference to the behaviour observed in the pristine sample. Indeed, at  $H_{app} = 2B_\phi$ , the effect is even greater with  $\alpha$  rising to  $1.08 \pm 0.035$  at 72K. This is, in fact, at a higher temperature than the macroscopic irreversibility point at this applied field. Even at 950G (less than  $B_\phi/2$ ) the value of  $\alpha$  reaches  $0.8 \pm 0.044$  at 78K before reducing substantially before  $T_c$ . Such a general increase in  $\alpha$  as a function of temperature at all fields has not been reported before and may possibly reflect a new ordering in the FLL or changes in the triplet correlation function  $C^3(q)$ . However, it is also important to consider  $\langle \Delta B^2 \rangle^{1/2}$  in this temperature range too. The variance, as stated in Chapter 4, is proportional to the two-body structure factor  $S(q)$  and such a reduction in this parameter would reflect an increase in the in-plane ordering of the vortices.

However, one must also consider that  $\langle \Delta B^2 \rangle^{1/2} \propto 1/\lambda^2$  in this region. As such, the increased  $P(B)$  linewidth can narrow considerably as one approaches  $T_c$  and consequently, it can be extremely difficult to separate out the contributions of both  $\lambda$  and  $S(q)$  to  $\langle \Delta B^2 \rangle^{1/2}$ . In order to assist with this problem though, the SANS technique can be used.

For the SANS measurements, the  $\text{BSCCO}_{1irr}$  sample is aligned such that the c-axis and columnar defects are parallel to the applied field and incoming neutron beam. In order to have a complete intensity pattern, a rocking curve as a function of  $\phi$  and  $\theta$  (see Figure 5.20) is performed for each measurement. The individual intensities  $I(q)$  from each angular position are then summed (using the GRASP analysis programme (Dewhurst 2007)) to obtain the

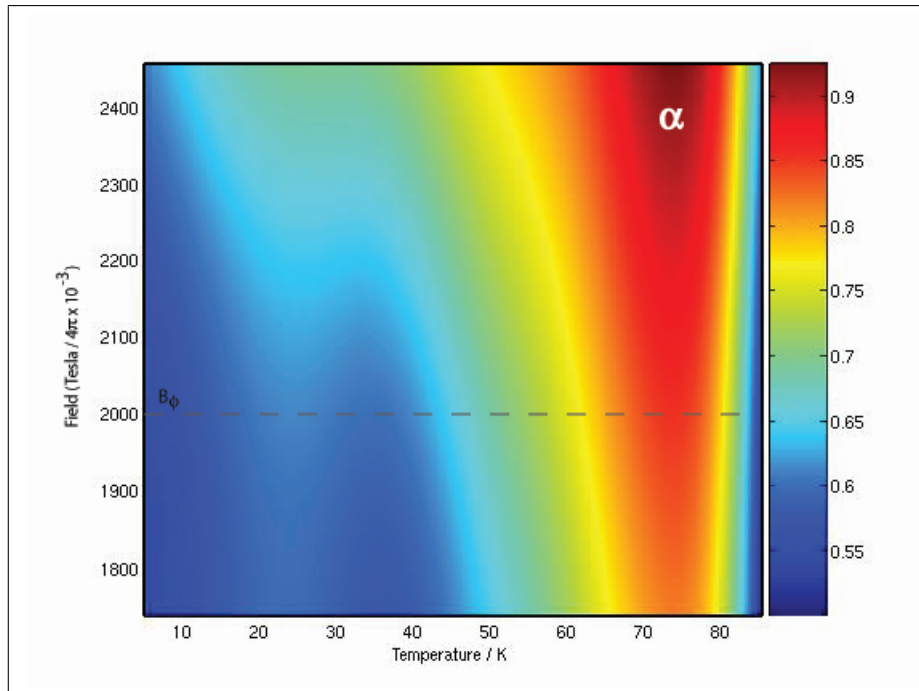


Figure 5.13:  $\text{BSCCO}_{1irr}$ : If one focuses on fields close to  $B_\phi=0.2T$  there appears to be a trend showing a very slight increase in  $\alpha$  between  $\sim 20\text{-}30\text{K}$  which is possibly a consequence of vortices depinning from point defects.

final diffracted intensity pattern (an example of which is shown in Figure 5.21). The resulting  $I(q)$  graph is a radial average sum of the intensity from  $q=0$  to the edge of the detector.

The behaviour of the FLL is investigated at applied fields of  $B_\phi$  and  $2B_\phi$  for 5K, 65K and 75K. These three different temperatures were taken because of the interesting physics that occurs within the regimes they represent: deep within the insulating state, close to the irreversibility line, and just above the irreversibility line. Other measurements at  $B_\phi/3$  were also proposed. However, due to the restraints of limited time on the SANS-I apparatus, only the following measurements were possible. Upon obtaining the total  $I(q)$  data for each measurement, a least squares fit was applied using the Percus-Yevick model (Ashcroft & Lekner 1966) that has been applied to diffraction patterns arising from the FLL in pristine HTSCs (an example of which is shown in Figure 5.22).

The Percus-Yevick model approximation is used to help solve the Ornstein-Zernike Equation; the latter being an integral equation that defines the direct correlation function. Such an approximation (and hence the Percus-Yevick equation) is used to describe the correlations within hard sphere systems and can be used to obtain to the radial distribution function (described in Chapter 3).

Considering first the  $S(q)$  arising at 5K for  $B_\phi$  (see Figure 5.23), one can see a relatively good agreement with the standard Percus-Yevick model. With a  $\chi^2$  value of 3.20 the peak of the fit also coincides well with that of the expected mean field value obtained from  $\mu\text{SR}$  measurements (0.192T). Indeed, the second peak occurring at twice the inter-vortex distance also agrees well with the Percus-Yevick model. However, it is noticeable that at low

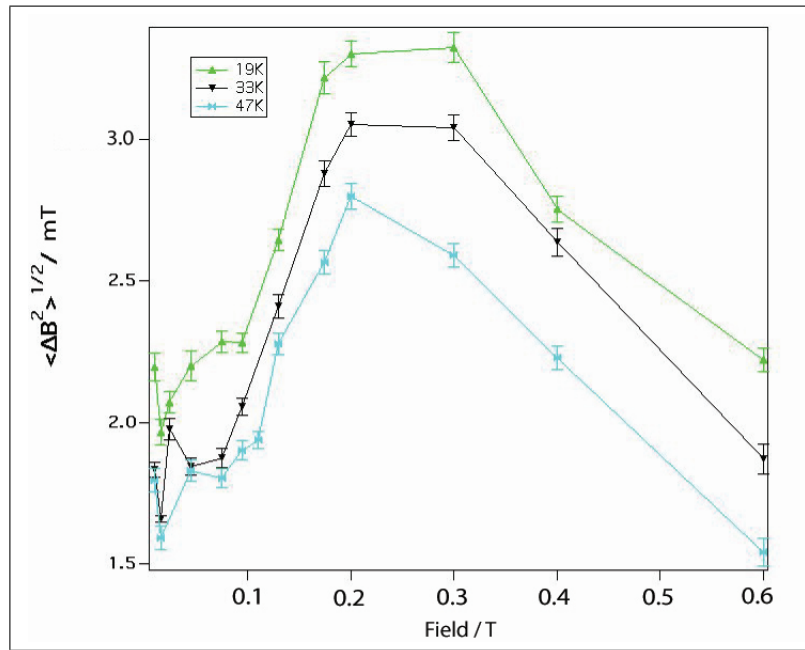


Figure 5.14: At temperatures well below the irreversibility line in  $\text{BSCCO}_{1irr}$ , there is an increase in the  $P(B)$  linewidth as a function of applied field up to  $B_\phi = 0.2\text{T}$  where, for example,  $\langle \Delta B^2 \rangle^{1/2} = 3.24\text{mT}$  at 19K. As one increases the field thereafter,  $\langle \Delta B^2 \rangle^{1/2}$  reduces in magnitude.

$q$ , just below the first peak, the data appears to be slightly broader than the fit suggests.

The resulting diffracted intensity:

$$I(q) = A_0 S(q) F^2(q) \quad (5.2)$$

is fitted to the data where the form factor  $F(q)$  is described by:

$$F(q) = \frac{1}{1 + q^2 \lambda^2} \quad (5.3)$$

and  $A_0$  and  $\lambda$  are the scaling parameter and penetration depth respectively. Figure 5.22 shows the reduction of intensity as a function of increasing  $q$  at 5K for an induction of 2000G.

Such behaviour points to the fact that at long-length scales (in real space) the FLL distortion provided by the columnar defects affects the long-range order that a normal pristine material may have as shown by the Percus-Yevick model. It is also interesting to note that when one fits the exponent 'n' of the form factor (i.e. the  $1/q^n$  component of Equation 5.3) to the data set, the exponent is 4.4 - close to the value of 4, generally accepted as being applicable to pristine HTSC materials.

As one increases the temperature to 65K, it is clear that the shape of the structure factor  $S(q)$  in Figure 5.24 changes. The most notable feature is the apparent broadening in the first peak of the data. As well as at low  $q$ , just below the first structure factor peak, the data above the expected mean field  $q$  value also serves to broaden the first  $S(q)$  peak.

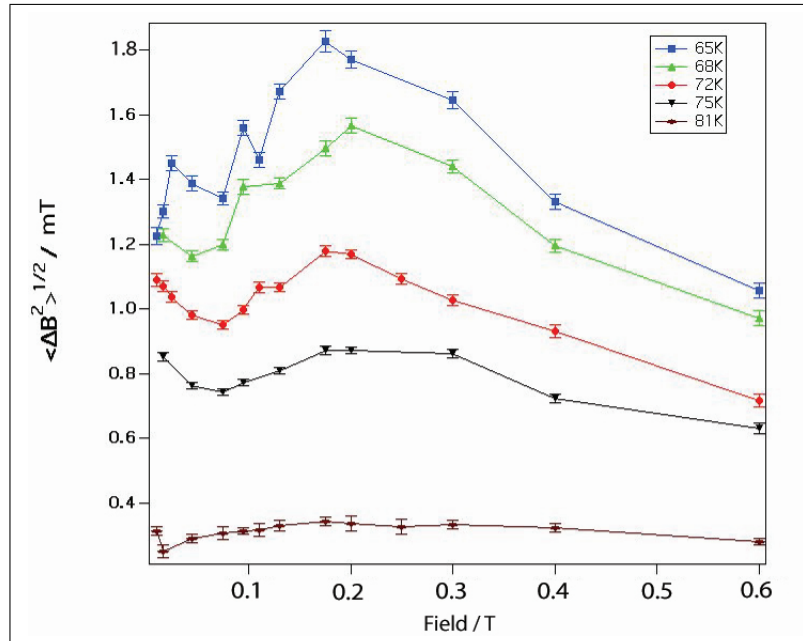


Figure 5.15: As one increases the applied field at temperatures above the irreversibility line, a subtle decrease in  $\langle \Delta B^2 \rangle^{1/2}$  occurs for inductions  $< 0.075T$  before increasing to a peak close to  $B_\phi = 2000G$  in  $\text{BSCCO1}_{irr}$ . Thereafter,  $\langle \Delta B^2 \rangle^{1/2}$  begins to reduce.

However, it is clear that one might easily expect that at higher temperatures, close to the irreversibility line, the vortices have a more enhanced thermal agitation than at 5K and thus, the scattered intensity will be subsequently reduced. This would be reflected in the larger error bars occurring for this data set. In addition, more statistics in these higher temperature regimes would also reduce the associated errors. Despite this however, the increased width of the first peak and subsequent improved fitting demonstrates that the Percus-Yevick model is more appropriate here than at 5K (where there is a much stronger correlated disorder). Even though the fitting of the exponent in the magnetic form factor  $F_m(q)$  is 4.9, the good qualitative fit is corroborated by  $\chi^2$  which has a value of 0.84.

Traversing the irreversibility line to 75K (see Figure 5.11), one can observe the reduction in the peaks of the structure factor  $S(q)$  (shown in Figure 5.25) due to the thermal excitation of the vortices, most of which are now free from the columnar defect pinning potentials. Interestingly though, the fitted exponent for the form factor  $F_m(q)$  decay has now jumped to 5.2 whilst  $\chi^2$  has reduced to 0.63. There has been some debate about whether the reduction in intensity is of  $1/q^4$  or  $1/q^5$  form for a FLL in most HTSCs (Ogrin 2000) (Don McK. 1993) as well as the other data sets at lower temperatures. The exponent for the form factor here appears to be closer to the former description for the decrease in intensity. However, it is difficult to draw any substantial conclusions about the data at 75K.

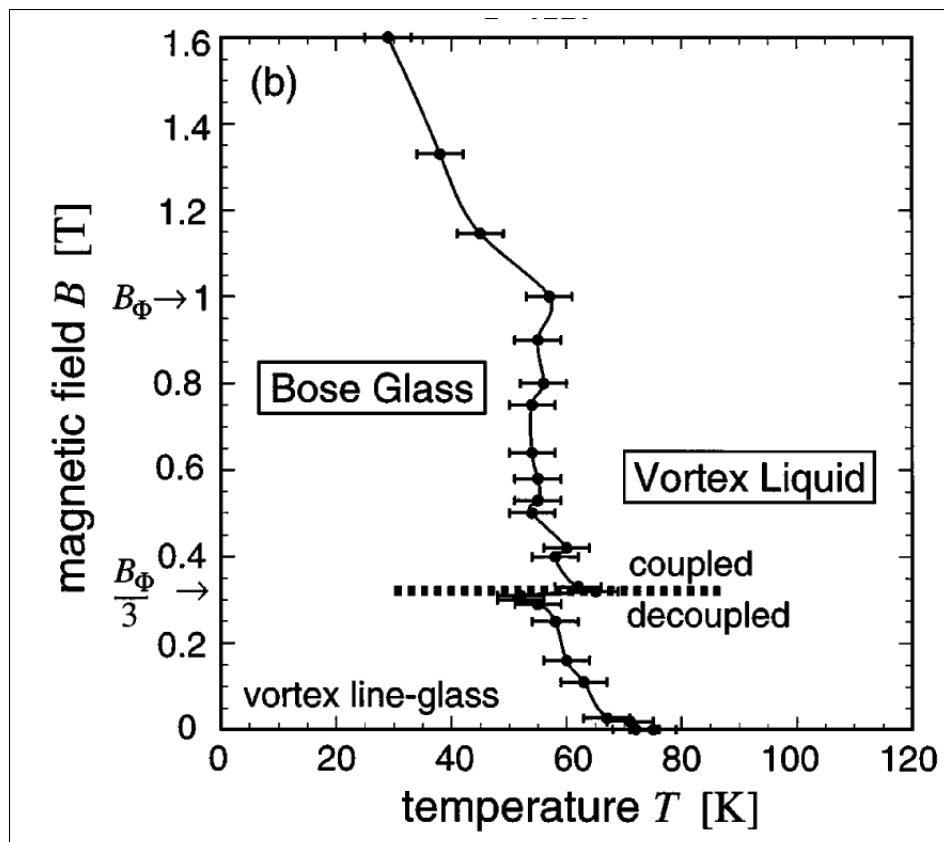


Figure 5.16: *Sugano et al. (1998)* showed a decoupling transition occurring between the Bose Glass and Vortex Glass states at  $B_\phi/3$  using the Josephson plasma resonance technique.

At such elevated temperatures, scattering is expected to be low and thus, more statistics are required in order to reduce the size of the errorbars and enhance the shape of the structure factor peaks. It is clear, however, that the lack of definitive  $S(q)$  peaks in the data are in agreement with the  $\mu\text{SR}$  contour plot of Figure 5.8 which shows that the square root of the second moment  $\langle \Delta B^2 \rangle^{1/2}$  of the  $P(B)$  lineshape decreases in this region too. Although the effect of the Debye-Waller factor  $\exp(-\mathbf{q}\langle u^2 \rangle)$  may have some influence in this regime and more counting statistics are needed, it is clear that, combined with the asymmetric skewness parameter  $\alpha$ , one can state that despite the effect of  $\lambda$  increasing significantly in this region, there is a definite change in the three-body correlations of the FLL due to an increase in the thermal freedom of the vortices.

If one now increases the applied field such that now  $H_{app}=2B_\phi$ , it is clear that at 5K there is a shift in the first  $S(q)$  peak in both the data and the fit (see Figure 5.26). This agrees well with the mean field calculation at this point ( $q = 0.0093\text{\AA}^{-1}$ ) and has a  $\chi^2$  value of 2.7. Interestingly though, unlike at  $B_\phi$ , the fit appears to match the data well

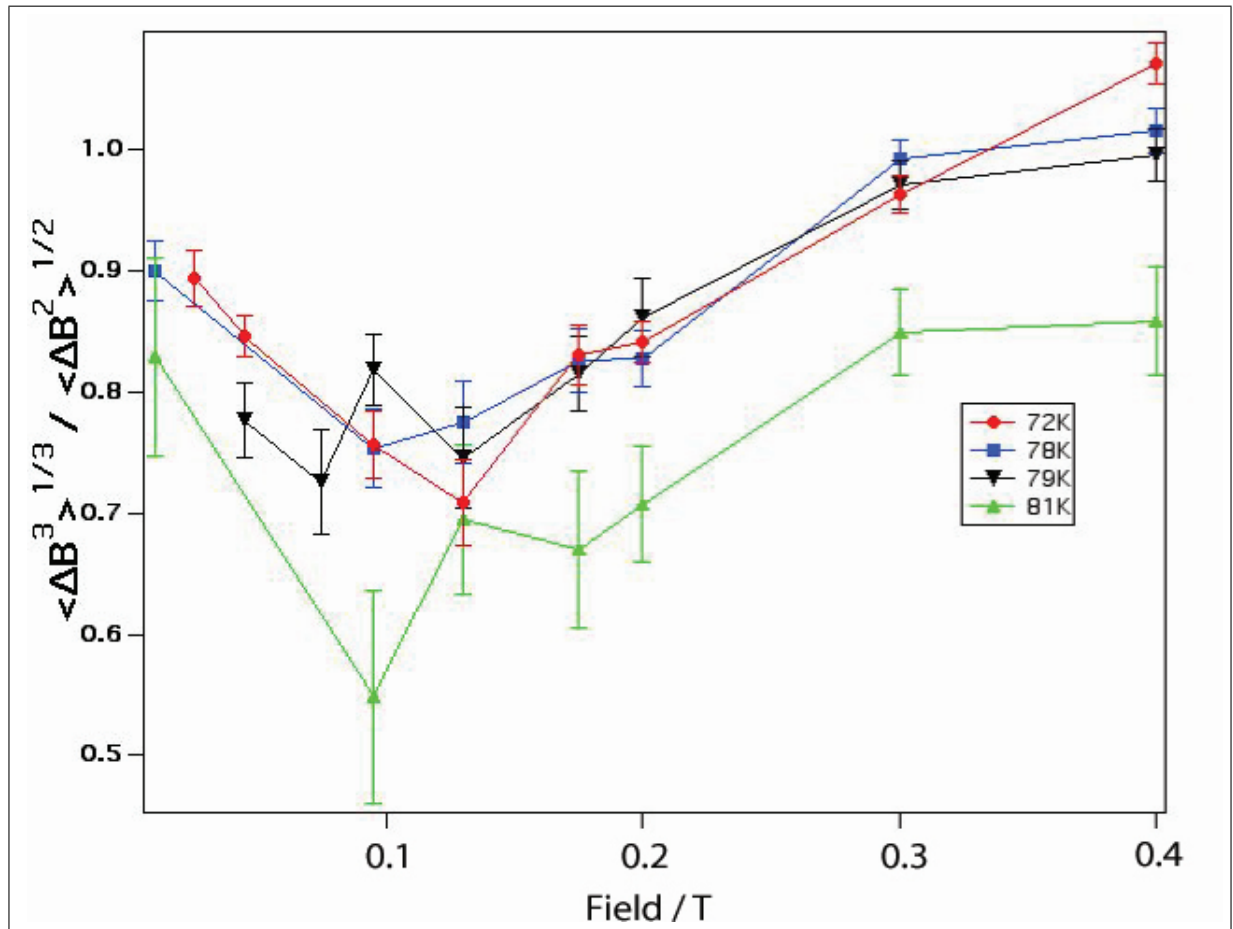


Figure 5.17: As one increases the field for  $\text{BSCCO1}_{irr}$  at temperatures approaching  $T_c$  there is a noticeable “trough” in the asymmetric skewness parameter around  $0.1T$  ( $B_\phi/2$ ). Thereafter,  $\alpha$  increases towards the value determined for the ideal FLL  $\alpha \sim 1.25$  (Menon et al. (1999)).

for low  $q$  (until  $q=0.005\text{\AA}^{-1}$ ), just below the first peak. This indicates that at longer length scales within real-space, the increase in the number of vortices means that some reside at interstitial sites within the columnar defect arrangement. This in turn, would change the arrangement of the FLL from the trivial disordered orientation as dictated by the columnar defects to that beginning to resemble a lattice in the pristine material, in agreement with the Percus-Yevick model. This is further corroborated by the exponent of 4.4. Indeed, one can see that in the  $\mu\text{SR}$  data of Figure 5.11, an asymmetric skewness of approximately 0.9 indicates a lattice that is well ordered along the vortex length. However, the corresponding  $\langle\Delta B^2\rangle^{1/2}$  plot in Figure 5.8 shows a large linewidth in this regime compared with that of the pristine material (see Chapter 4). This conversely shows that there is still a large amount of 2D in-plane disorder at 5K.

As one increases the temperature to 65K at  $2B_\phi$  (see Figure 5.27), the lattice becomes subject to increased thermal stimulation, as one expects. The first  $S(q)$  peak in the data agrees with that of the fit ( $\chi^2 = 0.90$ ) but also continues to corroborate reasonably well as one increases  $q$  to  $0.02\text{\AA}^{-1}$  again. Although the error bars are large at higher  $q$  and it is clear that more statistics are required before drawing a full conclusion, one can see that by binning in this region, the peaks and the troughs within the data coincide well with those of the fit. The fitted exponent of the form factor  $F_m(q)$  is 4.7 and differs from that at  $B_\phi$ . Moreover, the moving away of this factor from the generally accepted exponent of  $\sim 4$

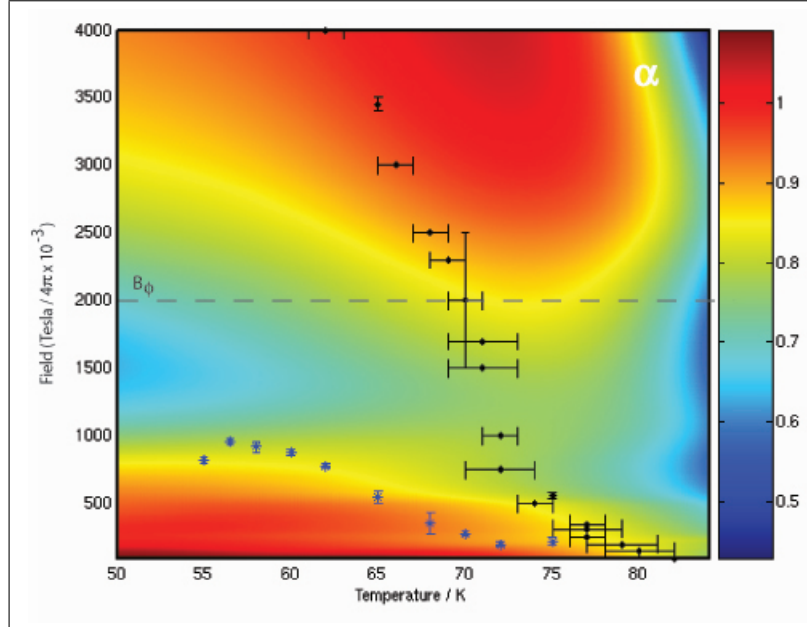


Figure 5.18:  $BSCCO1_{irr}$ : Although  $\alpha$  also signals the melting transition from the low field Bose Glass to the liquid regime, it does not follow  $\langle\Delta B^2\rangle^{1/2}$  as closely as it does in the pristine crystal. Here, as one increases the applied field at temperatures  $\sim 70\text{K}$ , the FLL undergoes entropically driven disorder (shown by the reduction in  $\alpha$  at approximately  $B_\phi/3$ ). The black points denote the irreversibility line whilst the blue data represents the macroscopic change  $B_{onset}$ .

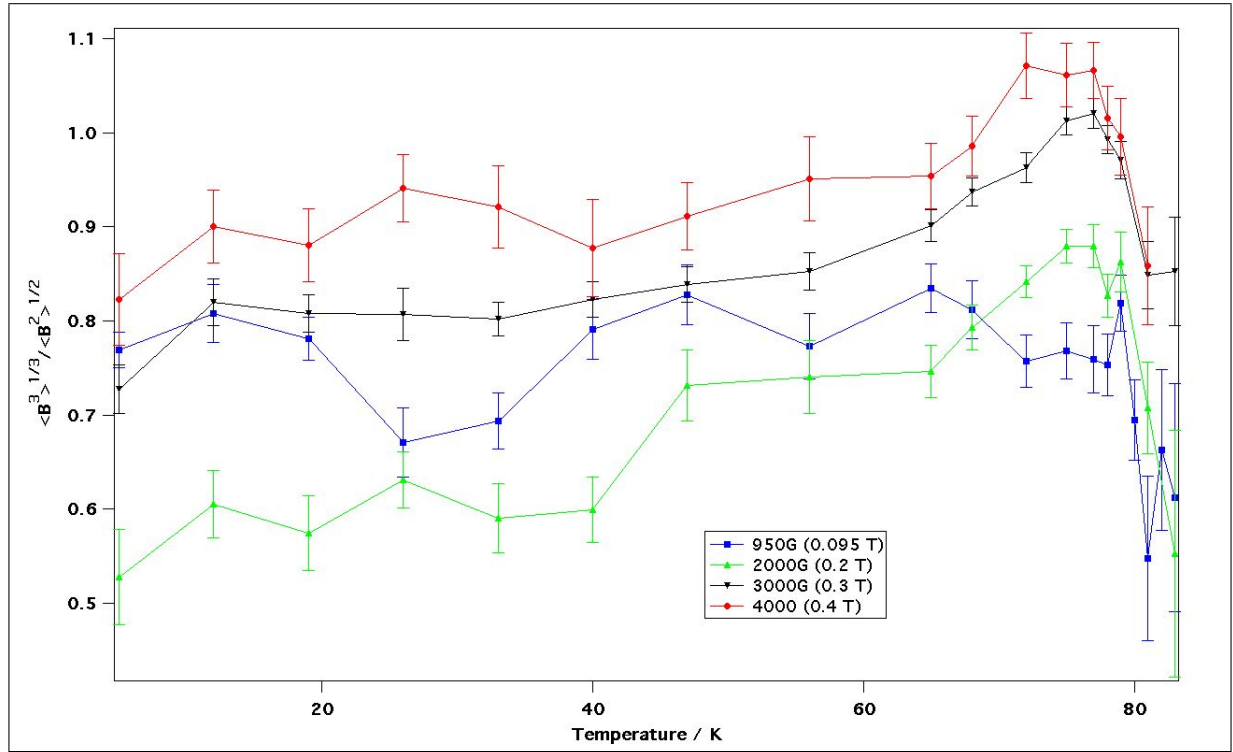


Figure 5.19: The increase in  $\alpha$  for  $\text{BSCCO1}_{irr}$  when  $B > B_\phi$  can be seen as one increases the temperature towards  $T_c$ . Such behaviour is even more striking as it occurs above the macroscopic irreversibility line.

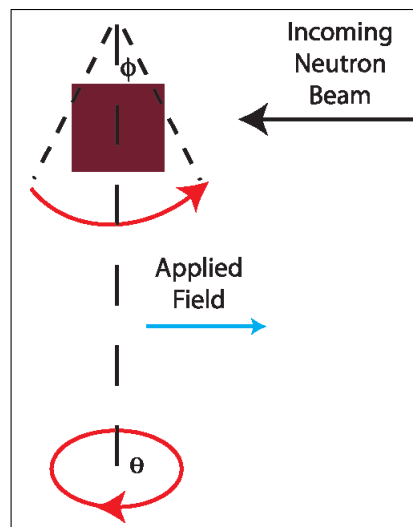


Figure 5.20: In order to obtain a full intensity pattern from a FLL, the sample (brown) is rocked through a range of angles (shown in red) in the  $\phi$  and  $\theta$  directions. The direction of the applied field is shown in blue.

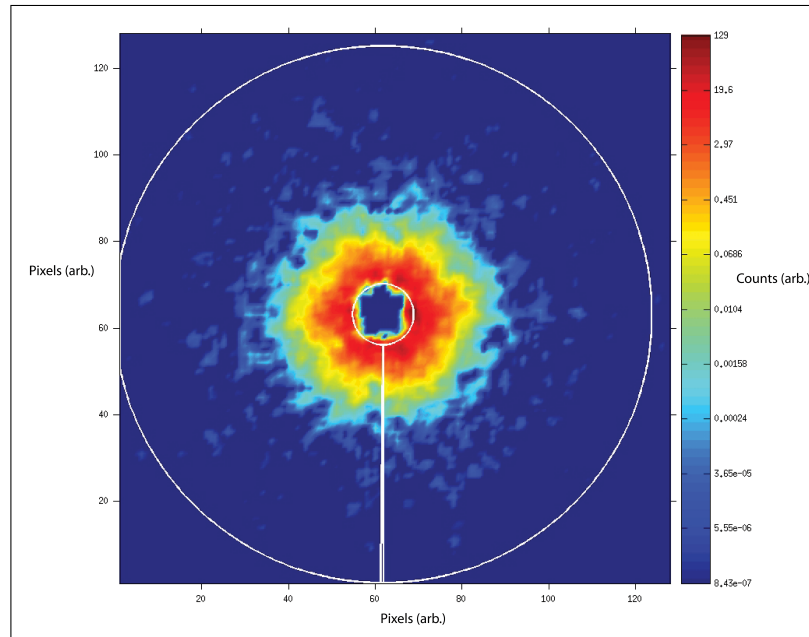


Figure 5.21: A complete diffracted intensity pattern (in  $q$ -space) can be obtained by summing the individual intensities obtained through various rocking positions.

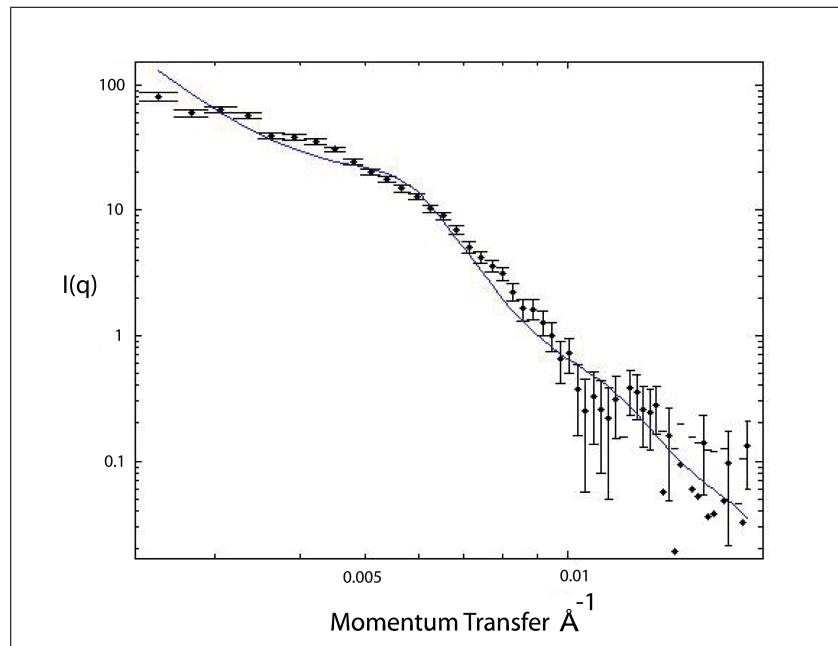


Figure 5.22: The diffracted intensity resulting from the FLL has been shown to fall off as approximately  $1/q^4$ . The black data points represent that at 5K with an induction of 2000G. The blue line represents a least squares fit to the data using a Percus-Yevick model.

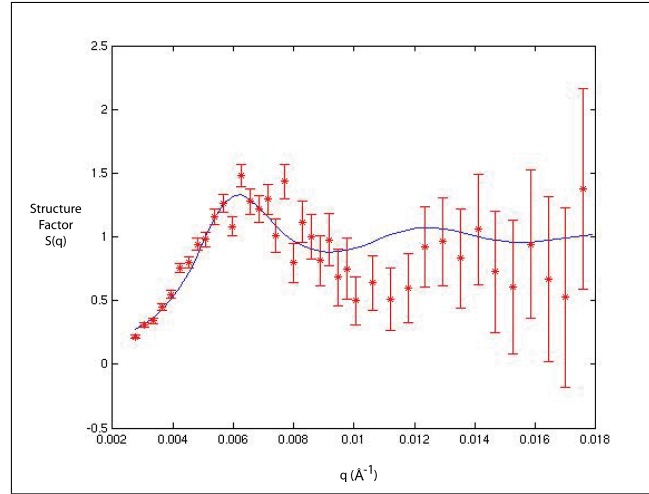


Figure 5.23:  $BSCCO1_{irr}$ : Extracting the  $S(q)$  at 5K, it is clear that the Percus-Yevick model (blue line) fits in agreement with the data (red points) at the matching field  $B_\phi = 0.2T$  ( $\chi^2 = 3.20$ ). Above  $q = 0.01\text{\AA}^{-1}$ , the data has been binned by a factor of 2.

for  $F_m(q)$  indicates that this is perhaps a novel region. Indeed, it is clear that if one also refers to the  $\mu\text{SR}$  data in this region, the increase in  $\alpha$  to values that have commonly been accepted as being those pertaining to an ideal FLL in the pristine material, suggests that a new orientational order may be taking shape.

Increasing to 75K at the same applied field, one can see that the features of the

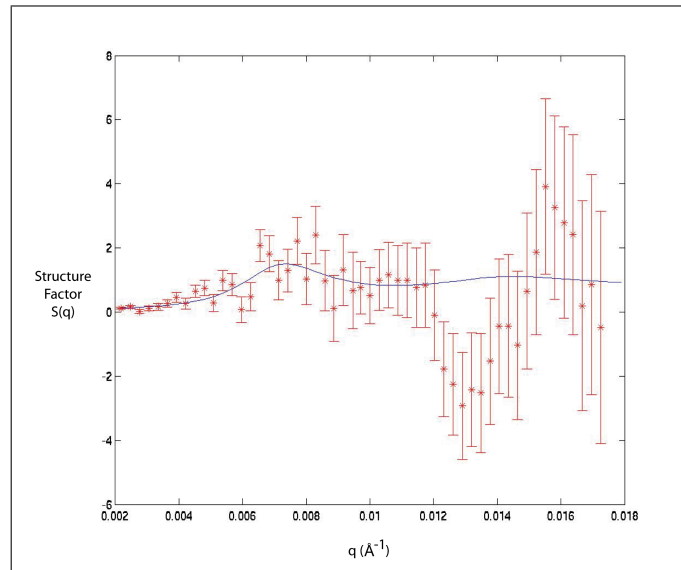


Figure 5.24:  $BSCCO1_{irr}$ : For  $H_{app} = B_\phi$  at 65K, the first structure factor peak is still prominent and combined with the  $\mu\text{SR}$  data reflects the fact that with no significant change in  $S(q)$ , the vortices must still be retaining its 3D structure. Here,  $\chi^2 = 0.84$ .

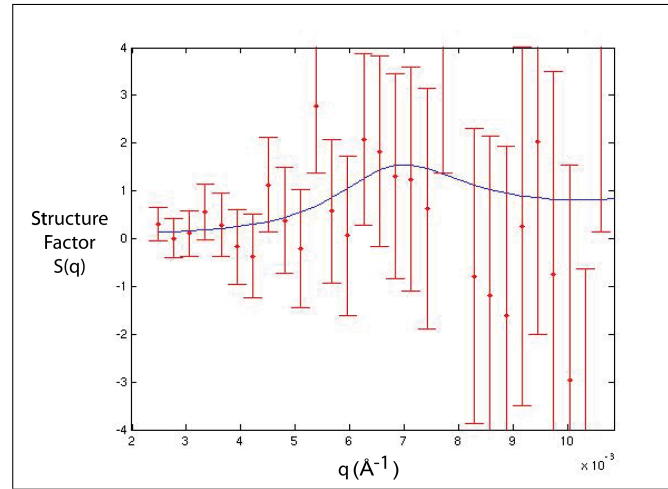


Figure 5.25:  $BSCCO1_{irr}$ : For  $H_{app}=B_\phi$  at  $75K$ , the ability of the model to fit the data is slightly reduced as expected and in agreement with the reduction in the second moment of the  $\mu\text{SR}$   $P(B)$  lineshape. However, it is also clear that it still fits within the error bars. In addition to this,  $\chi^2$  has reduced to 0.63.

structure factor  $S(q)$  in Figure 5.28 become increasingly noisy. Indeed, despite having a  $\chi^2$  value of 1.1, the least squares fit using a Percus-Yevick model has difficulty in obtaining a fit to the data. Such a lack of structural 2-body information is in agreement with the  $\mu\text{SR}$  data that strongly suggests a decrease in the FLL 2D in-plane order. However, in this irradiated material, it appears as though despite being deep within what has conventionally

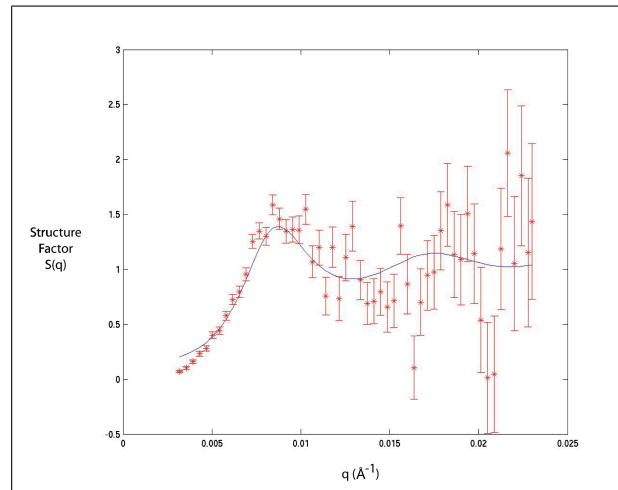


Figure 5.26: For  $H_{app}=2B_\phi$  at  $5K$ , the first structure factor peak in the data again agrees with that expected with the fit with  $\chi^2=2.7$ . As well as this, the exponent for the fit does not change from that when  $H_{app}=B_\phi$  at  $5K$  (4.4) and fits the data well below the first peak (until  $q=0.005\text{\AA}^{-1}$ ).

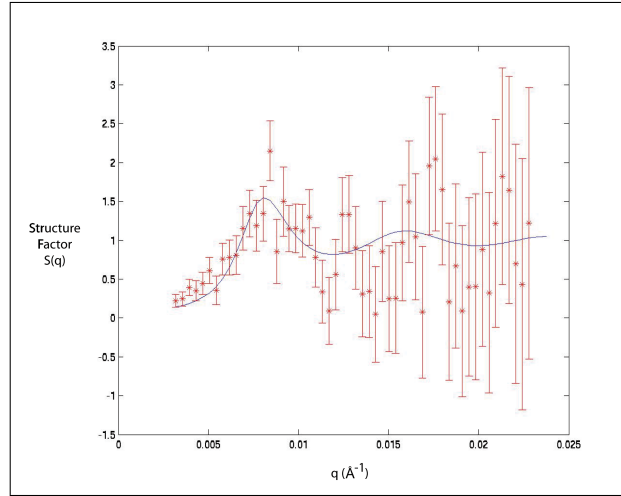


Figure 5.27: For  $H_{app}=2B_\phi$  at 65K, the first structure factor peak remains at approximately the same amplitude as that at 5K (1.5). As well as this, the exponent for the fit does not change significantly either at 4.7 while  $\chi^2=0.9$ .

been understood as a liquid phase, the vortices still maintain their 3D structure.

Overall it is clear from these SANS measurements that above the irreversibility line (in the data sets taken at 75K), although both the  $S(q)$  peaks and  $\langle \Delta B^2 \rangle^{1/2}$  in the  $\mu\text{SR}$   $P(B)$  reduce as expected through thermal excitation, the fact that the asymmetric skewness  $\alpha$  increases to a value greater than 1, indicates that three-body correlations are significantly changing in this region. These correlations are due to the increase in thermal energy of the FLL with the strong influence of the attractive pinning potential provided by the columnar defects.

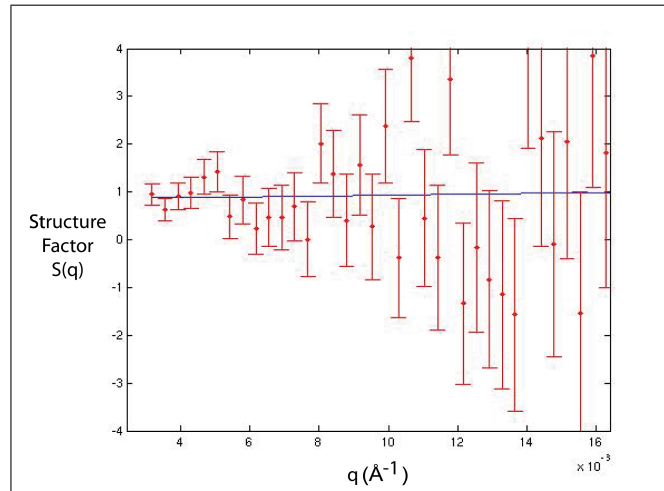


Figure 5.28: At 75K ( $H_{app}=2B_\phi$ ), the structure factor peaks become increasingly noisy as one moves beyond the irreversibility line, approaching  $T_c$  ( $\chi^2=1.1$ ).

One final point that is of significance is that, at the lowest measured temperature, the maximum disorder does not occur at the matching field  $B_\phi$  in the  $\langle \Delta B^2 \rangle^{1/2}$  contour plot of Figure 5.8. Correspondingly however,  $\alpha$  *does* demonstrate a minimum at 5K for  $H_{app}=B_\phi$ . Upon closer inspection, there is little difference between the  $\langle \Delta B^2 \rangle^{1/2}$  values at both  $B_\phi$  and  $2B_\phi$  at 5K although the discrepancy between the two values could be explained by the fact that just above the matching field the in-plane disorder caused by the columnar defects could be increased slightly further by the introduction of only a few more vortices into the material. As such, one might expect the disorder to increase slightly more before reducing as one approaches  $2B_\phi$ . This feature occurs in the low temperature region where mobility of the FLL is minimal, thus allowing a greater degree of in-plane disorder.

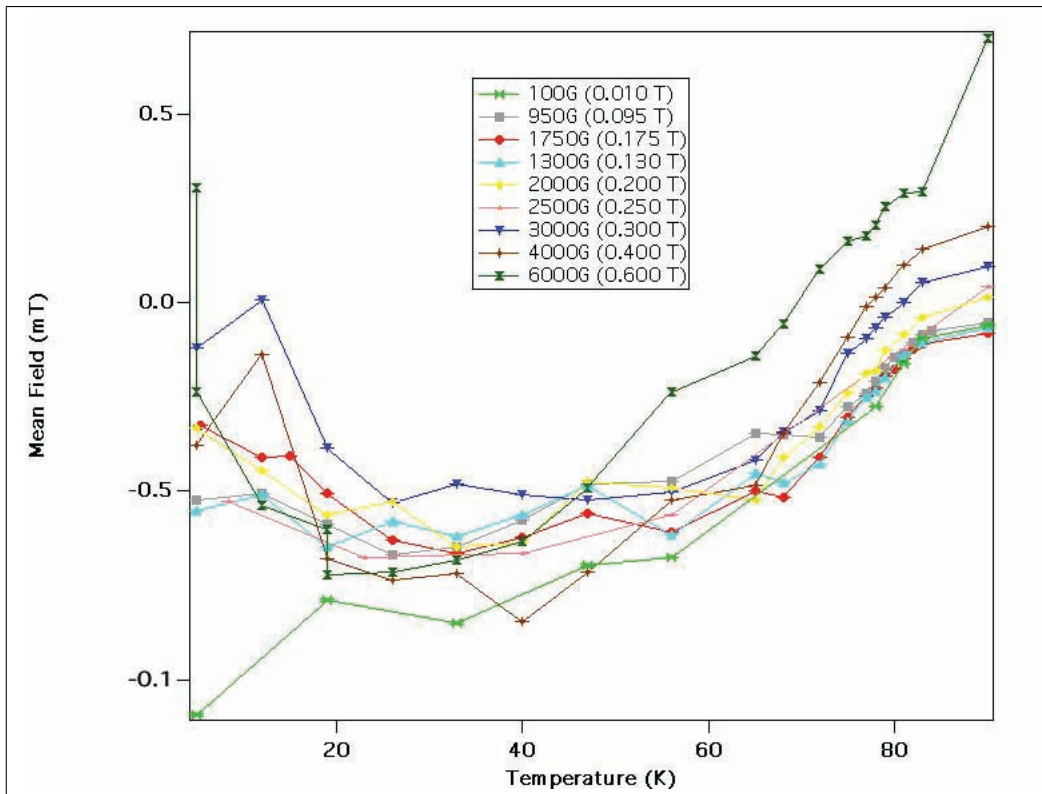


Figure 5.29: It is clear that as one decreases the temperature from  $T_c$  for a wide range of fields, the mean field (obtained from  $\mu\text{SR}$ ) reaches a minimum. Decreasing the temperature further results in an upturn in the mean field. Such an effect is also evident in the pristine material.

Further to the work investigating the variation of  $\alpha$  and  $\langle \Delta B^2 \rangle^{1/2}$ , an up-turn in the mean field has been observed for certain inductions. Figure 5.29 shows the variation in the mean field as a function of temperature obtained from  $\mu\text{SR}$  measurements. For fields greater than  $\sim 1500\text{G}$ , the increase in the mean field  $\langle B \rangle$  is evident as one decreases the temperature below  $\sim 30\text{K}$ . In addition to this, it appears that the magnitude of the upturn in  $\langle B \rangle$  increases as one increases the applied field. At  $6000\text{G}$  for example (labelled dark green in Figure 5.29), the mean field increases by  $1.4 \times 10^{-3} \text{ T}$  between  $19\text{K}$  and  $5\text{K}$ .

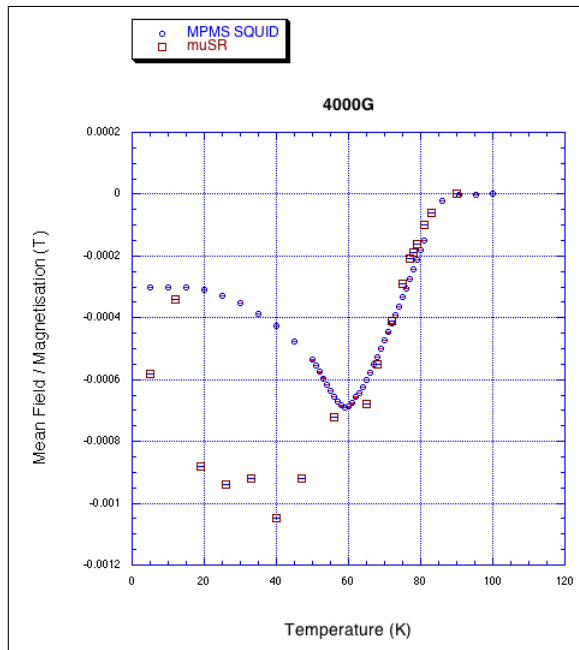


Figure 5.30: At an applied field of  $0.4\text{T}$ , both the  $\mu\text{SR}$  and MPMS SQUID data demonstrate an upturn in the mean field as a function of decreasing temperature. Both peak at  $12\text{K}$  and  $14\text{K}$  respectively and are very comparable in value ( $-0.00034\text{ T}$  as measured by  $\mu\text{SR}$  and  $-0.0003\text{ T}$  as measured by the MPMS SQUID). The  $\mu\text{SR}$  and MPMS data points are denoted by the red squares and blue circles respectively. However, it is currently unclear why there is dissonance between the  $\mu\text{SR}$  data and the SQUID data at temperatures below the dip in the magnetisation data.

Whereas at  $2000\text{G}$  (labelled yellow in Figure 5.29) the increase is only  $0.3 \times 10^{-3}\text{ T}$ .

One can then compare these mean field scans to the macroscopic magnetisation measurements obtained from the MPMS SQUID (see Figures 5.30, 5.31 and 5.32). In these latter plots, the mean field for the  $\mu\text{SR}$  data has been normalised by subtracting the values obtained within the superconducting state from that at  $T_c$ . The magnetisation data has been converted from emu into Tesla /  $\text{cm}^3$  (i.e.  $\mu_0\text{M}$ ) and then rescaled. At inductions above  $1500\text{G}$ , it is clear that as one reduces the temperature below  $T_c$  the mean field from the  $\mu\text{SR}$  data and the magnetisation from the MPMS SQUID both decrease as expected. However, the  $\mu\text{SR}$  data reaches a significantly lower minimum than that obtained from the macroscopic measurement. At  $0.4\text{T}$ , the minimum in the mean field is  $1.05 \pm 0.04\text{ mT}$  at  $40\text{K}$ , whereas in the corresponding magnetisation data it is  $-0.37 \pm 0.01\text{ mT}$  at  $60\text{K}$ . Likewise, at an applied field of  $0.3\text{T}$ , the mean field reaches a minimum of  $-0.61 \pm 0.05\text{ mT}$  (within the errorbars) at  $47\text{K}$ , but the magnetisation is only  $-0.33 \pm 0.01\text{mT}$  at  $65\text{K}$ .

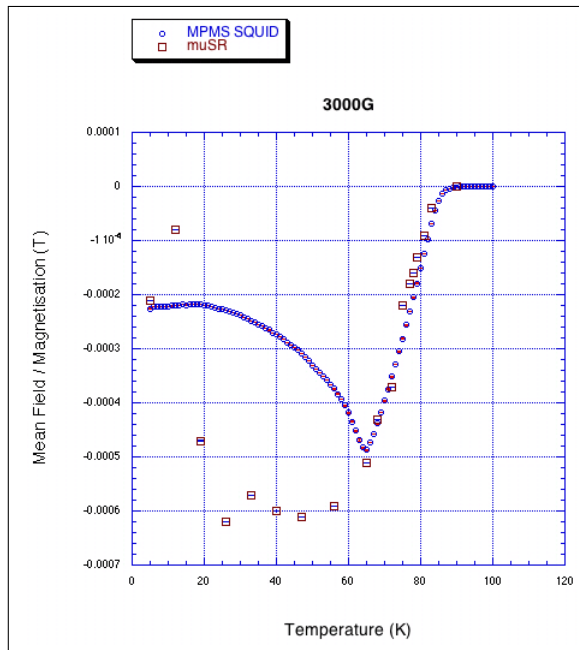


Figure 5.31: At an applied field of  $0.3\text{T}$ , both the  $\mu\text{SR}$  and MPMS SQUID data demonstrate an upturn in the mean field as a function of decreasing temperature. Both peak at  $12\text{K}$  and  $16\text{K}$  respectively and are very comparable in value ( $-0.00008\text{ T}$  as measured by  $\mu\text{SR}$  and  $-0.00022\text{ T}$  as measured by the MPMS SQUID). The  $\mu\text{SR}$  and MPMS data points are denoted by the red squares and blue circles respectively. However, it is currently unclear why there is dissonance between the  $\mu\text{SR}$  data and the SQUID data at temperatures below the dip in the magnetisation data.

In addition to this, both data sets (from magnetisation and  $\mu\text{SR}$ ) demonstrate an upturn. At  $0.4\text{T}$ , the  $\mu\text{SR}$  mean field attains a maximum of  $-0.34 \pm 0.06\text{mT}$  at  $12\text{K}$ , and the corresponding magnetisation reaches  $-0.16 \pm 0.01\text{ mT}$  at  $14\text{K}$ . For an induction of  $0.3\text{T}$ , the  $\mu\text{SR}$  mean field and macroscopic magnetisation reached  $-0.08 \pm 0.08\text{ mT}$  at  $12\text{K}$  and  $-0.15 \pm 0.02\text{ mT}$  at  $16\text{K}$  respectively.

Moreover, at fields less than  $\sim 1500\text{G}$ , the change in  $\langle B \rangle$  in the  $\mu\text{SR}$  data is signified only by a small discontinuity in the temperature scan. Figure 5.32 shows the comparison between the  $\mu\text{SR}$  and MPMS data at an applied field of  $1300\text{G}$ . In this plot, the discontinuity or maximum in the  $\mu\text{SR}$  mean field can be seen at  $\sim 12\text{K}$ . However, this discontinuity still occurs at the approximately the same temperature as the up-turns at higher fields do.

Such a similar effect has been seen in the  $(\text{Pb,Bi})_2(\text{SrLa})_2\text{CuO}_{6+\delta}$  system whilst using  $\mu\text{SR}$  (Khasanov 2008). Further to this it appears as though, despite the discontinuity observed at fields below  $\sim 900\text{G}$ , the more significant changes in the mean field (i.e. the up-turns in  $\langle B \rangle$ ) occur as one makes the transition from the Bose Glass to the Mott Insulator state around  $B_\phi$ .

However, when one considers the 2D mean field plot of Figure 5.33, it is clear that the macroscopic measurements display subtle agreement with the  $\mu\text{SR}$  data. Indeed, on the right hand side of the plot, the irreversibility line follows the contour line denoting the beginning of

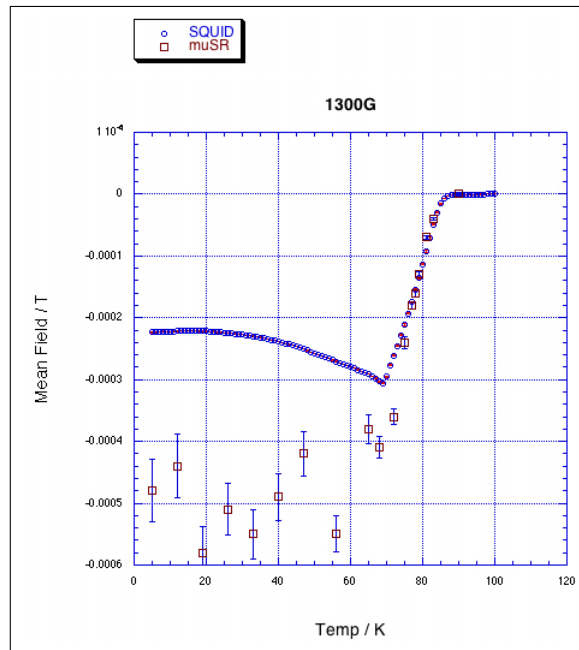


Figure 5.32: *Despite the upturn effect being seen at higher inductions, at fields below approximately 1500G, the upturn begins to diminish. Here, at an applied field of 0.13T, the possible upturn in the  $\mu\text{SR}$  data occurs as a possible small discontinuity at 12K. However, the upturn is evident in the MPMS SQUID data and occurs at 14K. The  $\mu\text{SR}$  and MPMS data points are denoted by the red squares and blue circles respectively. However, it is currently unclear why there is dissonance between the  $\mu\text{SR}$  data and the SQUID data at temperatures below the dip in the magnetisation data.*

the increase in the mean field towards  $T_c$ . However, the  $dM/dT$  peaks (highlighted in black on the left hand side of the plot) demonstrate only a small congruence with the peak in the up-turn of the higher field values. As discussed previously, the  $dM/dT$  data points can be explained as the point at which there is the greatest vortex dynamics and thus the greatest change in the magnetisation as a function of temperature. This macroscopic phenomenon lends itself well to the aforementioned description that at the point when the vortices are most mobile the mean field reduces as a function of increasing temperature.

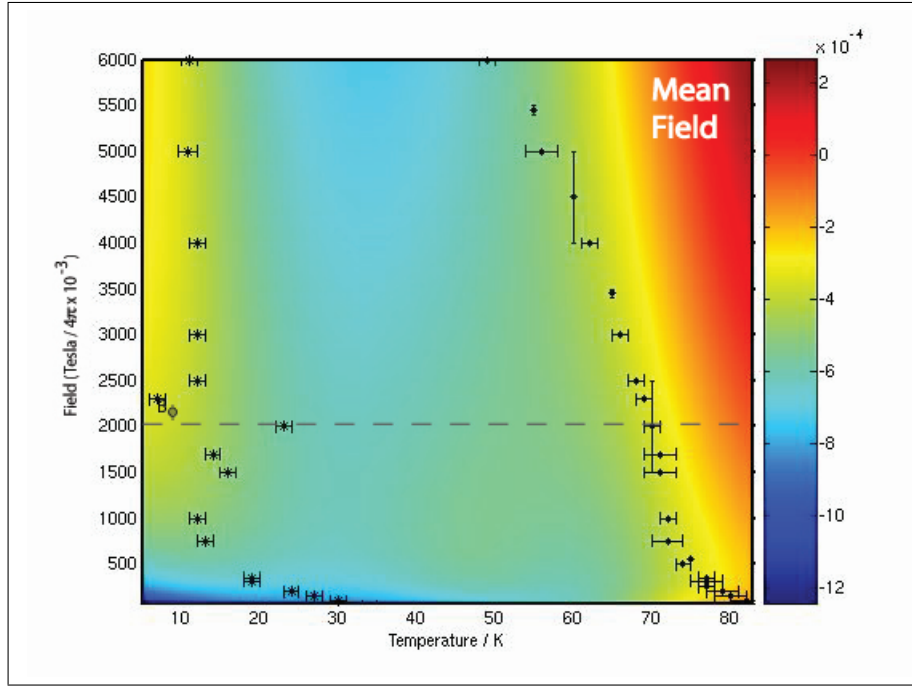


Figure 5.33: A 2D contour plot of the mean field shows the expected increase in  $\langle B \rangle$  as  $T$  approaches  $T_c$  as well as the small increase as a function of decreasing temperature for  $T < 20\text{K}$ . There also appears to be good agreement with the peak of this up-turn and the peak in the  $dM/dT$  macroscopic magnetisation data (highlighted in black on the left hand side). (The black data points to the right hand side of the plot represent the irreversibility line.)

Overall, the 2D B-T phase diagrams for the irradiated samples are somewhat different to those of the corresponding pristine samples. As already noted by other authors, the transition to the liquid regime is elevated to higher temperatures and the size of the Bose Glass is dependent upon the value of  $B_\phi$ . Interestingly though, it appears as though the transition from the Bose Glass to the liquid state is a second order phase transition. In the unirradiated sample, the crossover from Bragg Glass to a liquid is closely mapped onto the irreversibility line, strongly suggesting that such melting is of first order. However, here the transition appears to be more complicated. Upon increasing the applied field in the high temperature regime, one moves out of the Bose Glass state into a region disordered by entropy. Just below and above this temperature region exists in-plane and c-axis disorder respectively. The entropically driven disorder region represents the region where these two disorder mechanisms coincide.

It should also be noted that there is no region of negative  $\alpha$  in the irradiated  $\text{Bi}_{2.15}\text{Sr}_{1.85}\text{CaCu}_2\text{O}_{8+\delta}$  crystals - not even close to  $T_c$ . This may reflect the strong dominance that the columnar defects have over the entire B-T diagram. However, that is not to say that 3-body correlations do not exist, rather that there is not the sufficient balance between in-plane disorder and three-body correlations to facilitate a negative  $\alpha$  in this material.

Numerical modelling would help to understand further the suggested entropically driven disorder at high temperatures, just above the Bose Glass regime. Also, a closer ex-

amination of the behaviour within the Mott insulator state (in particular at temperatures around 30-50K) might improve the understanding of whether a small enhancement of the c-axis coherence was actually occurring in this region. In conclusion, it is clear from the  $\mu\text{SR}$  measurements and the 65K SANS measurements that 3D vortices exist at higher temperatures (unlike in the pristine sample). Moreover, it appears as though c-axis vortex coherence is significantly enhanced at higher temperatures (particularly at those applied fields above  $B_\phi$ ).

## Chapter 6

# Measurements on the layered material: Nb(20Å) / Py(200Å) / Nb(500Å) / Py(500Å) / Si

### 6.1 Overview of Previous LEM $\mu$ SR Work

There has been much interest in the interplay between the competing mechanisms of magnetism and superconductivity. Magnetic systems have a tendency to polarise electron spins in a certain direction, whereas superconductivity as explained by BCS theory, prefers the formation of a spin-singlet state. These phenomena are normally found to be mutually exclusive. However, instances have been discovered where both exist simultaneously. In such novel materials, different theoretical ideas have been proposed. Indeed, it is thought that the mechanism behind superconductivity in  $\text{Sr}_2\text{RuO}_4$  is a p-wave, triplet state, where the spins of the electrons are aligned parallel to one another, thus eliminating the effect of “pair-breaking” (Maeno 2004). This would result in a non-zero angular momentum for the pair, which are due to quantum constraints. In the s-wave superconductors (“spin singlet” state), the exchange field acts to break up the anti-parallel alignment of the spins in the Cooper pair, thus suppressing the superconducting order parameter. The kinetic energy of the pair subsequently increases significantly and results in the electrons possessing an energy exceeding that of the superconducting gap.

Aside from superconducting materials, much work has been conducted on multilayers consisting of normal metal and ferromagnetic (FM) slices sandwiched together. In these systems it has been predicted and observed from the magnetic impurities in the FM layer, that the exchange field can cause an oscillation of the electron spin density in the normal metal (Bruno & Chappert 1991). Such an oscillation is periodic and is determined by the extremal spanning vectors of the Fermi surface, via an increased response of the wavevector susceptibility at these values (Martin 1967). This is similar to that observed in the RKKY interaction (Ruderman & Kittel 1954) (Kasuya 1956*a*) (Kasuya 1956*b*) (Yosida 1957).

Another explanation for such phenomena has been used to describe possible coexistence in an Fe/Ag/Fe trilayer (Luetkens 2003). In this particular case, a quantum-well (QW) model ((Bruno 1999) (Stiles 1999) (Edwards 1991)) has been suggested as the reason behind

this phenomenon. However, the authors have also noted that this does not adequately explain the observed spatial variation in the electron spin density.

Systems that comprise SC/FM multilayers have also been investigated for some time (De Gennes 1966) and it has been shown by Wong (1986) that as the thickness of the FM layer increases, the superconducting transition temperature  $T_c$  decreases monotonically (Strunk 1994) (Jiang 1995) (Ogrin 2000).

Another explanation for this coexistence behaviour is described by the FFLO mechanism (Larkin & Ovchinnikov 1964) (Fulde & Ferrell 1964). In such a system, the spin singlet state persists but the electrons within the Cooper pair both have different kinetic energies. This results in a spatially oscillating superconducting wavefunction, the sign of which reverses periodically. It is clear that there is dissonance between this exotic behaviour and that from both the classical s- and p-wave systems and one should expect different explanations for different materials.

However, Khusainov and Proshin have refined the FFLO explanation to take into account the proximity effect (Khusainov & Proshin 1997), (Khusainov & Proshin 2000). Here, the Cooper pairs obtain a finite amount of momentum by tunnelling into the FM region resulting in a superconducting wavefunction that has a higher ground state energy than that acquired in the conventional BCS system. Consequently, a spin density wave (SDW) occurs in the FM region due to the oscillating exchange field being compensated by a periodic superconducting wavefunction. Such behaviour leads to an oscillatory, non-monotonic  $T_c$  that is dependent upon the thickness of the FM layer.

At this point, it is important to note a caveat. Such behaviour, as detailed above, has assumed an ideal scenario in which the boundaries between each component in the tri- and multilayer systems are smooth and clean. In reality however, such samples are difficult to grow. The exact details of the technical difficulties associated with growing thin films are not within the scope of this thesis. However, it is important to note that several groups have investigated if not the same, very similar, systems but have obtained different results. The oscillatory behaviour of  $T_c$  has been observed in V/Fe multilayers by Wong et al. (Wong 1986) but not by Koorevaar et al. (Koorevaar 1994). The non-monotonic behaviour has been observed in a range of multilayer and trilayer systems by some groups (Jiang 1995) (Jiang 1996) (Mühge 1996) (Mühge 1997) (Obi 1999) but not by others (Strunk 1994) (Mühge 1998) (Verbanck 1998). These discrepancies and contradictory reports bring to the fore a need for high quality samples in order for the experimental data and theoretical predictions to corroborate and, ultimately, to help fully understand the physics associated with these systems.

Recently, Drew et al. investigated a Fe/Pb/Fe trilayer system with reduced solubility between the layers (Drew 2005*b*). This implies that there is very little inter-diffusion across the boundary separating both the SC and FM regions. In addition to this, it was found that a SDW is induced in the normal state of the Pb layer by the exchange field originating from the FM region. Moreover, the SDW persisted into the superconducting state where one component of the phase had noticeably shifted. In particular, one wavevector making up the SDW (of a large spatial periodicity) is close to the ‘natural’ peak in the spin susceptibility of the superconductor as suggested by work done elsewhere (Anderson & Suhl 1959). Though not conclusive as yet, such a property may go some way in helping to determine the origin of this coexistence.

While an increasing amount of work is being conducted on such multilayer systems, several issues concerning the exact behaviour of how magnetism and superconductivity co-exist have clearly yet to be fully resolved. In order to do so, a number of areas need further exploration including: itinerant compared with local FM moment layers, type I vs type II for the SC layer(s), the differences between strong and weak moments in the FM layers, and the overall structural-influence differences between single, bi-, tri- and multilayer systems. In order to answer the questions associated with such topics, a long term plan of investigation is required.

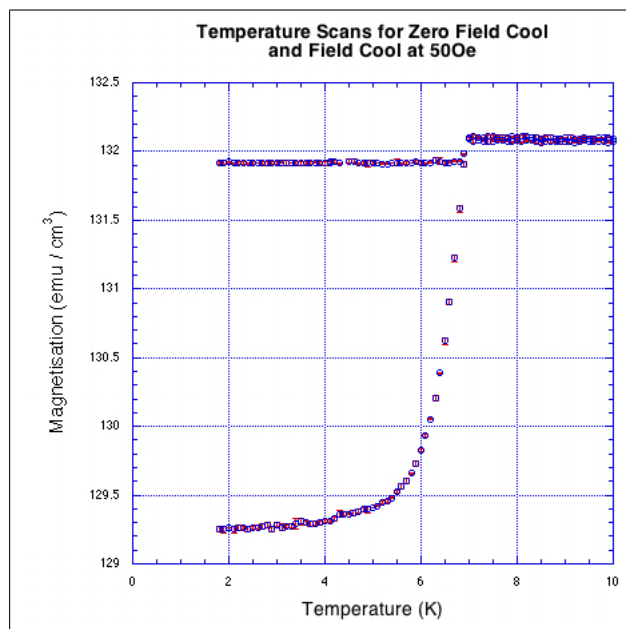


Figure 6.1: *SQUID magnetometry measurements are performed on the Py/Nb/Py material with a sequence comprising field cool FC and zero field cool ZFC temperature scans from which  $T_c$  is shown to be  $\sim 7K$ .*

This chapter discusses results obtained on another FM/SC/FM trilayer to see if the behaviour shown by Drew (2005b) can be seen in another similar system. These materials are analogous to normal metal spin-valve structures comprising FM/N/FM layers<sup>1</sup> in which the FM slices can be arranged either parallel or anti-parallel to one another via changes in the applied magnetic field. In a normal spin-valve the external magnetic field controls the resistivity of the sample. This is because in terms of the two-current spin model, the sample resistance is determined by the spin channel of lowest resistance. In the FM/N/FM structures, the layers which are aligned anti-parallel correspond to the high resistance states. However, typically, this situation is reversed in FM/SC/FM devices, since the parallel exchange fields lead to a greater suppression of the superconducting order parameter. This situation has been observed experimentally for weak FM layers with low spin polarisation

<sup>1</sup>N denotes a normal metal

(Potenza & Marrows 2005), and in this limit it is reasonably well understood from a theoretical perspective. However, these phenomena have been less explored in systems with a somewhat higher spin polarisation (approximately 45%)(Rusanov 2004) and with greater exchange fields, the results of which are now presented and discussed in the next section of this chapter.

## 6.2 Sample Preparation

The multilayer structure under investigation comprised the following constituents (starting with the bottom layer): Si(substrate)/Py(50nm)/Nb(50nm)/Py(20nm)/Nb(2nm)<sup>2</sup> where Py is a permalloy comprising 80% Ni and 20% Fe and chosen because it exhibits a strong exchange field and requires little applied field to align the electron spins  $\sim 400\text{G}$ . The top Nb layer (of thickness 2nm) acts as a capping layer to help prevent against oxidation of the sample.

ZFC and FC measurements are conducted on the material at a small induction of 50G and show that  $T_c \sim 7\text{K}$  (see Figure 6.1).

## 6.3 Discussion of PNR results

Prior to the discussion of the low energy muon measurements on the Si(substrate)/Py(50nm)/Nb(50nm)/Py(20nm)/Nb(2nm) material, it is sensible to conduct a characterisation using polarised neutron reflectivity. Performed on the CRISP instrument at ISIS (since the wavelength of the reflected neutrons is comparable to the layer thicknesses), the sample is mounted on the same aluminium plate as that used for the LEM measurements (whose properties, specific to the LEM experiment, are discussed in the next section).

The incoming neutrons are polarised such that they arrive at the sample (of dimensions (10mm x 10mm)  $\pm 0.2\text{nm}$ ) either parallel to the aligned itinerant electron moments or antiparallel (denoted as spin “up” or spin “down”) (See Figure 6.2). As such, this allows for the extraction of the combined nuclear and magnetic components of the scattering. Measurements are taken at 10K and 3.8K - above and below  $T_c$  - and at an applied field of 100G. The data is fitted using an algorithm comprising a least squares fit with the optical matrix method (the latter of which is discussed in more detail elsewhere (Blundell & Bland 1992)).

The two tables in Figure 6.3 show the parameters that have been fitted for the high and low temperature data sets respectively. The first column describes which parameters have been fitted. The first four rows represent the thicknesses for each material, starting with the top layer and in units of Angstroms.

The fifth and sixth row denote the density of both the Py layers and the sandwiched Nb layer. The values have been divided by each layer volume and are in units of  $10^{28}\text{m}^{-3}$ . In addition to this, the fitting has been simplified further by assuming that the number densities in each of the Py and Nb layers respectively is the same.

The flux density in each of the Py layers is also fitted (again, assuming that they both have the same values) whilst that of the Nb layer is fixed at zero both above and below

<sup>2</sup>Note that this will now be referred to as Py/Nb/Py.

the superconducting transition temperature. Analysis was also conducted in which the Nb layer was also fixed at  $-0.01\text{T}$  in the superconducting state. However, there is no substantial difference to that in which the Nb field is fixed at zero. Freeing these parameters during fitting, however, results in large negative fields for the Nb layer (i.e. of the order of  $-0.8\text{T}$ ) and the overall  $\chi^2$  fitting is significantly reduced.

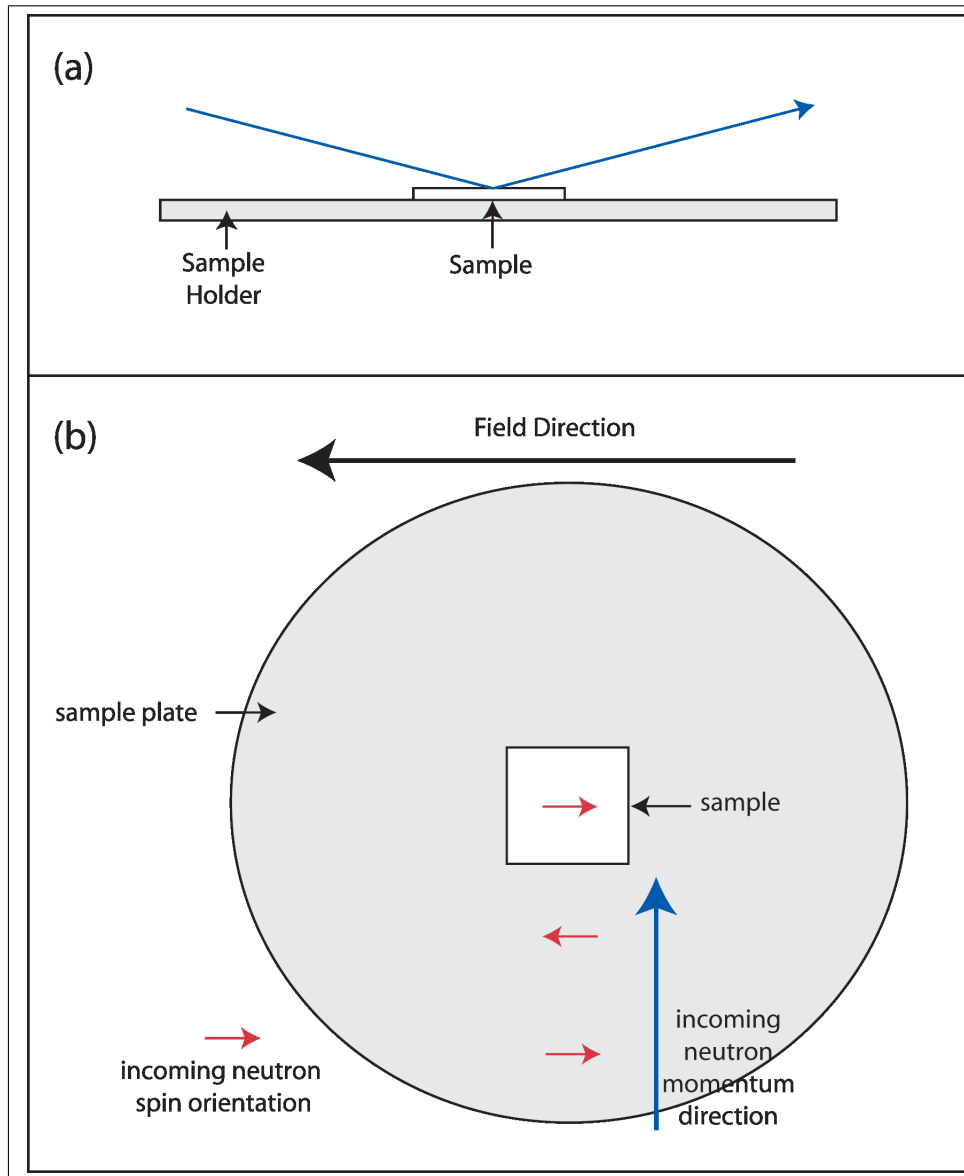


Figure 6.2: (a). A side-on view of the PNR setup. The incoming neutrons (whose momentum direction is denoted by the blue arrow) are reflected off the sample piece which is placed on top of the sample holder. The reflected neutrons are then registered by a detector. (b) A schematic cartoon demonstrating the orientation of the incoming neutron spins (up or down) relative to the sample surface and applied magnetic field direction.

In the final row, a scaling factor has also been fitted to each data set.

High Temperature			
Description	Initial	Final	Error
Nb layer (Å)	20	17.9	2.34
Py " (Å)	200	205.7	0.76
Nb " (Å)	500	479.4	0.22
Py " (Å)	500	485.0	0.39
Py Density	8.9	8.8	8.00E-05
Nb "	5.55	4.9	1.00E-04
Py Field	1.1	1.0	8.00E-06
Scaling	0.01	0.0	6.00E-10

Low Temperature			
Description	Initial	Final	Error
Nb layer (Å)	20	16.1	2.34
Py " (Å)	200	205.4	0.76
Nb " (Å)	500	476.7	0.22
Py " (Å)	500	490.7	0.39
Py Density	8.9	8.7	8.00E-05
Nb "	5.55	4.6	1.00E-04
Py Field	1.1	1.1	8.00E-06
Scaling	0.01	0.0	3.00E-07

Figure 6.3: The up and down spin data was fitted using a least squares fit combined with an optical matrix algorithm. The top table (a) shows the fit results obtained at 10K (above  $T_c$ ) and the bottom table (b) shows those obtained at 3.8K (below  $T_c$ ). Each table shows (first column) which parameter is fitted, (second column) the initial value, (third column) the obtained, fitted value, and (fourth column) the associated error.

Several parameters however have been fixed including a roughness parameter of approximately 10% for each layer, experimental resolution and scattering lengths - the latter of which is related to the number density. Through careful analysis it has been shown that “freeing” these parameters does not significantly enhance the overall fitting of the data.

The second and third columns show the initial nominal values and final fitted values for the respective parameters. As can be seen from the tables, there is close agreement between both the initial and final figures for each.

The errors are recorded in the fourth column.

Figures 6.4 and 6.5 show the corresponding data taken above and below  $T_c$  respectively. Considering the 10K data first, it is clear that the data is represented well by the fit for both up and down spin until approximately  $q=0.06\text{\AA}^{-1}$ . The critical edge for both agrees well with the fit - the up spin maintaining complete reflectivity until  $q=0.023\text{\AA}^{-1}$  compared with the down spin data which undergoes transmission into the sample at  $q=0.017\text{\AA}^{-1}$ . This is due to whether the neutron encounters a potential barrier or potential well, depending on its spin alignment defined earlier.

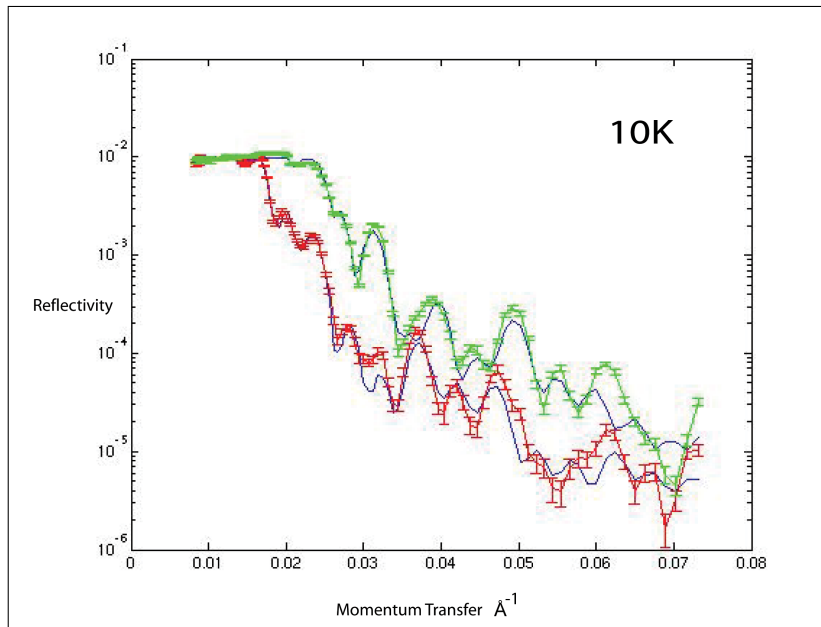


Figure 6.4: A reflectivity graph of Polarised Neutron Scattering data showing a combined fit to both the up (green) and down (red) data at 10K (above  $T_c$ ). The respective fits to each particular data set are shown in blue. There is good agreement with both the up and down data until  $\sim q=0.055\text{\AA}^{-1}$ .

For the high temperature data, the thickness of each layer as calculated by the fit agrees well with the nominal values. The magnetic flux density in each layer is also in good agreement with that predicted. For the first and second Py layers, the field has been calculated at  $1.03 \pm 0.0084\text{mT}$  with a fixed value of zero for the Nb layer. Such agreement can also be seen qualitatively too for both the up and down spin data when one observes the congruency between the small peaks in the data (assumed to be attributed to the magnetic flux density) and the corresponding maxima in the fits. Indeed,  $\chi^2 = 14.7$  and although a difference occurs for the data at higher  $q$  values (i.e. those  $> 0.06\text{\AA}^{-1}$ ), the data is well represented by the fit at low  $q$  and agrees well with the nominal structural and magnetic values of the sample.

Further to the normal state measurements, there is only a subtle change in the data as one decreases the temperature to within the superconducting state at 3.8K.  $\chi^2$  is very similar at 14.9 and again, the calculated thicknesses of each layer remain extremely similar to those obtained in the high temperature measurements. The field in the middle of the Nb layer however is more difficult to analyse. In this specific case, the flux density in the FM layers have been fitted but that within the SC layer has been fixed at zero. Thorough analysis has shown that freeing this parameter results in spurious results of extremely high negative field. As such, fixing this parameter to zero improves the fit substantially, resulting in the plot of Figure 6.5.

In order to observe subtle changes in the reflectivity data it is possible to plot the

associated asymmetries defined as:

$$Asymmetry = \frac{R_{up} - R_{down}}{R_{up} + R_{down}} \quad (6.1)$$

where  $R_{up/down}$  refers to the reflectivity of the different neutron spin states.

Considering, the asymmetry differences between the up and down spin data at 10K and 3.8K data, one noticeable feature is that although there appears to be very little difference between each asymmetry set (see top plot of Figure 6.6), the low temperature data does exhibit a small shift to higher  $q$  values. Further to this, the corresponding fits (see bottom plot of Figure 6.6) also show this change.

In addition, the plots showing subtle differences between the high and low temperatures for both up and down neutron spin states have also been plotted in Figure 6.7. Since there is no significant difference in the fitting routine when one uses either  $-0.01T$  or zero field for the flux density of the Nb layer in the superconducting state, such small shifts in both the up and down spin states, combined with the subtle shift in the asymmetries at high and low temperatures (Figure 6.6), appear to be the consequence of a systematic change in the experimental setup between the high and low temperature scans. However, despite this, the plots of Figures 6.4 and 6.5 both above and below  $T_c$  respectively are evidence that the reflectivity data comprising both the structural and magnetic information can be very well described by the model.

There is a high possibility that this could be due to the very strong influence of the FM fields masking the effect of the flux expulsion from the Nb layer. As such, performing

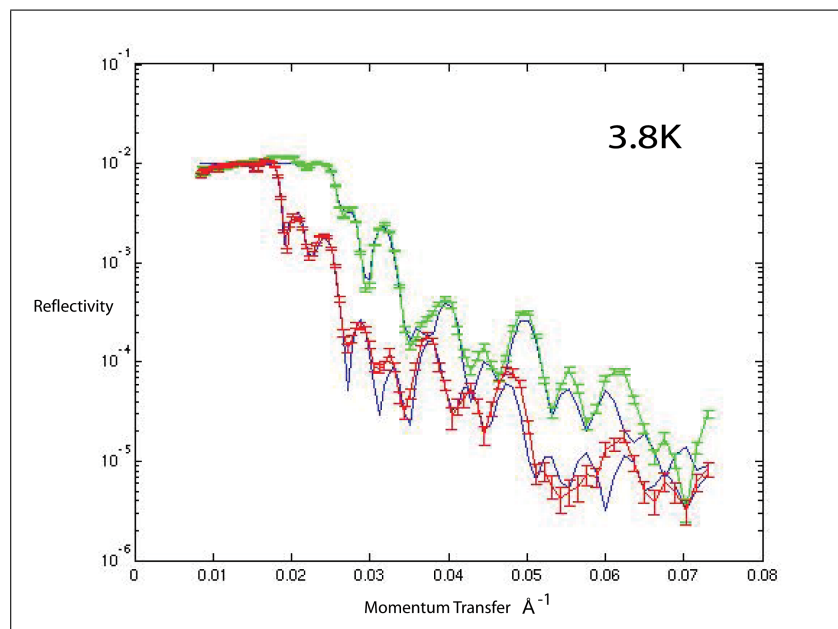


Figure 6.5: A reflectivity graph of Polarised Neutron Scattering data showing a combined fit to both the up (green) and down (red) data at 3.8K (below  $T_c$ ). The respective fits are shown in blue and agree well with the data until approximately  $q=0.055\text{\AA}^{-1}$ .

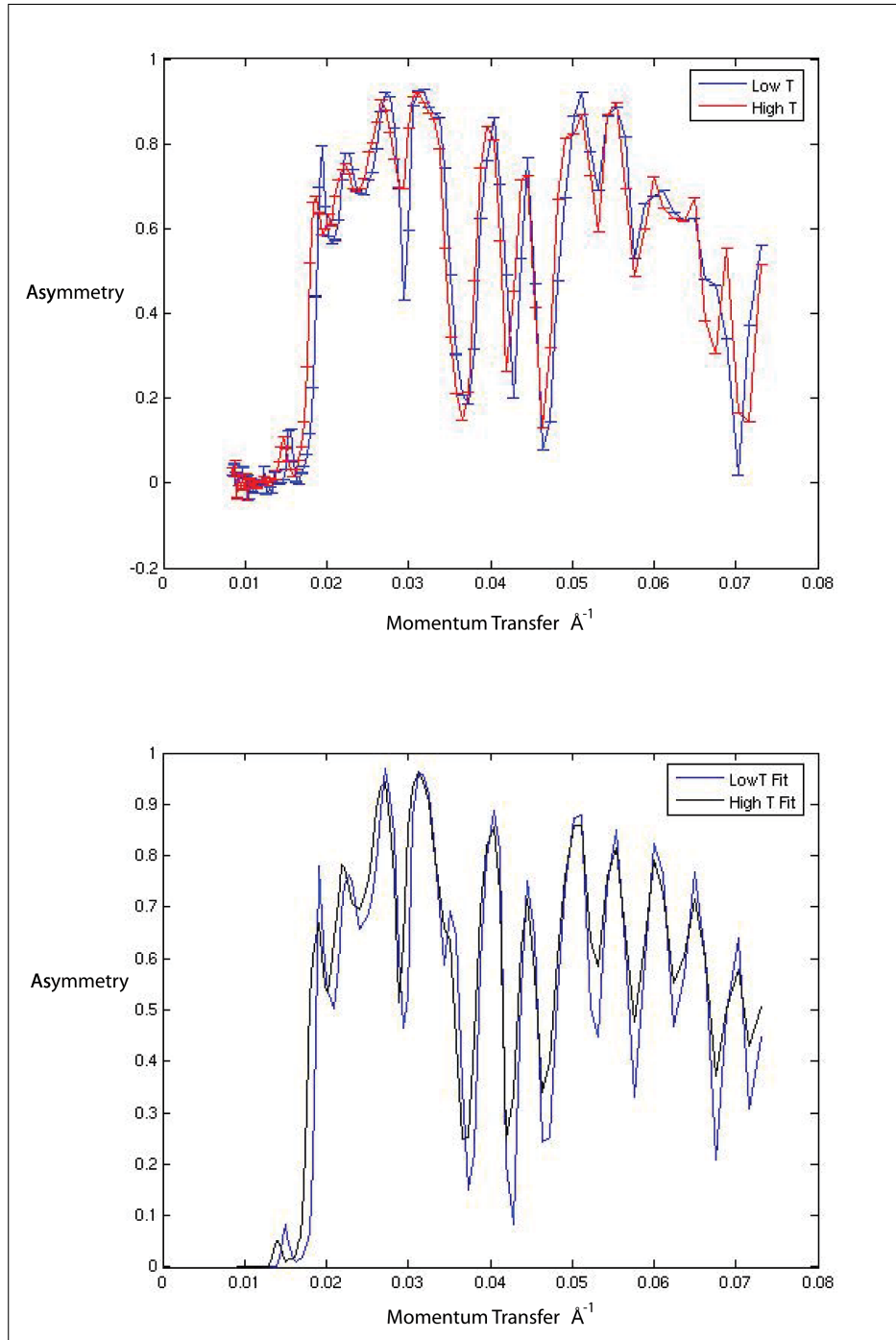


Figure 6.6: For the PNR data the difference between the asymmetries (difference between up and down spin) above and below  $T_c$  are extremely small, showing almost exactly the same trend. The top plot shows the up and down asymmetry between at low (blue) and high (red) temperatures. There is, noticeably, a distinct shift between that in the normal and superconducting states. The bottom plot shows the same asymmetries between the fits.

low energy muon experiments will help to probe the microscopic behaviour of the sample and allow insight into the the magnetic profile of the system, in particular, close to the boundary of the Py/Nb layers.

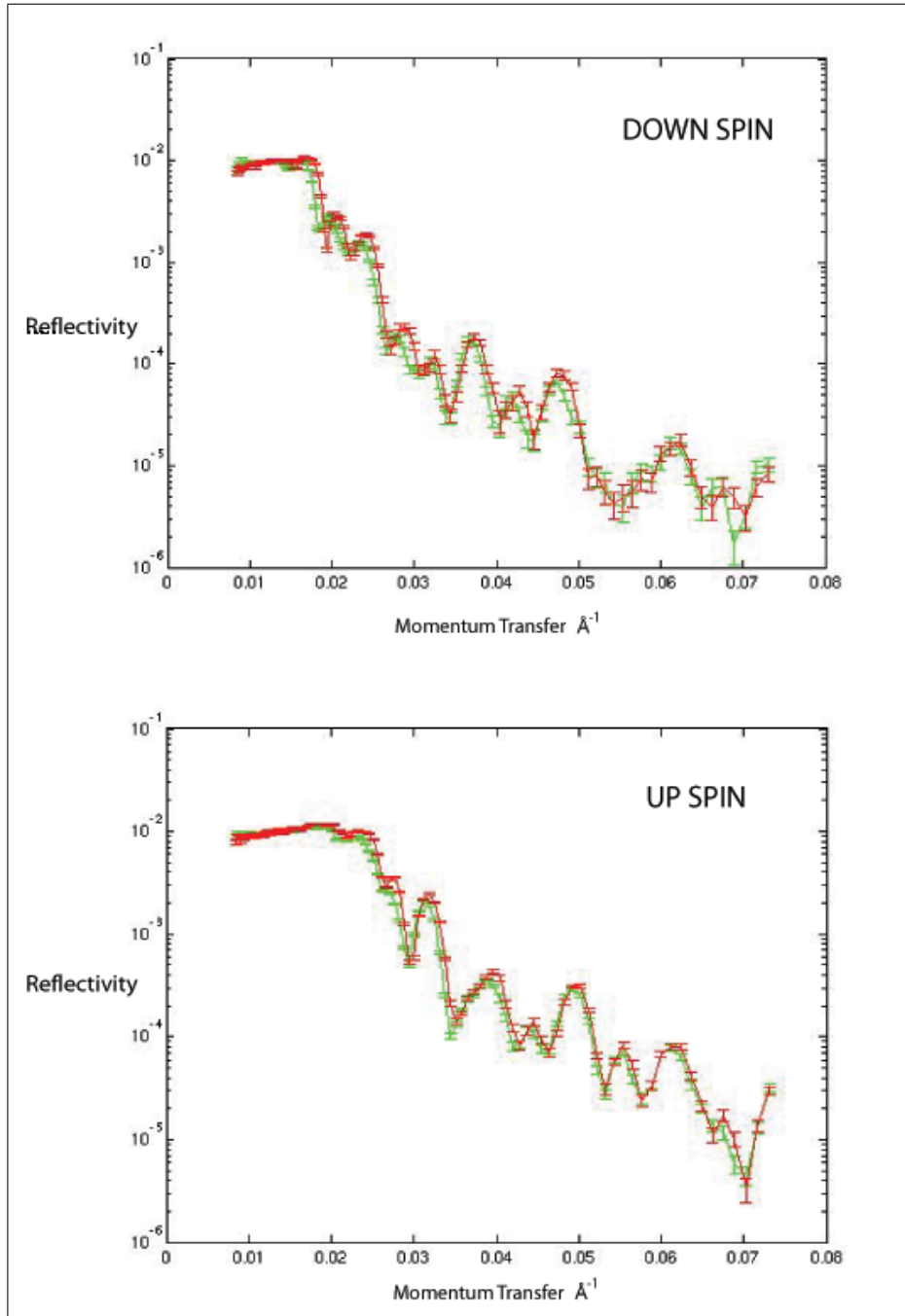


Figure 6.7: The top plot shows the very small difference between down spin reflectivity curves for the high (red) and low (green) temperatures. The bottom plot also shows the same subtle change between the up data sets at 10K and 3.8K. Such a difference is currently attributed to small, systematic changes in the experimental setup.

## 6.4 Discussion of Low Energy $\mu$ SR results

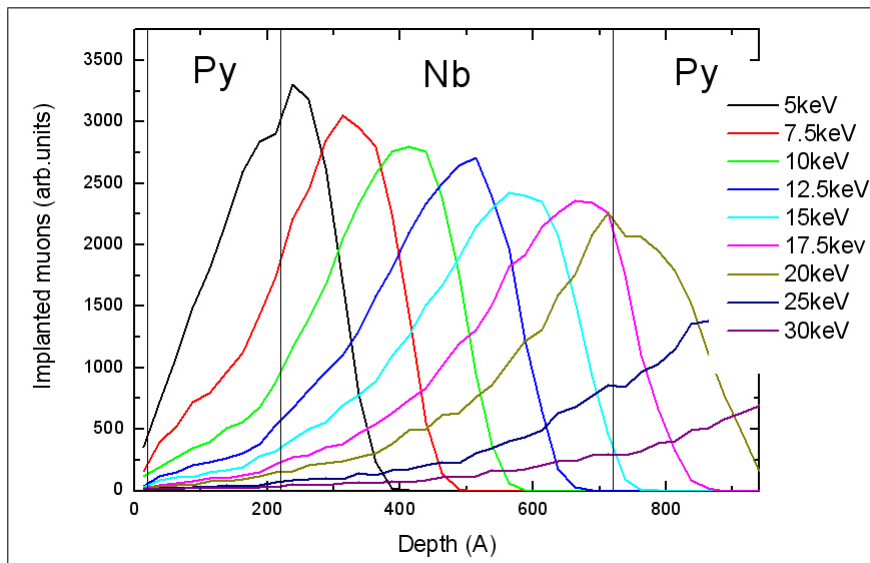


Figure 6.8: A series of muon implantation depths (and associated energies) for the Py/Nb/Py material are calculated using a Monte Carlo algorithm. (Source: (Luetkens, 2007))

For the LEM experimental setup, there are four sample pieces (each having a surface area of  $(10\text{mm} \times 10\text{mm}) \pm 0.2\text{nm}$  as described previously) arranged in a square mosaic on a circular, conducting, aluminium plate (diameter 70mm) with a thin Ag coating. By having several sample pieces orientated in this way, it is possible to minimise the background from the sample holder (although this effect is not totally eliminated as discussed later). The mosaic is mounted on the plate with a Ag paste that takes several hours to dry, after which it exhibits good thermal and electrical conductivity<sup>3</sup>. The side of the mosaic is approximately 20mm from the edge of the plate so that the muon beam can be well centred over the entire sample and it is aligned such that the applied field is parallel to the surface of the multilayer.

The sample is initially cooled down from room temperature to 10K and a field of 400G is applied to it in order to initially magnetise the FM layers. Thereafter, all the measurements are conducted in an applied field of 100G, where the 3.8K measurements are FC before obtaining the data.

In order to investigate the  $\mu$ SR spectrum at the FM/SC boundary, a series of energy scans were performed (representing the implantation depth of the incoming muons) at both 3.8K and 10K. Further to this, temperature scans at 5keV and 10keV were performed to investigate the variation in magnetic profile as a function of temperature at the FM/SC interface and at the centre of the Nb layer (see Monte Carlo simulation of Figure 6.8). Initially the Maxent technique was used for each measurement, where 7.5 million positron events were detected as this was sufficient enough to give satisfactory statistics. An example

<sup>3</sup>A resistance test is performed between the “paste contact” and the plate for which a reasonable value of a few hundred Ohms is expected. This gives a potential difference of the order of kV, which is required for the acceleration/deceleration of the incoming muons.

of the resulting  $P(B)$  distributions is shown in Figure 6.9 where the central peak at the applied field (observed for all measurements) is due to the large fraction of muons stopping in the aluminium sample holder. This fraction has been calculated as approximately 18% (Luetkens 2003). Subsequently, the total obtainable asymmetry is  $\sim 0.23$ , of which the background arising from the sample holder is  $\sim 0.05$  (Luetkens 2007) (Lister 2007).

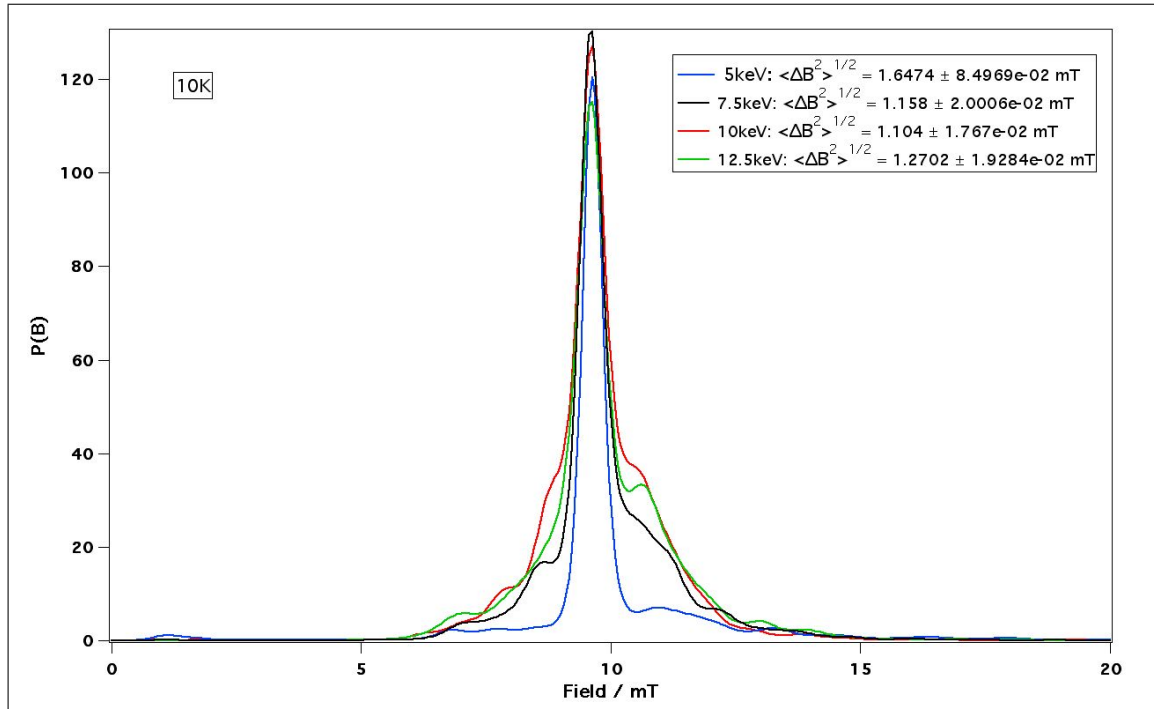


Figure 6.9: At 10K it is clear that the width of the Maxent  $P(B)$  lineshape decreases as a function of implantation energy. (Note that the respective errors for  $\langle \Delta B^2 \rangle^{1/2}$  are denoted in brackets.)

The analysis for the data sets was initially conducted using Maxent (detailed in the previous chapters). However, as described later, an additional time-domain analysis method was used to further understand and complement the results obtained.

We consider first the variation of the  $P(B)$  lineshape at both 3.8K and 10K as a function of energy. At 10K (Figure 6.9),  $\langle \Delta B^2 \rangle^{1/2}$  decreases as one moves away from the first Py/Nb interface towards the centre of the Nb layer. At 5keV the linewidth is calculated by Maxent as being 1.65mT. This reduces to 1.10mT at the centre of the SC layer (10keV) before increasing again to 1.27mT as the implantation depth of the muons moves towards the second FM/SC boundary at 12.5keV. However, upon comparison of the 5keV  $P(B)$  at 3.8K with that of the corresponding 10K lineshape, there is a distinct difference in  $\langle \Delta B^2 \rangle^{1/2}$ . Figure 6.10 shows how the linewidth at 5keV has substantially decreased to 1.28mT at 3.8K from 1.65mT at 10K.

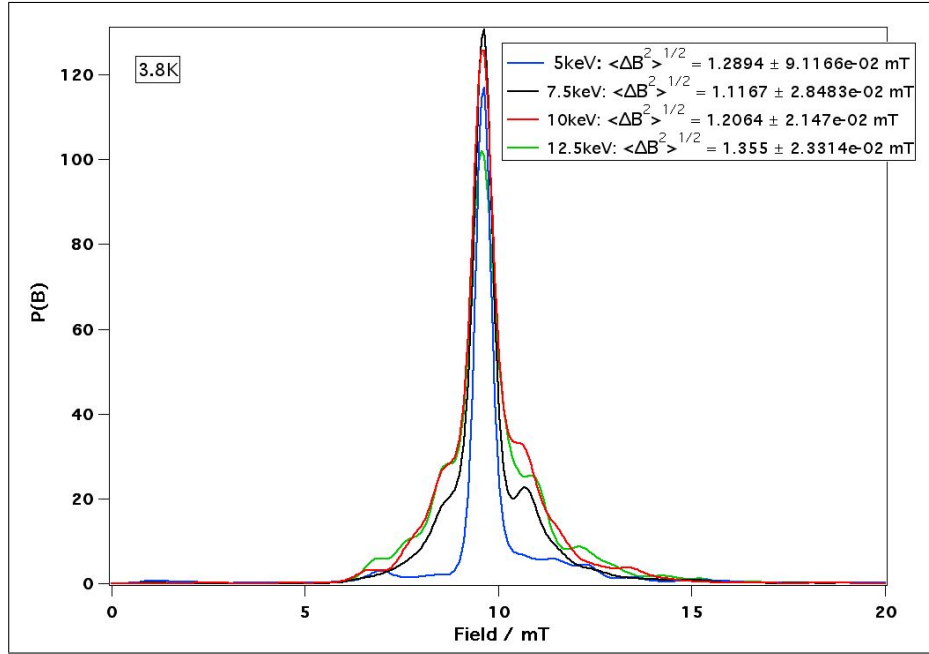


Figure 6.10: The Maxent  $P(B)$  lineshapes for different implantation energies at 3.8K. The corresponding values of  $\langle \Delta B^2 \rangle^{1/2}$  have also been noted with the respective errors for denoted in brackets.

However, of most significant note is what, at a first glance, appears to be the existence of small satellite peaks about the central frequency. Such an effect has been seen by both Drew (2005b) and Luetkens (2003) in which both authors describe the existence of such undulations as that caused by a SDW induced by the FM Fe layers and permeating throughout the central layer (as shown by Figure 6.11). The subsequent variation in the magnetisation  $M$  over a distance  $x$  into the centre layer, as discussed in the previous section, has been explained as the phenomenon occurring in the Fe/Pb/Fe system (Drew 2005b) and has been described in the Fe/Ag/Fe system as (Luetkens 2003):

$$M(x) = \sum_i C_i x^{-\alpha_i} \sin((2\pi x/\Omega_i) + \phi_i) \quad (6.2)$$

Here,  $C_i$  and  $\alpha_i$  are the initial amplitude and attenuation of each oscillation,  $\phi$  is the phase of each component  $i$ , and  $\Omega$  is the Fermi-surface spanning vector. This latter parameter has been calculated by Stiles (1999) as having a period of 29.4Å for Nb.

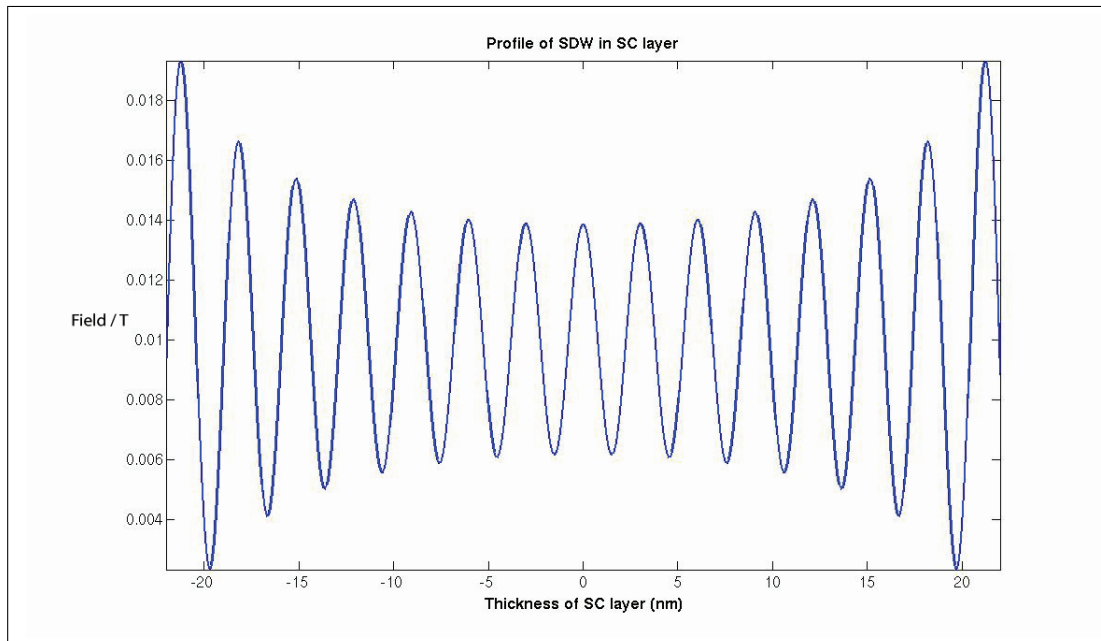


Figure 6.11: *The magnetic profile of a SDW can be simulated for the Py/Nb/Py material for an implantation energy of 10keV, applied temperature of 10K and magnetic induction of 100G. The SDW model has been explained by Drew et al. (2005) and Luetkens et al. (2003) as being responsible for satellite peaks in  $\mu$ SR  $P(B)$  lineshapes (see text).*

One can then apply this model to the current Py/Nb/Py system to simulate a SDW (based on an RKKY-type interaction) which has two harmonic terms, each originating from a FM interface, permeating into the SC layer (such that the arrangement of the layers is FM/SC/FC) and decaying according to a power law. The waves are then superimposed upon one another when they interfere (see Figure 6.11). Figures 6.12, 6.13 and 6.14 show a simulated  $P(B)$  lineshape based on a SDW model at 10K describing the data at implantation energies of 7.5keV, 10keV and 12.5keV respectively (Lister 2007)<sup>4</sup>. The simulation is denoted by the shaded area on each and is compared with the Maxent generated  $P(B)$  (solid line). The best description of the data shown at an implantation energy of 10keV is with an exponent of  $\alpha=0.35$  and an x-direction offset of 6nm. This is in addition to the phase shift  $\phi$  of the harmonic terms of 0.7. It is clear from comparison with Luetkens (2003) that the decay exponent of the SDW described here is different to that obtained in the Fe/Ag/Fe trilayer in which  $\alpha=0.8$ .

<sup>4</sup> It should be noted that 5keV simulations are more complex due to the large internal fields at the FM/SC boundary.

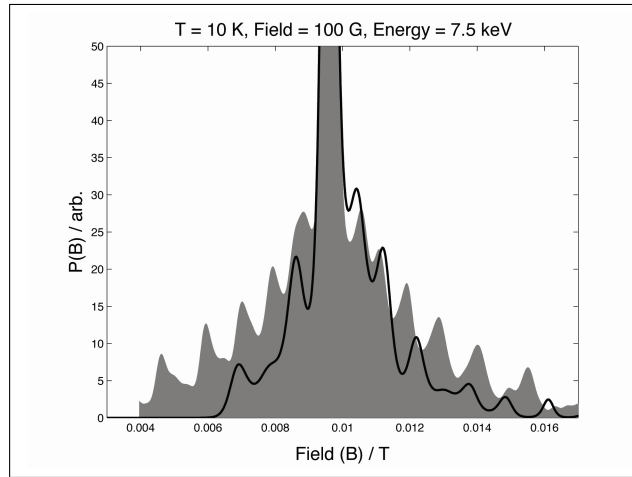


Figure 6.12: (Shaded area): A  $P(B)$  generated from a simulation of a SDW model at 10K and 100G for an implantation energy of 7.5keV. (Solid line): The corresponding  $P(B)$  generated from Maxent. It is clear that there is little agreement between the peaks in the data and those from the fit. (Source: Lister (2007))

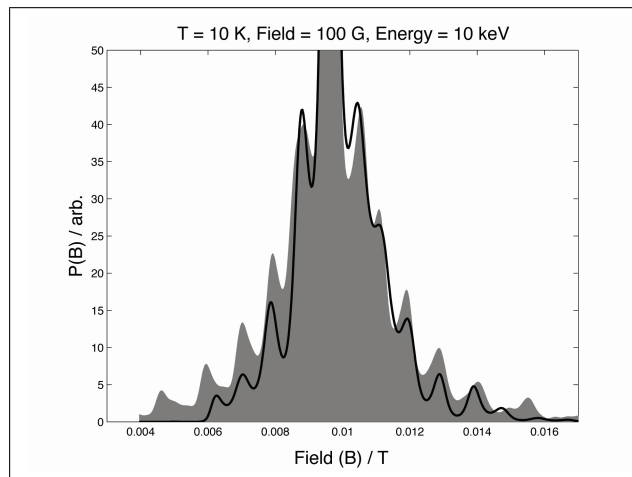


Figure 6.13: (Shaded area): A  $P(B)$  generated from a simulation of a SDW model at 10K and 100G for an implantation energy of 10keV. (Solid line): The corresponding  $P(B)$  generated from Maxent. It is clear that there is little agreement between the peaks in the data and those from the fit. (Source: Lister (2007))

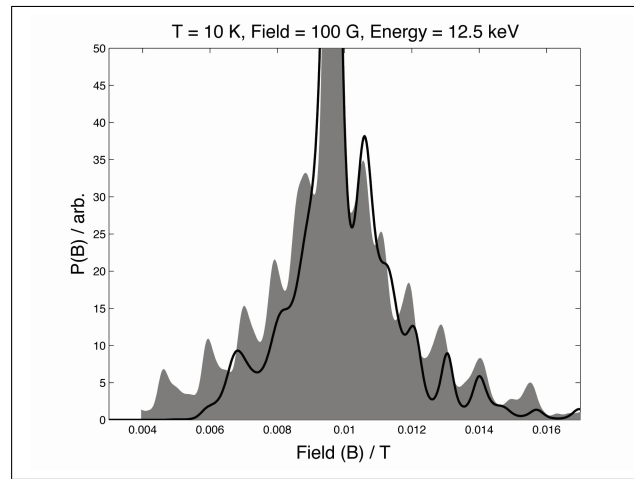


Figure 6.14: (Shaded area): A  $P(B)$  generated from a simulation of a SDW model at 10K and 100G for an implantation energy of 12.5keV. (Solid line): The corresponding  $P(B)$  generated from Maxent. It is clear that there is little agreement between the peaks in the data and those from the fit. (Source: Lister (2007))

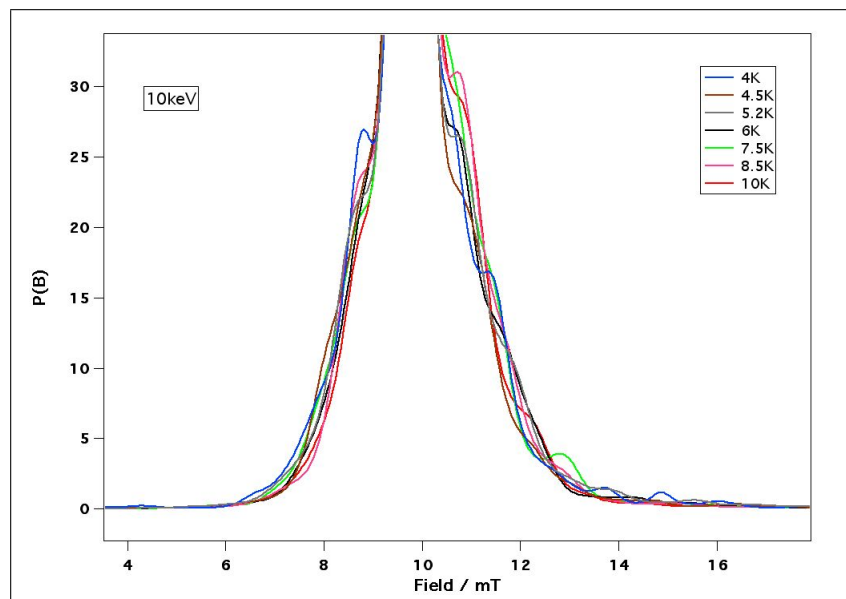


Figure 6.15: A series of Maxent  $P(B)$  distributions at approximately the centre of the Nb layer (10keV) over a range of temperatures. Note that the position and sizes of the satellite peaks about the central field appear to vary randomly as a function of temperature.

Upon comparing each simulated  $P(B)$  with its corresponding Maxent lineshape however, it is clear that there is a distinct lack of congruency between both. Indeed, even for the best description of the data at 10K, 10keV (Figure 6.13), not all of the peaks are correctly represented at the lowest and highest sampled fields. In addition to this, it should be added

that the Maxent produced  $P(B)$  has been applied by changing the looseness factor (described further in Chapter 3) from 1.03 to 1.00, allowing for an increased sharpness of the satellite peaks. Even with this enhanced factor, it is not possible to replicate the sharpness of the peaks in the simulated  $P(B)$ . Most notably, although at 7.5keV and 12.5keV there is a small amount of agreement on the right hand side of the central peak (i.e. to higher fields), there is almost no agreement between the lineshapes at lower fields, where dissonance regarding the number, amplitude and position of each peak occurs.

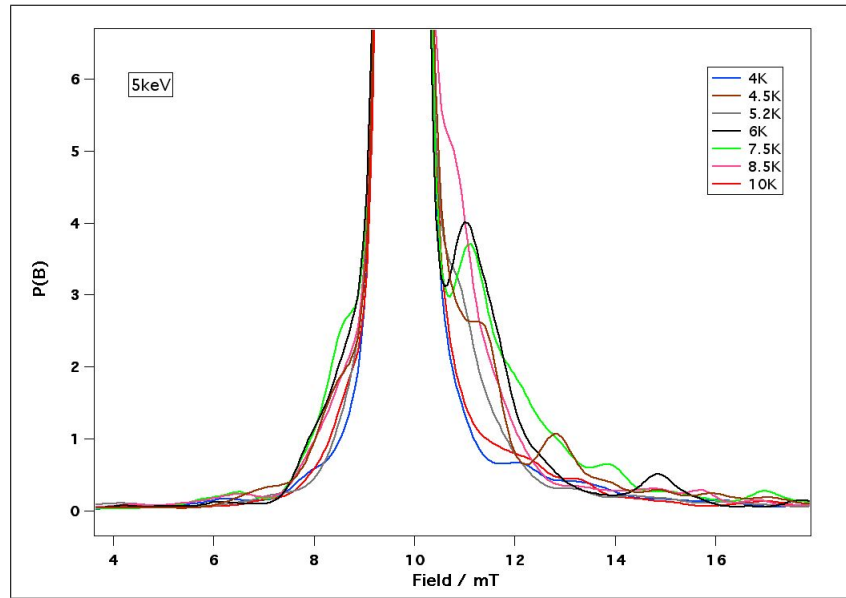


Figure 6.16: At the boundary between the FM and SC layer (5keV), the sizes of the satellite peaks (produced within the Maxent  $P(B)$  distributions shown here) about the central field are greatly reduced (when compared to 10keV) and the positions appear to vary randomly as a function of temperature.

Further to this, if one returns to the individual  $P(B)$  lineshapes, it is of particular significance that the positions and amplitude of the satellite peaks on either side of the central frequency do not consistently agree with one another for any implantation energy or temperature. At both 10keV and 5keV for example (see Figures 6.15 and 6.16 respectively), one would expect the *magnitude* of the satellite peaks to vary as a function of temperature if one were considering a SDW model (as shown in Figure 6.11). As the muon stopping profile traverses the Nb layer, the number of muons sampling different regions of the SDW varies (as shown in Figure 6.8) and thus so does the magnitude of the corresponding  $P(B)$ . Indeed, even in the normal state it is expected that the behaviour of the conduction electrons forming any SDW would not deviate on the scale suggested by the dissonance in the  $P(B)$ s of both 8.5K and 10K. Overall, the position of the SDW in the sample should not change and thus the peaks should be seen in the same *position* for all implantation energies. However, no such behaviour or evident trends as a function of temperature are observed here.

Despite reducing the values of the looseness during the Maxent analysis, it is not possible to improve on the comparison of similarities between the  $P(B)$ s of the simulations

and the actual data. It is clear, therefore at this point that, if a SDW exists, it is not entirely responsible for the effects observed in the P(B) distributions and hence the final magnetic profile within the Nb layer. Figure 6.17 shows the time domain data at 10K, 10keV for the Maxent fit. It is clear that the signal is not sufficiently damped at longer time intervals (i.e. approaching  $10\mu\text{s}$ ). Such behaviour represents the fact that the large fraction of muons arriving in the sample holder rather than the sample itself has an adverse impact on the experimental setup. Although this background effect remains constant, as shown above, Maxent is clearly unable to separate out the real signal emanating from the sample from this background component.

Further to this, the time window in the Maxent analysis acts as a top-hat function, which, once Fourier Transformed becomes a sinc function. The undulations observed in the P(B) spectra produced by Maxent are most likely due to this. Consequently, this sinc function is included in the convolution of all the components during the analysis of Maxent and is clearly not observed when one analyses the  $\mu\text{SR}$  data within the time domain.

As further investigation, a time-domain fitting routine is proposed. This simplified model encompasses the summation of a Gaussian and Lorentzian term, describing the signal resulting from the background (bgnd) and sample (norm) respectively:

$$y = e^{-t\Delta t/\tau_\mu} (1 + e^{-\lambda_{norm}t} \cos(\omega_{norm}t + \phi) + e^{-(\lambda_{bgnd}t)^2} \cos(\omega_{bgnd}t + \phi))$$

The Gaussian component is a relatively undamped signal resulting from those muons decaying in the sample holder. The Lorentzian is a damped term resulting from muons in the actual sample. The data at 10K (i.e. the normal state) is considered first.

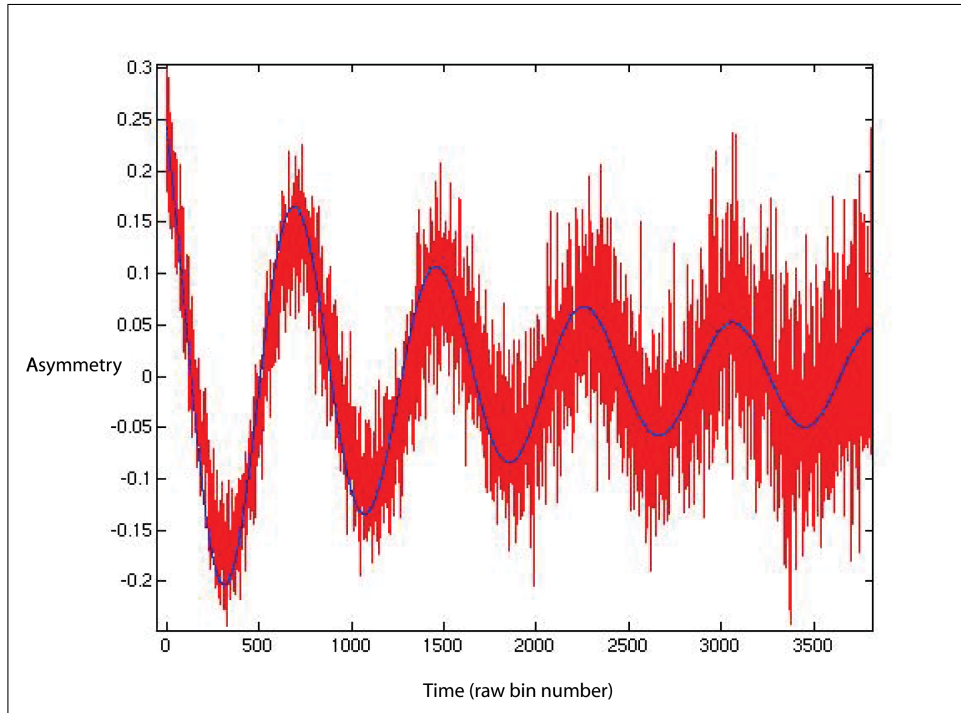


Figure 6.17: *The time domain data (red) with corresponding Maxent fit (in blue) at 10K, 10keV clearly shows a significant lack of damping at longer time intervals. The undamped signal is attributed to those muons arriving in the aluminium sample holder and contributing to the background signal.*

Figure 6.18 shows the change in the fit of the time domain signal comprising the summation of a Gaussian and Lorentzian as a function of implantation energy at 10K. One expects that the Gaussian signal should not change regardless of implantation energy and temperature. However, the Lorentzian signal should change and reflect the magnetic profile experienced by the muons inside the actual sample.

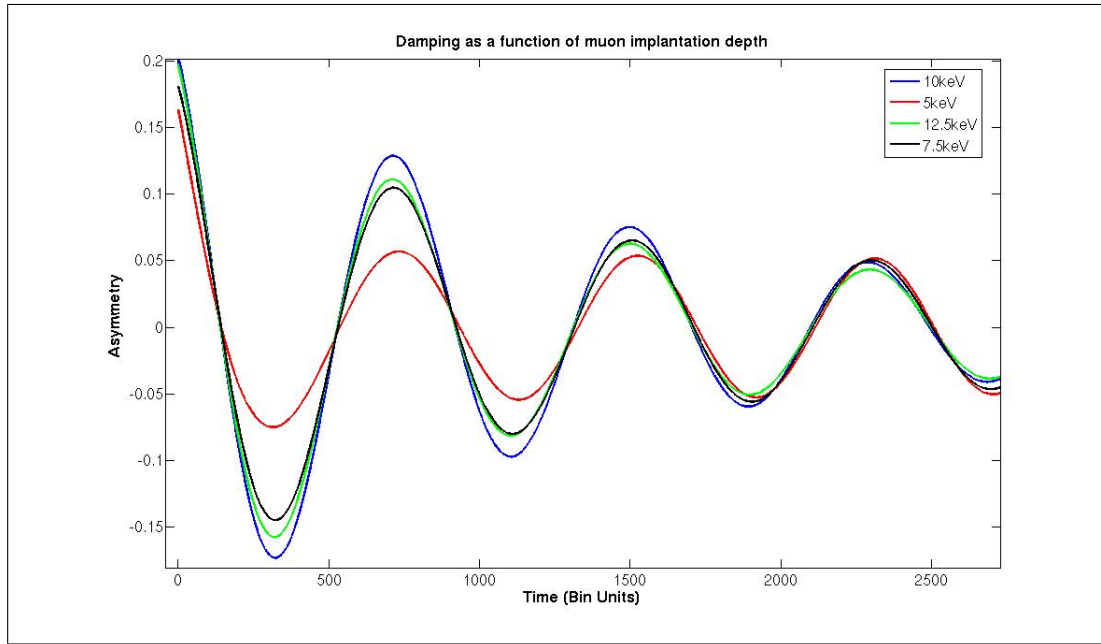


Figure 6.18: A plot showing a comparison of only the individual fits to the data (without the data) at 10K for the different implantation energies. Comprising both a Gaussian and Lorentzian term, it is clear that there is a large step, as expected, between the 7.5keV and 5keV data sets as one moves closer to the Py/Nb interface. Further, the signal at all energies appears to be relatively undamped at longer times - most notable in the 5keV fit.

From a first observation it is clear that there is an increase in the damping of the signal as one approaches the boundary of the Py/Nb layer (i.e. at 5keV) (see Figure 6.18). When combined with the quantitative plot of Figure 6.20, it is clear that at 10keV (at the centre of the Nb layer), the damping is measured at  $0.00111 \pm 7.9 \times 10^{-5}$  T. At 7.5keV, though, the asymmetry (as plotted in Figure 6.22) is  $0.154 \pm 0.02$  with an increased damping of  $0.00155 \pm 4.3 \times 10^{-5}$  T. Indeed, the asymmetry at 5keV is  $0.124 \pm 0.03$  but with a further increased damping of  $0.00692 \pm 3.8 \times 10^{-4}$  T. In addition to this, it is clear, upon increasing the implantation energy further towards the other FM layer, that the damping begins to increase again to  $0.00142 \pm 4.7 \times 10^{-5}$  T at 12.5keV. The 12.5keV and 7.5keV values are in agreement with one another as expected - here, the influence of the FM layers in this region starts to be significant. However, what is distinctly noticeable is the magnitude of the jump in the damping of the time domain envelope as one increases the energy from 5keV to 7.5keV. Further energy scans are required to investigate whether a similar non-linear step in the Lorentzian damping occurs at energies close to the second Py/Nb boundary (i.e. between 12.5keV and 15keV). It is clear from the data recorded here, that the effect of the magnetisation in the Nb layer from the Py is very strong close to the interface but exhibits a rapid decay towards the centre of the Nb layer. Such a fast decay in the magnetisation as a function of distance from the Py/Nb layer is reflected in the Lorentzian signal which is highly damped at 5keV but only slightly damped at 7.5keV and energies thereafter.



Figure 6.19: For an infinitely thin FM layer (i.e. a single chain of dipoles all aligned in the same direction), the return fields exist extremely close to the edge of each dipole axis (blue). Further still, at the top and bottom of each dipole axis the fields are cancelled by those from adjacent dipoles (examples of which are circled in red).

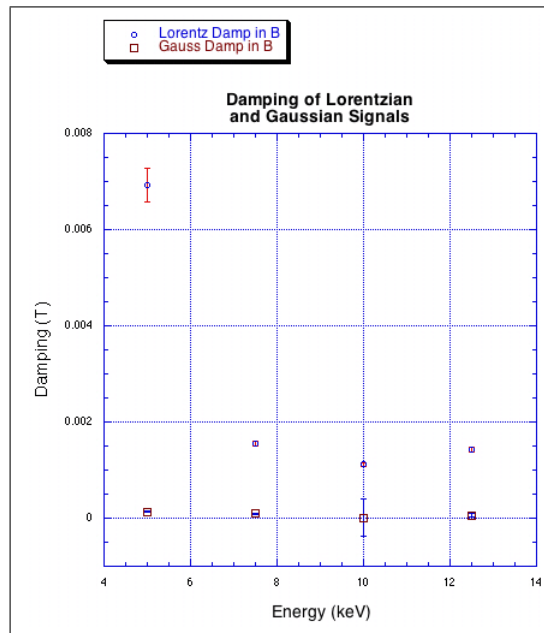


Figure 6.20: A large increase in the damping of the Lorentzian component (blue circles) at 10K can be seen as one reduces the implantation energy from 7.5keV to 5keV. (As expected, the Gaussian signal (red squares) remains constant throughout.)

In addition to this, the Lorentzian frequency component also changes as a function of energy. Figure 6.21 shows a decrease in frequency as one increases the implantation energy towards the centre of the Nb layer. At 10keV the magnitude of the Lorentzian component of the field reaches a minimum at  $0.00971 \pm 3.1 \times 10^{-5}$  T. Such a dip in the field at this point agrees with the understanding that the effect of the magnetisation from the FM layer should be least at the centre of the Nb layer. Indeed, as one increases or reduces the implantation energy of the muons to either 12.5keV or 7.5keV respectively, one observes that the field correspondingly increases to  $0.00980 \pm 4.7 \times 10^{-5}$  T as a greater fraction of the muons moves towards a Py/Nb boundary. Despite the large error at 5keV, it is clear that the trend of the data indicates that there is a marked increase in the magnitude of the Lorentzian field component at this energy. The sudden increase in the field at 5keV to  $0.00991 \pm 4.6 \times 10^{-4}$  T from  $0.00978 \pm 5.3 \times 10^{-5}$  T at 7.5keV is as a direct result of the rise in the overall field

profile experienced by the muons at the Py/Nb interface due to the large internal fields of the FM layer.

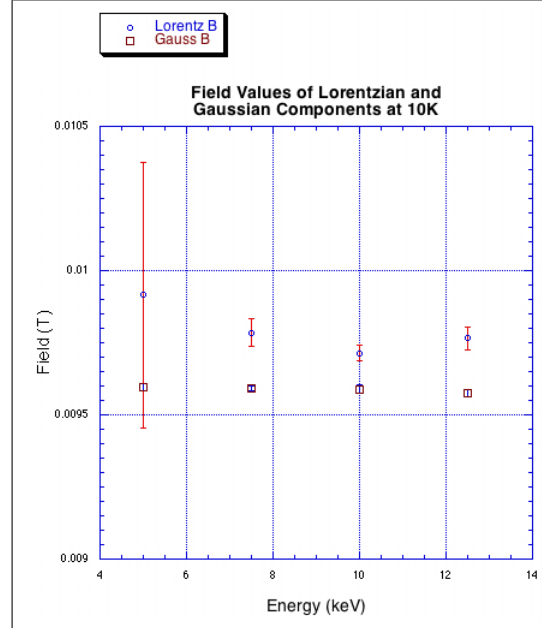


Figure 6.21: A large increase in the Lorentzian frequency/field (blue circles) at 10K can also be seen as one reduces the implantation energy from 7.5keV to 5keV. (As expected, the Gaussian component (red squares) remains constant throughout.)

At this point, it is sensible to consider the possible behaviour of the magnetic field lines at the Py/Nb boundary. If one considers an isolated dipole system of magnetic moment  $\mu$ , it is possible to describe the decay of the field B over a distance r perpendicular to the dipole axis by the general equation:

$$B(\mathbf{r}) = \frac{\mu_0 \mu}{4\pi \mathbf{r}^3} \quad (6.3)$$

This extent of the decay of the magnetic field is dependent, amongst others, upon the length l of the dipole.

If one now expands this model to an arrangement of dipoles in an infinitely thin FM layer, the return fields do not extend far and are extremely close to the axis of the dipole. In addition to this, because the each dipole axis is perfectly aligned with the others, the return fields within the layer at the top and bottom of the dipole itself are cancelled out by other adjacent dipoles (see Figure 6.19). Because of the infinitely small thickness of the system, the fields outside are also returned within the layer thickness and thus do not permeate outside of this.

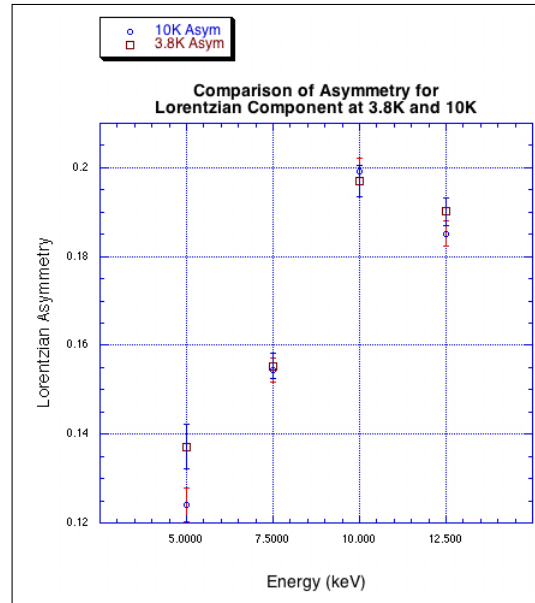


Figure 6.22: *The asymmetry of the Lorentzian signal at 3.8K (red squares) clearly reaches a peak at the centre of the Nb layer - as it does at 10K (blue circles). Of particular note though is that the asymmetry at 5keV for the superconducting state is greater than that for the corresponding normal state. (NB. Although not shown here, the Gaussian signal for both above and below  $T_c$  remains constant.)*

However, if one were now to introduce a boundary condition such that a ferromagnet was interfaced with another non-descript layer and if, in a non-ideal system, roughness at this interface exists, the dipoles at the edge of the Py can be affected such that the ability of their fields to cancel out those of adjacent dipoles reduces. Because these dipolar fields are only partially cancelled, they begin to permeate further into the adjacent layer. Consequently, muons within the Nb layer are able to sample regions close to the boundary which are highly affected by such permeating fields.

If one now compares the 10K (normal state) data to that inside the superconducting state, one can observe noticeable changes (see Figure 6.22). At 3.8K, it is clear that the asymmetry rises and falls at exactly the same energy values as it does at 10K. For 10keV at 3.8K, the asymmetry is  $0.197 \pm 0.003$  (compared to  $0.199 \pm 0.002$  at 10K) and  $0.155 \pm 0.003$  at 7.5keV (compared with  $0.154 \pm 0.002$  at 10K). However, despite the similarities in the asymmetry values for most energies above and below  $T_c$ , it is noticeable that the 5keV values do differ from one another outside of the corresponding error margins. At 3.8K, the asymmetry is  $0.137 \pm 0.004$ , whereas at 10K it is  $0.124 \pm 0.003$  - an increase of 10.4% as one enters the superconducting state. This dissonance at 5keV is of particular significance since, unlike the Maxent analysis, it demonstrates that there is some suppression of the magnetism from the FM layer at the interface when one enters the superconducting state.

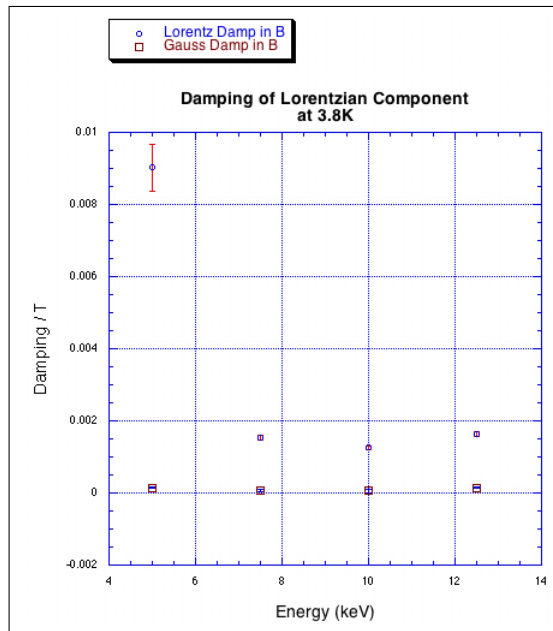


Figure 6.23: At 3.8K, the Lorentzian damping (blue circles) as a function of implantation energy is similar to that at 10K. However, more specifically within the superconducting state, the damping at 5keV is significantly higher at 0.00901T compared with 0.00692T at 10K.

In addition to this, the damping of the Lorentzian signal at 3.8K is of interest too. At 10keV, it is again clear from Figure 6.23 that, like the corresponding normal state scenario, the decay of the Lorentzian component of the  $\mu$ SR signal reaches a minimum. Of particular notice though is that for almost all implantation energies the damping is higher in the superconducting state than it is in the normal regime. At 10keV, the damping is  $0.00125 \pm 3.6 \times 10^{-5}$ T compared with  $0.00111 \pm 7.9 \times 10^{-5}$  T at 10K. At 12.5keV the damping at 3.8K is  $0.00164 \pm 7.2 \times 10^{-5}$ T which is greater than that measured at 10K ( $0.00142 \pm 4.7 \times 10^{-5}$ T). The 5keV data also shows a clear increase in the damping is observed from  $0.00692 \pm 3.8 \times 10^{-4}$  T at 10K to  $0.00901 \pm 6.8 \times 10^{-4}$  T at 3.8K. Even though at 12.5keV the damping is slightly less at 3.8K ( $0.00153 \pm 7.2 \times 10^{-5}$ T) compared with that at 10K ( $0.00155 \pm 4.3 \times 10^{-5}$ T), the difference is within the error bars and does not affect the observation that the overall damping of the time domain signal is greater in the superconducting state than it is at 10K.

Moreover, Figure 6.24 shows that a down-turn to a Lorentzian field component of 0.00902T is observed for an implantation energy of 5keV at 3.8K. Although the value has a large error of 0.00063T which exists within the errorbars of the other measurements taken, after careful analysis it becomes clear that the trend points to a significant decrease in the size of the field close to the Py/Nb boundary. Further to this, the data for other implantation energies at both 3.8K and 10K does not change significantly in value. For example, at 10keV, the Lorentzian component of the field in the normal state is 0.00971T (with an error of  $2.6332 \times 10^{-5}$ T) and 0.00959T (with an error of  $3.7141 \times 10^{-5}$ T) at 3.8K. As can be seen from the graphs, the measurements at 7.5keV and 12.5keV also follow this. However, what is most noticeable between 3.8K and 10K is the change in the trend of the Lorentzian

component as a function of energy. Whereas at 10K, there is a minimum in the Lorentzian signal at 10keV, a maximum occurs at 3.8K for the same implantation energy. Such data points to two contrasting magnetic profiles both above and below  $T_c$ .

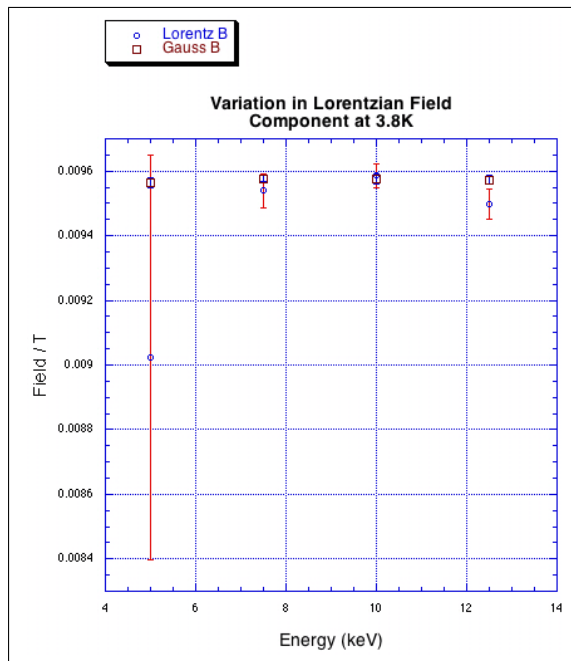


Figure 6.24: At 3.8K, a sudden drop in the Lorentzian component (blue circles) of the magnetic field is observed at 5keV, close to the Py/Nb boundary. This is directly opposite to the behaviour observed at 5keV in the normal metallic state in which an upturn in the magnetic induction is observed (see Figure 6.21).

To further these results, temperature scans have been performed at both 5keV and 10keV implantation energies. Considering first Figure 6.25 which shows a temperature scan for the mean field components at 10keV, one can see that whilst the Gaussian component of the overall field remains constant (aside from at 3.8K), the Lorentzian part however continues to increase from 0.00959T at 3.8K to 0.00984T at 7.5K, just above  $T_c$ . Thereafter, the frequency of the Lorentzian signal remains relatively constant, reflecting no change within the normal state. This result agrees with conventional superconductivity theory that as the ability of the supercurrents to screen out the FM field decreases with the Cooper pairs breaking up, the mean field inside the Nb layer begins to increase.

The variation in the damping of the Lorentzian signal at 10keV (displayed in Figure 6.26) shows a relatively constant value at approximately 0.0013T (within the errorbars) at low temperatures before decreasing just before  $T_c$  to 0.00121T at 6K. Above  $T_c$ , the damping remains close to  $\sim 0.0011$ T. Such a decrease in damping corroborates well with the increase in the mean field observed in Figure 6.25 due to the effect of the supercurrent screening reducing in this region. However, the resulting Lorentzian asymmetry at 10keV is relatively constant as one crosses  $T_c$  into the normal metallic regime (Figure 6.27). The undulation in the data that occurs just above  $T_c$  is covariant with the corresponding Gaussian components

and thus would remain constant.

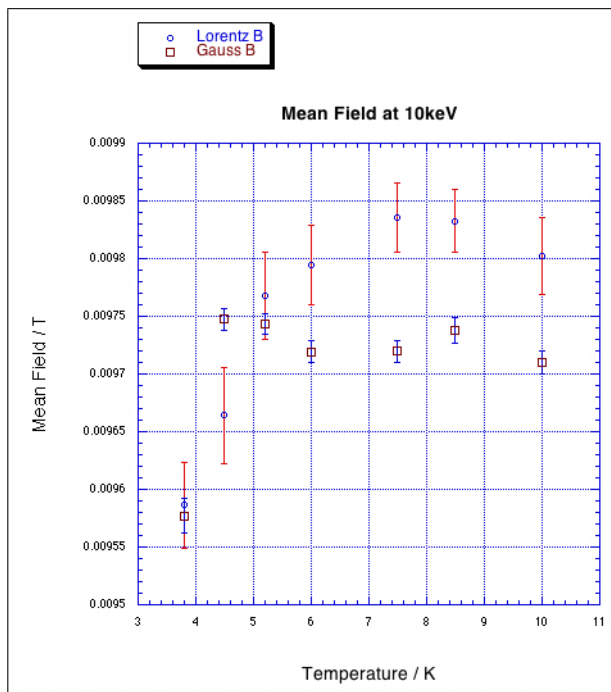


Figure 6.25: *It is clear that as one increases the temperature towards  $T_c$  at 10keV, the Lorentzian component of the mean field (blue circles), as measured by  $\mu$ SR increases too.*

The 10keV data set demonstrates behaviour that one would expect in the centre of a superconducting layer; as  $T_c$  is approached from lower temperatures, the effect of the screening currents becomes less and the subsequent mean field rises. With this, one also observes a decrease in the damping of the Lorentzian component of the field. However, at the interface of the Py/Nb sections (i.e. at an implantation energy of 5keV), understanding of the magnetic profile becomes more complex, but shows very interesting results.

Upon considering Figure 6.28, one can observe a general, overall decrease in the asymmetry of the Lorentzian component of the overall time domain signal as one increases through the transition temperature from approximately 0.135 below  $T_c$  to 0.130 above  $T_c$  (within the errorbars). (The discrepancies at 3.8K and 10K are expected since these data points were taken separately and are part of the field scans shown above.)

Following on from the asymmetry, the damping of the magnetisation as a function of temperature at 5keV shows a similar trend to that observed at 10keV (see Figure 6.29). Within the errorbars, a higher damping occurs below than above  $T_c$ , as one expects with the supercurrent screening out the magnetisation from the FM layer (discussed previously).

Aside from this, when one compares directly with the 10keV temperature scan, it is clear that the damping is nearly an order of magnitude higher at the interface than in the centre of the Nb layer. At 4.5K for example, the Lorentzian width is  $0.0107 \pm 0.0007T$ , whereas for the corresponding temperature at 10keV the damping is  $0.0013 \pm 0.00006T$ . Such dissonance between the damping for the 5keV and 10keV data represents the effect of the high FM field penetrating at very short distances into the Nb layer, more so when one

considers the superconducting screening currents below  $T_c$ . Indeed, one would expect the screening at the centre of the Nb layer to be greater than at the interface.

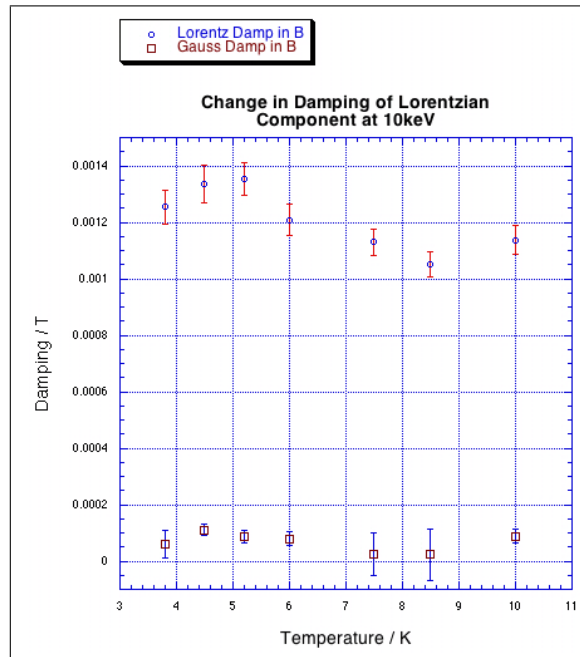


Figure 6.26: At 10keV, a decrease in the Lorentzian component of the damping (blue circles) can be observed at 6K (just before  $T_c$ ), congruent with the increase in the mean field within the Nb layer.

It is also important to consider the variation in the magnitude of the mean field at the Nb/Py interface (see Figure 6.30). It is clear that as one increases the temperature towards  $T_c$  the mean field, as measured by  $\mu$ SR, remains relatively constant within the errorbars. However, upon crossing through  $T_c$  there is a small decrease in the mean field to  $0.00983 \pm 0.00047T$ , though it is clear that such a decrease is almost negligible due to the large field emanating from the FM layer. Because this internal field leaking from the permalloy section is so high, it is clear that subtle changes in the mean field are masked. One point of note though is that the data at 3.8K does not agree with the rest of the data in this temperature scan. However, this point is not considered spurious since all of the errorbars are consistently large in this temperature scan, and that the 3.8K data agrees with the trend shown in Figure 6.24.

Such behaviour is in distinct contrast to the 10keV data which, as discussed previously, shows a noticeable increase in the mean field within increasing temperature. Indeed, the values of the mean field for the 5keV data set are all higher than the corresponding points at 10keV. Again, this is to be expected with the decay of such high fields being more noticeable towards the centre of the Nb layer rather than at the interface.

In order to attempt to rectify the fitting of the data close to the Py/Nb boundary, an additional Lorentzian term is included to capture the data at low times (i.e. at times less

than  $\sim 0.05\mu\text{s}$ ). The fitting routine now comprises:

$$y = \exp(-t\Delta t/\tau_\mu)(1 + \exp(-\lambda_{fast}t)\cos(\omega_{fast}t + \phi) + \exp(-\lambda_{norm}t)\cos(\omega_{norm}t + \phi) + \exp(-(\lambda_{bgnd}t)^2)\cos(\omega_{bgnd}t + \phi))$$

where “fast”, “norm” and “bgnd” correspond to the fast, normal and background components respectively.

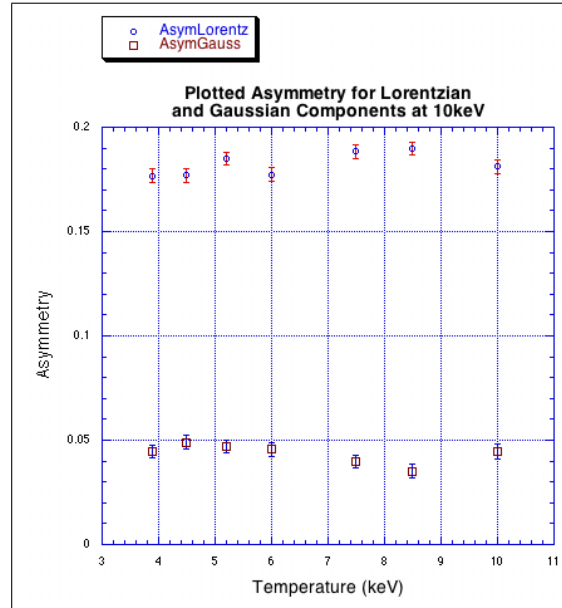


Figure 6.27: *It is clear that the Lorentzian asymmetry component is covariant with the Gaussian component (red squares) and that it is relatively constant across the transition temperature.*

It is clear from the bottom plot of Figure 6.32 that the fit is improved for short, fast time scales. Indeed, one can see that the upturn in the data is matched by the fit. This is due to the additional Lorentzian term that has been incorporated to capture the fast decaying signal just inside the Py/Nb interface. Such an adjustment to the fitting is not necessary for the 10keV data set since the damping of the magnetisation at the centre of the Nb layer is, as already mentioned, not as great as that at 5keV. The other Lorentzian term remains so as to account for the normal decay of the magnetisation (as per the 10keV data). However, despite the improved agreement with the short time data, the overall quality of the fitting of the entire time domain signal for each temperature point at 5keV is reduced compared with the standard Lorentzian + Gaussian combination (see Figures 6.31 and 6.33 showing the asymmetry and mean frequency/field respectively). As such, the data appears “noisy” with no apparent increase or decrease with temperature.

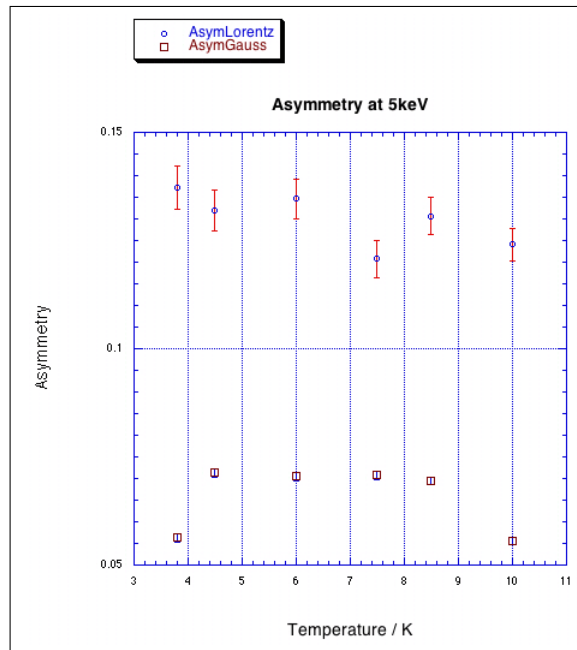


Figure 6.28: At 5keV, a subtle decrease in the Lorentzian component of the asymmetry (blue circles) can be observed as one crosses  $T_c$  into the normal regime.

Thus, by using just the Lorentzian + Gaussian model, the data at 5keV shows very significant results and clearly shows some distinct interaction between the magnetism and superconductivity at the FM/SC interface. Considering the data below  $T_c$ , if a pure Meissner state existed one would observe a minimum in the field at the centre of the Nb layer, rising towards the Py/Nb interface. With the introduction of a FM layer sandwiching the Nb layer, one observes, above  $T_c$ , (as per Figure 6.21), the mean field decreasing towards the centre of the Nb layer. Within the Meissner state, one would expect that this reduction in the mean field would be more enhanced as a function of increasing implantation energy due to the superconducting currents screening out the field from the centre of the Nb layer. However, significantly at 3.8K, the mean field appears to be a maximum at the centre of the Nb layer (i.e. at 10keV) and *decrease* towards the interface (see Figure 6.24), reaching a minimum at 5keV. The asymmetry shown in Figure 6.22 also lends weight to this, where an increase at low temperatures within the superconducting state reflects the fact that more muons are now accessing measurable fields, rather than the high FM internal fields from the permalloy. It follows from this that the magnetic profile within the Nb layer must substantially change to an unexpected form when the system enters the superconducting state.

From the evidence detailed above, the magnetism is clearly suppressed at the interface before increasing towards the centre of the SC layer. Such data clearly points to a potential novel system in which there is a change in the conventional superconducting order parameter.

Overall, it is clear that currently analysis within the time domain using a combination of a Lorentzian and Gaussian summation is the most effective method to describe the magnetisation within the Nb layer using  $\mu$ SR. Indeed, Maxent is too sensitive to background interference and the effect of the time window.

However, it is clear that there is some form of exotic coupling between magnetism and superconductivity at the interface between the FM and SC layers. Indeed, such results are extremely interesting and provide extra scope for further work as it appears as though the ferromagnetism is suppressed at the boundary before rising towards the centre of the Nb layer. Clearly, however, despite being satisfactory for the 10keV data, at the centre of the SC layer, the current fitting routine is still not sufficiently adequate to describe the data at the Py/Nb interface. In addition to this, further data detailing the evolution of the magnetisation of the sample as a function of energy from the first Py/Nb interface to the second may help to solidify the conclusions made here, in particular at low temperatures within the superconducting regime. Such information may also help further the understanding of the nature of the competing mechanisms of superconductivity and magnetism, certainly at energies close to the FM/SC interface.

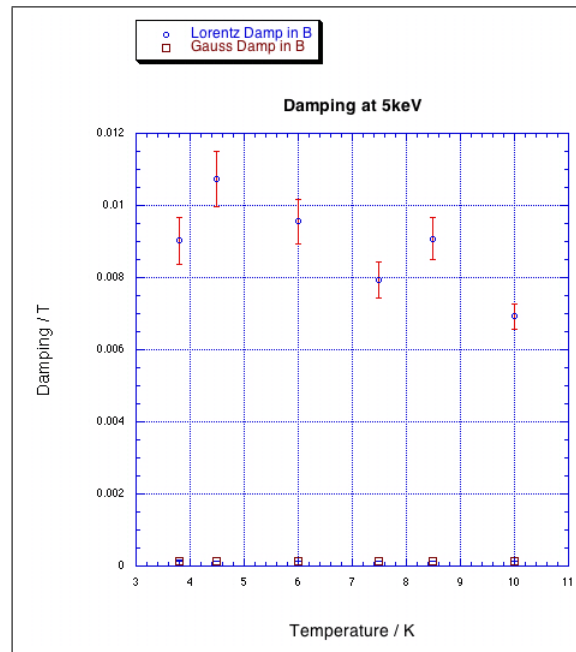


Figure 6.29: As one decreases the temperature below  $T_c$  the Lorentzian component of the damping (blue circles) of the magnetisation from the FM layer increases significantly at 5keV.

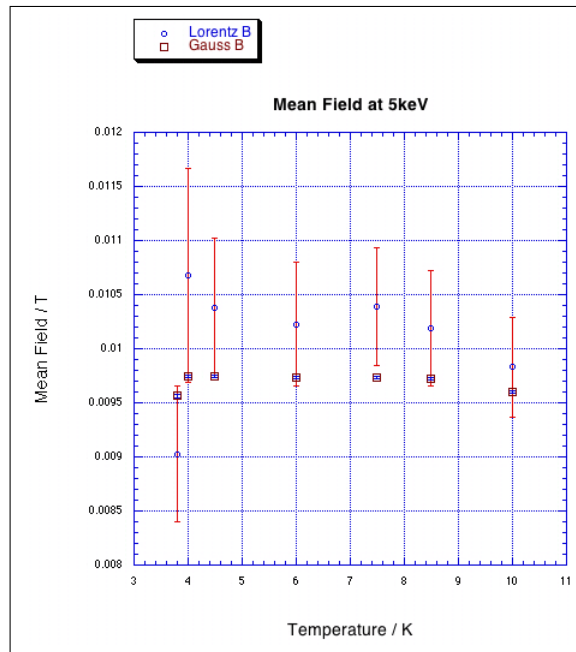


Figure 6.30: At 5keV, the Lorentzian component of the mean field (blue circles) appears to remain relatively constant within the error bars. The point at 3.8K is of particular interest since it appears to differ from the trend given here but agrees with that shown in Figure 6.24.

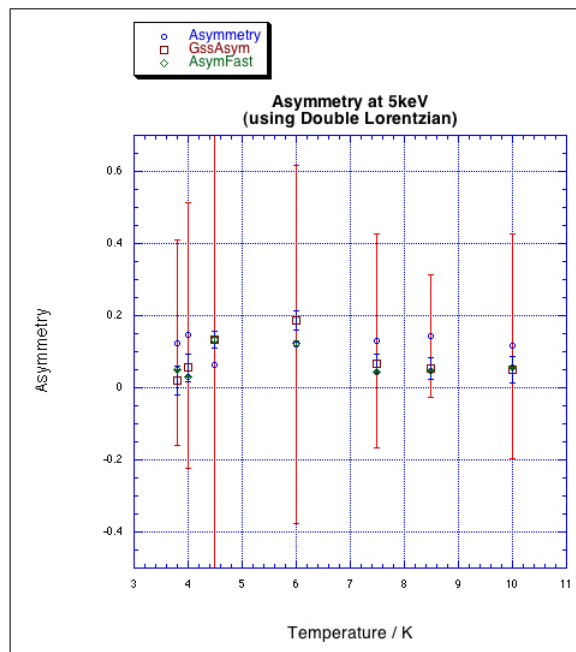


Figure 6.31: Although the fitting at low times is enhanced using two Lorentzian components (normal and fast decaying) in the fitting routine, the overall ability to produce consistent results for the asymmetry is reduced. Here, the normal Lorentzian component is denoted by the blue circles, the fast Lorentzian component by the green diamonds, and the Gaussian component by the red squares. Further analysis has shown that by fixing the Gaussian components the Lorentzian components produce spurious values.

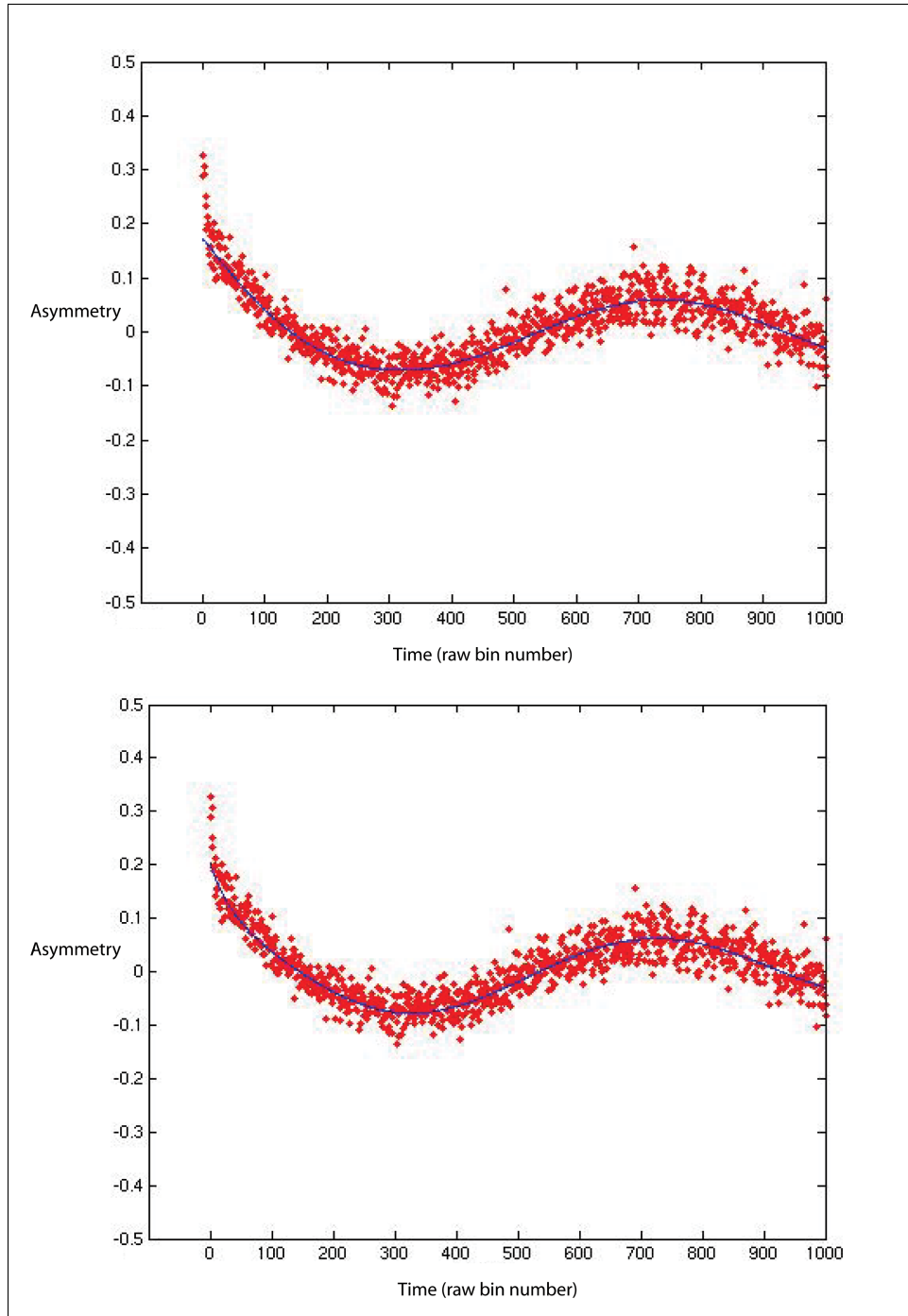


Figure 6.32: *Top* : At 3.8K, 5keV the time domain data is fitted using a Lorentzian + Gaussian fitting routine. *Bottom* : By using two Lorentzian terms and a Gaussian term to fit the time domain  $\mu$ SR data it is possible to improve the fit at low times, close to  $t=0$ s. However, using this method produces results that are spurious as a function of temperature (see text and Figures 6.31 and 6.33).

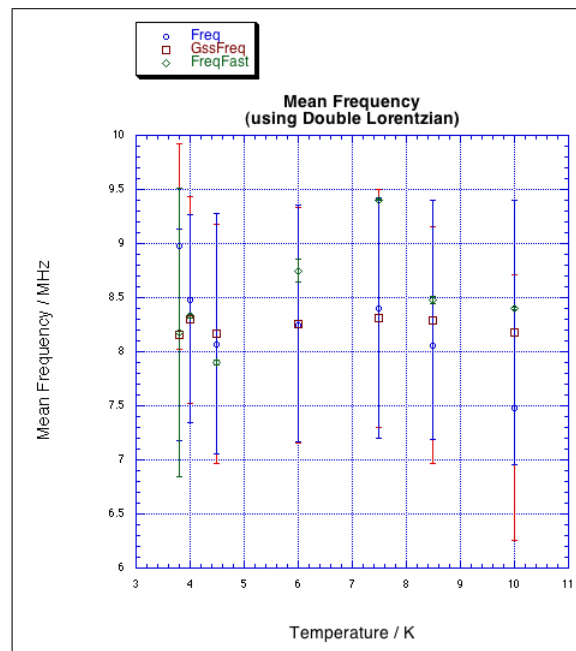


Figure 6.33: Again, like the asymmetry plot of Figure 6.31, the use of two Lorentzian components (normal and fast decaying) is not satisfactory enough to produce consistent results for the mean frequency, despite its ability to improve the fit at times  $< 0.05\mu\text{s}$ . Here, the normal Lorentzian component of the mean frequency/field is denoted by the blue circles, the fast Lorentzian component by the green diamonds and the Gaussian component by the red squares.

# Bibliography

- Abrikosov, A. A. (1957), ‘On the magnetic properties of superconductors of second kind’, *Sov. Phys. JETP* **5**.
- Aegeter, C. M. *et al.* (1996), ‘Dimensional crossover in the magnetic phase diagram of  $\text{Bi}_{2.15}\text{Sr}_{1.85}\text{CaCu}_2\text{O}_{8+\delta}$  crystals with different oxygen stoichiometry.’, *Phys. Rev. B* **54**(22), 15661.
- Aegeter, C. M. *et al.* (1998), ‘Evidence for a square vortex lattice in  $\text{Sr}_2\text{UO}_4$  from muon-spin-rotation measurements’, *Journal of Phys.: Cond. Matt.* **10**(33), 7445.
- Anderson, P. W. & Suhl, H. (1959), ‘Spin alignment in the superconducting state’, *Phys. Rev.* **116**(4), 898.
- Ashcroft, N. W. & Lekner, J. (1966), ‘Structure and Resistivity of liquid metals.’, *Phys. Rev.* **145**, 83.
- Bardeen, J. Cooper, L. N. & Schrieffer, J. R. (1957), ‘Theory of superconductivity’, *Phys. Rev.* **108**(5), 1175.
- Barford, W. & Gunn, J. M. F. (1988), ‘The theory of the measurement of the London penetration depth in uniaxial type II superconductors by muon spin rotation’, *Physica C* **156**, 515.
- Bean, C. P. (1962), ‘Magnetization of hard superconductors’, *Phys. Rev. Lett.* **8**(6).
- Bednorz, J. G. & Muller, K. A. (1987), ‘Possible high  $T_c$  superconductivity in the BaLaCuO system’, *Z. Physik* **64**(189).
- Bernhard, C. *et al.* (1995), ‘Anisotropy and dimensional crossover of the vortex state in  $\text{Bi}_2\text{Sr}_2\text{CaCu}_2\text{O}_{8+\delta}$  crystals.’, *Phys. Rev. B* **52**(10), R7050.
- Blasius, T. *et al.* (1999), ‘Evidence for a two-stage melting transition of the vortex matter in  $\text{Bi}_2\text{Sr}_2\text{CaCu}_2\text{O}_{8+\delta}$  single crystals obtained by muon spin rotation.’, *Phys. Rev. Lett.* **82**(24), 4926.
- Blasius, T. *et al.* (2000), ‘Low-temperature vortex structures of the mixed state in underdoped  $\text{Bi}_2\text{Sr}_2\text{CaCu}_2\text{O}_{8+\delta}$ .’, *Physica B* **289**, 365.
- Blatter, G. *et al.* (1994), ‘Vortices in high-temperature superconductors’, *Rev. Mod. Phys.* **66**(4).

## Bibliography

---

- Blatter, G. *et al.* (1996), ‘Low-field phase diagram of layered superconductors: The role of electromagnetic coupling’, *Phys. Rev. B* **54**(1).
- Blundell, S. (2001), *Magnetism in Condensed Matter*, Oxford University Press.
- Blundell, S. J. & Bland, J. A. C. (1992), ‘Polarized neutron scattering: An optical matrix method.’, *Phys. Rev. B* **46**, 3391.
- Brandt, E. H. (1988), ‘Magnetic field density of perfect and imperfect flux line lattices in type II superconductors. I. Application of periodic solutions’, *Journal of Low Temp. Phys.* **73**, 355.
- Brandt, E. H. (1991), ‘Magnetic-field variance in layered superconductors’, *Phys. Rev. Lett.* **66**(24).
- Brandt, E. H. (1997), ‘Precision Ginzburg-Landau solution of ideal vortex lattices for any induction and symmetry’, *Phys. Rev. Lett.* **78**(11), 2208.
- Bruno, P. (1999), ‘Theory of interlayer exchange interactions in magnetic multilayers’, *Journal of phys.: Cond. matt.* **11**, 9403.
- Bruno, P. & Chappert, C. (1991), ‘Oscillatory coupling between ferromagnetic layers separated by a nonmagnetic metal spacer’, *Phys. Rev. Lett.* **67**(12), 1602.
- Buck, B. & MacCaulay, V. A., eds (1994), *Maximum Entropy in Action*, Second edn, Oxford.
- Cava, R. J. *et al.* (1987), ‘Bulk superconductivity at 36K in  $\text{La}_{1.8}\text{Sr}_{0.2}\text{CuO}_4$ ’, *Phys. Rev. Lett.* **58**(4).
- Chadwick, J. (1932), ‘Possible existence of a neutron’, *Nature* **192**, 312.
- Chaikin, P. M. Lubensky, T. C. (1995), *Principles of condensed matter physics*, Cambridge.
- Chikumoto, N. *et al.* (1998), ‘Magnetic studies on the field-driven transition from decoupled to coupled pancake vortex phase in  $\text{Bi}_2\text{Sr}_2\text{CaCu}_2\text{O}_8$  with columnar defects.’, *Phys. Rev. B* **57**(22), 14507.
- Christen, D. K. *et al.* (1977), ‘Study of the intermediate mixed state in niobium by small angle neutron scattering’, *Phys. Rev. B* **15**(9), 4506.
- Civale, L. *et al.* (1991), ‘Vortex confinement by columnar defects in  $\text{YBa}_2\text{Cu}_3\text{O}_7$  crystals: Enhanced pinning at high fields and temperatures’, *Phys. Rev. Lett.* **67**(5).
- Clem, J. R. (1991), ‘Two-dimensional vortices in a stack of thin superconducting films: A model for high-temperature superconducting multilayers’, *Phys. Rev. B* **43**(10), 7837.
- Colson, S. *et al.* (2004), ‘Vortex liquid transition in  $\text{Bi}_2\text{Sr}_2\text{CaCu}_2\text{O}_{8+\delta}$  with a high density of strong pins’, *Phys. Rev. B* **69**.
- Cooper, L. N. (1956), ‘Bound electron pairs in a degenerate fermi gas’, *Phys. Rev.* **104**, 1189.

## Bibliography

---

- Cox, S. F. J. (1984), *Muons in Pions and Materials Research*, North Holland.
- Cubitt, R. (1994), *Ph.D Thesis*, University of Birmingham, U.K.
- Curie, P. (1895), 'Magnetic properties of materials at various temperatures', *Ann. Chim. et Phys.* **7**(5), 289.
- Daemen, L. L. *et al.* (1992), 'Flux line lattice in uniaxial superconductors at low magnetic inductions.', *Phys. Rev. B* **46**(6).
- De Gennes, P. G. (1966), 'Coupling between ferromagnets through a superconducting layer', *Phys. Lett.* **23**(1), 10.
- Dewhurst, G. (2007), 'GRASP programme for SANS analysis: (<http://www.ill.eu/instruments-support/useful-tools/grasp/>)'.
- Divakar, U. *et al.* (2004), 'Direct observation of the flux-line vortex glass phase in a type II superconductor', *Phys. Rev. Lett.* **92**(23), 237004.
- Dobrzynski, L. & Blinowski, K. (1994), *Neutrons and solid state physics*, Ellis Horwood Series.
- Don McK., P. *et al.* (1993), 'The flux line lattice in high temperature superconductors.', *Physica B.* **192**, 70.
- Drew, A. J. (2005a), Neutron Scattering and Muon-Spin rotation studies of superconducting materials., PhD thesis, University of St. Andrews.
- Drew, A. J. *et al.* (2005b), 'Coexistence and coupling of superconductivity and magnetism in thin film structures', *Phys. Rev. Lett.* **95**, 197201.
- Edwards, D. M. *et al.* (1991), 'Oscillations of the exchange in magnetic multilayers as an analogue of de Haas-van Alphen effect', *Phys. Rev. Lett.* **67**(4), 493.
- Feinberg, D. (1994), 'Vortex lines in layered superconductors: I: From 3d to 2d behaviour.', *J. Phys. III, France* **4**, 169.
- Fisher, D. S. *et al.* (1991), 'Thermal fluctuations, quenched disorder, phase transitions, and transport in type II superconductors', *Phys. Rev. B* **43**(1), 130.
- Fisher, M. P. A. *et al.* (1989), 'Boson localization and the superfluid-insulator transition', *Phys. Rev. B* **40**(1).
- Ford, G. W. & Mullin, C. J. (1957), 'Scattering of polarized dirac particles on electrons', *Phys. Rev.* **108**(2), 477.
- Forgan, E. M. (1998), *Small Angle neutron scattering experiments on vortices in copper oxide superconductors*, (edited by A. Furrer). Kluwer, Dordrecht.
- Forgan, E. M. *et al.* (1995), 'Comment on vortex dynamics and melting in Niobium.', *Phys. Rev. Lett.* **74**(9).

## Bibliography

---

- Frisch, H. L. & Salsburg, Z. W. (1968), *Simple Dense Fluids*, Academic Press.
- Fulde, P. & Ferrell, A. (1964), ‘Superconductivity in a strong spin exchange field’, *Phys. Rev.* **135**, A550.
- Giamarchi, T. & Bhattacharya, S. (2001), ‘Vortex phases’, *Cond. Matt.* p. 0111052.
- Giamarchi, T. & Le Doussal, P. (1995), ‘Elastic theory of flux lattices in the presence of weak disorder.’, *Phys. Rev. B* **52**(2), 1242.
- Giller, D. *et al.* (1997), ‘Disorder-induced transition to entangled vortex solid in Nd-Ce-Cu-O crystal.’, *Phys. Rev. Lett.* **79**(13), 2542.
- Ginzburg, V. L. & Landau, L. D. (1950), ‘On the theory of superconductivity’, *Zh. Eksp. Teor. Fiz.* **20**, 1064.
- Glazman, L. I. & Koshelev, A. E. (1991), ‘Thermal fluctuations and phase transitions in the vortex state of a layered superconductor’, *Phys. Rev. B* **43**(4), 2835.
- Greer, A. J. & Kossler, W. J., eds (1995), *Low Magnetic Fields in Anisotropic Superconductors*, First edn, Springer.
- Haken, H. & Wolf, H. C. (2000), *The physics of Atoms and Quanta*, Springer.
- Hansen, J. P. & MacDonald, I. R. (1986), *Theory of simple liquids*, Academic Press.
- Harshman, D. R. *et al.* (1987), ‘Generation of slow positive muons from solid rare-gas moderators’, *Phys. Rev. B* **36**(16), 8850.
- Harshman, D. R. *et al.* (1991), ‘Magnetic penetration depth and flux dynamics in  $\text{Bi}_2\text{Sr}_2\text{CaCu}_2\text{O}_{8+\delta}$ ’, *Phys. Rev. Lett.* **67**(22), 3152.
- Houghton, A. *et al.* (1989), ‘Flux lattice melting in high- $T_c$  superconductors’, *Phys. Rev. B* **40**(10).
- Jackson, T. J. *et al.* (2000), ‘Depth resolved profile of the magnetic field beneath the surface of a superconductor with a few nm resolution’, *Phys. Rev. Lett.* **84**(21), 4958.
- Jaynes, E. T. (1957), ‘Information theory and statistical mechanics’, *Phys. Rev.* **106**(4), 620.
- Jiang, J. S. *et al.* (1995), ‘Oscillatory superconducting transition temperature in Nb/Gd multilayers’, *Phys. Rev. Lett.* **74**(2), 314.
- Jiang, J. S. *et al.* (1996), ‘Superconducting transition in Nb/Gd/Nb trilayers’, *Phys. Rev. B* **54**(9), 6119.
- Kasuya, T. (1956*a*), ‘Electrical resistance of ferromagnetic metals’, *Prog. Theor. Phys.* **16**, 58.
- Kasuya, T. (1956*b*), ‘A theory of metallic ferro and antiferromagnetism on Zerner’s model’, *Prog. Theor. Phys.* **16**, 45.

## Bibliography

---

- Khasanov, R. *et al.* (2008), ‘B-T phase diagram of (Pb,Bi)(Sr,La)CuO<sub>8+δ</sub> investigated with  $\mu$ SR and ARPES.’, *To be submitted*.
- Khaykovich, B. *et al.* (1997), ‘Vortex phase transitions in Bi<sub>2</sub>Sr<sub>2</sub>CaCu<sub>2</sub>O<sub>8-δ</sub>: Effects of weak disorder’, *Phys. Rev. B* **56**, 517.
- Khusainov, M. G. & Proshin, Y. N. (1997), ‘Possibility of periodically reentrant superconductivity in ferromagnet/superconductor layered structures’, *Phys. Rev. B* **56**(22), 14283.
- Khusainov, M. G. & Proshin, Y. N. (2000), ‘Errata: Possibility of periodically reentrant superconductivity in ferromagnet/superconductor layered structures’, *Phys. Rev. B* **62**(10), 6832.
- Klein, M. L. & Venables, J. A. (1976), *Rare Gas Solids*, Academic Press, New York.
- Klein, T. *et al.* (2001), ‘A Bragg glass phase in the vortex lattice of a type II superconductor.’, *Nature* **413**, 404.
- Klemm, R. A. *et al.* (1974), ‘The upper critical field of layered superconductors.’, *J. Low. Temp. Phys.* **16**.
- Koorevaar, P. *et al.* (1994), ‘Decoupling of superconducting V by ultrathin Fe layers in V/Fe multilayers’, *Phys. Rev. B* **49**(1), 441.
- Koshelev, A. E. *et al.* (1996), ‘Columnar defects and vortex fluctuations in layered superconductors’, *Phys. Rev. B* **53**(14).
- Krupicka, S. & Sternberg, J. (1968), *Elements of Theoretical Magnetism*, Iliffe Books Ltd.
- Langevin, P. (1905a), ‘Magnetisme et theorie des electrons’, *Ann. Chim. et Phys.* **5**, 70.
- Langevin, P. (1905b), ‘Sur la theorie du magnetisme’, *Journ. de Phys.* **4**, 678.
- Larkin, A. I. & Ovchinnikov, Y. N. (1964), ‘Inhomogeneous state of superconductors (Production of superconducting state in ferromagnet with Fermi surfaces, examining Green function)’, *Zh. Eksp. Teor. Fiz.* **47**, 1136.
- Lattes, C. M. G. *et al.* (1947), ‘Processes involving charged mesons’, *Nature* **159**, 694.
- Lawrence, W. E. & Doniach, S. (1971), ‘Theory of layer-structure superconductors’, *Proc. 12th Int. Conf. Low Temp. Phys.* **12**.
- Le Cochee, J. *et al.* (2000), ‘Effect of doping on the linear temperature dependence of the magnetic penetration depth in cuprate supraconductors’, *Cond. Matt.* **0001045**.
- Lee, K. H. *et al.* (1993a), ‘Flux pinning and phase transitions in model high-temperature superconductors with columnar defects’, *Phys. Rev. B* **48**(2), 1233.

## Bibliography

---

- Lee, S. L. *et al.* (1993*b*), ‘Evidence of flux lattice melting and a dimensional crossover in single-crystal  $\text{Bi}_2\text{Sr}_2\text{CaCu}_2\text{O}_{8+\delta}$  from muon spin rotation studies’, *Phys. Rev. Lett.* **71**(23).
- Lee, S. L. *et al.* (1993*c*), ‘Role of electromagnetic coupling in the low-field phase diagram of  $\text{Bi}_2\text{Sr}_2\text{CaCu}_2\text{O}_{8+\delta}$ ’, *Phys. Rev. B* **48**(17).
- Lee, S. L. *et al.* (1995), ‘Evidence for two-dimensional thermal fluctuations of the vortex structure in  $\text{Bi}_2\text{Sr}_2\text{CaCu}_2\text{O}_{8+\delta}$  from muon spin rotation measurements’, *Phys. Rev. Lett.* **75**(5).
- Lee, S. L. *et al.* (1998), ‘Observations of suppression of static and dynamic disorder in  $\text{Bi}_{2.15}\text{Sr}_{1.85}\text{CaCu}_2\text{O}_{8+\delta}$  crystals by columnar defects’, *Phys. Rev. Lett.* **81**(23).
- Lee, S. L., Kilcoyne, S. H. & Cywinski, R., eds (1999*a*), *Muon Science. Muons in physics, chemistry and materials*, IOP Bristol.
- Lee, S. L., Kilcoyne, S. H. & Cywinski, R., eds (1999*b*), *Muon Science. Muons in physics, chemistry and materials*, IOP Bristol.
- Li, T. W. *et al.* (1994), ‘Growth of  $\text{Bi}_2\text{Sr}_2\text{CaCu}_2\text{O}_{8+\delta}$  single crystals at different oxygen ambient pressures’, *Cryst. Grow.* **135**(3).
- Lister, S. J. (2007). Private Communication.
- London, F. & London, H. (1935), ‘The electromagnetic equations of the superconductor’, *Proc. Roy. Soc.(London) A* p. 71.
- Luetkens, H. (2007). Private Communication.
- Luetkens, H. *et al.* (2003), ‘Observation of the conduction electron spin polarisation in the Ag spacer of a Fe/Ag/Fe trilayer’, *Phys. Rev. Lett.* **91**(1), 017204.
- Maeno, Y. *et al.* (2004), ‘The intriguing superconductivity of Strontium Ruthenate’, *Physics Today* **54**, 42.
- Majer, D. *et al.* (1995), ‘Separation of the irreversibility and melting lines in  $\text{Bi}_2\text{Sr}_2\text{CaCu}_2\text{O}_{8+\delta}$  crystals’, *Phys. Rev. Lett.* **75**(6), 1166.
- Majewski, P. (1994), ‘BiSrCaCuO High- $T_c$  superconductors’, *Adv. Mat.* **6**(6), 440.
- Martin, D. H. (1967), *Magnetism in solids*, Iliffe Books Ltd., London.
- Martinez, J. C. *et al.* (1992), ‘Magnetic anisotropy of a  $\text{Bi}_2\text{Sr}_2\text{CaCu}_2\text{O}_x$  single crystal’, *Phys. Rev. Lett.* **69**(15).
- McElfresh, M. (1994), *Fundamentals of magnetism and magnetic measurements*, Quantum Design, San Diego.
- Menon, G. I., *et al.* (1999), ‘Muon-spin rotation spectra in the mixed phase of high- $T_c$  superconductors: Thermal fluctuations and disorder effects’, *Phys. Rev. B* **60**, 7607.

## Bibliography

---

- Menon, G. I. *et al.* (2006), ‘Muons as local probes of three-body correlations in the mixed state of type-II superconductors’, *Phys. Rev. Lett* **97**.
- Morenzoni, E. *et al.* (1994), ‘Generation of very slow polarized positive muons’, *Phys. Rev. Lett.* **72**(17), 2793.
- Mühge, T. *et al.* (1996), ‘Possible origin for oscillatory superconducting transition temperature in superconductor/ferromagnet multilayers’, *Phys. Rev. Lett.* **77**(9), 1857.
- Mühge, T. *et al.* (1997), ‘Magnetism and superconductivity in Fe/Nb/Fe trilayers’, *Phys. Rev. B* **55**(14), 8945.
- Mühge, T. *et al.* (1998), ‘Proximity effect in superconductor/ferromagnet layered system. Influence of superconductivity on magnetic properties of Nb/Fe epitaxial bilayers’, *App. Mag. Res.* **14**(4), 567.
- Muller, A. & Bednorz, K. M. (1986), ‘Possible high  $T_c$  superconductivity in the Ba-La-Cu-O system’, *Z. Physik B* **64**, 189.
- Nelson, D. R. & Vinokur, V. M. (1992), ‘Boson localization and pinning by correlated disorder in high temperature superconductors.’, *Phys. Rev. Lett.* **68**(15).
- Nelson, D. R. & Vinokur, V. M. (1993), ‘Boson localisztion and correlated pinning of superconducting vortex arrays.’, *Phys. Rev. B* **48**(17).
- Nideröst, M. *et al.* (1996), ‘Low-field vortex dynamics over seven time decades in a  $\text{Bi}_2\text{Sr}_2\text{CaCu}_2\text{O}_{8+\delta}$  single crystal for temperatures  $13 \leq T \leq 83$  K’, *Phys. Rev. B* **53**(14), 9286.
- Obi, Y. *et al.* (1999), ‘Oscillation phenomenon of transition temperatures in Nb/Co and V/Co superconductor/ferromagnet multilayers’, *Physica C* **317**, 149.
- Ogrin, F. Y. *et al.* (2000), ‘Vortex studies in heavy-ion irradiated  $\text{Bi}_{2.15}\text{Sr}_{1.85}\text{CaCu}_2\text{O}_{8+y}$  probed by  $\mu\text{SR}$  and small-angle neutron scattering.’, *Physica B.* **289**, 355.
- Okun, L. B. (1965), *Weak Interactions of Elementary Particles*, Pergamon, Oxford.
- Onnes, H. K. (1911), ‘The discovery of superconductivity’, *Leiden Comm.* **120**.
- Particle Data Group* (1947), *Particle Properties Data Booklet*, North Holland.
- Pastoriza, H. *et al.* (1992), ‘Two-step transition towards the reversibility region in  $\text{Bi}_2\text{Sr}_2\text{CaCu}_2\text{O}_{8-\delta}$  single crystals’, *Physical Review B* **46**(14), 9278.
- Pauli, W. (1920), ‘Theoretische bemerkungen uber den diamagnetismus einatomiger gase’, *Z. Phys.* **2**, 201.
- Pedersen, J. S. *et al.* (1990), ‘Analytical treatment of the resolution function for small-angle scattering’, *Journal Appl. Cryst.* **23**, 321.

## Bibliography

---

- Potenza, A. & Marrows, C. H. (2005), ‘Superconductor-ferromagnet CuNi/Nb/CuNi trilayers as superconducting spin-valve core structures’, *Phys. Rev. B* **71**, 180503.
- Pratt, F. (2000), ‘WiMDA: A muon data analysis program for the Windows PC’, *Physica B* **289**, 710.
- Prober, D. E. *et al.* (1977), ‘Fluctuation-induced diamagnetism and dimensionality in superconducting layered compounds: TaS<sub>2</sub> and NbSe<sub>2</sub>.’, *Phys. Rev. B* **15**(11).
- Prokscha, T. (1999), ‘ $\mu$ SR studies on thin films with low-energy muons at energies between 0 and 30 keV’, *Proc. of the XXXIII winter school of PNPI* **33**, 313–330.
- Prokscha, T. *et al.* (2005), ‘A new high-intensity, low-momentum muon beam for the generation of low-energy muons at PSI’, *Hyp. Inter.* **159**, 385.
- Prokscha, T. *et al.* (2006), ‘The new high-intensity surface muon beam  $\mu$ E4 for the generation of low-energy muons at PSI’, *Physica B* **374**, 460.
- Rainford, B. D. & Daniell, G. J. (1994), ‘ $\mu$ SR frequency spectra using the maximum entropy method’, *Hyper. Inter.* **87**(1), 1129.
- Riseman, T. M. & Forgan, E. M. (2000), ‘Comparison of maximum entropy and FFTs of  $\mu$ SR data’, *Physica B* **289**, 718.
- Ruderman, M. A. & Kittel, C. (1954), ‘Indirect exchange coupling of nuclear magnetic moments by conduction electrons.’, *Phys. Rev.* **96**(1), 99.
- Rusanov, A. Yu., *et al.* (2004), ‘Enhancement of the superconducting transition temperature in Nb / Permalloy bilayers by controlling the domain state of the ferromagnet’, *Phys. Rev. Lett.* **93**(5), 05002.
- Sato, M. *et al.* (1997), ‘Recoupling of decoupled vortex liquid by columnar defects in Bi<sub>2</sub>Sr<sub>2</sub>CaCu<sub>2</sub>O<sub>8+y</sub>’, *Phys. Rev. Lett.* **79**(19).
- Schenck, A. (1985), *Muon Spin Rotation Spectroscopy*, Adam Hilger Ltd.
- Schilling, A. *et al.* (1993), ‘Irreversibility line of monocrystalline Bi<sub>2</sub>Sr<sub>2</sub>CaCu<sub>2</sub>O<sub>8- $\delta$</sub> : Experimental evidence for a dimensional crossover of the vortex ensemble’, *Phys. Rev. Lett.* **71**(12), 1899.
- Science (2006), ‘Nanocolumns give YBCO wires a big boost’, *Science* **311**, 1850.
- Shannon, C. E. (1948*a*), ‘A mathematical theory of communication’, *Bell. Sys. Tech. J.* **27**, 379.
- Shannon, C. E. (1948*b*), ‘A mathematical theory of communication’, *Bell. Sys. Tech. J.* **27**, 623.
- Sherwood, J. E. *et al.* (1954), ‘Stern-Gerlach experiment on polarized neutrons’, *Phys. Rev.* **96**, 1546.

## Bibliography

---

- Sidorenko, A. D. *et al.* (1990), ‘Muonic study of type II superconductors’, *Hyper. Inter.* **63**(1-4), 49.
- Song, Y. Q. (1995), ‘Vortex fluctuation effects to  $\mu$ SR linewidth in high-temperature superconductor’, *Physica C* **241**(1), 187.
- Song, Y. Q. *et al.* (1993), ‘Low temperature fluctuations of vortices in layered superconductors’, *Phys. Rev. Lett.* **70**(20), 3127.
- Sonier, J. *et al.* (1994), ‘New muon-spin-rotation measurement of the temperature dependence of the magnetic penetration depth in  $\text{YBa}_2\text{Cu}_3\text{O}_{6.95}$ ’, *Phys. Rev. Lett.* **72**(5), 744.
- Sonier, J. *et al.* (1997a), ‘Magnetic field dependence of the london penetration depth in the vortex state of  $\text{YBa}_2\text{Cu}_3\text{O}_{6.95}$ ’, *Phys. Rev. B* **55**(17), 11789.
- Sonier, J. *et al.* (1997b), ‘Measurement of the fundamental length scales in the vortex state of  $\text{YBa}_2\text{Cu}_3\text{O}_{6.60}$ ’, *Phys. Rev. Lett.* **79**(15), 2875.
- Sonier, J. *et al.* (1997c), ‘Muon-spin rotation measurements of the magnetic field dependence of the vortex-core radius and magnetic penetration depth in  $\text{NbSe}_2$ ’, *Phys. Rev. Lett.* **79**(9), 1742.
- Squires, G. L. (1996), *Introduction to the theory of neutron scattering*, Dover.
- Stiles, M. D. (1999), ‘Interlayer exchange coupling’, *Journal of Mag. and Mag. Mat.* **200**, 322.
- Strunk, C. *et al.* (1994), ‘Superconductivity in layered Nb/Gd films’, *Phys. Rev. B* **49**(6), 4053.
- Sugano, R. *et al.* (1998), ‘Field-driven coupling transition in the vortex state of irradiated  $\text{Bi}_2\text{Sr}_2\text{CaCu}_2\text{O}_8$ : Computer simulation study’, *Phys. Rev. Lett.* **80**(13), 2925.
- Thiemann, S. L. *et al.* (1989), ‘Field structure of vortex lattices in uniaxial superconductors’, *Phys. Rev. B* **39**(16).
- Tinkham, M. (1975), *Introduction to superconductivity*, McGraw Hill.
- Van der Beek, C. J. *et al.* (1995), ‘Vortex dynamics in a  $\text{Bi}_2\text{Sr}_2\text{CaCu}_2\text{O}_8$  crystal with columnar defects’, *Phys. Rev. B* **51**(21).
- Vanderah, T. A. (1992), *Chemistry of Superconducting Materials*, Noyes.
- Verbanck, G. *et al.* (1998), ‘Coupling phenomena in superconducting Nb/Fe multilayers’, *Phys. Rev. B* **57**(10), 6029.
- von Laue, M. (1913), ‘Interferenzerscheinungen bei rontgenstrahlen’, *Annalen der Physik* **346**, 971.
- Waldmann, O. *et al.* (1996), ‘Temperature and doping dependence of the penetration depth in  $\text{Bi}_2\text{Sr}_2\text{CaCu}_2\text{O}_{8+\delta}$ ’, *Phys. Rev. B* **53**(17), 11825.

## Bibliography

---

- Wen, H. H. *et al.* (2000), ‘Anomalous magnetization transition accompanying the irreversibility line in high-temperature superconductors’, *Phys. Rev. B* **62**(1), 716.
- Wong, H. K. *et al.* (1986), ‘Superconducting properties of V/Fe superlattices’, *Journal of Low Temp. Phys.* **63**(3-4), 307.
- Wu, M. K. *et al.* (1987), ‘Superconductivity at 93K in a new mixed-phase Y-Ba-Cu-O compound system at ambient temperature’, *Phys. Rev. Lett.* **58**(9).
- Yaouanc, A. *et al.* (1997), ‘Effect of the vortex core on the magnetic field in hard superconductors’, *Phys. Rev. B* **55**(17), 11107.
- Yosida, K. (1957), ‘Magnetic properties of Cu-Mn alloys’, *Phys. Rev.* **106**, 893.
- Zech, D. *et al.* (1995), ‘Correlation of flux lines in single-crystal  $\text{Bi}_2\text{Sr}_2\text{CaCu}_2\text{O}_{8+\delta}$  with columnar defects’, *Phys. Rev. B* **52**(9).
- Zech, D. *et al.* (1996), ‘Phase diagram of  $\text{Bi}_2\text{Sr}_2\text{CaCu}_2\text{O}_x$  in the presence of columnar defects’, *Phys. Rev. B* **54**(9).
- Zeldov, E. *et al.* (1995), ‘Thermodynamic observation of first-order vortex lattice melting transition in  $\text{Bi}_2\text{Sr}_2\text{CaCu}_2\text{O}_{8-\delta}$ ’, *Nature* **375**, 373.
- Zhou, S. & Ruckenstein, E. (2000), ‘High-order direct correlation functions of uniform fluids and their application to the high-order perturbative density functional theory’, *Phys. Rev. E* **61**(3).